ENHANCED OIL RECOVERY THROUGH INTEGRATION OF ULTRASOUND AND POLYMER FLOODING

Kabiru Jega HASSAN

Ph.D. Thesis **2020**

ENHANCED OIL RECOVERY THROUGH INTEGRATION OF ULTRASOUND AND POLYMER FLOODING

Kabiru Jega HASSAN

School of Science, Engineering and Environment
The Petroleum and Gas Engineering Division
University of Salford, Manchester, UK

Submitted in Partial Fulfilment of the Requirements for the Degree of Doctor of Philosophy,

December 2020

Abstract

Initially, when an oil well is drilled the oil gushes to the surface at high pressure. However, with time the pressure declines leaving more than 50% of the oil trapped in the reservoir. Even with the introduction of current technologies, more than 40% of the oil remains unrecoverable. Enhanced oil recovery from these mature and declining oilfields is receiving extensive research attention. Cost effectiveness and environmental impact are vital factors for consideration. Ultrasound application, as a cheap and environmentally friendly recovery method, is independently being investigated, to a limited extent, in enhanced oil recovery. Other forms of enhanced oil recovery that employ chemical injection including polymer flooding are being studied separately, but full potentials and mechanisms involved are yet to be fully understood. It is in view of this, that this experimental investigative research combined both ultrasound and polymer flooding, as a novel and innovative approach for increasing the overall recovery from carbonate and sandstone reservoirs at petroleum reservoir conditions.

The methodology involved petrophysical and geophysical analysis. The petrophysical analysis included interfacial tension measurements and characterisation of hydrolysed polymer acrylamide polymer solutions. The geophysical analysis characterised the pore properties of sandstones and carbonates. The other components of the methodology entailed the investigation of oil recovery from polymer flooding without ultrasound, and polymer flooding with ultrasound as well as the evaluation of enhanced oil recovery (EOR).

Hydrolysed polyacrylamide (HPAM) polymer solutions of varying molecular weight ranging from 6 million Daltons to 23 million Daltons were characterised through analysis of the viscosity and viscoelastic properties at different concentrations. HPAM polymer solution concentrations were 400ppm, 800ppm, 1200ppm, 1600ppm and 2000ppm. The viscosity, viscoelasticity as well as hysteresis behaviour increased with increased concentration.

Sandstone and carbonate reservoir rocks were subjected to computed tomography scans to determine and confirm pore size and pore distribution. The scan images obtained were reconstructed with VG MAX 2.2 Volume graphics to determine pore properties. The sandstone core samples were Berea upper and Berea lower, and the carbonates were Guleph dolostone, Indiana Limestone and Edward brown. The scans indicated the confirmation of the presence of interconnected pores. Sandstones showed greater pore uniformity than carbonates.

An acoustic core holder and signal power amplifier were used to generate ultrasound waves. The frequency of the waves ranged from 20 to 100KHz. Preliminary core flooding indicated highest power, intensity and fluid displacement occurred at a frequency of 20±0.5 KHz. Thus, subsequent core floods were conducted at 20±0.5 KHz.

Two displacement positions were considered with UFS-200 core flooding equipment: horizontal displacement and vertical displacement. In both displacement scenarios, the highest oil recovery was obtained from the sandstone cores irrespective of the pore volume injected when compared with carbonate core oil recovery. The highest recovery for sandstones was 80% and 68% for carbonates. High differential pressures were obtained in all the carbonate core samples with the application of 400ppm HPAM and lower differential pressure in sandstones. This was attributed to the anionic charge of HPAM and the cationic charge of carbonates leading to blockage of the interconnected pores and potential for formation damage. The utilisation of 400ppm HPAM solution during core flooding enhanced safety and minimised the potential for pore blockage as well as reduced potentials for excessive pressure generation.

The application of ultrasound and polymer flooding simultaneously showed improved oil recovery in sandstone and carbonates. The acoustic coupling potential of HPAM was confirmed as wave transmission improvement was observed. However, the use of anionic HPAM for carbonate reservoirs was deemed unfavourable in oil recovery.

Declaration

Unless otherwise stated, the work in this thesis is that of the author, and has not previously been submitted in part or in whole, in this or in any other work

Author:

Kabiru Jega Hassan …. ……

Supervisors:

Dr Godpower C Enyi……

Professor Ghasem G. Nasr…….

List of Publications and conference papers

- **Publications (In press and under review)**

1. Hassan, K. J; Enyi, C.G. and Nasr G. G. (2020) Residual oil desaturation potential of hydrolysed polyacrylamide polymer solutions, Journal of Petroleum Science and Engineering

2. Hassan, K. J, Enyi, C.G. and Nasr G. G. (2020) Green technology: Ultrasound enhanced oil recovery in sandstone and carbonate reservoirs. Journal of Petroleum Science and Engineering

3. Hassan, K. J; Enyi, C.G. and Nasr G.G. (2020) Hysteresis and polymer polydispersity for Design and Rheological Characterisation of HPAM Polymer solutions for enhanced oil recovery

- **Conference Presentations**

1. Hassan, K. J; Enyi, C.G. and Nasr G. G. (2019) Hydrolysed polyacrylamide polymer solution for residual oil desaturation, 8th International conference on Petrochemistry and Oil-Gas Marketing, Amsterdam, Netherlands.

2. Hassan, K. J; Enyi, C.G. and Nasr G. G. (2019) Sound to Pound, Salford Postgraduate Research Conference, Media City, University of Salford, United Kingdom

3. Hassan, K. J; Enyi, C.G. and Nasr G. G. (2018) Viscosity and viscoelasticity of Hydrolysed polyacrylamide polymer solutions for Enhanced oil recovery, Salford Postgraduate Research Conference, Media City, University of Salford, United Kingdom

Acknowledgement

I would like to start by saying “Alhamdulillah” thanking God Almighty for seeing me to the end of this very successful research journey leading to this thesis. It has indeed been full of challenges, but Allah’s strength and guidance has seen me through.

To my supervisors: Dr Godpower C. Enyi and Professor Ghasem G. Nasr I truly appreciate your immensurable support and guidance throughout the years of the PhD journey. I have learnt a lot that would shape me for a distinguished and excellent future.

The Doctoral School and the university administration and support staff were always available to give a helping hand, I am most grateful to you all.

To my parents, family, friends and colleagues: you have been most supportive right from the onset- giving advice and prayers as well as motivating me always to keep going when the road got tougher.

Mr Allan Mappin, the experiments conducted in this research would have been difficult without your timely and immense support. You always made sure that the right materials and equipment accessories were procured. And to the companies that provided me free materials, I thank you immensely.

Last but certainly not least, I thank the Petroleum Technology Development Fund (PTDF) and the University of Salford for supporting my research.

Table of Contents

Nomenclature

Q	Volumetric flow rate (mL/min)
P	Permeability (Darcy)
P_a	Outlet pressure (psi)
P_b	Inlet pressure (psi)
μ	Viscosity (cp)
L	Length of core sample (cm)
ρ	Density (Ib/ft^3)
F	Force (N)
x, y	Space variables
U	Small displacement (ft)
c_f	Compressibility
μ_f	Fraction of the pore volume
D	Effective elastic tensor of the rock
$E(U)$	Elastostatic tensor (strain)
A^i	Elemental pore volume (ft^3)
α^i	Stress tensor on the pore component
P	Pressure of fluid (psi)
ΔP	Pressure drop
W	Small rock displacement
τ	the shear stress (lb/100ft^2),
K	consistency factor (cp)
γ	shear rate (s^{-1})
n	fluid behaviour index (dimensionless)

List of Figures

List of Tables

CHAPTER ONE
INTRODUCTION

1.1 Introduction

The growing desire to obtain maximum recovery of hydrocarbon from the reservoir at minimum cost, with least environmental impact has become a central point for oil production activities. Ultrasound application as a technique for enhancing oil recovery, which possess virtually little or no environmental impact and low cost of the equipment, is fast gaining acceptance across the world-from Asia to North America and Europe (Abdulfatah, 2018; Agi, Junin, & Chong, 2018; Meribout, 2018; Mullakaev, Abramov, & Abramova, 2015; Wang, Xu, & Suman, 2015). The process involves stimulating the reservoir with acoustic waves referred to as ultrasound waves to increase recovery and productivity from the reservoir. Various theories have been postulated to account for the increase in recovery in the reservoir when subjected to ultrasound, however, the exact mechanisms involved are yet to be fully understood.

The procedure to enhance recovery using ultrasound first came into limelight in 1964 when researchers (Duhon & Campbell, 1965) through flooding of Torpedo sandstone core using diesel oil (SAE oil) with saline water, witnessed an increase in the recovery of oil. The magnitude of the sonic frequency was varied, and the oil recovery was measured. Here, an attempt was made to highlight and explain the mechanisms involved in enhancing flow in the porous media. Many factors were proposed namely cavitation, emulsification, coagulation, and chemical reaction as being major contributors to the enhancement of recovery.

Engineers and scientists thereupon, have taken interest and conducted a series of experiments to try to understand as well as explain the mechanisms behind the phenomenal recovery from the reservoir when stimulated with acoustic waves- ultrasound.

In one of the pioneer researches (Biot, 1956) in the study of the behaviour of acoustic waves in a porous media, the theory of the propagation of elastic waves in a fluid saturated porous media, three different types of waves were associated with an acoustic wave namely; two dilatational waves and the other a rotational wave. The concept is that of stresses and tensors being impacted on the porous media and fluid. The theory was for both high frequency and

low frequency ranges. Because of the nature of porous medium, many assumptions were made to enable mathematical simulations to develop particular wave equations that would explain the behaviour of acoustic waves. These assumptions include uniformity of pore sizes and distribution such that for all cross sections in the isotropic porous medium the ratio of the fluid area to that of the solid is the same. Other assumptions are that the fluid in the pore was taken as incompressible which is quite unrealistic since a large number of porous mediums have or possess compressible fluids. The existence of deficiencies were also highlighted by several other researchers (Diallo & Appel, 2000; Jack Dvorkin, Richard, Nolen-Hoeksema, & Nur, 1994). This, therefore, supports the case for experimental analysis rather than numerical analysis to fully comprehend the behaviour of acoustic waves in a petroleum reservoir. Therefore, the bulk of the work in this thesis is centred on experimental analysis of results obtained rather than numerical analysis to fully comprehend the mechanisms involved in recovery enhancement from the petroleum reservoir.

Several experiments have been conducted to investigate the mechanisms of ultrasound enhanced oil recovery through imbibition (Hamida & Babadagli, 2005, 2007, 2008a, 2008b; Hamidi, Mohammadian, Rafati, Azdarpour, & Ing, 2015; K. Naderi & Babadagli, 2008; Khosrow Naderi & Babadagli, 2010), core flooding (Alhomadhi, Amro, & Almobarky, 2013; Amro, Al Mobarky, & Al-Homadhi, 2007; Duhon & Campbell, 1965; Mohammadian, Junin, Rahmani, & Idris, 2013; Mohammadian, Shirazi, & Idris, 2011), and pendant drop (Hamida & Babadagli, 2005, 2008b). Other researchers (Hamida & Babadagli, 2005, 2008a; Junin et al., 2014) have also included the use of the Henshaw method in which two permeable layers were used as porous media to study the effects of ultrasound on the porous medium. However, none of these experiments included the utilisation of an additional viscous medium to increase oil displacement and overall oil recovery.

The development of downhole facilities to provide ultrasonic stimulation is actively being pursued based on early research (Wang et al., 2015). However, full laboratory explanation of the phenomenon is yet to be fully understood.

Recent developments in ultrasound have seen combination with other chemicals such as CO_2 and low salinity applications to enhance oil recovery. Staged and intermittent application of ultrasound on the reservoir has also received attention (Abdulfatah, 2018; Agi et al., 2018).

A numerical experiment was conducted using the finite element method (FEM). The experiment determined pore fluid wave motion within a one-dimensional fluid-saturated

porous permeable elastic solid medium which is embedded in a non-permeable elastic semi-infinite solid (Jeong, Kallivokas, Huh, & Lake, 2014). The numerical experiment indicated the viability of elastic vibrational wave stimulation to mobilise trapped oil in heterogeneous reservoir. The numerical analysis supported and proposed the potential introduction of an elastic displacing front with favourable mobility ratio was to complement wave stimulation. Polymer flooding which alters the mobility ratio adequately fits this scenario. Therefore, this experimental research is centred on the hypothesis that the integration of ultrasound elastic wave for vibro-mechanical stimulation of the reservoir and polymer flooding for favourable mobility ratio leads to increased oil displacement and enhanced oil recovery.

1.2 Contribution to Knowledge

The contribution to knowledge in this work hinges on the non-existence in the literature reviewed including all available publications studied where ultrasound had been utilised in conjunction with polymer flooding to enhance oil recovery at reservoir conditions. All the experiments conducted to address the mechanism of improved oil recovery have shown limitations of varying degree. There is no adequate correlation between the oil recovery and ultrasound with polymer at reservoir pressures. In addition, all the previous experiments conducted were limited to surface conditions and sandstone formations. Limestone and Dolomite were inadequately studied in ultrasound oil recovery. In Appendix A, the knowledge gaps and limitations of previous research are presented. This research catered for all the three major reservoir formations for proper assessment and determination of the effect of ultrasound on pore pressures and the role of rock microstructure on recovery. The oil recovery from ultrasound wave vibrations and polymer flooding is investigated for sandstone and carbonate reservoir formations with a view to maximise as well as enhance oil recovery.

1.3 Aim and Objectives

1.3.1 Aim

The aim of this research is to investigate enhanced oil recovery (EOR) through the integration of ultrasound and polymer flooding in sandstone and carbonate reservoirs.

1.3.2 Objectives

The objectives of this research are enumerated:

(i) Determination of the petrophysical properties namely, interfacial tension, viscosity and viscoelasticity and hysteresis behaviour of hydrolysed polyacrylamide solutions for enhanced oil recovery

(ii) Determination of the role of microstructure and porosity in a reservoir stimulated with ultrasound and polymer flooding for enhance oil recovery by conducting computed tomography scans and volume graphic reconstruction on limestone, sandstone and dolostone cores for pore characteristics

(iii) Investigation of the effects of ultrasound on reservoir pore pressure (differential pressure) across the different types of conventional reservoirs

(iv) Determination of the oil recovery from the integration of ultrasound and polymer flooding with a view to maximise oil recovery from saturated cores.

1.4 Justification

(i) There is a global demand for green and low-cost recovery methods of EOR that minimise environmental impact and give high oil recovery, which is applicable to ultrasound

(ii) The existence of gaps in the theories and experiments conducted to explain the mechanism of ultrasound enhanced oil recovery necessitates further research.

(iii) The absence of comprehensive experimental data for ultrasound enhanced oil recovery as it relates to the three reservoir formations sandstones, limestones and dolostones. All previous researchers have either investigated sandstones or in a few cases limestone, but none has considered the effect of lithology of the three reservoir formations-sandstone, limestones and dolostones. Hence, there is a wide gap in the understanding of the behaviour of reservoir fluids when subjected to acoustic waves in petroleum reservoirs.

(iv) No information has been published or research is available where the laboratory experiments where conducted at reservoir conditions in the investigation of ultrasound waves (Ghamartale, Escrochi, Riazi, & Faghih, 2019; Gil Cidoncha, 2007). Hence, this novel approach will open an entire new frontier in EOR with acoustics.

(v) Insufficient in-depth research conducted using varying reservoir oil displacement scenarios to determine the mechanisms and reservoir oil displacement behaviour of ultrasound enhanced oil recovery (Alhomadhi et al., 2013).

(vi) Numerous papers have described the use of polymer with acoustics as being impracticable due to the disintegration of the polymer as a result of the vibrations (Rambeau, Alves, Andreu, Loriau, & Passade-Boupat, 2016). However, it is the informed view of this researcher that since ultrasound could increase permeability and effective porosity, it is practicable that polymer flooding can be used after the reservoir has been stimulated to increase vertical sweep in the reservoir. Hence, in this research polymer flooding coupled with ultrasound waves were used to further buttress the benefits of integrated approach.

(vii) New initiatives are advocating for the combination of ultrasound with other chemicals (Meribout, 2018) to enhance oil recovery. Furthermore, a numerical analysis conducted on the application of ultrasound, supports increasing the displacement fluid mobility ratio (Jeong et al., 2014). Hydrolysed polyacrylamide polymer has the properties for increasing the fluid mobility. The combination of ultrasound with polymer as proposed in this research is within new global research area in enhanced oil recovery.

1.5 Structure of Thesis

This thesis is structured based on five chapters: Chapter One Introduction, Chapter Two Literature Review and Governing Principles, Chapter Three Materials, Apparatus and Methodology, Chapter Four Results and Discussions and Chapter Five Conclusions and Recommendations. Each chapter has an introduction for the reader on what to expect and at the end, a short summary of the contents of the chapter.

Chapter One: Introduction. A general background information on acoustics and ultrasound in enhanced oil recovery and its development over the years. It highlights key research work undertaken in ultrasound and recent developments. It links ultrasound to polymer flooding as well as gives a brief background on polymer flooding. Key headings in Chapter One include Aims and Objectives, Contribution to Knowledge, Justification and Structure of thesis.

Chapter Two: Literature Review and Governing Principles. In this chapter the main types of petroleum reservoirs and their characteristics are discussed. The oil recovery drive mechanisms starting from primary to secondary and tertiary are detailed. In addition, reservoir properties in terms of porosity and fluid mechanics are highlighted. Acoustics and polymer flooding are discussed extensively. The principles and theories on acoustics are comprehensively detailed. The mode of ultrasound wave propagation and related equations for its transport in porous media are discussed. Similarly, principles related to computed tomography scan and core flooding are also detailed. Polymer flooding and its application as well as its recovery mechanism are also discussed.

Chapter Three: Materials, Apparatus and Methodology. In this chapter the main materials such as hydrolysed polyacrylamide (HPAM), sandstone and carbonate rock types used as well as the type of oil used for enhanced oil recovery experiments are presented. The main equipment used, namely core flooding equipment, computed tomography scanner, OFITE viscometer, oscilloscope, signal generator and power amplifier are detailed. The mode of data acquisition (DAQ) and supporting software are also discussed. The detailed, step by step, procedure adopted in this experimental work is presented. Starting from the reservoir selection criteria, Petrophysical analysis including preliminary interfacial tension measurement, polymer preparation, viscosity and viscoelasticity measurement are also detailed. Geophysical analysis including computed tomography scan for pore size and pore distribution were explained. The step-by-step procedure for the running of the coreflooding machine and its auxiliary acoustic instruments: acoustic core holder oscilloscope and signal generators and amplifier are also fully explained

Chapter Four: Results and Discussions. The results obtained from the petrophysical analysis of injection fluids and geophysical analysis of the reservoir cores are presented and discussed in chapter four. The oil recovery from the sandstone and carbonate reservoir rocks are compared and analysed based on pore volume injected. The reasons behind the variations in oil recovery in sandstone and carbonate rocks are discussed.

Chapter Five: The conclusion and recommendations for future research are in Chapter Five. The conclusion highlighted the impact of hydrolysed polyacrylamide polymer and ultrasound on sandstone and carbonate reservoirs in enhanced oil recovery. It also detailed areas for further research.

1.6 Chapter Summary

In this chapter, the overall concept and purpose of the research were brought to fore. Some notable investigations carried out by numerous scientists and engineers were discussed. The aims and objectives were clearly outlined. The justifications for this research in ultrasound and polymer flooding for enhanced oil recovery were centred on addressing current limitations in an innovative and comprehensive method. The hypothesis stated that the integration of ultrasound elastic wave for vibro-mechanical stimulation of the reservoir and polymer flooding for favourable mobility ratio would increase oil displacement and significantly enhance oil recovery.

At the tail end of the chapter, the thesis structure provided a short overview of the content of the chapters. It also showed the sequence of the experimental investigations.

CHAPTER TWO
LITERATURE REVIEW AND GOVERNING PRINCIPLES

2.1 Introduction

In this chapter, an overview of the relevant information and previous progress in research obtained from various literatures and sources are comprehensively presented. Major considerations are on reservoirs and their petrophysical properties, acoustics and their impact on enhanced oil recovery, EOR. Several mechanisms related to EOR from ultrasound application in a porous media are discussed. In addition, relevant reservoir fluid flow characteristics for this research such as Darcy's Law as well as techniques of enhancing oil recovery are discussed. Also included is the application of polymer for flooding in EOR.

2.1.1 Petroleum reservoirs

Petroleum reservoirs are basically subsurface porous and permeable rocks that contain recoverable petroleum (Craft B.C. & Hawkins M., 1991). The two major oil producing formations are shown in Figure 2.1 They are often product of clastic rocks referred to as sedimentary rocks. There are three types of reservoir rocks namely sandstones, carbonates and shales. The carbonate rocks are further categorised into limestones and dolomites. The difference between dolomites (dolostones) and limestones is the presence of a magnesium atom in a molecule of dolomite, obtained through dolomitisation, which is absent in limestones.

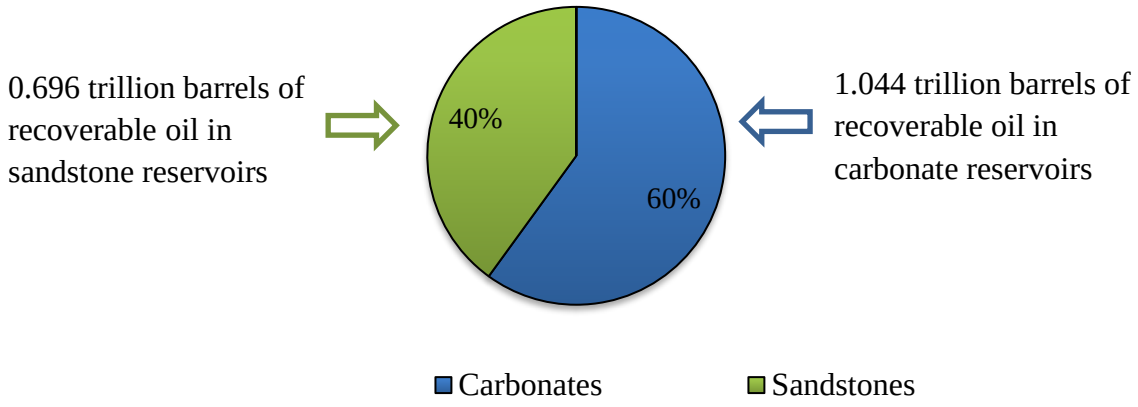

Figure 2.1 Conventional petroleum reservoirs with recoverable reserve of 1.74trillion barrels (source British Petroleum: Statistical review of World Energy 2020)

2.1.1.1 Sandstones reservoirs

Sandstone reservoirs constitute about 696billion barrels of the entire hydrocarbon producing formations globally. This constitutes approximately 40% of global recoverable oil reserve (Figure 2.1) Sandstones are clastic sedimentary rocks composed of mainly sand particles of 1/8 and 2mm (Weimer & Tillman, 1982), minerals and sometimes small portions of other rocks. Their characteristic is based on the mode of deposition, composition and grain cementation. Diagenesis due to post deposition can also alter the characteristics of the rock. However, sandstone reservoirs generally exhibit varying level or degree of permeability and porosity that varies from 10 to 30%. The porosity is dependent on the sorting of the grains that constitute the overall structural framework of the sandstone.

Upon a visual inspection of sandstone, the colour ranges from tan to dark brown or reddish brown depending on the primary composition and texture. Sandstones are further classified according to the quantity of grains of other minerals constituents. For example, when the content of the quartz is high, it is referred to as quartz sandstone, similarly if the quantity of shale is high or clay content is appreciable, it is referred to shaley sandstone. Where the content of feldspar is high, it is referred to arkosic sandstone.

The consolidation of sandstone reservoirs varies substantially for different formations because of difference in cementations ranging from poorly consolidated to highly consolidated. The poorly consolidated formations tend to fracture or disintegrate and produce more sands during production or recovery leading to large quantity of produced sands resulting to a lot of wear and tear on production facilities. The wear and tear by implication constitutes a major production economic loss. The consolidation of the rock consideration is vital in this research to ensure rock particles do not cause pore blockage and rock disintegration during core flooding at reservoir temperatures and pressures.

A lot of research has been done on sandstones and their respective reservoirs highlighting their contrasting properties and characteristics. These contrasting properties are significant in determining the appropriate recovery strategy to consider for adoption.

2.1.1.2 Carbonate reservoirs

Carbonate reservoirs are sedimentary rocks which fall in the category of clastic rocks. They are derived from remains of aquatic organisms providing a skeletal framework for the formation. The organisms sourced could have dwelled in fresh or salt waters. These are primarily called neritic and benthic respectively. Irrespective of the environmental habitat,

the main characteristic of carbonate reservoirs is their precipitation from organisms at any particular location.

It has been shown in literature that carbonate reservoirs constitute about 20.5% of sedimentary formations. It is also estimated that about 1,044billion barrels of recoverable oil, 50-60% of the global proven reserve of hydrocarbon, are in carbonate reservoirs as shown in Figure 2.1. This is a substantial percentage which cannot be ignored in any research that will impact on the enhanced recovery of hydrocarbon. In addition, it is estimated that about 40% of the total output from producing wells globally are from carbonate reservoirs (Ritesh Kumar Sharma, Chopra, & Ray, 2014). Carbonate reservoirs exhibit a varying degree of heterogeneity in porosity and permeability due to several factors; these are primary and secondary processes that are related to the formation of the carbonate reservoirs. The variation in heterogeneity of carbonate reservoirs lends credence to the elasticity variability across different carbonate formations. Hence, rock fabric and facies are the major considerations in characterising carbonate reservoirs.

The primary factors that lead to the heterogeneity of carbonate reservoirs and increases their complexity for analysis and enhanced recovery considerations are the depositional conditions leading to carbonate formation and environment as well as facies changes that have occurred with time on the formation. The secondary factors, on the other hand, are the burial and the diagenesis the carbonate undergoes. Other factors which are part of the secondary processes include faulting, fracturing and degree of cementation (Inês, Bizarro, & Ribeiro, 2015).

Several researchers (Lucia, Kerans, & Jennings, 2003) have made attempts to characterise carbonate reservoirs to enable predicting their behaviour and performance to enhance recovery. This is difficult due to the heterogeneity of carbonate reservoirs as even during water flooding over 50% of oil in place is left unable to be recovered. Low waterflooding recovery in carbonate reservoirs is due to the inability of the water during waterflooding (alone) to contact trapped oil and sweep. Observed rock fabric indicated that carbonate reservoir heterogeneity in porosity and permeability could vary in a region of inches or feet of the reservoir. This, therefore, signifies little spatial correlation, especially where it has been reported that within a small spatial consideration the permeability can vary by a high multiple of 10. Further complicating any enhanced recovery method applicable is that the

permeability can vary across the strata randomly without any predictable order, posing many challenges for its oil exploitation.

The absence of definitive continuity and distribution of pores of carbonate reservoirs and the variations relative to facies make it also complicated to develop adequate reservoir models in characterising reservoir matrices and developing pattern recognition algorithms for predicting the permeability of the reservoir such as the multi-resolution graph based clustering (MRGC) (Al-Amri, Mahmoud, Al-Yousef, & Al-Ghamdi, 2015). The entire pore systems comprising of the pore geometry, pore sizes and pore throat are subject of inherent variation in carbonate reservoirs. Therefore, the non-ease of representative sampling is evident in carbonate reservoirs because of the heterogeneous nature of the rock.

Other researchers (Lucia et al., 2003) have shown that the rock fabrics is an important parameter in characterising carbonate reservoirs. This is quite evident since the rock facies provide the essential geologic descriptors that encompass all the key petrophysical properties and parameters which characterise the carbonate pore size. These petrophysical properties are particle size, particle distribution and particle sorting. Others are the interparticle and vuggy porosity.

Diagenesis has been reported to play a major role in the determination of the overall characteristic of the reservoir rock. The degree of transformation that can occur on the rock can vary depending on the porosity, permeability and pore throat size (Lucia et al., 2003). Rock fabric facies have advantage of giving an overall and encompassing description of the detailed characteristics across the carbonate reservoir, especially through stacking, hence can be used to develop algorithms for simulation and prediction of performance of carbonate reservoirs. These algorithms in conjunction with informative 3D imagery of the reservoir provide potential field production capabilities for synchronisation across wells.

Additional study to characterise carbonate reservoir (Inês et al., 2015) combined data on deposition and diagenesis utilising a multistage approach. Porosity and permeability from core data were correlated to diagenetic and depositional environment and facies including pore system geometry. This provided a good insight to the spatial trend and captured the interrelationship existing between the petrophysical properties, the architecture of the pores and the production sweep efficiency expectancy of the carbonate reservoirs. The benefit deduced from this study is the attempt to enable modelling of carbonate reservoirs. Similarly, an attempt to quantify the influence of geological factors on carbonate pore types

on reservoir permeability (Huang & Sun, 2015) utilised the shear frame which includes compressional and acoustic velocity shear on carbonate reservoirs. The shear frame flexibility factor utilised enabled classification of carbonate pore types as a function of acoustic velocity, carbonate reservoir core elastic properties and core permeability.

An early study of the properties of carbonate reservoirs indicated that the carbonate cores with porosities less than 5% produced a very small quantity of oil. However, carbonate cores with porosity of 2% and 0.01md produced no oil (Craze, 1950). The study also showed that when the pore size distribution is wide or high, the permeability could decrease sharply. The texture and pore size distribution of the carbonate reservoirs distinguish them from other reservoir rocks. This is because other rocks show greater homogeneity than in their pore size distribution. The geometry of the pore determines the geometry of the pore channel opening. The pore channels are not regular though interconnected and tortuous, but overall provide a regular macroscopic porosity and permeability. Four basic porosities, as shown in Figure 2.2, have been observed in carbonate cores intracrystalline, intergranular, fissure and vug. The porosities and permeabilities of carbonate reservoirs are shown in Table 2.1.

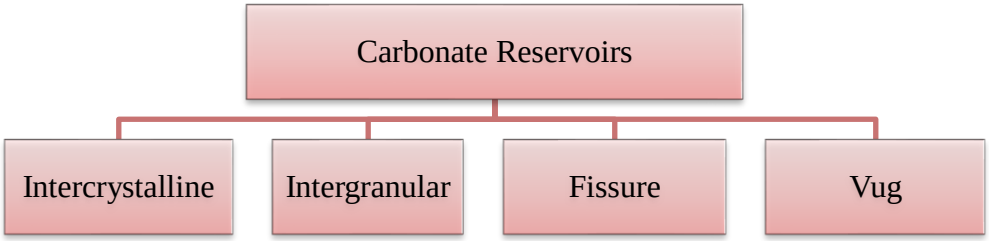

Figure 2.2 The four carbonate reservoir porosities

Table 2:1 Porosities and permeabilities of carbonate reservoirs

Porosity Type	Percentage (%)	Permeability (md)
Intracrystalline		
Microgranular	20-35	1-10
Fine to Coarse	10-20	10-100
Intergranular	25-45	300-5000+
Fissure	2-10	300+
Vug	10-35	10-300

Source: Craze's identified Carbonate reservoirs porosities with modifications (Craze, 1950)

2.1.1.2.1 Types of carbonate reservoirs

Carbonate reservoirs are classified under two distinct categories: limestone (calcium carbonate) with molecular formula $CaCO_3$ and dolomite (calcium magnesium carbonate) which has $CaMg(CO_3)_2$ as its molecular formula. Figure 2.3 shows the two major carbonate reservoirs. The underlining difference between the two is the presence of Magnesium atom in dolomite which is absent in limestones. Essentially, dolomites are formed from the solution recrystallization of limestones leading to the introduction of the Magnesium ion into the molecule. The diagenesis of limestone to dolomite leads to the increase of the crystal and pore sizes of the rock. The resulting allochems therefore also increases the porosity and permeability of the dolomite reservoir rock (Ritesh Kumar Sharma et al., 2014). The dolomitization of carbonates increases the reservoir quality (Huang & Sun, 2015).

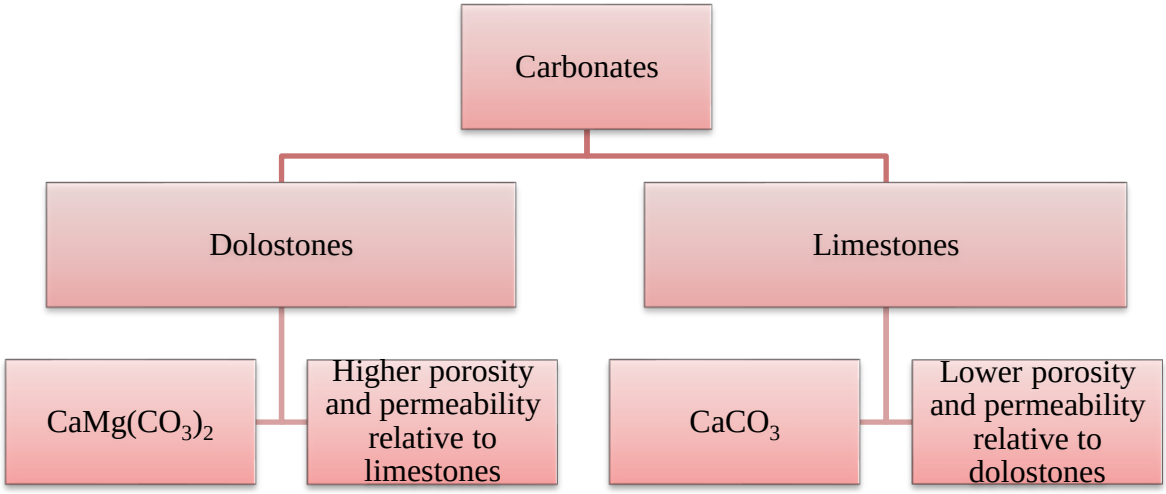

Figure 2.3 Carbonate reservoirs

2.1.1.3 Impact of rock surface on oil mobility

The nature of the reservoir in terms of its rock surface characteristics has a significant impact on the oil mobility. The high electronegative nature of crude oil tends to have a repulsive effect on the surface of the sandstone, which exhibits electronegativity as well. This repulsive force exhibited by sandstone and the oil allow the water to form a surface layer on the rock. Therefore, causing a water wet surface in terms wettability. Ca^{2+} and Mg^{2+} in the vicinity serves to bind or provide a bridge between the sandstone surface of the pore oil, thereby increasing oil contact.

In the case of carbonates where the Ca^{2+} and Mg^{2+} dominates the tendency of oil wetness is more prevalent. The electrostatic forces of attraction therefore can lead to two scenarios- oil wet or mixed wet reservoir surfaces.

2.1.2 Methods and stages of oil recovery

There are essentially three recovery stages in operations in the life of a reservoir. They are primary stage, secondary stage and tertiary stage recovery operations.

2.1.2.1 Primary recovery

Primary recovery utilises the natural drive mechanisms of the reservoir for production. It can be characterised by either the reservoir fluid expansion of gas in solution, reservoir fluid displacement, drainage as a result of gravitational drive as well as capillary expulsion (Craft B.C. & Hawkins M., 1991). The drive mechanisms are highlighted in Figure 2.4. These drive mechanisms stem from the natural reservoir or artificially through pumps and lifts processes. However, in another detailed description of primary recovery (Satter & Iqbal, 2016), it was proposed the inclusion of one or more of the following drives: the expansion of the reservoir rock and liquid drives resulting in pressurised flow of fluid to the surface. Others are release of gas in solution drive, reservoir gas cap drive, under laying aquifer water drive, segregation of the gas drive and drive because of reservoir compaction due to depletion. It is also estimated that during the primary production, the maximum recovery is about 10% of recoverable oil in place. Hence, the need to move to additional oil recovery strategy to complement the primary stage is imperative.

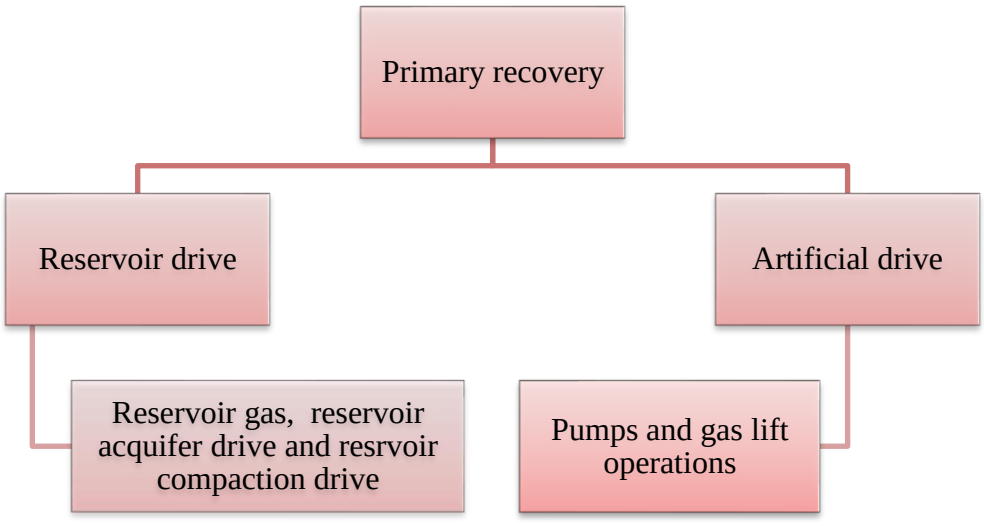

Figure 2.4 Mechanisms of primary recovery

2.1.2.2 Secondary recovery

In secondary recovery operations, natural gas or water is injected into the reservoir to maintain pressure. The two major secondary drive mechanisms are shown in Figure 2.5. When gas is injected, it is referred to as gas injection, and when water is injected, it is referred to as waterflooding. Any secondary recovery technique or pressure maintenance programme to be employed to the reservoir is put into consideration at the planning stage of the field development to adequately optimise production. Some of the factors that are attributed to drop in recovery are capillary forces which include interfacial tension; mobility ratio becomes high during production and pressure declines with increase in water cut (Alhomadhi et al., 2013).

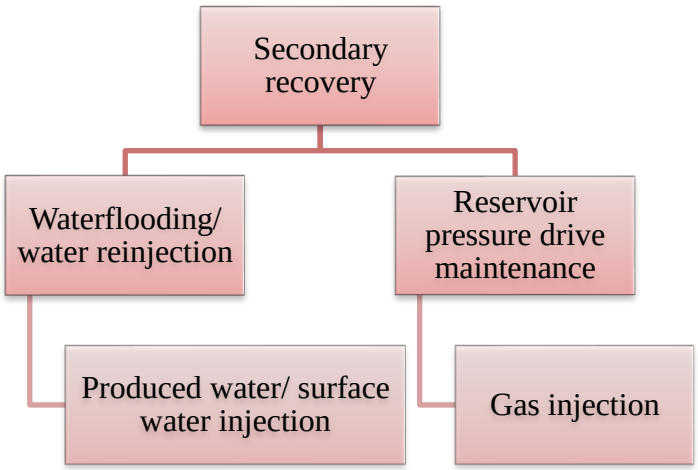

Figure 2.5 Secondary recovery

2.1.2.3 Tertiary and enhanced oil recovery

At a stage when the secondary recovery has become ineffective and less economically viable, due to decline in production, additional work is carried out on the reservoir. At this stage of the production life of the reservoir, chemicals and water are injected into the reservoir to increase production and ensure maintenance of reservoir pressure. Figure 2.6 shows the various tertiary recovery strategies and techniques employed in the recovery of oil.

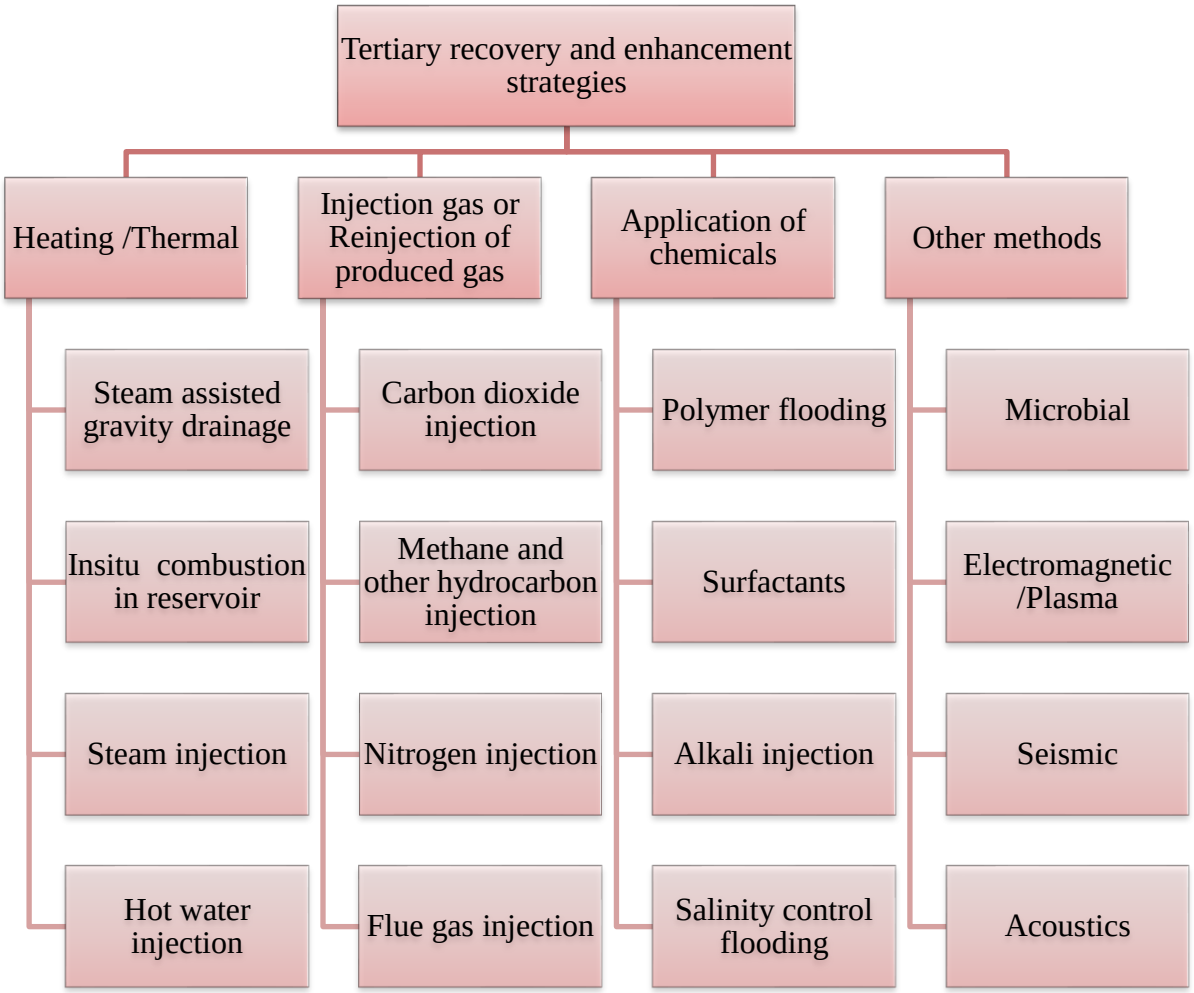

Figure 2.6 Tertiary recovery and enhancement strategy

The main objective of all enhanced recovery methods is to increase the overall recovery efficiency. The overall efficiency of any recovery operation is dependent on its ability to increase the efficiency at both vertical and areal as well as at the microscopic level -pore scale. Figure 2.7 shows the three major factors of an efficient EOR.

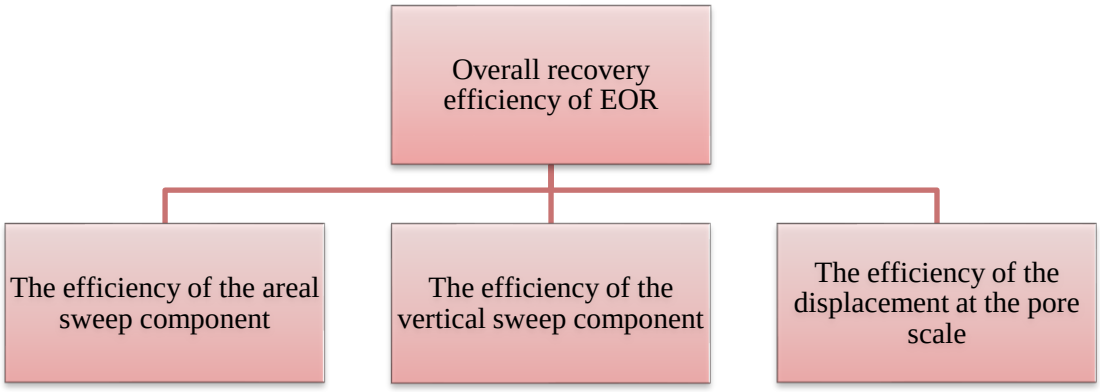

Figure 2.7 The three major factors of an efficient EOR

A further classification of the displacement is in terms of the microscopic displacement and macroscopic displacement efficiency.

Microscopic displacement efficiency: The microscopic displacement efficiency is governed by recovery at the pore level. These include conditions such pore pressure, pore geometry, fluid mobility, pore size, porosity distribution. These constitute the first line of action in sweep.

Macroscopic displacement efficiency is determined by several factors. These include the extent of homogeneity of the reservoir as well as the mobility ratio between the injected fluid and the recovered fluid. Others are the rock matrix and the direction in which injected fluid is being sent into the reservoir can influence the displacement at the macroscopic level.

2.1.3 Petrophysical properties of reservoirs

The petrophysical properties of petroleum reservoirs are important parameters for understanding their behaviour and are determined through experimental study. Some of these parameters can be itemised as follows: porosity, permeability, fluid saturation, pore size and distribution, pore structure, fluid characteristics, interfacial tension etc. However, in this research methodology the determination of the pore characteristics is presented as a geophysical property of the formation.

2.1.3.1 Porosity

Porosity is the ratio of the void space to the volume of the pore of a reservoir rock. The effective porosity is the connected porosity of the rock that is also connected to the exterior of the rock, which allows the channelling, or passage of reservoir fluid. Figure 2.8 provides

an illustration of porosity. It can vary in magnitude as a result of many factors increase in overburden pressure as a result of production and fines migration.

The saturated pores of reservoir rocks that contain fluids usually exert an internal pressure on the internal pore space walls. There is an additional external pressure exerted from the strata confining the pore spaces, which is referred to as overburden pressure. Figure 2.8 illustrates the major features of a reservoir rock. As the production increases or the reservoir is depleted, the internal pressure in the pores decreases leading to a decrease in the bulk volume of the reservoir rock. At this stage, the volume of the reservoir rock decreases as a result of the pressure decrease and the porosity of the reservoir rock decreases. It is estimated that the decrease is approximately 5% per 1000psi change in the internal fluid pressure (Craft B.C. & Hawkins M., 1991).

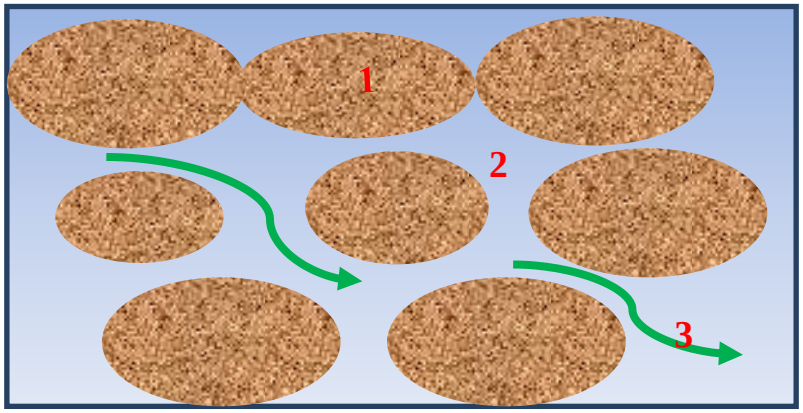

1 Grain **2** Void space **3** Interconnectivity

Figure 2.8 Simple illustration of porosity of a reservoir rock

The effective porosity of a reservoir rock is based on the interconnected pores and can be expressed mathematically as $Porosity = (interconnected\ pore\ space)/(Pore\ volume)$

2.1.3.2 Fluid mechanics

The transportation and movement of reservoir fluid form the central aspect of petroleum recovery and production. Here, the concept of fluid flow in a porous medium is reviewed based on the Darcy's Law of flow through a porous media. Henry Darcy derived the law in a flow experiment conducted in which water, used as fluid, was passed through a filtered bed made of unconsolidated sand. Though, several scientists have faulted its absolute

reliability due to its inability to account for unsteady state flow, heterogeneity of the pores amongst others, , it has, however, provided good grounds for the study of flow in petroleum reservoirs (Craft B.C. & Hawkins M., 1991). Darcy's law states that the rate of flow of a homogeneous fluid in porous media is directly proportional to the pressure difference (driving force) and inversely proportional to the viscosity of the fluid.

This can be expressed mathematically as follows:

$$Q = \frac{-KA(P_b - P_a)}{\mu L} \qquad 2.1$$

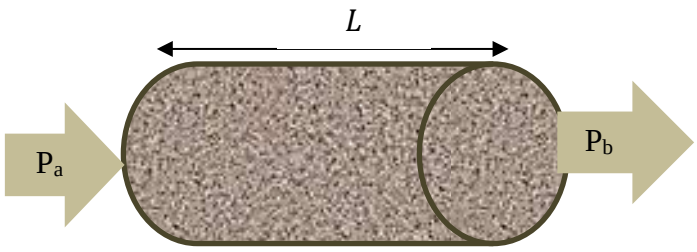

Figure 2.8 Fluid pressure drop across a reservoir core

Where $Q$is the volumetric flow rate, $P_b - P_a$ is the pressure difference, L is the core length, K is the permeability and A is the area of the core and μ is the viscosity.

The concept of fluid being driven by a driving force, as illustrated by the pressure gradient, has been under review. Figure 2.8 shows a core sample with fluid flowing through its pores and with pressures in and out of the core. Darcy's law has certain short comings, in that, it does not apply in turbulent flow where flow rate is high and the rate at which the pressure gradient changes is so large compared to the rate of flow of reservoir fluid. Hence, best results are obtained when the flow is laminar. Measurements obtained from the Darcy's law are at a macroscopic scale, and the individual pore's flow characteristics are averaged over the region of known dimensions is being considered. Therefore, it can be inferred that microscopic scale analysis of flow cannot be determined with the Darcy's Law. Another setback is the uniformity of pore channels as it generalises all pore properties.

Permeability across the reservoir can vary in different directions- vertically and horizontally as well as diagonally due to variation in porosity. It is, therefore, pertinent to state that a

core sample cannot, in any way, provide the overall characteristics of the reservoir. It can, however, provide a working tool for further analysis.

An advantage of the Darcy equation is that it enables the determination of the mobility ratio which is the ratio of permeability to viscosity. In a situation where two fluids are flowing together to the surface in a hydrocarbon reservoir, for instance oil and water, the mobility ratio is the ratio of the mobility of oil to that of water that determines the quantities or volumes of each component recovered. Hence, the mobility ratio is significant in any EOR recovery strategy implemented where flooding or injection into the reservoir is being carried out to enhance displacement efficiency.

The Darcy equation can be applied in simple core analysis in the laboratory with a good level of accuracy.

2.2 Acoustics and polymer flooding

2.2.1 Introduction to Acoustics and polymer flooding

In this section, the fundamentals of acoustics and ultrasound wave are discussed in depth. The types of acoustic waves and modes of acoustic wave propagation in porous media both saturated and unsaturated, are detailed extensively. Computed tomography analysis method which employs x-rays with characteristic propagation behaviour as acoustic waves is also explained in detail. In addition, to complement the chapter, polymer flooding a recovery drive mechanism for enhanced oil recovery is also explained comprehensively.

2.2.2 Acoustics and ultrasound

Acoustics waves are vibrational sound waves that are capable to mechanically transport through a medium. The audible sound waves are usual waves measured in decibels. They fall within the lower band of the frequency chart. Ultrasound waves are often measured in terms of their frequency. They are inaudible and have high frequency in the range of 20KHz and beyond. The acoustic waves utilised in this research falls within the 20KHz band. Hence, ultrasound is the region of acoustics spectrum of main concern in this research. Since this study integrates acoustics with polymer flooding as a means of enhanced oil recovery, the application of polymer is highlighted at the tail end of the chapter.

2.2.3 Theory of acoustics in a porous media

In an earlier ground breaking work on the theory of acoustic wave propagation in a porous media (Biot M. A., 1955), the behaviour of elastic waves propagated in a porous elastic solid, in which a compressible viscous fluid is saturated was determined. It was proposed that the propagation takes place at a lower frequency range. At the lower frequency range, the validity of the Poiseuille flow holds. The Poiseuille flow law states that the flowing velocity of a liquid through a capillary tubing is directly proportional to the pressure of the liquid and also the fourth power of the radius of the capillary as well as inversely proportional to the viscosity of the liquid and the length of the capillary tube. It highlighted four non-dimensional parameters, one characteristic frequency, two dilatational waves and one rotational wave. The researcher attempted to develop and explain the principle theory behind the behaviour of propagated elastic waves in a porous saturated elastic solid. The two dilatational waves were categorised as the first kind and second kind, respectively. The second kind waves were found to be dispersed more readily and attenuated in high proportion, similar to the behaviour of heat conduction. The first kind waves, however, behaved like true waves and showed far lower attenuation properties compared to waves of the second kind. The stress and strains from the elastic wave on the microstructure of a porous media as well as the pressure of the fluid in an assumed impervious porous media with averaged sized pores were considered. It was observed that when the frequency was increased there was a corresponding increase in the phase velocity of rotational waves. This phenomenon was also exhibited in the first kind waves. The absorption coefficients were also shown to be proportional to the square of the frequency for waves of the first kind and rotational waves. In terms of attenuation of the first kind wave, Biot could not conclude similarity between rotational waves and waves of the first kind. He inferred that first kind waves could exhibit a different attenuating behaviour depending on the type of material.

Rotational waves are referred to as secondary waves, S-waves, shear waves or tangential waves. On the other hand, dilational waves are referred to as primary waves, P-waves, fast waves or compressional waves. They are the fastest waves most likely to be propagated in an isotropic linear elastic porous medium. A sequel to low frequency range was produced to account for higher frequency range (Biot M. A., 1956). This is where the Poiseuille's flow law does not hold, but still retained the theory based on assumption of common densities for fluid and porous solid. Figure 2.9 shows the three types of waves classified based on their properties.

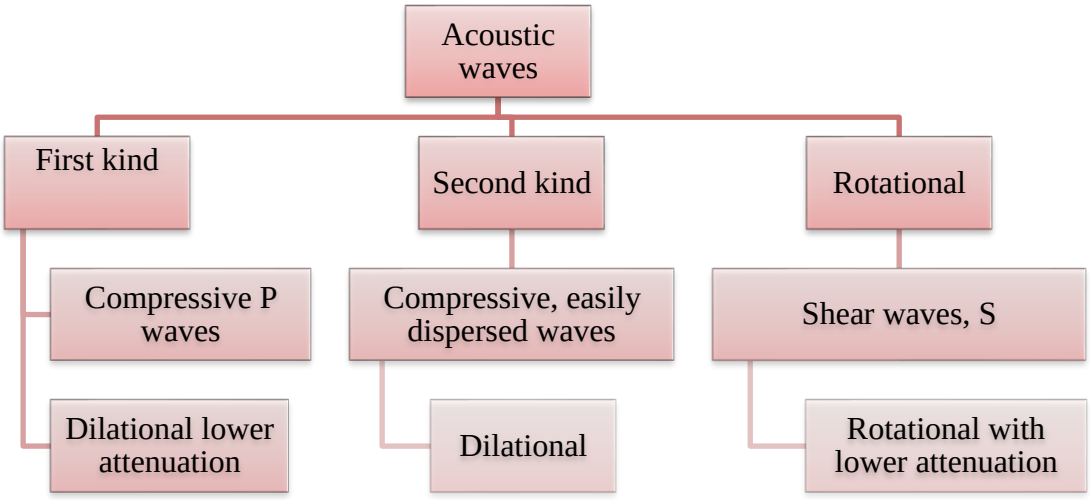

Figure 2.9 Classification of acoustic waves based on Biot identification

Numerical assumptions made on the porous medium as having isotropic properties with identical properties in all directions is very unlikely. Some of these assumptions include perfect and uniform elasticity of the porous solid, uniformity of the pore size and uniform mineral content amongst others. However, for the ease of analytical interpretation, the rocks are generally anisotropic. The most appropriate form of analysis would be experimental determinations. A rock is an aggregate of several solid elements in which the pore space could be partially or fully saturated. All the aggregate elements in the solid element including the fluid saturation, have their own characteristic elastic moduli. Furthermore, the shape of a pore provides a characteristic elastic behaviour. A spherical pore and a flat surfaced pore will definitely react differently when subjected to a wave front. Microcracks and inclusions play major roles in the bulk elastic moduli of rocks (Bourbie, Coussy, & Zinszner, 1987).

Biot (1956) made several assumptions to enable the theory to hold. First assumption was that the wavelength of a propagated wave is greater than the dimensions of the microscopic element. Secondly, all the displacements were in small increments. Thirdly, that a continuity of the liquid phase existed, and the matrix becomes the disconnected pore and the solid component, and fourthly, an isotropic and elastic solid matrix were assumed. Hence, Biot opined that the disconnected pore and the solid structure constituted the solid matrix.

The implication of these assumptions is that homogeneity is considered in the overall process. The periodicity of a homogeneous repetitive characteristic nature would inevitably

give and enable repetitive solutions. This would enable generalisation and modelling from the microscopic scale to the macroscopic scale. Another implication of these assumptions is that in the attempt to assume a characteristic asymptotic behaviour, there was no guarantee that the heuristic-practical approach would work.

However, the earlier work of Biot (1956) in explaining the phenomenon of acoustic stresses and strains on fluid saturated porous media at a macroscopic level was unable to account for all the numerical values for the stress and strain coefficients for macroscopic properties as well as the behaviour at the macroscopic level. This wide gap was narrowed (Auriault, Borne, & Chambon, 1985) by considering the macroscopic structure of the pore at periodic intervals which permitted the determination of the effective coefficients at the macroscale from the microscale.

Biot's theory further assumed the non-existence of any form of chemical reaction during the propagation of waves in the porous media. The only existing factors, according to Biot were displacements attributed to the strains and stresses on the porous media.

Biot had opined that the behaviour of acoustic waves in a porous media was very much similar to or comparable to the movement of two separate entities in which the fluid and solid undergo different degree of displacements independently. A similar conclusion was also brought to fore by other researchers (Johnson & Plona, 1982) after observing results obtained from an experiment with packed glass beads saturated with water, and concluded that the speed of acoustic waves vary in fluid saturated porous medium. The first recorded experiment where the existence of waves of the second kind was validated and confirmed was conducted by the same researcher -Plona. Thus, establishing confirmation for the numerical analysis carried out by Biot in an experimental set up.

A generalised Darcy coefficient to account for both low and high frequency behaviour was obtained in which the coefficients that could not be accounted for by Biot were deduced as the pulsation was increased to infinite level. The overall conclusion deduced from this is the need to use experimental analysis or computing periodicity of the macrostructure for greater reliability.

2.2.4 Wave propagation and principles of elastodynamics

The theory of propagation of acoustic waves in porous media cannot be fully comprehended and analysed without understanding the elastodynamic properties of the reservoir core

samples and the continuum mechanics principles applied. In the elemental study at cell level, from microscopic to macroscopic scale, the wave phenomena can be geometrically upscaled from a homogenous system to a heterogeneous system enabling adequate study of different rock materials as they are subjected to the stresses and strains associated with propagated acoustic waves. Elastodynamics, concisely, is the study of the behaviour of an elastic material, in this case the rock when it is subjected to an acoustic wave leading to deformation or displaced movement of the cell element of the rock and or fluid in the rock. The main constituents of elastodynamics include strain tensors, stress tensors, linear elasticity, geomechanic moduli namely Young's modulus, Lame's modulus, bulk modulus and dynamic moduli.

2.2.4.1 Strain tensor

Strain tensors are vector quantities representative of the deformation of rock material resulting from directional wave forces or pressure(s) applied. This deformation can be reversed if the elastic limit is not exceeded. This is a clear case of Hooke's law displayed in rocks since it falls within its elastic limit. The impact of wave propagation in a porous medium can hardly exceed the elastic limit, as the forces are usually below the elastic limit of the reservoir in acoustic wave propagated deformations. The tensors are in the orthogonal x, y, z direction. In the case of acoustic waves, the strain deformation is small limited by the energy of the acoustic wave. There is a corresponding change in the dimensions in the three axes of the porous media. Here, assuming a cube like shape for a cell, subjected to strain tensor cause a change in the values of x, y, z coordinates. A three-dimensional deformation of a cube is shown in Figure 2.10

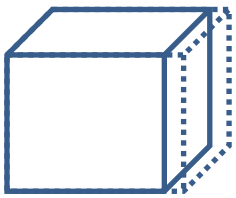

Figure 2.10 Three-dimensional deformation of rock cell element subjected to elastic wave indicated by dotted line

The small increment in volume as a result of strain tensor from the deformation is indicated by the dotted line.

2.2.4.2 Stress tensors

When vector forces are applied on the three-dimensional faces of an elemental cube with the x, y and z planes leading to an incremental deformation in dx, dy, dz, the elemental constituents cause a resistance to occur to prevent the deformation. These opposing forces at the elemental level are known as stress tensors.

2.2.5 Wave attenuation and acoustic velocity

It is accepted that wave attenuation and acoustic velocity of waves in a porous medium such as reservoir rocks are widely affected by the nature of the rock. These characteristics such as crystal structure and mineral constituents, microcracks, pore geometry, pore size and distribution as well as the pore fluid properties: viscosity and composition. In addition, research has shown that the acoustic properties of rocks are affected by level of fluid saturation- a dry rock or unsaturated rock has significantly different attenuation and acoustic velocity properties when compared with an identical rock that is partially or fully saturated. It is worthy to state that more intensive studies have been done on wave velocity in porous media than on attenuation (Winkler & Murphy III, 1995). The application of acoustic velocity in well logging for the determination of porosity, perhaps, could be the major reason it has received greater attention.

The porosity of reservoir rocks can be determined by the time average equation for sandstones but apparently cannot be used accurately for carbonate reservoirs. The reason is that the carbonate rocks give lower porosity values than their true porosity due to the existence of vugular pore shapes (Winkler & Murphy III, 1995). Pore shapes such as thin flat cracks when compared to spheroidal pores exhibit lower velocities. This has been attributed to the influence of the microcracks on the stresses perpendicular to the crack surfaces. This influence is remarkably less in spheroidal pores. Different constituents such as silica and clay content influence the cementation of reservoir rocks. Similarly, the cementation affects the acoustic properties of rocks.

An increase in the confining pressures as well as a decrease in pore pressure of reservoir rocks corresponds to an increase in acoustic velocity and as well as a decrease in attenuation. This is due to the decrease in pore size that occurs when stress is applied on the pores of the microstructure. The pore sizes are closed further as confining stress is increased leading to a more stiffened rock. The effective stress, a difference between confining pressure and

pore pressure has been shown to vary with acoustic velocity. The increasing confining pressure corresponds to increase in acoustic velocity. Similarly, anisotropic stresses which are generally not normal on a particular plane and not evenly distributed as a result of microcracks and mineral alignment cause the acoustic wave velocity to have non-uniform direction. Most of these findings were conducted on water-saturated rocks.

2.2.6 Equation of the homogeneity of acoustic waves

Having considered the implications of the Biot theory in the propagation of acoustic waves in a porous medium, it was proposed that a more generalised equation that accounts for dynamics of the porous media and caters for the effects of the pore fluid compressibility as well as the non-connectivity of the pores be provided. Since the earlier theories were based on the total pore connectivity, which in practice is not realistic, it became evident that a new approach or model should be proposed that catered for this deficiency. In this regard, Malinouskaya (I. Malinouskaya, 2011) proposed a new equation, based on a macroscopically uniform structure which is significantly smaller than the wavelength of the acoustic wave. This development utilises the concept of a spatially periodic macroscopic structures which enables the determination of the effective coefficients associated with elastic waves (Hermana, Ghosh, & Sum, 2016).

The theory of Navier's elastodynamics equation was used to account for the solid component while Navier- stokes equation caters for the interstitial fluid. At the interface where the fluid meets the solid, there is continuity of stress involved in the displacements. Therefore, fundamentally the impact of compressible interstitial fluid is fully considered. In addition, the earlier assumption of absolute continuity of pore spaces was rejected. Pores were considered to be partially closed or partially disconnected.

Hence, the stresses and displacements in terms of slow and fast varying space for x and y can be deduced.

2.2.6.1 Navier's elastodynamics equation for a solid

The Navier's elastodynamics equation accounts for the linear variation of elasticity of the rock with variation in time. The elasticity of the rock enables the restoration force from the wave as it meets the rock.

$$\mu\nabla^2 u + (\mu + \alpha)\nabla(\nabla \cdot u) + F = \rho\frac{\partial^2 u}{\partial t^2} \qquad 2.2$$

2.2.6.2 The Naiver-Stokes equation

The Navier-Stoke's equation defines the motion of reservoir fluids. It derives its origin from Newton's second law of motion. Since the reservoir fluids are compressible, they are likened to the usual compressible Newtonian fluids and are impacted by the laws that govern such fluids. The Navier-Stoke's equation provides four different terms, which are namely; the inertial forces, fluid pressure forces, fluid viscous forces and external force applied on the system.

$$\rho\left(\frac{\partial u}{\partial t} + u \cdot \nabla u\right) = -\nabla p + \nabla \cdot (\mu(\nabla u + (\nabla u))^T) - \frac{2}{3}\,\mu(\nabla \cdot u)I) + \; F \qquad 2.3$$

$$\frac{\partial \rho}{\partial t} + \nabla \cdot (\rho u) = 0 \qquad 2.4$$

The two equations above, the Navier-Stokes equation and the continuity equations, respectively, can be solved together to provide the solutions based on conservation of momentum and mass.

2.2.6.3 The modified Christoffel equation for acoustic wave propagation

The application of a two-scale expansion on the displacement and stresses in terms of a slow and fast varying space variables x and y can be represented mathematically with an expression in the form of a power series to sum up the overall displacements of all elemental pore components of the rock. Since the individual microscopic displacements are driven by harmonic deformation that come with a pulsation, the overall displacements in terms of a macroscopic scale can be expressed with a power series where the $u^{(j)}$ exhibits periodicity in y space variable.

$$u(x,y) = \sum_{j=0}^{\infty} \eta^j u^{(j)}(x,y)e^{i\omega t} \qquad 2.5$$

The characteristic parameter that relates the microscopic size of the pore and the wavelength is given by $\eta = \frac{l}{2\pi\lambda}$

The solutions based on the dynamics of the Darcy-scale poro-elastic equations are obtained as follows (for $i = 1,2, \ldots \ldots \ldots N$):

$$i\omega W^i = -\frac{1}{\mu_f} K^i \cdot \left(\nabla P^i - \rho_f \omega^2 U\right) \quad 2.6$$

$$\nabla \cdot D : E(U) + \sum_{i=1}^{N} \nabla \cdot \alpha^i P^i = -(\rho)\omega^2 U - \rho_f \omega^2 \sum_{i=1}^{N} W^i \quad 2.7$$

$$\nabla \cdot W^i = A^i : E(U) + \sum_{j=1}^{N} B^{ij} P^j - \epsilon^i c_f P^i \quad 2.8$$

The subscript i in the equation denotes the microscopic pore component of the rock and P the pressure of the fluid. U , is the small displacement of the rock, W is the displacement of the fluid relative to the rock, K represents the permeability tensor,c_f is the fluid compressibility and μ_f is the fraction of the pore volume, and D represents the effective elastic tensor of the dry porous rock. The effective elastic tensor is determined by applying the macroscopic strain tensors $E(U)$ in the elastostatic tensor of the rock. When macroscopic deformation occurs due to the strain tensors $E(U)$, the change in elemental pore volume is A^i. B^{ij} stands for the change in the volume of the pore as a result of a corresponding change in the pore pressure , P^i while α^i is stress tensor on the pore component.

2.2.7 Mechanisms of ultrasound enhanced oil recovery (EOR)

In this section, some of the mechanisms associated with the application of ultrasound for enhanced oil recovery as investigated by numerous researchers are brought to fore and discussed in detail.

2.2.7.1 Interfacial tension

The interfacial tension of a reservoir fluid plays a major role in determining the efficiency of an enhanced oil recovery technique (Abdallah & Stukan, 2012). Figure 2.11 illustrates how static pressure increases leading to the formation of cavitation, which eventually implodes and causes the release of jet like force or energy in the liquid within the vicinity of the pore space. In this illustration small bubbles come into contact and coalesce to form a larger bubble and as wave vibration continues the large bubble grows and eventually

reaches a resonance size before eventually imploding or collapsing. These bubble activities alter the interfacial tension.

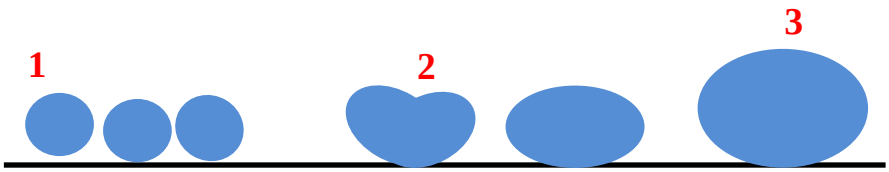

1 Microbubble
2 Bubble coalescence
3 Jet like energy released due to cavitation imploding of large bubble

Figure 2.11 Cavitation formation and collapse.

2.2.7.2 Cavitation

Cavitation is a phenomenon generated by wave perturbation through an aqueous solution resulting in dissolved gas gaining coalescence or rectified diffusion and forming bubbles. These waves transmit sinusoidal pressures on the aqueous solution and the bubbles formed. As the waveform contracts and expands, the size of the bubble increases. The bubble growth during expansion (rarefaction) is much higher than the size reduction during contraction (compression). This therefore implies that the net size of the bubble is favoured towards growth. At a point when the bubble has reached its maximum size, referred to as resonance size it becomes unstable. With the continuous passage of the waves and growth of the unstable bubble implosion or collapse of the bubbles occurs. The collapse of the large unstable bubbles leads to formation of smaller fragmented bubbles. A large amount of energy released during the collapse of bubble creates luminescence. A bright light is emitted lasting 3 microseconds. Energy released from the luminescence creates hot spots as well as increase in pressure within the vicinity of the collapsed bubble. The small fragmented bubbles now created serve as nucleus for the formation other larger bubbles (Leong, Ashokkumar, & Kentish, 2011).

The equation relating the growth of a bubble and its resonance frequency during growth is given by the following equation:

$$R_r = \left(\frac{3\gamma P_\infty}{\rho\omega^2}\right)^{\frac{1}{2}} \qquad 2:9$$

In Equation 2:9 R_r is linear resonance radius, γ represents the specific heat ratio of the gas in the bubble, P_∞ stands for the liquid pressure at ambient conditions, ρ is the density of the

liquid and ω represents the angular frequency of the oscillating wave of the ultrasound. Equation 2:9 is an estimate of bubble radius size since bubble sizes fluctuate when under the influence of ultrasound waves.

If the bubbles grow large enough and the pressure within the containment (reservoir) is sufficient to keep the gas in solution the buoyancy effect would be low. However, if the containment is oil and reservoir pressure is very low or to a level that can best be described as undersaturated, the bubbles could rise to the surface or to the gas cap.

The cycle of bubble creation and bubble collapse continues with the generation of numerous unstable bubbles from an aqueous solution or oil reservoir. The mechanism of bubble collapse plays a major role in stimulating additional energy and pressure desired for enhanced oil recovery. Numerous researchers have contributed on this discussion; however, overall mechanisms for enhanced oil recovery are yet to be fully understood. The two main mechanisms for bubble formation in ultrasound-irradiated fluids are:

i) Existence of undissolved bubbles in liquid or solution that are stable and remain that way due to the bubble surface having impurities that constitute a layer on the bubble and prevents its dissolution. During the application of ultrasound, the bubbles coalesce and grow to the resonance size. Beyond this resonance size with continuous irradiation with ultrasound the bubble could either collapse and release energy or oscillates in accordance with the wave cycle.

ii) Existence of crevices of the containment unit and motes containing trapped gas. This trapped gas forms the basis for nucleation of additional bubbles during ultrasound irradiation.

Several mathematical expressions on the phenomenon of bubble formation and cavitation as well as its growth have been postulated. Equation 2.10 depicts, for a single bubble, the fundamental behaviour when subjected to oscillating (ultrasound) waves.

$$R\dot{R} + \frac{3}{2}R^2 = \frac{1}{\rho}\left[\left(P_O + \frac{2\sigma}{R}\right)\left(\frac{R_O}{R}\right)^{3\gamma} - \frac{2\sigma}{R} - (P_O - P_A sin\omega t)\right] \qquad 2:10$$

Where R is the radius of the bubble formed at any time, t, during ultrasound application, $\dot{R}$ is the velocity at the wall, R_O is the radius at steady state, ρ represents the liquid density (fluid density), P_O stands for steady state pressure, P_A is the driving pressure wave

amplitude, σ represents surface tension and γ stands for specific heat ratio of the gas inside the bubble.

A single bubble formed below the rectified diffusion pressure can easily return to solution. Therefore, as the pressure continues bubble formation growth and collapse must be beyond a certain threshold. This explains why when ultrasound waves are removed, or application discontinued, a fall in the pressure is observed sometimes a decline in productivity with time.

In previous research (Leong et al., 2011), it has been postulated that an uneven mass transfer into a gas bubble is due to two effects. These are the area and shell effects. In the case of area effect, the diffusion into the gas bubble occurs when the bubble is at its largest size and gas leaves the bubble through diffusion, when the bubble contracts it exerts compression on the gas in bubble during the compression phase and gas leaves the bubble. Evidently, the rate of diffusion is proportional to the surface area. The surface area during the expansion stage is far greater than in the compression period. This, therefore, implies that a larger volume of a gas is absorbed by the gas bubble than is diffused by the gas bubble. The net gas in and out of the bubble favours the in-mass transfer path. As a result, as the sound wave cycle continues, the bubble increases in size due to an overall net inflow of gas into the bubble.

The shell effect refers to the boundary layer of the bubble in which mass transfer occurs. The bubble layer is most thinner during the rarefaction stage allowing and facilitating mass transfer. As the bubble shrinks in size, the bubble wall or boundary layer becomes thicker therefore reducing inflow during the compression stage. In addition, concentration gradient is enhanced during the expansion phase.

Mechanisms for bubble coalescence:

1. One or more bubbles are contacted and form a film which has a thickness of 1 to 10um
2. At the next stage the thickness of the film is reduced
3. As the thickness of the film continues to reduce, the wall breaks. This ruptured film then takes another bubble into it, leading to coalescence.

2.2.7.2.1 Sonoluminescence and the Bremsstrahlung Radiation effect

During the violent transient collapse of bubbles, light is emitted. It is believed that this occurs because of the high temperatures and pressures generated when the pressure is at a maximum within and outside the bubble leading to transduction of the acoustic energy to light energy. The emission period is very short. It could be single bubble sonoluminescence (SBSL) or multi-bubble sonoluminescence (MBSL).

Factors which affect the luminescence observed include the nature of the gas in the bubble or solution, the applied sound pressure wave, the hydrostatic pressure and the frequency of the ultrasound wave applied.

Several researchers (Bhangu & Ashokkumar, 2017; Leong et al., 2011) had identified that sonoluminescence is due to electron accelerated during the compression phase of the sound wave cycle leading to the contents of the bubble to be heated. A weak plasma is formed in the heated bubble which results in collision of ions or atoms in the bubble.

Research carried out by F.R. Young had shown that as the gas thermal conductivity increases, the sonoluminescence was observed to decrease (Leong et al., 2011). This indicates a correlation between the sonoluminescence of an ultrasound exposed bubble and the thermal conductivity of the gas of its content.

2.2.7.2.2 Radical formation

When oscillating wave come into contact with water it could dissociate to form a high reducing agent (H^+) and high oxidising agent (OH^-).

$H_2O = H^+ + OH^-$

H^+ is a high reducing agent and OH^- a strong oxidising agent. The radicals formed have the potency to form other products with other active ions in the vicinity. This is important in understanding the behaviour of water molecules when subjected to ultrasound waves during enhanced oil recovery. The presence of high oxidising agents could result in the formation of other molecules. Earlier, the variation in electronegativity between sandstone and carbonates were discussed. The oxidising agents have potential to alter the polarity of the reservoir fluids and reservoir pores.

2.2.7.2.3 Shear and mechanical mixing of materials

The collapse of the ultrasound waves leads to shock waves being released, microjets created and micro streams projected. This provides turbulence and additional shear force

on the mass transport phenomenon. The turbulence has the potential to significantly aid alter the oil-water contact as well and the fluid-rock contact resulting in increase in oil displacement and overall oil recovery.

2.2.8 Computed tomography (CT) scan

Computed tomography (CT) can be described as the process or technique of acquiring two-dimensional images using x-rays on either microfocus or nanofocus settings. The samples (core) that is to be scanned is subjected to x- rays. The x rays are generated from an X-ray tube and directed to the desired sample which partially absorbs the x-rays prior to their contact with an x ray detector surface plate. The x-rays that have penetrated the sample are collected on the detector surface. In modern CT scanners, the sample usually undergoes a series of rotations in a slow motion at an angular position during the scanning processes while the image is being acquired. From this point, the conversion of the x rays to digital images takes place within the computer processor and made visible on the screen. An industrial type CT scanner is illustrated in Figure 2.12. The process of CT scan earlier described is shown in Figure 2.13.

1 CT Scanner **2** Graphic user interface **3** Sample position controller

Figure 2.12 Computed tomography scanner

The fact that all fluid transport phenomena in enhance oil recovery are associated with the characteristic of the reservoir at pore scale, it is significant to understand what and how the structure of the pore is, in terms of pore characteristics, topology, topography etc. that can

influence any potential recovery or field development strategy. Moreover, it is a fact that reservoir formations are highly heterogeneous in nature and therefore the better the properties are understood at the pore scale, the better the overall characteristics of the reservoir formations are determined for field development strategy. Any attempt in modelling the properties of a reservoir at insitu condition can only be reliable when considerations are made at the pore scale (Katsevich et al., 2015).

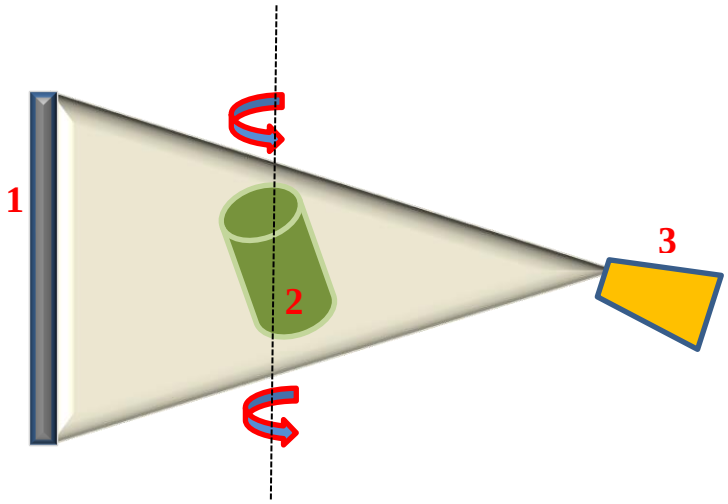

1 Detector **2** Rotating core sample **3** Source of X-ray

Figure 2.13 Computer tomography scan process

The utilisation of computed tomography scanning in core analysis has become widely recognised as an acceptable tool in reservoir engineering and reservoir studies. Figure 2.13 also highlights the major components of a computer tomography scan. This development has spanned over several decades with improvements in its application as it gains global acceptance. An attempt to group previous studies on the use of CT in core analysis was carried out (Withjack, Devier, & Michael, 2003). Here, a detailed account of the various reservoir applications of the computed tomography scanner were outlined. Some of these applications are in core description, desaturation studies, hydrates studies, improved oil recovery, acid treatment, stimulation, formation damage, analysis of perforators, amongst others. The research cuts across a wide spectrum of works conducted by several researchers. More recently, the use of computed tomography in the determination of heterogeneous

reservoir rocks was shown (Skinner, Tovar, & Schechter, 2015). In Table 2.2 the main applications of CT scan in the oil and gas industry are detailed.

Table 2:2 Reservoir applications of Computed tomography scanner

Research category	Characteristic/process
CT methodology	Data acquisition & Processing
Core inspection	Core log reconciliation Fracture analysis Sample characterisation
SCAL- Special Core Analysis Laboratory	Relative permeability Capillary pressure Resistivity determination
Recovery studies	Displacement mechanism Waterflooding Chemical flooding CO_2 Flooding Gas displacement
Heavy oil	Recovery process Relative permeability
Hydrates	Mechanisms
Geothermal	Sample characterisation Recovery process Scale
Formation damage	Invasion
Simulation	Acid treatment Hydraulic fracturing
Perforators	Penetration Damage
Microtomography	Sample characterisation Recovery processes

2.2.8.1 The operation of computer tomography scan

Generated x-rays are directed to the core samples and received on the detector; a tomographic slice of the core is produced from the data collected by the measurement of the relative number of the x-rays transmitted to the detector. The x rays have different radial and azimuthal coordinates that enable imagery processing. Since x rays are electromagnetic waves, there is a tendency for attenuation to occur. Therefore, at the point in which the collection of x rays takes place, the logarithm of the inverse of the relative number of the photons transmitted are integrated to obtain the linear coefficients of attenuation. This data is used for the construction of the algorithms to produce an image. All the images contain the matrices of the linear attenuation coefficient for a thin slice of the core. The ratio of the intensity of the incident x ray beam on the core sample to the intensity of the transmitted beam divided by the thickness of the core in log value is defined as the linear attenuation coefficient. The value of the linear attenuation coefficient is dependent on the atomic number of the core sample as well as the density of the core sample and the amount of energy possessed by the x- rays (Coles, Hazlett, Spanne, Muegge, & Furr, 1995). Therefore, atomic number, core diameter or thickness and x-ray intensity are vital parameters that enable characterisation of the rock core in computed tomography.

The imaging process allows mapping of attenuation coefficients along the outstretch of numerous points on the core. The numerical equation that gives the relationship between the incoming x rays to the core and the outgoing x rays, to the core sample is given by equation 2.11.

$$\frac{I}{I_O} = e^{-\frac{\mu}{\rho}\rho x} \qquad 2.11$$

In equation 2.11, I is the intensity of the incoming x-ray (transmitted from the transmitter), I_o is the intensity of the outgoing x rays and density of the core is ρ. The value of x is dependent on the distance across the core which, in this case, is the thickness of the core sample at any point.

The CT scan has two settings. These settings are the microfocus and the nanofocus. The microfocus is for samples that are considered to be dense and or have a tendency to absorb a large amount of x rays while the nanofocus is generally applied for less dense materials.

The nanofocus can provide images with resolutions in the order of 300nm (Singhai, Grande, & Zhou, 2013). This enables the visualisation of the internal three-dimensional structure of materials with very fine scale features.

Some of the challenges associated with the use of the CT scans are beam hardening and artifacts. Beam hardening is caused because of the absorption of low energy photons in the x ray by the scanned substance leading to a situation where the x rays gain more energy than they would ordinarily have with the presence of low energy photons. Hence, a higher intensity and more hardened beam is received at the detector and as it hardens, the attenuation decreases. This results in the non-uniformity of transmission through the sample. In a situation where the scanned material is cylindrical for example, a greater absorption is seen in the central region of the cylindrical core than on the edges of the same cylindrical core. Thus, as hardening continues in the central region of the specimen the image becomes darker. This eventually leads to a distorted image on the detector. The solution to this problem is the use of filters. The filters commonly used are made from lead, copper, silicon and aluminium to eliminate the lower energy level photons discharged from the transmitter from the spectrum. However, when filters are applied, exposure parameters are increased to account for the fall in the flux of the transmitted x ray. These exposure parameters are current and voltage settings as well as the scanning duration (time). In certain instances, the specimen may swing out of the field of view of the detector at certain positions creating a bright ring along the boundary during the reconstruction stage of the image. The ring artefact, however, can be removed using mathematical tools in the computer during the reconstruction stage. Another cause of artifact is the presence of defects on the detector leading to reduced image quality. When the rotation of the specimen on the sample stage is central, on certain occasions, incongruent nonlinear response is observed in the pixels of the detector leading to a ring artifact (Singhai et al., 2013).

In another research conducted to compare the two different trajectories one in a stitched circular mode and the other in a continuous helical mode, it was observed that the best trajectory was obtained from the helical reconstructed images. These gave higher quality images when compared with those obtained from standard circle beam trajectory (Katsevich et al., 2015). In all CT scans, the images are received on the detector and there upon undergo magnification geometrically. A sample is subjected to rotation as images of the projections are acquired in equal and similar angular increments. The reconstruction of the 3D image is done using Filtered back projection algorithm (FBP). The FBP is common in the

conventional circular rotation CT scanners. However, the helical algorithm for the reconstruction was developed from medical operations to minimise x ray exposure to patients receiving medical attention. Adapted to the FBP algorithm, the Katsevich Filter Back Algorithm caters for the helical trajectory which differs from the standard circular trajectory but based on the same principles. In the helical rotation, an unwinding process at 360^{o} was employed to enable continuous scanning in the absence of slip rings to accommodate feeding electrical signals. Other benefits observed from the helical scanning process are reduced image acquisition time. Here, the incident flux on the detector can be adjusted to high "cone angle" without creating undesired artifacts, which is common in the standard circular rotation scanner, when projected at high incidence angle. A scan at 6^{o} for carbonate rocks gave the best image for circular scans. When the scan angle was increased to 12^{o} the image quality diminished. However, when the same sample of carbonate core was subjected to the helical scan trajectory at angle far exceeding 12^{o}, up to 32^{o}, improved images were obtained. Thirty-two degrees, (32^{o}) is more than 5 times the angle for circular scan without artifacts and with improved imagery.

2.2.8.2 CT Scan Data acquisition

Figure 2.14 illustrates a reconstruction of a rock sample with VG Max 2.2 Volume graphics with a section of the rock taken to illustrate the interior properties.

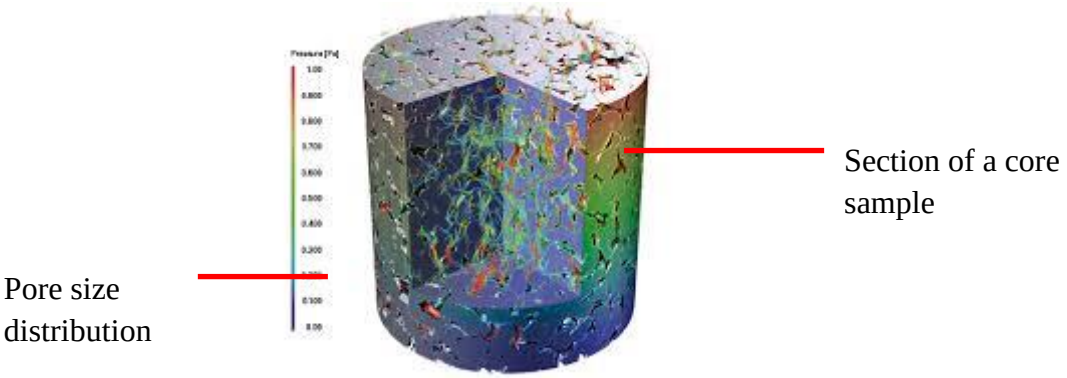

Figure 2.14 Reconstruction of a core sample (source: Volume graphics)

2.2.9 Core flooding equipment

Core flooding equipment has become a central part of petroleum laboratory research on reservoir cores to determine the behaviour of reservoirs in small scale for upscaling to actual reservoir conditions for prediction of performance as well as for planning development strategies (Alhomadhi et al., 2013; Amro et al., 2007; Duhon & Campbell, 1965;

Mohammadian et al., 2013; Mohammadian et al., 2011). Over the years, the core flooding equipment has been improved and made today to mimic actual reservoir conditions. The core flooding equipment is made of three essential parts: the upstream, core block and the downstream. The upstream constitutes the saturation component where fluid injection is sustained into the core to obtain saturation. The syringe and piston accumulator assembly are integral parts of the upstream. The core block houses the core sample and provides confining pressure and containment as well as support for the core sample. The downstream component is the collection part where effluents are received from the core block (Baldygin, Nobes, & Mitra, 2014).

This researcher (author) is in agreement with other researchers (Baldygin et al., 2014) on the inherent limitations of modern core flooding equipment. First of all, the susceptibility of the syringe pump and the piston accumulator to undesired corrosion is a setback. Secondly, the traditional core flooding equipment has limited space for volumes injected due to small size of the piston accumulator. Thirdly, the non-availability of a post-effluent collection component that would be able to provide for compositional analysis of the effluents significant for any EOR strategy also was a setback. Thus, the analysis is often conducted separately. Fourthly, where reinjection is desired from the effluent back into the core block in EOR, it cannot be achieved, as there is no facility to do so. With the current designs, in the absence of nitrogen, adequate pressurisation cannot be achieved. A new design of a core flooding equipment was fabricated which caters for the deficiencies observed with the traditional core flooding equipment. One of the corrections was that the syringe and pump assembly were made with alloys to prevent corrosion, inclusion of fraction collector for post effluent separation and reinjection. A newly developed core holder with eight points for tapping pressures across the core was incorporated to obtain a more comprehensive pressure profile across the core samples during flooding.

2.2.10 Pore pressure

The pore pressure of the formation using acoustic velocity can be monitored by developing a transform which takes into account the velocity to pore pressure profile (Sayers & Woodward, 2001). The generation of a tomography reflects the magnitude of the pressure and the acoustic wave transmitted. The characteristic of the tomography is based on the rock type and variation in lithology, nature of reservoir fluid and the reservoir- fluid pore pressure. The formation pore pressure is a dependent on other factors such as reservoir

depth; reservoir fluid compressibility and the pore size and distribution. The higher the porosity, the more space is available for reservoir fluids and the smaller the porosity, the smaller the volume of space available for reservoir fluids. Therefore, for the same compaction, the pore pressure will be different. A fluid that is subjected to high compressibility will tend to exhibit higher pore pressure as a result of over burden pressure or stress (Yao & Han, 2009).

2.2.11 Polymer flooding

Polymer flooding is the process of injecting high molecular weight soluble polymers into the reservoir to increase microscopic recovery sweep efficiency usually as an enhanced recovery operation where the water cut in a producing well is high. However, the application of polymer flooding can also occur to cater for a heterogeneous reservoir where certain zones exhibit high permeability and produce a lot of water. The basic idea is to increase the mobility ratio between the oil and the water in the entire reservoir or a selected part of the reservoir in the case of layers of high permeability zones that are prone to high water production and thus, increase recovery from regions with low permeability (Al-Hashmi, Divers, Al-Maamari, Favero, & Thomas, 2016). Additionally, polymer flooding is applicable in decreasing the residual oil saturation in reservoirs taking into consideration the viscoelastic characteristics of polymers to increase oil recovery.

The mobility ratio usually designated as $M_{mobility}$ can be expressed mathematically as (Clarke, Howe, Mitchell, Staniland, & Hawkes, 2016).

$$M_{mobility} = \left[\frac{K_w}{\mu_w} \Big/ \frac{K_o}{\mu_o}\right] \qquad \text{Or} \qquad M_{mobility} = \left[\left(\frac{K_w}{K_o}\right)\left(\frac{\mu_o}{\mu_w}\right)\right] \qquad 2.12$$

$M_{mobility}$ is the mobility ratio, K_w is the relative permeability of oil, μ_w is the viscosity of water, K_o represents the relative permeability of oil and μ_o is the viscosity of oil respectively. The mobility ratio is considered favourable when its value is less than 1 and when greater than 1 it's highly unfavourable. The reason is that the displacing fluid viscosity is less than the viscosity of the fluid displaced, hence recovery efficiency reduced considerably. The recovery efficiency is the product of field volumetric sweep efficiency and the pore-scale displacement efficiency. Therefore, the overall oil recovered is dependent on the recovery at the pore and the ability of the polymer to mobilise oil and by sweeping volume of oil at the field level.

Accordingly, the application of polymer flooding depends on several factors such polymer concentration, molecular weight, polymer type, polymer hydrophobicity, injection water salinity, reservoir pressure and the temperature of the reservoir (Wilton & Torabi, 2013). However, it was observed, in the same study, that the impact of injection water salinity and temperature were reported to be detrimental to the polymer flooding process. The need to address the temperature and salinity limitation has recently received attention. A new technique which involves the use of micro emulsion technique and suspension polymerisation was adopted in a new particle-type polymer with capability to withstand reservoir temperatures up to 120^{o}C and salinity of high proportion reaching up 200000mg/L were developed and found to be operational. The particle size of the new polymer ranged between 30nm to 112µm. The mechanism of operation of the new polymer is attributable to the property of the polymer, which is, its unique ability to form a discontinuous liquid with soft interlinked polymer particles. This allows the polymer to have, in addition to the thermal properties, the ability to extend dynamically the reach to more microscopic regions of the reservoir pores. This is one of the major advantages of the new polymer (Wu et al., 2015). Hitherto, the maximum attainable temperature regime in which several polymers can function optimally was 93.3^{o}C (James J. S., Bernd L, & Nasser A., 2015). The implication is that approximately 40^{o}C increase in temperature between conventional and the new polymer. Gradually, the barrier for the utilisation of polymer flooding in high temperature reservoir is being removed.

There are several mechanisms associated with polymer flooding applications. The major mechanisms are as follows: decrease in the viscous fingering in the reservoir and improvement in the profile of the water injection due to the crossflow across the layers in a layered reservoir with heterogeneity. The others are reduction of the relative permeability of water in a higher proportion than the permeability of oil and permeability reduction after polymer flooding which increases the effectiveness of the subsequent waterflooding carried out (James J. S. et al., 2015).

The use of polymers both synthetic and natural is, in fact, gaining more global acceptance and advances towards improving its existing performance is receiving more attention. Research is ongoing to continually improve on the performance of the polymer as more and more challenging and hostile terrains are encountered in the effort to recover more oil from the reservoir. This is evident in the growing applications in many enhanced oil recovery strategies and operations (Al-Amrie et al., 2015; Koh, Lee, & Pope, 2016; Li et al., 2014;

Lu et al., 2015; Rambeau, Alves, Andreu, Loriau, & Passade-Boupat; Rodriguez Manrique, Rousseau, Bekri, Djabourov, & Bejarano, 2014; S., 2015; Wilton & Torabi, 2013).

The non-application of ultrasound in EOR in conjunction with polymers was hitherto based on the assumption that the ultrasound could lead to the disintegration of the long-chained molecules of the polymer by the vibrations of the acoustic waves. The vibration has the effect of decreasing the viscosity of the polymer solution. Therefore, virtually little research has been carried out on the applicability of polymer flooding in conjunction with ultrasound. However, in one of the ground breaking papers (Hamida & Babadagli, 2007) while investigating the capillary interaction with the application of acoustic waves, the researchers extended experimentation to include polymer with acoustic simulation and surfactant on saturate Indiana limestone cores and saturated Berea sandstone cores. The application of polymer Xanthum gum at 0.03% resulted in a 12% increase in the oil recovery, but when at 0.09% concentration there was decrease in the percentage of oil recovered from the EOR. This was attributed to the degradation of the polymer by the frequency vibration of the acoustic wave, which forms a form of entanglement leading to reduced mobility of the reservoir pores. It further concluded that unless the percentage xanthan does not exceed 0.09% the frequency of the acoustic wave applied is proportional to the quantity of oil recovered. This appears to echo a defined threshold once reached results in the poor performance of the injected polymer in the reservoir.

Polymer flooding with application of hydrolysed polyacrylamide (HPAM), in previous researches indicated high capability for reducing the irreducible oil saturation values than water flooding (Koh et al., 2016). In an experiment performed by Koh et al, it was observed that with the application of HPAM a 24% increment in the oil recovery was obtained. The phenomenon of the decrease in the irreducible oil saturation is associated with the viscoelasticity of the hydrolysed polyacrylamide. Elastic turbulence was observed with the application of HPAM using an NMR diffusion device. It illustrated that the sweep efficiency of polymer is dependent upon exhibiting a viscoelastic property where the shear rate overcomes a critical value for any given polymer in the reservoir to effectively recover oil.

2.2.11.1 Polydispersity and viscoelasticity of polymer solutions

A lot of research has been conducted to determine the influence of viscoelasticity of polymer on enhanced oil recovery (Alvarado, Moradi Bidhendi, Garcia-Olvera, Morin, & Oakey, 2014; Chen et al., 2011; Clarke et al., 2016; Denney, 2009; Hu, Chung, & Maxey, 2015;

Mishra, Bera, & Mandal, 2014; Qi, Ehrenfried, Koh, & Balhoff, 2016; Urbissinova, Trivedi, & Kuru, 2010; Wilton & Torabi, 2013). It has been observed that HPAM has the potential to increase oil displacement efficiency through the stripping of residual oil, changing the steady state profile polymer flow in the reservoir and generating hysterical coil conformation. The hysteresis was attributed to the apparent thickening of HPAM during high flow in the reservoir because of the stretching of the polymer molecules. When the polymer molecules expand and become elongated through the microscopic pores of the reservoir usually there is insufficient time for the molecules to revert to their initial flow pattern and status when elongated. This provides an elastic strain on the polymer chain molecule leading to an extended relaxation time. The extended relaxation time, to the physical observer of the phenomenon, seems as an apparent thickening process of the polymer. However, in reality, what is occurring is numerous polymer molecular elongations and stretching with numerous molecular relaxation times giving a thickened and more viscous polymer (Clarke et al., 2016). The stretched polymer flexible molecular random coils lead to a resultant coil-conformation thickening of the polymer and high increase in the resultant energy of the polymer molecules to drag residual oil by making enhance contact with the pore surfaces. Here, the polymer's drag coefficients are increased. The polymer molecular elongation and viscoelastic flow behavior through porous media is illustrated in Figure 2.15

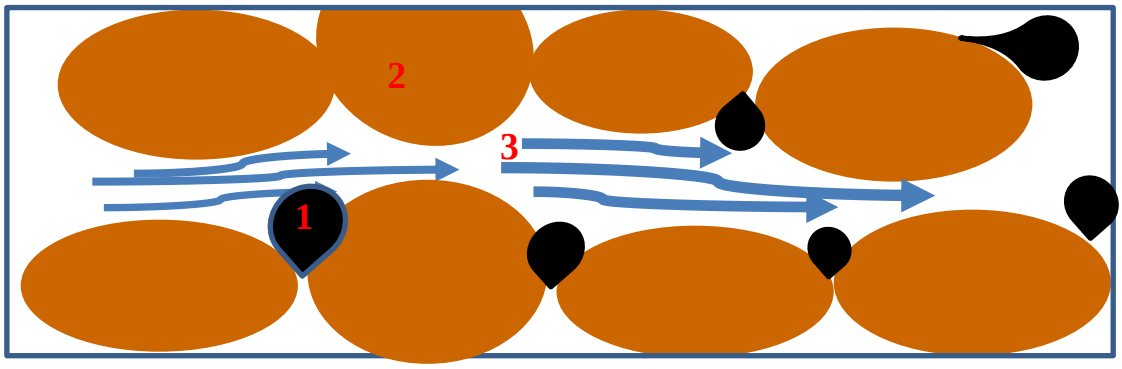

1 Oil **2** Sand grains **3** Stretched polymer chain

Figure 2.15: Polymer molecular elongation and flow through a porous media

2.2.11.1.1 Polydispersity

Polymer solution polydispersity, where polymer solutions are configured or blended with various molecular weight size distribution of polymers, has been shown to increase the

elasticity of polymer solutions formed. The main advantage is increase in displacement efficiency during enhanced oil recovery by allowing smaller size molecules of polymer to penetrate the complex and tortuous reservoir micro pores and micro structures of the reservoir formations more readily and strip residual oil which ordinarily would have been trapped and not recovered. The role of polymer elasticity in enhanced oil recovery has gained a lot of interest. The average molecular weight of the blended solution can be expressed as a function of the sum of the fractions of the individual component molecular weight distributions of polymers in the solution (Veerabhadrappa, Doda, Trivedi, & Kuru, 2013; Veerabhadrappa, Urbissinova, Trivedi, & Kuru, 2010). The equations for the preparation of polymer blend are shown in Equation 2.13 and Equation 2.14. With these equations, various polymer fluid designs as well as numerous configurations of blends can be made to fit reservoir characteristics and pore geometry. This is, even more, since no two reservoirs have identical properties. Hence, optimising polymer designs and selections for peculiar reservoirs can be enhanced oil recovery.

$$M_{W.B} = \prod_{i=1}^{n} \omega_i M_{w,i} \tag{2.13}$$

$$I = \frac{M_w}{M_n} = \left[\sum_{i=1}^{n} \omega_i M_{w,i}\right]\left[\sum_{i=1}^{n} \frac{\omega_i}{M_{w,i}}\right] \tag{2.14}$$

The average molecular weight of the solution based on blended fraction of HPAM is expressed as $M_{W.B}$, the fraction of individual polymer (grade) in the blended solution is denoted by ω_i and the average molecular weight of the individual component polymer (grade) in solution is represented by $M_{w,i}$. Furthermore, the polydispersity index which indicates the degree of polymer molecular weight distribution (MWD) variation is denoted by the letter, I. The polydispersity index is the ratio of the sum average polymer molecular weight, M_w and the number average of the individual component polymer molecular weights, M_n.

2.2.11.2 Power law

The power law describes the Newtonian behaviour of a fluid. It provides the relationship between shear rate and shear stress (Silva, Aguiar, Rezende, Monsores, & Lucas, 2018). The expression τ, is the shear stress (lb/100ft^2), K represents the consistency factor (cp), γ is the shear rate (s^{-1}) and n is the fluid behaviour index (dimensionless).

$$\tau = K\gamma^n \quad 2.15$$

When the value of n is equal to 1 the fluid is Newtonian, when n is less than 1 the fluid is pseudoplastic and when n is greater than 1, the fluid is dilatant.

2.2.12 Acoustic velocity and transducer assembly

The acoustic velocity and transducer assembly enable ultrasound waves applications. Ultrasonic waves which are mechanical pressure waves are formed by actuating ultrasonic transducers with high frequency, high voltage current generated by electronic oscillators (power generators).

2.3 Trend in ultrasound research and limitations

The first experimental investigation of ultrasound in enhanced oil recovery was conducted in 1964 by Duhon and Campbell (Hamidi, Mohammadian, Asadullah, Azdarpour, & Rafati, 2015) . Since then, significant research both experimental and theoretical have been carried out. Appendix A describes the key trends in research in ultrasound enhanced oil recovery over the years leading to the current state. It also details the limitations and knowledge gaps as well as highlights some aspects which make this current research novel.

2.4 Chapter summary

In this Chapter (Chapter Two), an overview of the petroleum reservoirs, namely sandstone and carbonates were presented. The characteristics of these reservoirs in terms of their porosity and permeability were also highlighted. In addition, current recovery techniques and strategies for enhanced oil recovery were addressed. Fluid flow behaviour and measurement in terms of Darcy's flow equation were presented to facilitate hydrocarbon flow behaviour analysis.

Furthermore, acoustics waves and their theories and principles were discussed. Acoustic wave classifications and mode of propagation as well as electrodynamics and attenuation were highlighted. The principles of computed tomography scans and their applications in relation to rock study and in determining size and structure of grains and reservoir micropores and microstructures for enhanced oil recovery were presented. Equally, the modus operandi of coreflooding equipment and polymer flooding, a recovery method, and its optimisation strategies were discussed.

CHAPTER THREE
MATERIALS, APPARATUS AND METHODOLOGY

3.1 Introduction

Chapter three provides detailed description of the materials, apparatus and the procedures adopted for this research work. It systematically explains the methods adopted and details precautions taken to ensure accuracy of results. The steps taken ensured overall safety of the experimental process carried out. A simplified flow chart mapping out the methodology is shown in Figure 3.1. The main sections are the petrophysical analysis, geophysical analysis, oil recovery and evaluation of enhanced oil recovery (EOR). Each section has strategies and outcomes leading to enhanced oil recovery.

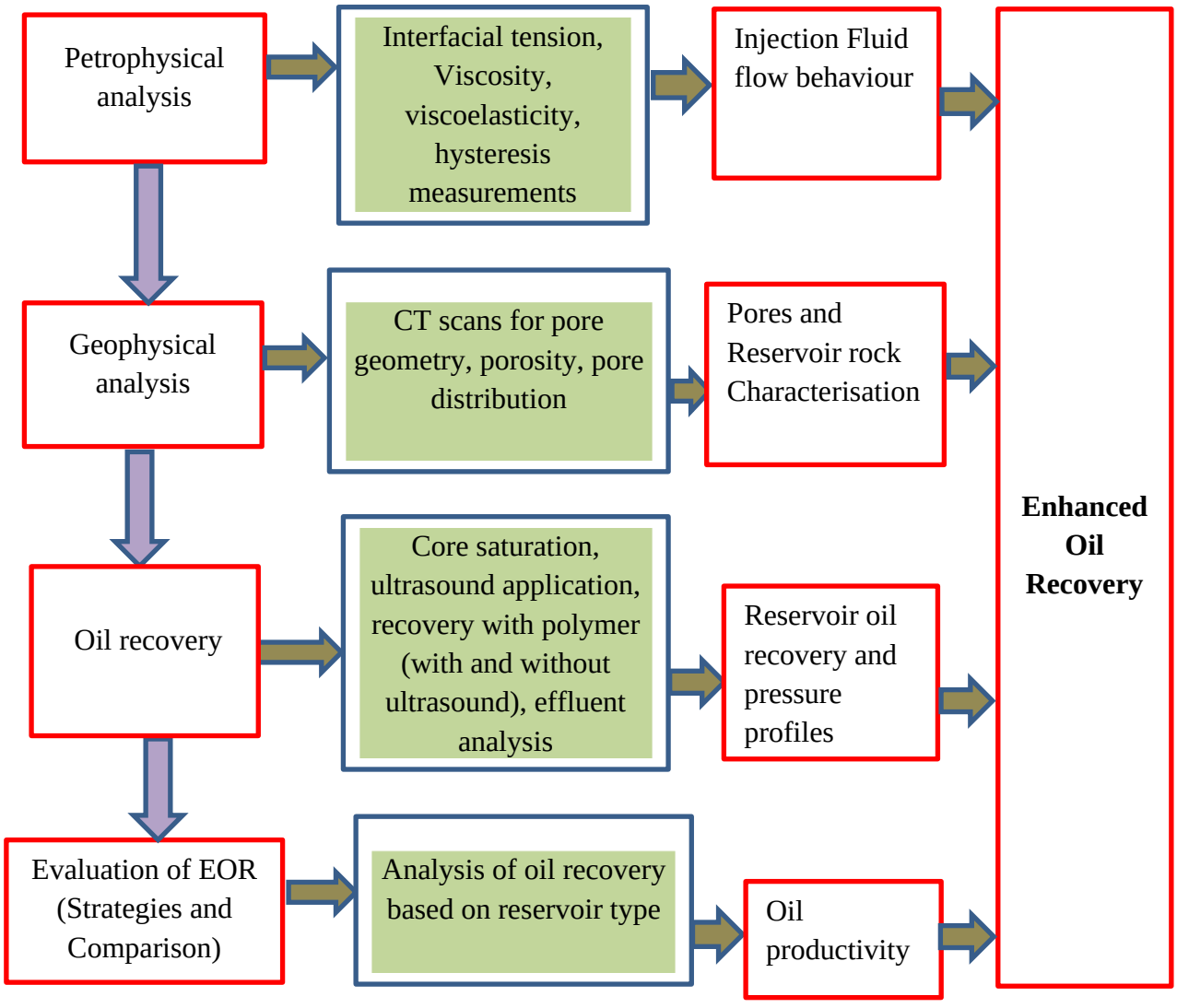

Figure 3.1: Experimental flow chart

3.1.1 Selection of reservoir conditions based on temperature and pressure

The selection of the reservoir conditions for conducting this research is based on the characteristics of petroleum reservoirs (Graph gradients sourced from the Society of Petroleum Engineers (SPE)). Figure 3.2 indicates that for a 3000 to 6000ft depth reservoir the temperature regime falls between 100 and 180°F. Hence, all experiments were conducted within the range of 100 to 180°F at reservoir conditions. The regime demarcated supports the UFS 200 coreflooding equipment, which has a maximum operating temperature of 100°C (212°F) and operating pressure of 5,000psi respectively.

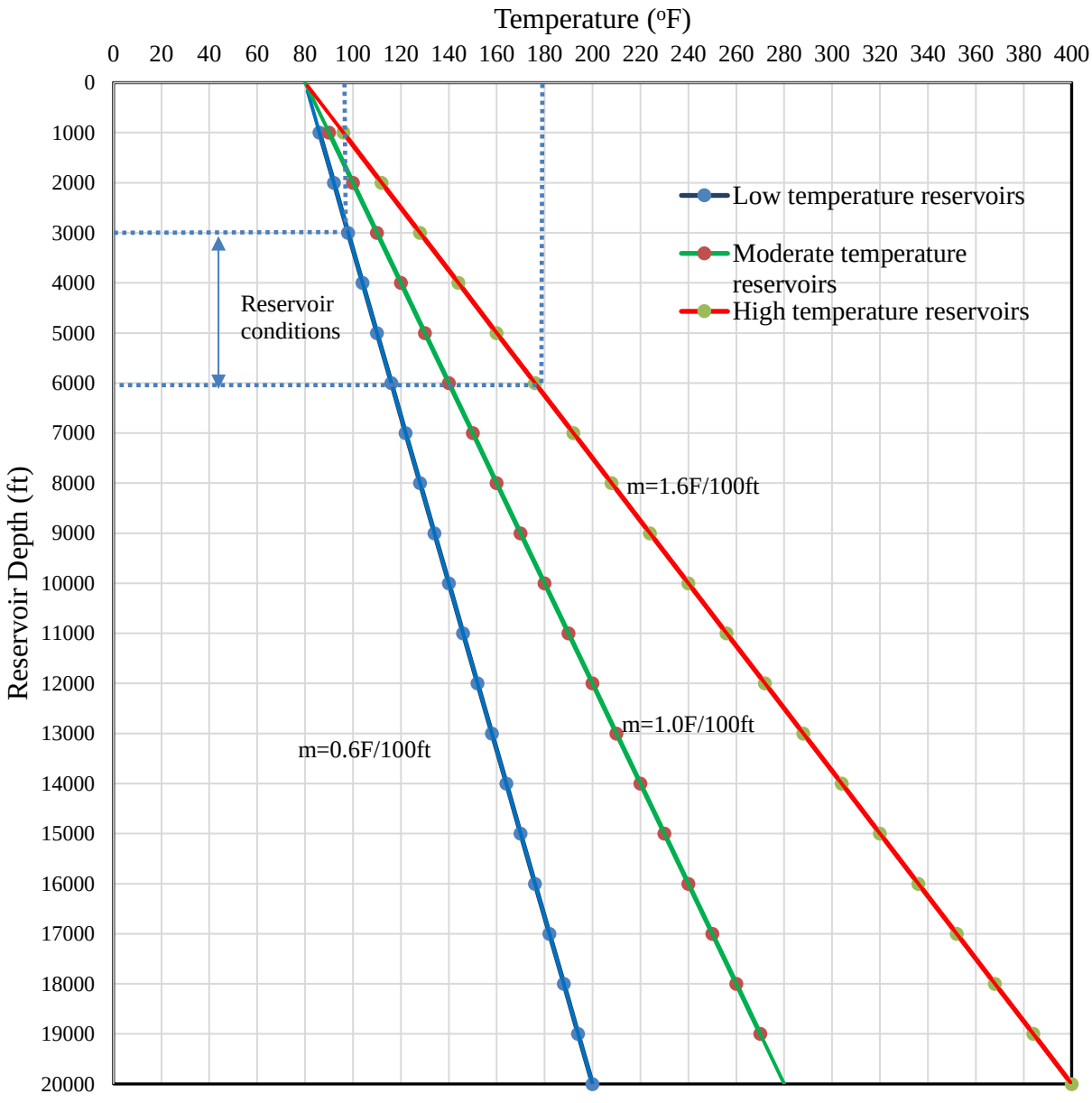

Figure 3.2: Temperature- reservoir depth profile (Gradients sourced from SPE)

Figure 3.3 shows the pressure -depth profile for a typical reservoir. The region of interest is clearly demarcated on the graph. The pressure-depth profile is vital for overburden pressure application on the rock samples which have a UCS value less than 6000psi. Hence, fit for purpose, for a UFS -200 coreflooding equipment with a capacity of 5,000 psi operating pressure.

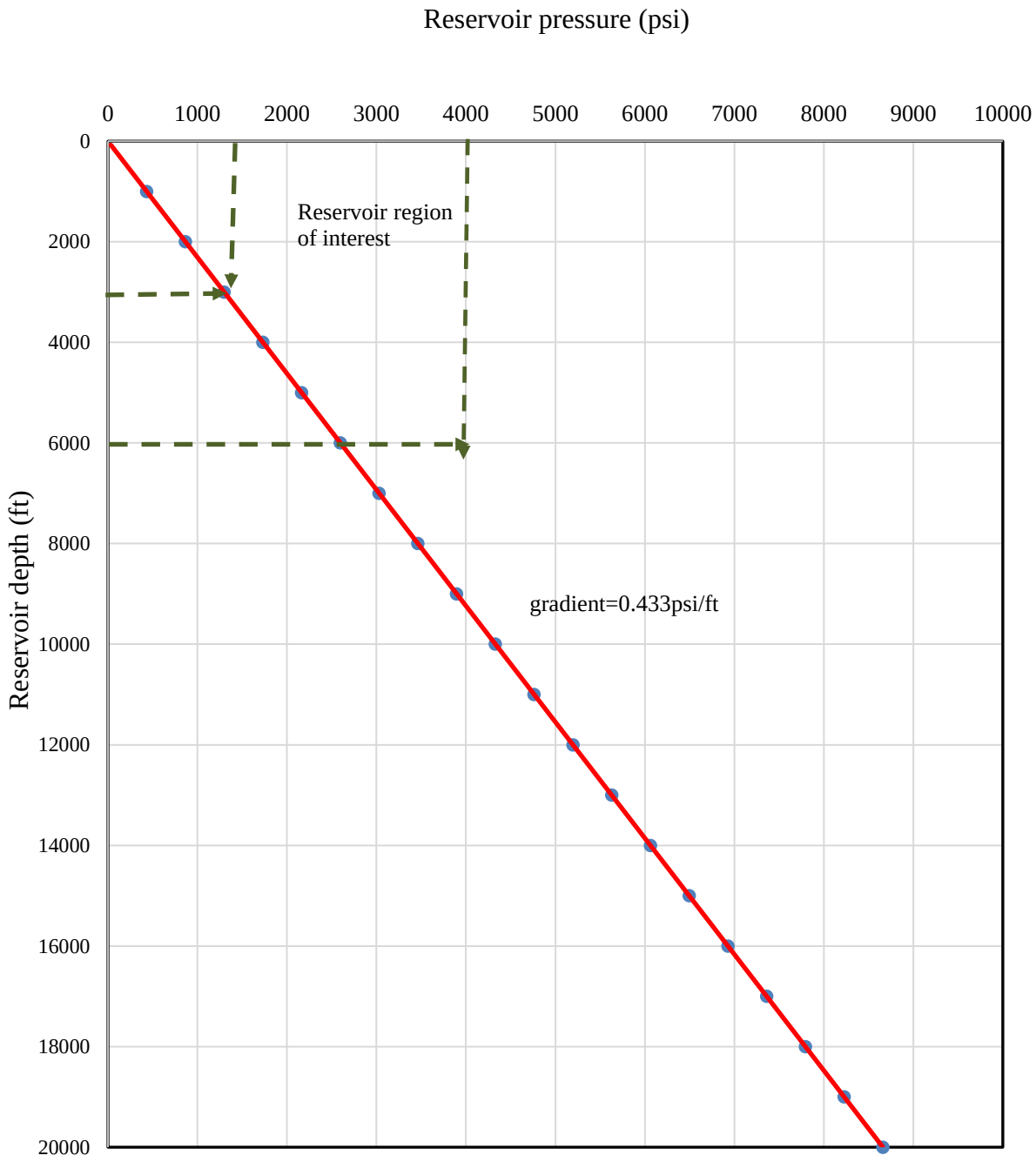

Figure 3.3: Pressure versus depth profile (Gradient sourced from SPE)

3.2 Petrophysical analysis

The petrophysical aspect of this research consists of the analysis of the fluid properties of the oils and the injection fluids in line with the objectives of this research work. The petrophysical properties investigated and determined were integrated into the experimental process to enable the proper assessment as well as characterisation of the role of individual fluid properties in the overall enhanced oil recovery research. These properties include interfacial tension, viscosity and viscoelasticity and fluid flow indices as well as hysteresis behaviour amongst others.

3.2.1 Interfacial tension

With the aid of the IFT equipment, the interfacial tension for oils/water was obtained. This enabled the understanding of the influence of interfacial tension and reservoir conditions as well as reservoir pressure on oil recovery. IFT values were measured prior to coreflooding as part of the consideration of the influence of interfacial tension on recovery as depicted in literature (Abdallah & Stukan, 2012). Figure 3.4 shows the interfacial tension measurement equipment used for the IFT measurements.

3.2.1.1 Interfacial tension measurement equipment

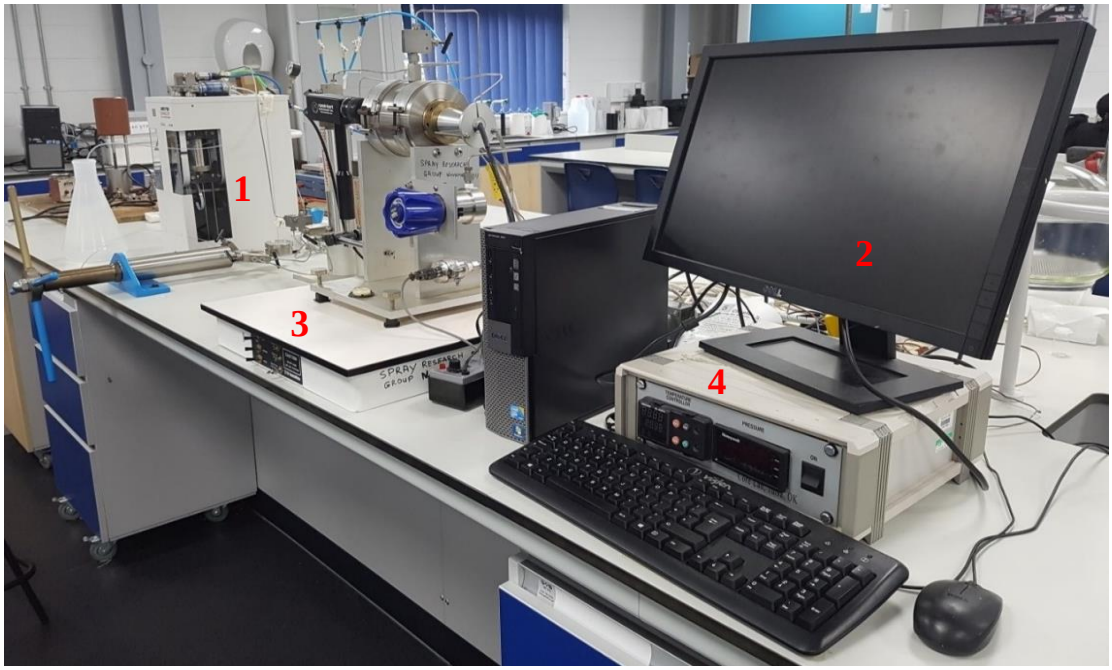

1 Delivery Chamber
2 Graphic User Interface
3 IFT Analyser
4 Temperature and Pressure Control

Figure 3.4: Interfacial tension measurement equipment

3.2.1.2 Hydrolysed polyacrylamide polymer

The polymer for this experiment is hydrolysed polyacrylamide, which is the Petroleum industry's most utilised polymer for enhanced oil recovery, EOR. The polymer molecular weight distribution was designed to provide a wide range of molecular weights. The polymer samples were obtained from two companies: Kemera Oyj, Helsinki, Finland and Sinofloc Chemicals Ltd, Beijing, China. The polymers utilised in this experimental investigation are tabulated in Table 3.1. The polymer properties namely percentage hydrolysis, ionic charge and molecular weight in millions, Daltons, are detailed. Figure 3.5 illustrates hydrolysed polyacrylamide granules (HPAM) used and the molecular formula is shown in Figure 3.6. The three-dimensional structure of acrylamide is shown in Figure 3.7. The three-dimensional structure of hydrolysed polyacrylamide is shown in Figure 3.8. The three-dimensional images were drawn with ACD/ChemSketch software.

Figure 3.5: Hydrolysed polyacrylamide granules

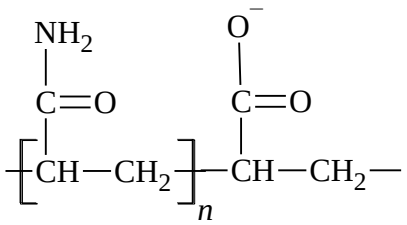

Figure 3.6: Molecular formula of hydrolysed polyacrylamide

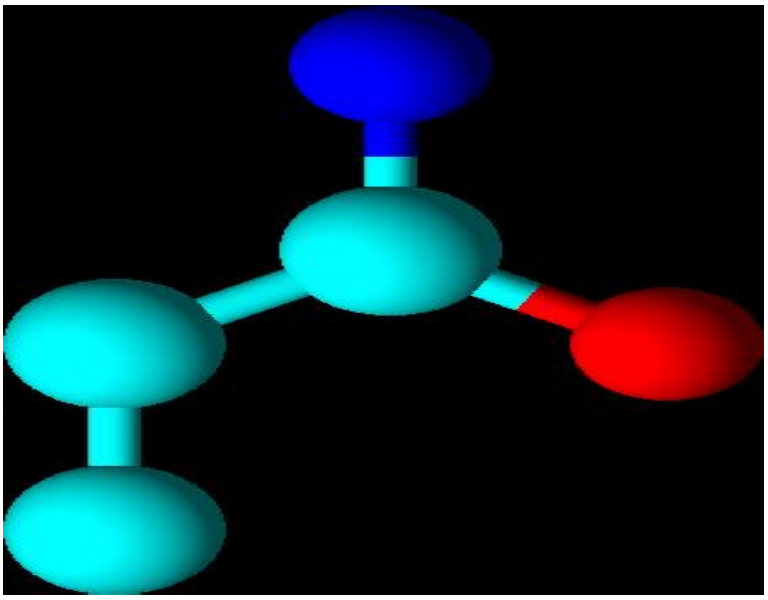

Figure 3.7: Three-dimensional structure of acrylamide

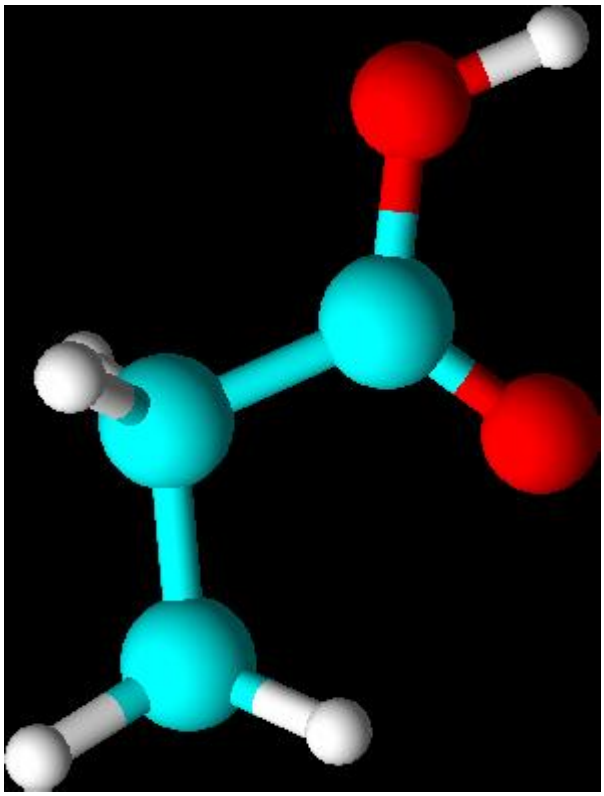

Figure 3.8: Three-dimensional structure of hydrolysed acrylamide

Table 3:1: Hydrolysed polyacrylamide polymer properties

Name of polymer	Reference Grade	Ionic charge	Percentage (%) hydrolysis per mol	Molecular weight in million (Daltons)	Mean Molecular weight in million (Daltons
Kemira/Sinofloc 9224	HPAM1	anionic	24-28	22-24	23
Sinofloc 9219	HPAM2	anionic	24-28	17-19	18
Sinofloc 9216	HPAM3	anionic	24-28	14-16	15
Sinofloc 9113	HPAM4	anionic	9-13	11-13	12
Sinofloc 9410	HPAM5	anionic	38-42	6-8	7

3.2.2 Polymer solution preparation

Polymer solutions were prepared using distilled water to eliminate the effect and impact of monovalent and divalent cations that are prevalent in produced water (Seright, Campbell, Mozley, & Han, 2010). The cations include sodium (Na^{+}), calcium ($Ca^{2+)}$, Magnesium (Mg^{2+}), iron (Fe^{2+} and Fe^{3+}). These chemical species (ions) when present in solution weaken the polymer molecular chain. The eventual impact is the destruction of the polymer molecular chains and subsequent reduction of the performance of the polymer flood. The carbonyl group in the polymer chain is affected. Hence the use of distilled water in polymer solution preparation. Therefore, the presence of any of these ions would affect the final viscosity of the polymer and that is not a desirable output as the essence is to increase the viscosity of the flooding water to enhance sweep efficiency. The presence of significant quantity of cations in polymer (HPAM) solution can lead to polymer precipitation and degradation and the resultant decrease in viscosity especially when temperatures, at reservoir conditions, of up to fifty to eighty degree centigrade (50-80^{o}C) exist. The maximum limit of divalent should not exceed 20mg/L in any polymer solution where maximum efficiency in polymer sweep is desired. Limits greater than 20mg/L can increase relative hardness of the water and polymer precipitation through the formation amides in HPAM solutions.

The polymer solutions after undergoing adequate mixing are filtered using a Millipore filter to prevent the infiltration of dissolved solids likely to cause blockage of the pores

during core flooding. Previous research had shown HPAM passes the 1.2 micron filter (Levitt & Pope, 2008)

3.2.2.1 Polymer concentration

The concentration of the HPAM solutions were varied by increasing the quantity of polymer in each solution in the following proportions: 200mg/L, 600mg/L, 1000mg/L, 1200mg/L, 1600mg/L and 2000mg/L respectively. The unit of mg/L is equivalent to ppm of polymer solution. By increasing the concentration of the polymer, the viscosity and viscoelastic properties as well as the hysteresis behaviour at various concentration could be investigated. The HPAM solutions were prepared using a varied method where time intervals of 60 seconds were added to allow dissolution of the polymer rather than the continues placement of the polymer in the vortices during mixing. This allowed a more effective mixing of the polymer.

3.2.2.2 Polydispersity and design of polymer solutions

The composition of the polymer solutions was varied by changing the molecular weight composition of subsequent HPAM solutions through alteration of the polydispersity. Variation of the molecular weights distribution of the compounds results in variation of the elasticity of the polymer solution. Here, the Dehghanpour equation for polydispersity was used (Veerabhadrappa et al., 2013; Veerabhadrappa et al., 2010) to enhance the polymer solutions produced. Thus, taking account of polymer molecular weight sizing. By mixing various molecular weight samples, the characterisation of the rheological behaviour of the polymer fluids during polymer solution analysis and during polymer core flooding operations was made more comprehensive. The impact of each configuration adequately presented. Furthermore, the best-case scenarios for maximum oil recovery readily identified. The properties of the fluid in terms of elasticity and the relationship to shear viscosity were detailed.

3.2.2.3 Precautions:

3.2.2.3.1 Low polymer fluid stirring rates

Apart from using of distilled water in the preparation of the polymer, during the mixing process, low stirring rates were employed to ensure that polymer molecular chains were not disrupted and broken leading to mechanical loss of viscosity. High stirring rates would lead to the breakage of the long polymer molecular chains.

3.2.2.3.2 Mixing in absence of air (with limited exposure to oxygen)

The exposure of polymer mixtures to air (oxygen) to the surrounding environment during mixing was limited by sealing the container with transparent plastic. The reason is that dissolved oxygen during mixing, preparations and polymer injection affects and hampers the performance of HPAM by causing oxidative degradation. All the solutions prepared were mixed in relatively sealed containers during the mixing process to eliminate or reduce to the barest minimal, the impact of oxygen polymer degradation. While ensuring adequate stirring, the polymer solutions are relatively free of dissolved oxygen. This would ensure polymer molecular backbone chains are not oxidised during preparation leading to low viscosity measurements and reduction in performance analysis.

3.2.2.3.3 Vortex used for all polymer additions

To increase the uniform blending of the polymer during the additions, all additions were done gradually by spreading the powdered polymer across the vortex during stirring. This was to prevent lumping and non-uniform dissolution of the polymer and creation of a maximised surface contact area for the water and polymer leading to total hydration of the polymer and therefore maximum viscosity obtained for the concentrations of polymer desired of the mixture. The digital mixer is shown in Figure 3.9.

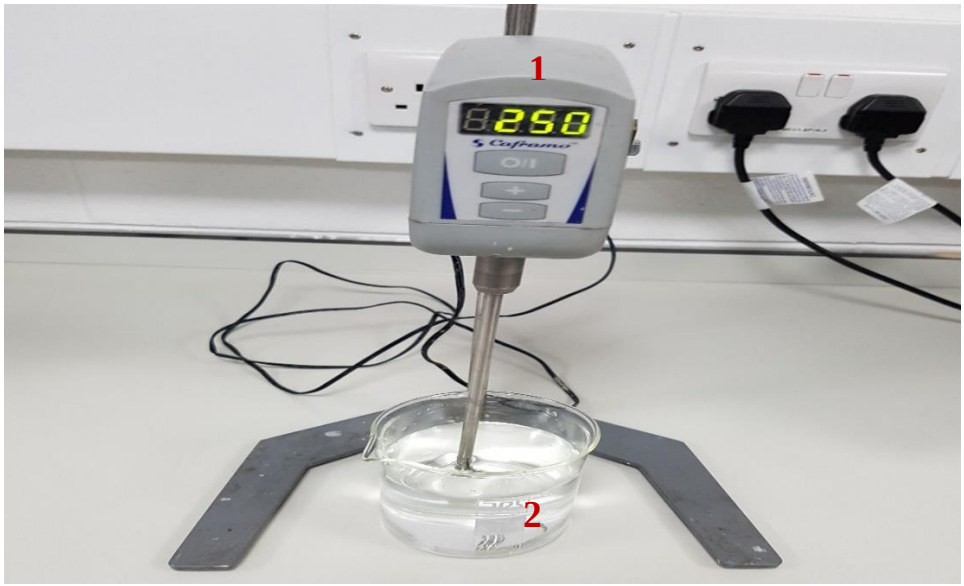

1 Mixer with Digital control **2** Polymer solution

Figure 3.9: Mixer for polymer solution

3.2.3 Determination of the rheological characteristics of polymer solutions with viscometer

1 Control panel/ pressure regulator
2 Viscometer
3 Sample cup
4 Heat bath
5 Graphic user interface with ORCADA software

Figure 3.10: OFITE Model 1100 pressurised viscometer with graphic user interface (laptop computer**)**

3.2.3.1 Viscometer

The fluid rheological properties namely viscosity, shear rate, shear stress and flow behavioural indices, n values and flow consistency coefficient, K, were determined with the Model 1100 pressurised viscometer shown in Figure 3.10. The Model 1100 pressurised viscometer has a fully automated data acquisition ORCADA software that enables full control of the viscometric system during operations. The data acquisition software enabled readouts processed for full analysis including graphical representation.

The design and operational specifications of the viscometer are detailed in Table 3.2

Table 3:2: Viscometer design and operation specifications

Design and operational parameter	Magnitude	Units
Minimum shearing rate	0.01	s^{-1}
Maximum shearing rate	1000	s^{-1}
Maximum pressure rate	2,500	Psi
Maximum temperature	260	^{o}C
Bob and rotor rates	0-4000	dyne
Power	230	Volts

3.2.3.2 Calibration of Model 1100 pressurised viscometer

The OFITE Model 1100 pressurised viscometer was calibrated with the calibration fluid pre-prepared by the Viscometer manufacturer for calibration fluid in conjunction with ORCADA software. The pre-prepared calibration fluid was specifically made for calibration of the instrument. The first step was the selection of the "utilities" icon and the "calibrate shear stress" from the drop menu and shear stress raw values observed on the graphic user interface. The RPM values were set below 300 in accordance with instrument manufactures design calibration specifications. The rc^2 values were calculated and the values obtained were found to be greater than 0.9990. This implied that the calibration was within the desired level of accuracy. The straight-line calibration graph shown in Figure 4.3 was constructed.

Table 3.3 details the polymer solution design based on polydispersity index (PI) derived from equation 2.2 earlier discussed in Chapter two. The determination of the composition of the desired polymer solution was carried out through an iterative process of varying the percentages or fractions of each of the HPAM molecular weight and determining their respective polydispersity index. HPMAG7 was identified as the best option due to its high polydispersity index and complete inclusion of all the molecular weights available.

$$I = \frac{M_w}{M_n} = \left[\sum_{i=1}^{n} \omega_i M_{w,i}\right]\left[\sum_{i=1}^{n} \frac{\omega_i}{M_{w,i}}\right] \quad 2.14$$

Table 3:3: Design of HPAM solution based on polydispersity index for selection purposes

Reference grade	Fraction of polymer weight by grade					Average molecular weight (x10^6) in Dalton	PI
	HPAM1	HPAM2	HPAM3	HPAM4	HPAM5		
HPAMG1	0	0.2	0.1	0.3	0.4	11.5	**1.1491**
HPAMG2	0	0.4	0.4	0.1	0.1	15.1	1.0798
HPAMG3	0.1	0.1	0.1	0.4	0.3	12.4	**1.1527**
HPAMG4	0.1	0.3	0.3	0.1	0.2	14.7	1.1483
HPAMG5	0.1	0.2	0.4	0.2	0.1	14.9	1.0918
HPAMG6	0.3	0.3	0	0.2	0.2	15.8	**1.1935**
HPAMG7	0.3	0.2	0.2	0.1	0.2	15.8	**1.1848**
HPAMG8	0.3	0.2	0.2	0.2	0.1	13.6	1.1252
HPAMG9	0.2	0.2	0.2	0.2	0.2	14.8	**1.1658**
HPAMG10	0	0	0.4	0.4	0.2	12.2	1.0806

3.3 Geophysical analysis

The geophysical properties of the rocks which deals with the internal structure and rock grain properties of the rock such as its porosity, pore geometry, pore distribution and acoustic properties such as wave attenuation were determined. When all these properties are integrated, the behaviour of the reservoir formation when subjected to acoustic waves as well as the degree to which the formation responds to the EOR strategy can be properly assessed. The heterogeneity of the core samples contributes significantly to the overall behaviour of the formation when subjected to any form of EOR method, more especially in acoustic EOR.

3.3.1 Materials

Table 3:4: Reservoir core sample properties

Rock type, formation	Homogeneity	Unconfined Compressive Strength (UCS) in psi	Permeability millidarcy (mD)	Porosity (%)	Pore Volume (mL)
Berea Upper Sandstone, Devonian	Homogeneous	6,500	380	21	5.41
Berea Lower Sandstone, Devonian	Homogeneous	8,000	110	19	4.89
Indiana 70 Carbonate, Missipian	Homogeneous	4,500	95	18	4.63
Guleph dolomite, Carbonate, Silurian	Non-homogenous	9,000	8	9	2.57
Silurian dolomite, Carbonate, Silurian	Non-homogeneous	11,000	55	16	4.11
Edward brown, Carbonate, Upper Cretaceous	Non-homogeneous	3,000	210	39	10.29

The photo images of the rock utilised in the experiments are shown in Figure 3.11 to Figure 3.16

Figure 3.11: Berea Upper Sandstone 1"x 2" size photographic image

Figure 3.12: Berea Lower sandstone 1"x 2" size photographic image

Figure 3.13: Silurian dolomite (Carbonate) 1"x 2" size photographic image

Figure 3.14: Indian limestone 1"x 2" size photographic image

Figure 3.15: Edward brown 1"x 2" size photographic image

Figure 3.16: Guelph dolomite 1"x 2" size photographic image

3.3.1.1 Apparatus

The main equipment utilised for the core sample pore and pore distribution determination was the computed tomography scanner with Volume graphics 2.2 Max for image reconstruction and analysis

3.3.1.2 Computed tomography scanner

The computed tomography scanner used for this experiment has two foci settings: microfocus and nanofocus. The phoenix v|tome|x s Industrial high-resolution CT Scanner was utilised for all core samples scan conducted for this research study. The operations and mechanism of the industrial CT scanner have been extensively discussed in Section 3.2.5. Figure 3.17 and Figure 3.18 show the CT tubes and x-ray detector.

1 Microfocus tube **2** Core sample stand **3** Nanofocus tube

Figure 3.17: CT scanner Nano and Macro tubes

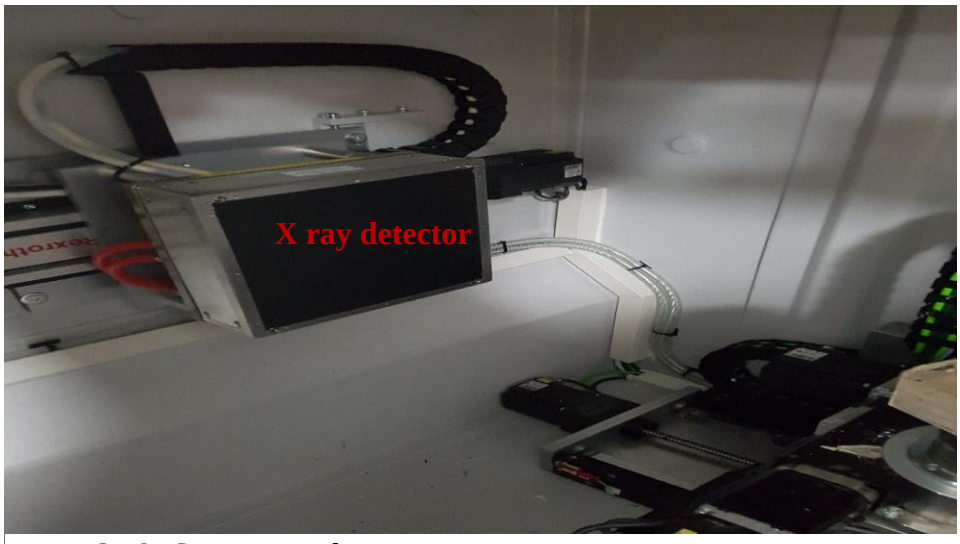

Figure 3.18: CT scanner detector

3.3.2 Computed tomography scan

The carbonate and sandstone core samples of 1inch diameter and 2inch length each were subjected to computed tomography scan with a phoenix v|tome|x s Industrial high-resolution CT Scanner.

Table 3:5: Computed tomography setting applied on core samples

Computed tomography scan setting	Magnitude	Units
Voltage	140	kilovolts
Current	80	Amperes
Power	11.2	Kilowatts
Timings	333	ms
Average	3	
Skip	1	
Binning	1 x 1	
Sensitivity	2000	
V sensor	1	
Focus	Standard (Std)	
Filter cupper thickness	0.1	mm
Image focus	150	

3.3.2.1 Precautions

Core samples x rayed at an angle: The core samples were placed at an inclined position of 30^{o} to the horizontal on the sample stage to prevent beam artifact that can occur because of x-ray hardening due to difference in photon energy absorption. At an inclination, the absorption of lower energy photons was minimised resulting in a less hardened beam that reaches the CT detector plate. Thus, improving the overall quality of the images obtained.

Copper filter: Another precaution taken was the addition of a 0.1micromillimeter copper filter to reduce or eliminate the lower energy photons of x ray beam that could produce

artifact and result in poor 3D imagery with significant noise. Here, as low energy photons are released from source x ray tube, the x-ray pass through the filter and are absorbed by the copper filter, and a uniform beam passes through the core samples ensuring that more high-energy photons make it to the detector plate. This provides high-resolution images with detailed micro-structural features and architecture.

Stability of sample: To prevent the movement of the samples from the field of view (FOV) of the detector during the rotation, the samples were secured firmly to the sample stage. This prevented the creation of additional artifact and noise in the image due to vibrations and rotation of the core samples during the scanning process.

3.3.2.2 Data acquisition through image reconstruction and analysis

The CT images acquired were subsequently reconstructed with the aid of the Volume graphics VG studio MAX 2.2 software. Surface determination was initially performed by identifying the grey values of the core samples and background to obtain the data sets using 3 dimensional settings.

3.3.2.3 Determination of porosity, pore geometry, pore distribution

The core samples, sandstones and carbonates, were placed in the industrial computed tomography scanner to obtain pore geometry and porosity of the core samples as well as the pore distribution. The scanning was conducted using the most suitable settings on the microscale for the different core samples selected for analysis. The images obtained were sent to the Volume graphics component of the scanning process for adequate reconstruction. The reconstruction of the scanned images using the VG-max software provided projections and slices needed for interpretation of pore properties, which include pore geometry, pore distribution and general pore characteristics. Figure 3.19 illustrates the VG-max pore analysis user interface used to determine the properties of the core samples. In Table 10 the settings and specifications used on the Volume graphic VG-max are revealed.

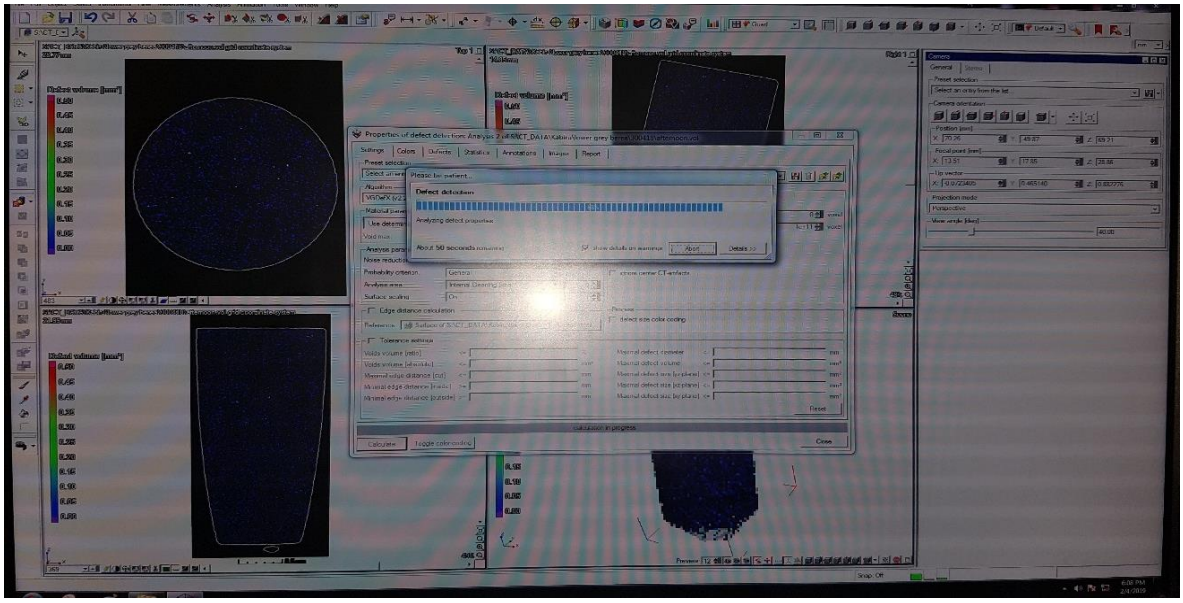

Figure 3.19: VG max pore analysis user interface

Table 3:6: Volume graphics VG-max setting for porosity, pore size and pore distribution

Property	Setting (Mode)
Algorithm	VGDef (2.2)
Material parameters	Use determined surface
Noise reduction	Low
Probability criterion	General
Analysis area	Internal clearing small
Surface sealing	On
Filter result	On
Analysis	Void or Inclusion (Void for porosity)
Probability threshold	0.1
Minimum diameter	0.01mm
Maximum volume	25000000mm

3.4 Oil recovery

The saturation and desaturation of the reservoir core samples was carried out to determine oil recovery with varied drive mechanisms. The drive mechanisms were waterflooding, polymer flooding and polymer flooding with ultrasound.

3.4.1 Materials

The materials for the core flooding were the core samples detailed earlier in Table 3.4, mineral oil, polymer solutions prepared, low salinity brine 200ppm and distilled water. The use of synthetic oil was due to safety concerns and the need to ensure material balance is achieved in the inflow and outflow of the acoustic core assembly. Crude oil contains volatile constituents which would need to be accounted for, and therefore, complicating the material balance. The core flooding effluent system is not designed for both liquid and gas simultaneous separation and analysis.

Table 3:7: Oil specification

Parameter	Magnitude (with units)
Specific gravity @25^{o}C	0.8376
Specific gravity @15^{o}C	0.8418
Kinematic viscosity	9.7cp

3.4.2 Apparatus

The core flooding, equipment fitted with custom made acoustic core holder assembly.

3.4.2.1 Coreflooding equipment

The UFS-200 core flooding equipment shown in Figure 3.20 was utilised for saturation of the core samples and pore pressure generation at reservoir conditions. It was manufactured by Core Laboratory, USA with six major sections: dual piston syringe pump, accumulators, differential pressure system, overburden system, backpressure controller, ambient effluent collection and graphic user interface coupled with a computer for data collection and acquisition.

1 Graphic user interface
2 Pressure transducers
3 Control panel
4 D series Syringe pump
5 Overburden hydraulic fluid
6 Accumulators
7 Injection fluid chamber
8 Core holder assembly

Figure 3.20: UFS-200 coreflooding equipment

A view of the fittings of the acoustic core holder assembly with the distribution plug is shown in Figure 3.21. The threaded frame provides adequate pressure containment during coreflooding. A detailed interior view of the receiving plug is shown in Figure 3.22

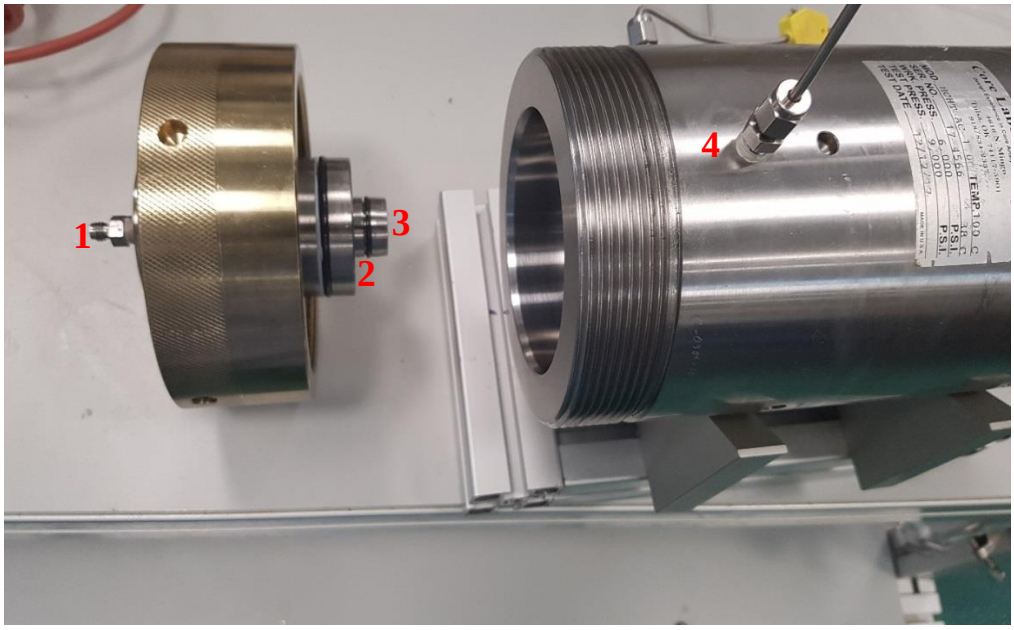

1 Fluid inflow connector
2 Transmitting transducer
3 Distribution plug
4 Overburden flow line

Figure 3.21: Acoustic core holder distribution plug and acoustic transmitter

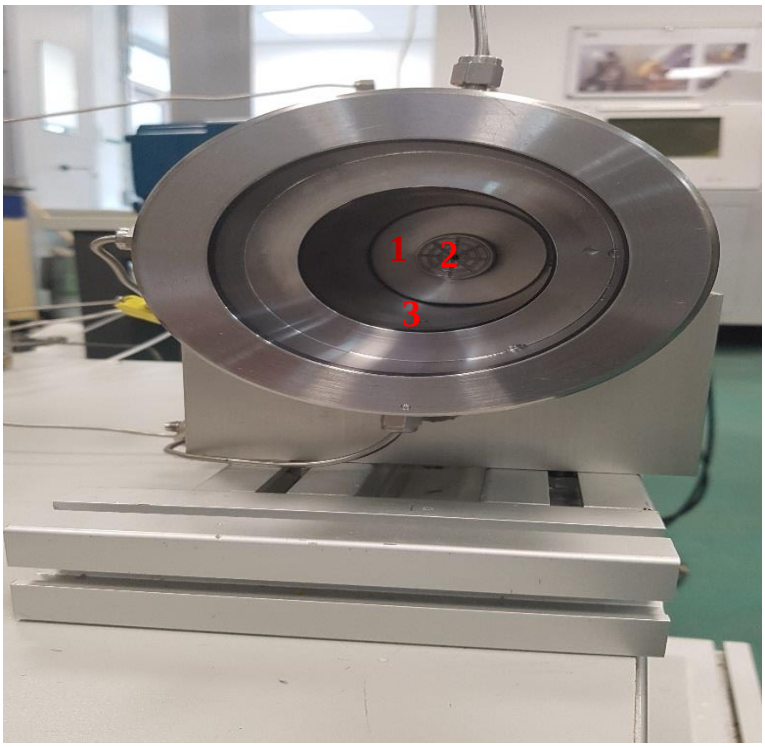

1 Interior face of receiving transducer
2 Distribution plug (receiver)
3 Inner core for overburden oil

Figure 3.22: Interior view of acoustic core holder showing the receiving distribution plug

Figure 3.23 and Figure 3.24 show the acoustic transducer receiver end of the core holder and the core sample sleeve fitted with a core sample. The core sample sleeve fits into the acoustic core holder enabling core flooding operations through injection of fluids.

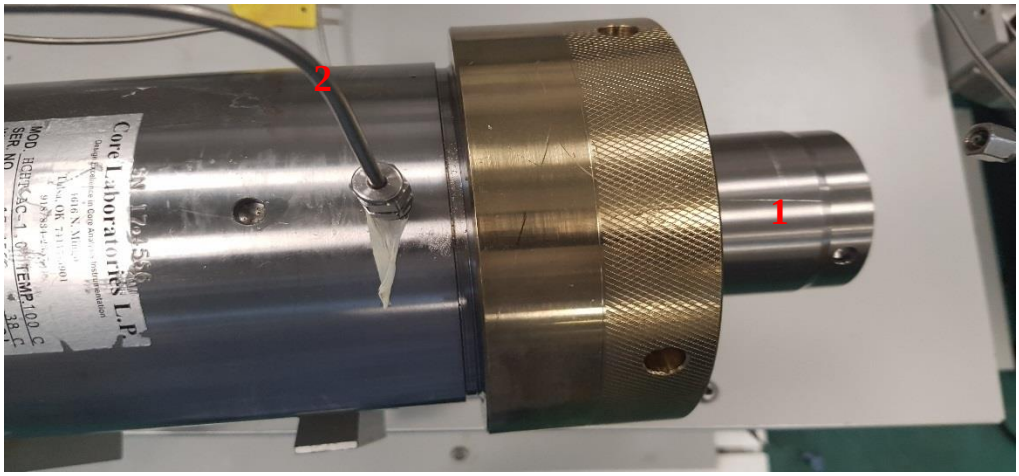

1 Receiver acoustic transducer **2** Overburden connection

Figure 3.23: Acoustic core holder transmitter assembly

1 Core sample sleeve **2** Core sample

Figure 3.24: 1"x 2" Core sample sleeve (top view)

The core sample in Figure 3.24 was fitted to provide the distribution plug adequate contact with the core sample circular face. An allowance of half - inch was made on both sides of the core sleeve for fitting of the core sample.

In Figure 3.25 the acoustic core holder is vertically stationed to determine the impact of vertical displacement of reservoir fluid and possible impact of gravitational pull.

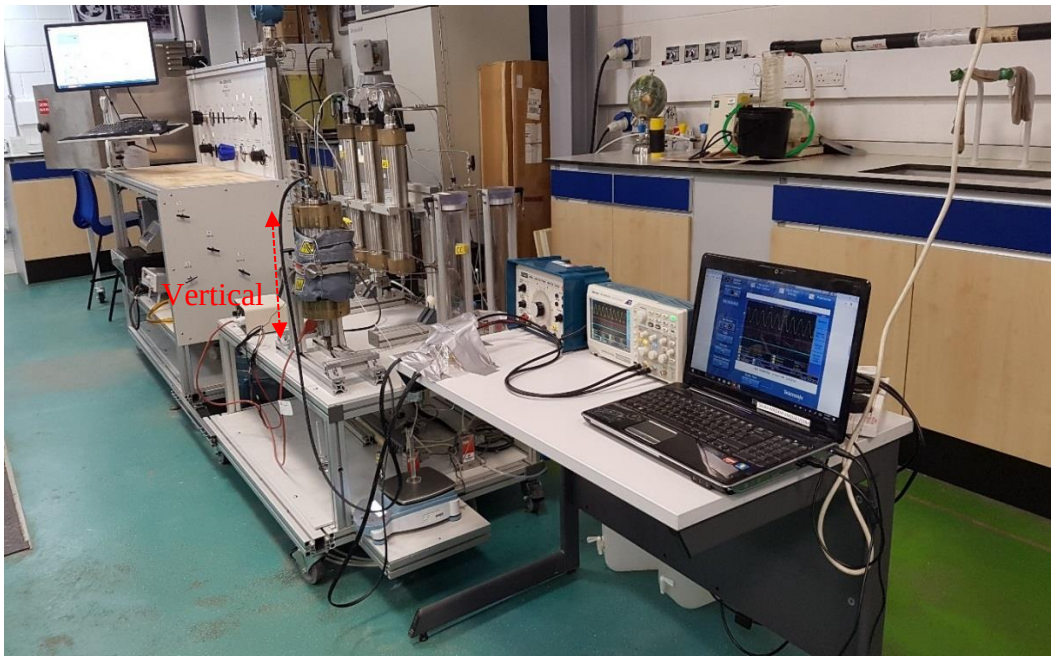

Figure 3.25: Vertical position of acoustic core holder in experimental rig

The horizontal acoustic core holder position arrangement is shown in Figure 3.26. It enabled the determination of fluid horizontal displacement during core flooding operations.

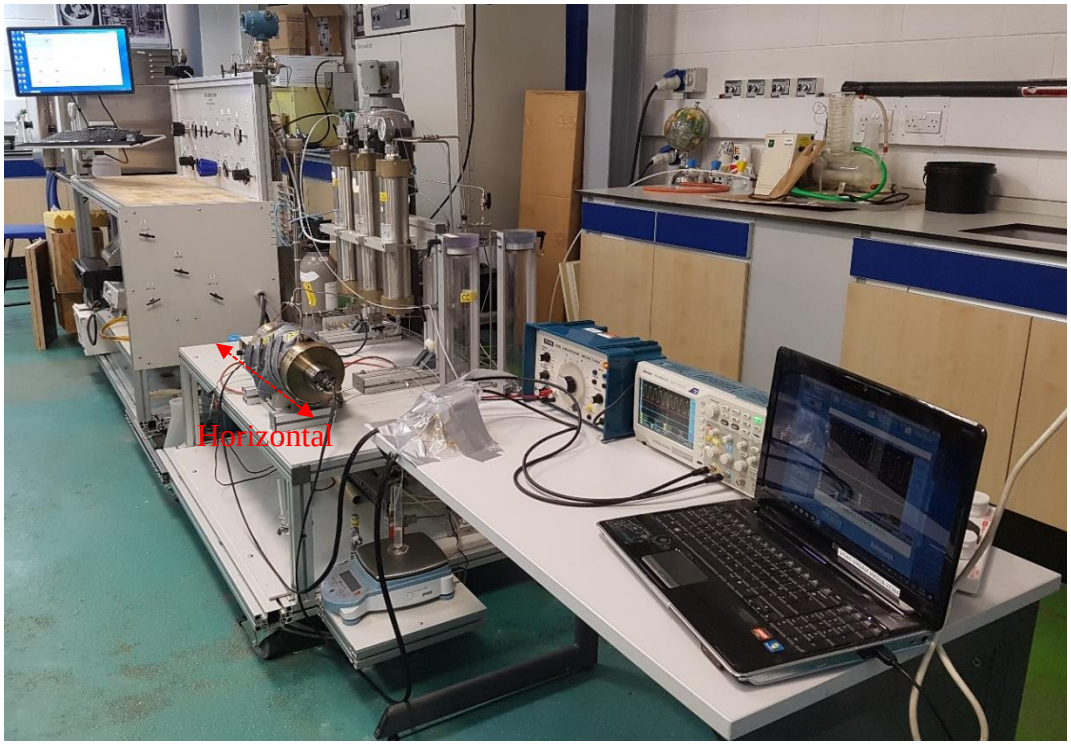

Figure 3.26: Horizontal position of acoustic core holder in experimental rig

Figure 3.27 shows the control panel of the UFS core flooding equipment. The backpressure, overburden pressure and system air pressures are regulated from the control panel. In addition, the purging and discharge of stored fluids in the accumulators are carried out with regulation of the valves on the control panel. Furthermore, the pressure differential which is the difference between fluid inlet and fluid outlet pressure can be monitored.

1 System air gauge
2 Pressure transducer
3 Gas regulators
4 Purge valve
5 CC cell control
6 Air to pump

Figure 3.27: Core flooding equipment control panel

In Figure 3.28, core flooding injection pump regulators and overburden oil containment. The D series syringe control panel controls the injection rates at either constant pressure mode or constant flow mode. All the experiments conducted in this research were in constant flow mode. The overburden oil containment was graduated to enable the determination of appropriate volume of oil to be injected into the core holder. The overburden hydraulic oil injected provide adequate to the overburden pressure to the core holder assembly. The resistivity tester, a component of the core flood equipment for measuring the resistivity of core samples, was not utilised. The central processing unit (CPU) is also housed adjacent to the resistivity tester.

CPU

1 D series syringe pump control
2 Overburden hydraulic fluid
3 Injection pumps
4 CPU
5 Resistivity tester
6 Purge reservoir

Figure 3.28: Core flooding system fluid and Pressure control system

In Figure 3.29 the four injection pumps A, B, C and D are shown. The four pumps allow continuous injection operations. As Pump A discharges, Pump B would refill. Similarly, when Pump C discharges, Pump D would refill. Furthermore, Pump A and B are connected to accumulator A while Pump C and D are connected to accumulator B

1 Pump A
2 Pump B
3 Pump C
4 Pump D

Figure 3.29: Rear view of the core flooding equipment showing the injection pumps and flowlines

In Figure 3.30 the core holder flowlines are shown. These flowlines provide linkage and communication between the core flood process units and the control panel. The overburden pressure, fluid inlet pressure, fluid outlet pressure, and system back pressures are controlled and regulated via the connecting flowlines. Apart from the pressure controls, the flowline also enables the control and regulation of system air. The system air is used to purge the overburden pressure. The system air is also employed for filling and discharging the fluid from the injection chamber (cc cells).

Figure 3.30: Core holder flowlines to pressure transducers

The flowlines in Figure 3.30 are coloured to match corresponding connectors for ease of line tracing especially during maintenance and pressure fluctuations.

The side view of the control panel is shown in Figure 3.31. The differential pressure control valves of the core flooding for fill, zero, outlet, and inlet are shown. The settings of the outlet and inlet pressure valve were set for steady state coreflooding. At steady state fluid properties are monitored and analysed with greater convenience and accuracy. In addition, steady state core flood is prevalent in laminar flow. All injections were conducted at laminar fluid flow regimes.

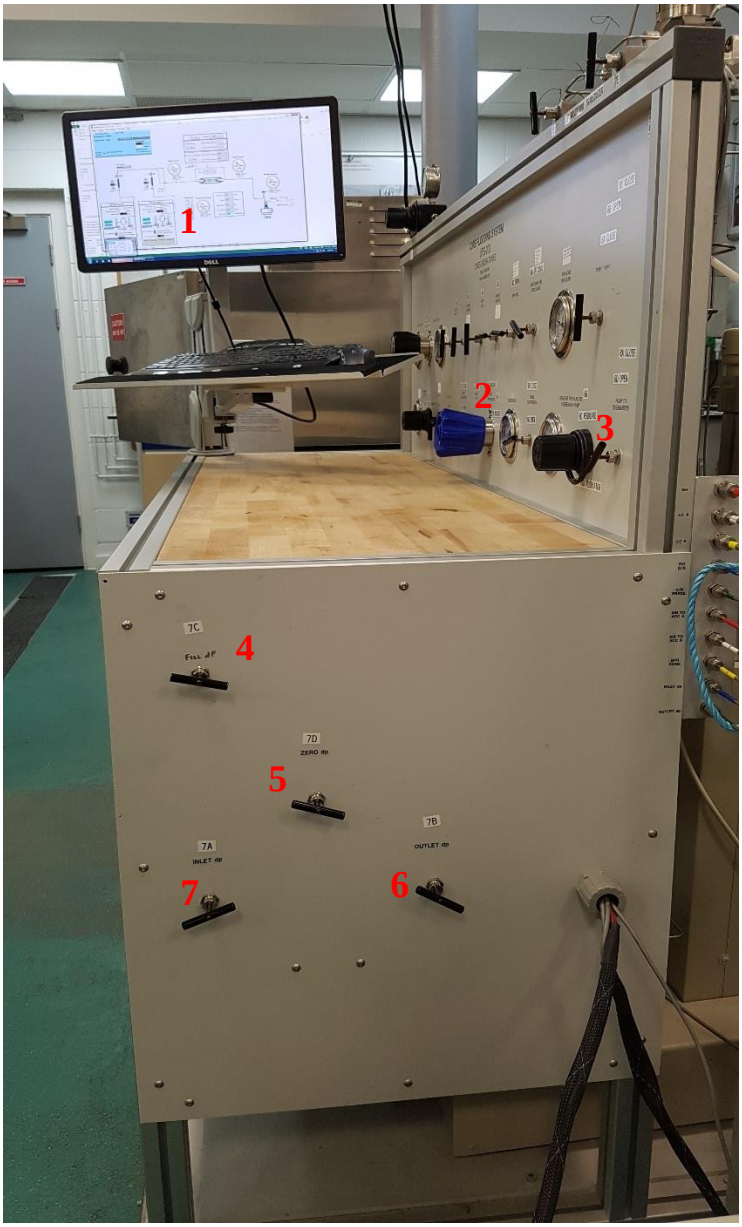

1 Graphic user interface
2 Overburden regulator
3 Air to overburden
4 Fill differential pressure
5 Zero differential pressure
6 Outlet differential pressure
7 Inlet differential pressure

Figure 3.31: Sideview of the control panel showing the differential pressure control valves

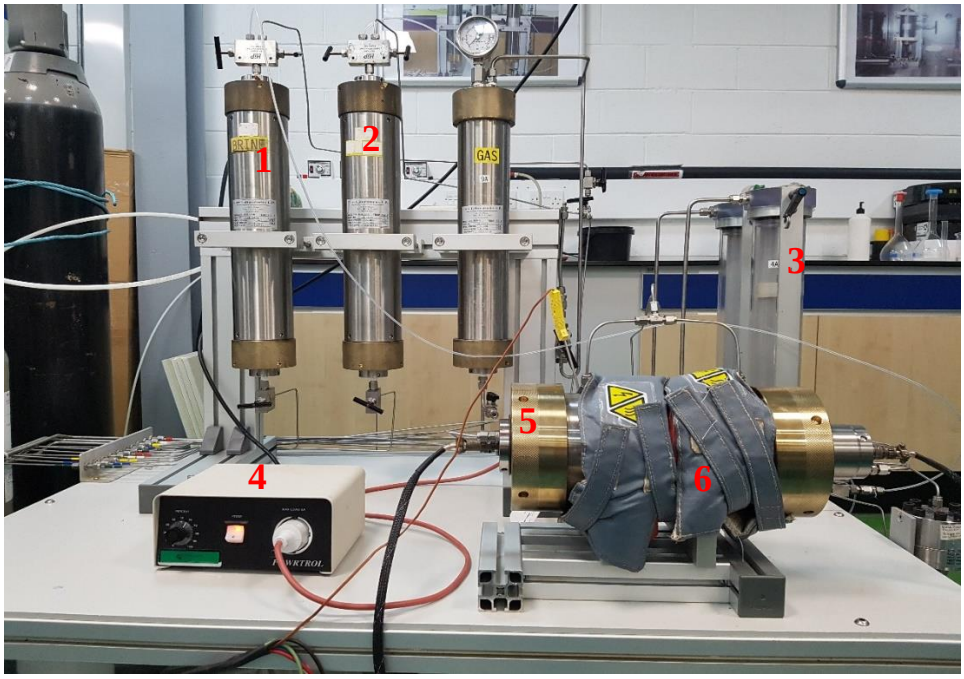

1 Accumulator A (Brine/Polymer)
2 Accumulator B (Oil)
3 Injection fluid chamber (CC cells)
4 Heater
5 Acoustic core holder
6 Jacket

Figure 3.32: Core flooding injection cells and acoustic core holder assembly

1 Gas pressure gauge
2 Injection pumps
3 Fluid injection pumps
4 Acoustic transducer
5 Discharge flowline
6 Backpressure diaphragm

Figure 3.33: Coreflooding

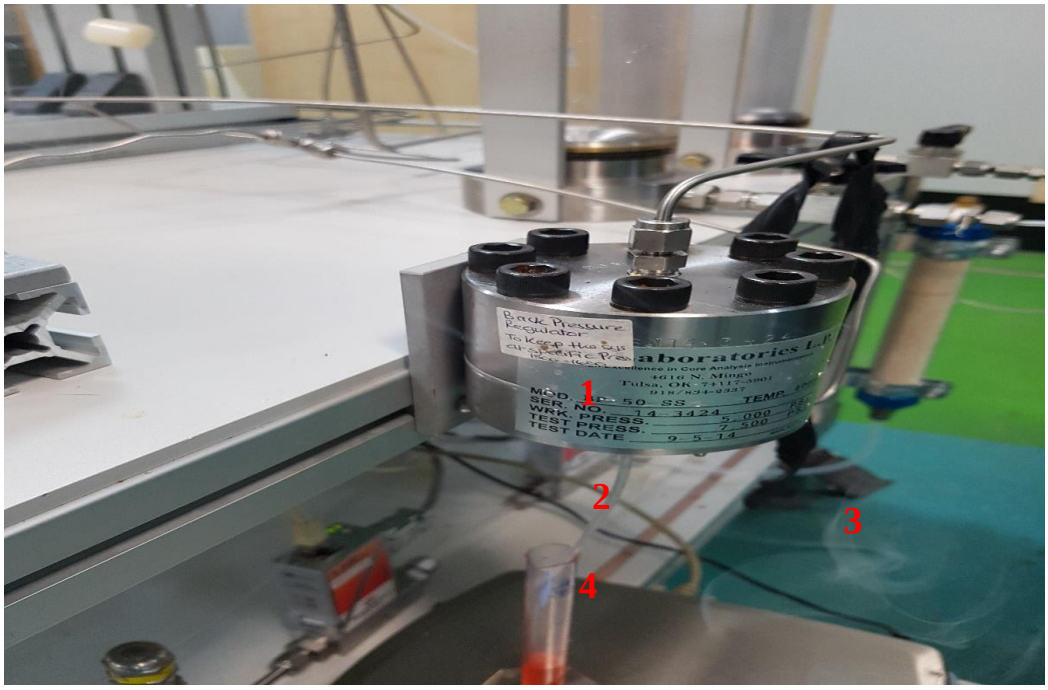

1 Back pressure regulator **3** Dust fumes
2 Delivery tube **4** Effluent tube

Figure 3.34: Fumes from collapsed rock back pressure exiting effluent

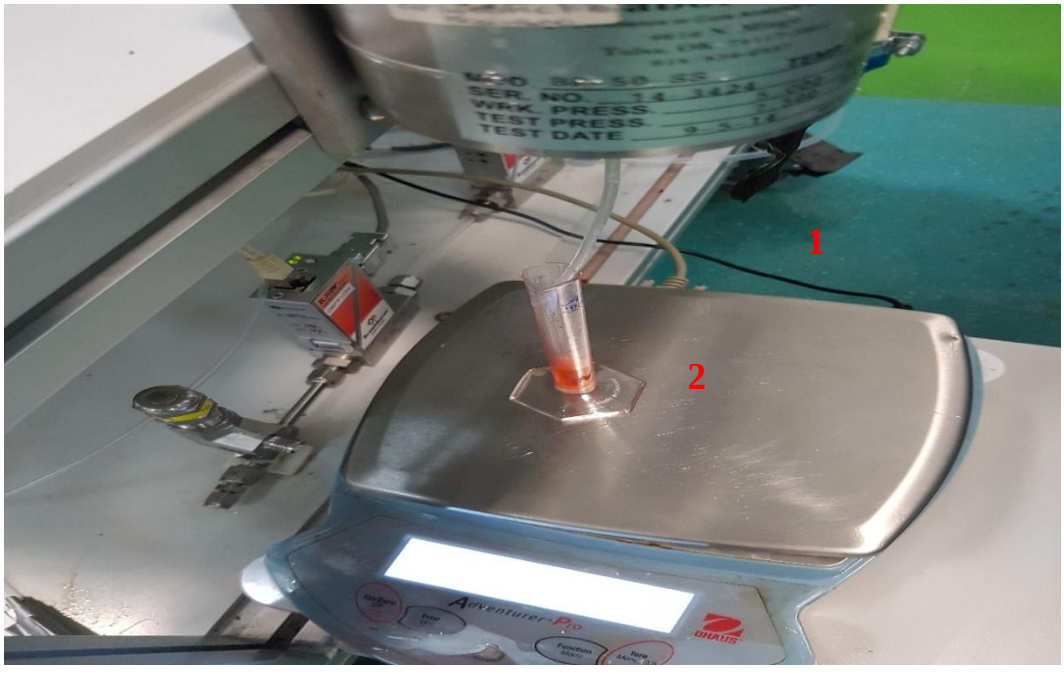

1 Absence of fumes **2** Weighing balance

Figure 3.35: Fumes stopped after 4minutes and effluent flow terminates

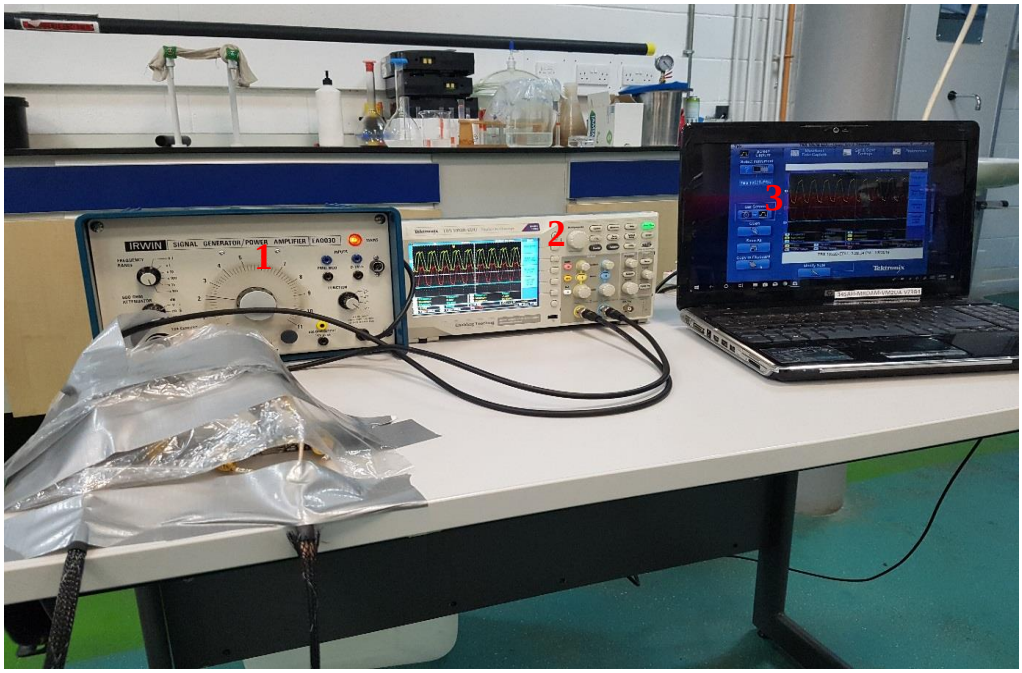

1 Signal generator/amplifier **2** Oscilloscope **3** Graphic use interface

Figure 3.36: Ultrasound generation, amplification and Graphic user interface

Table 3:8: Major components of the core flooding equipment

Design operational properties	Description	Magnitude (capacity)	Unit
Accumulator Capacity	Two equal size accumulators	500	cc
Maximum overburden	Pressure for regulation of fluid	6000	psi
Maximum Pore pressure	Fluid inlet and out pressure during injection	3750	psi

3.4.2.1.1 Dual piston syringe pump

The coreflooding equipment has a dual piston syringe pump which incorporates a manifold and a controller for adequate control of fluid flow and injection into the core samples. It provides adequate continous fluid transport at a pulse free fluid delivery rate. The fluid pressure and fluid rates are easily regulated to a fixed or constant rate as desired by the

operator. The operating pressure of the dual piston syring pump is 3750psig. The minimum rate of injection flow is 0.0001millitres per minute and the maximum is 204 millitres per minute. This is based on a maximum capacity of 1000mL (1L) which is the capacity of the accumulators.

3.4.2.1.2 Accumulators

The coreflooding equipment has two stainless steel piston accumulators each with a capacity to contain 500ml of fluid for injection. This therefore implies that a combined total of 1000ml is available for injection during any continuous flooding operation. The accumulators have pistons coated with teflon and with viton seals. A stand is also incorporated with the accumulators to provide adequate support to the accumulators to forestall and prevent vibrations.

3.4.2.1.3 Differential pressure system

For the measurement of pressure during operation, the coreflood equipment has two pressure gauge transducers that provide accurate pressure readings to 0.05% with respect to full scale measurements with interface on a computer. Also included for pressure measurements are two transducers for accurate differential pressure determination which provide 0.075% accuracy at full scale.

3.4.2.1.4 Overburden system

The overburden on the core sample assembly is effectivley controlled with an overburden setup which regulates the net confining pressure on the system. It is regulated with the aid of hydraulic pump system. The maximum operating overburden pressure for safety considerations is 5000psig. To ensure maximum safety during all coreflooding operations the overburden was never permitted to reach 4,500psig.

3.4.2.1.5 Back pressure controller

Coreflooding operations were conducted with the back pressure fully controlled. The maximum back pressure is 5000psig. The regulation of backpressure allowed the desired flow of injected fluid to be set and achieved. The back pressure is regulated through a gas loading of the dome back pressure regulator. The back pressure provides a stable reservoir pressure and permits elevation of the pressure to the desired level and controls system pressure regulation.

3.4.2.1.6 Ambient effluent collection

The effluent obtained from the coreflooding process was received and collected in a graduated effluent collection device. It enabled adequate measurement of the recovered products of all effluents from the coreflooding machine. With the aid of a stop watch the effluent recovery rate was monitored and ascertained. The effluent recovery rate was compared with the rate on the computer for aggreement. Further analysis of the effluent was carried out through a discharge vessel.

3.4.2.1.7 Mode of data acquistion (DAQ)

The automatic data acquistion system, fixed to the coreflooding equipment, was enabled through a computer system with RAM of 128MB and a hard drive with a capacity of 60GB for adequate data processing. The visual graphic user interface provided core sample inlet and outlet pressures as well as inlet and outlet fluid flow rates during coreflooding operations. The DAQ system allowed operator to set and regulate experimental processes for effective control of experiments. Figure 3.37 illustrates the graphic user interface for the core flooding equipment. In it, the entire process diagram realtime is observed.

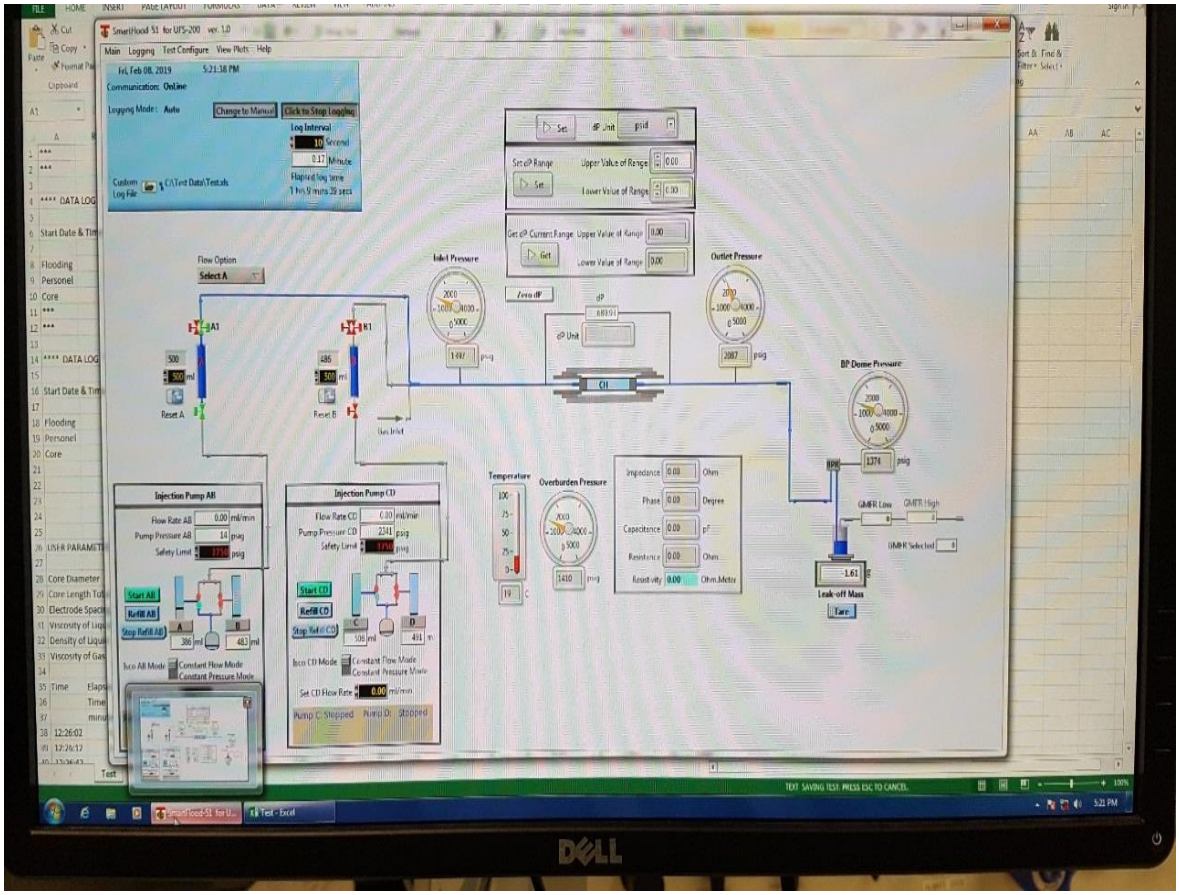

Figure 3.37: Coreflooding UFS 200 graphic user interface

3.4.2.2 Loading of accumulator cell and Lexan cc cells of UFS-200 core flooding equipment machine.

1000ml of both distilled water and prepared polymer and oil were poured into the Lexan cc cells at different injection periods as desired. The air pressure valve was set at 95psi to enable sufficient air supply to the pneumatics of the coreflooding equipment. With the aid of the cc cell pressurize valve, air was sent into the Lexan cc cells, which enabled flow of fluid into the accumulator. The core sample was encased in a plastic sheath and the sheath heated to enable all parts that could cause leakages during flooding to be sealed. The core sample was then placed in a sleeve and inserted into the core holder. The two ends of the core holder were then screwed and fastened. The core holder was then connected to the coreflooding equipment. The core holder connection assembly was made to facilitate the flow of fluid in and out of the core sample during flooding operations. Figure 3.38 illustrates the cc cells filled with fluid for discharge to the accumulators.

1 Polymer/ Brine **2** Oil

Figure 3.38: Oil and polymer/brine cc cells for discharge to accumulators

The injection pump and computer hardware were turned on, and the error signal appeared on the computer indicating that the balance was not switched. This prompted the switch of the balance to be turned on. The overburden pressure was raised to 3000 psi and the backpressure raised to 1500 psi. Flow and injection of fluid was performed with the pump set at continuous flow mode of 1.0 to 2.0mL/min at constant pressure mode of 1500 psi. Fluid injection was controlled from the graphic user interface of the computer attached to the coreflooding machine

3.4.3 Precautions

In order to ensure accuracy and precision of data obtained from the coreflooding equipment as well as ensure safety of operator and equipment precautions were taken.

3.4.3.1 Core sample handling:

The core samples were inserted slowly into the sleeve with the support of a soft plastic material during insertion into the core sleeve, as the core sample was pushed into the sleeve gradually. This was done to minimise or eliminate completely any potential damages to the core sample that could negatively affect the pore surfaces of the core sample leading to formation damage and reduction or loss of permeability.

3.4.3.2 Pressure build-up control and monitoring:

During the flooding process, pressure build-up was monitored on the graphic user interface and continuously regulated at the control panel by returning the fluctuating pressures back to the desired pressures. This was more prevalent during the heating of the core holder to temperatures above $40^{o}C$ to mimic reservoir conditions. The over burden pressure rose continuously which necessitated constant draining of the overburden valve to adjust for pressure fluctuations. The pump flow rates were gradually decreased from 2mL/min to 1mL/min when pressure build up was noticed. The first indication of pressure build-up in the system was noticed when pump pressure rose and approached the overburden pressure applied. The sudden rise in pump pressure noticed on the monitor screen was attributed to pore space filling and blockage as well as the non-conformity of flow rate applied to the permeability of the porous rock used for the experiment. Many instances abound where pressure rose to 200psi within the safety limit of the overburden pressure even though the settings applied were for overburden pressure at greater than 500psi. The setting of overburden greater than 500psi is part of the equipment manufactures safety factor to prevent rupture of sleeve and ensure the stability of the experimental process.

3.4.3.3 Bleeding of feed lines:

The feed flow lines were bled to ensure constant flow of injected fluid reached the core holder prior to full flooding operations. Checks and monitoring of flow lines ensured that flow lines were adequately suppling at the desired flow rates. In addition, the effect of dead volume was reduced to the barest minimum to enhance the accuracy of measurements taken through the bleeding processes.

Wettability of the core samples: All the core samples were subjected to water –wet reservoir conditions. The core samples were flooded with brine, 200ppm sea salt, until all the pores were fully saturated and then oil flooding commenced with the core flooding equipment. The main concept of wettability inclusion was to ensure individual reservoir cores behaved as natural occurrence and to mimic real scenario petroleum exploitation.

3.4.3.4 Effluent measurement and analysis

The effluents obtained at each stage of coreflooding were subjected to visual analysis to determine volume of fluid displaced from the core sample and any particle segregation, and fines content production. In Figure 3.39, effluent collected from the backpressure diaphragm is delivered to a graduated measuring cylinder. The density difference between the oil and water, and injected polymer lead to instant separation. Therefore, enabling measurement of all the components of the displaced fluid.

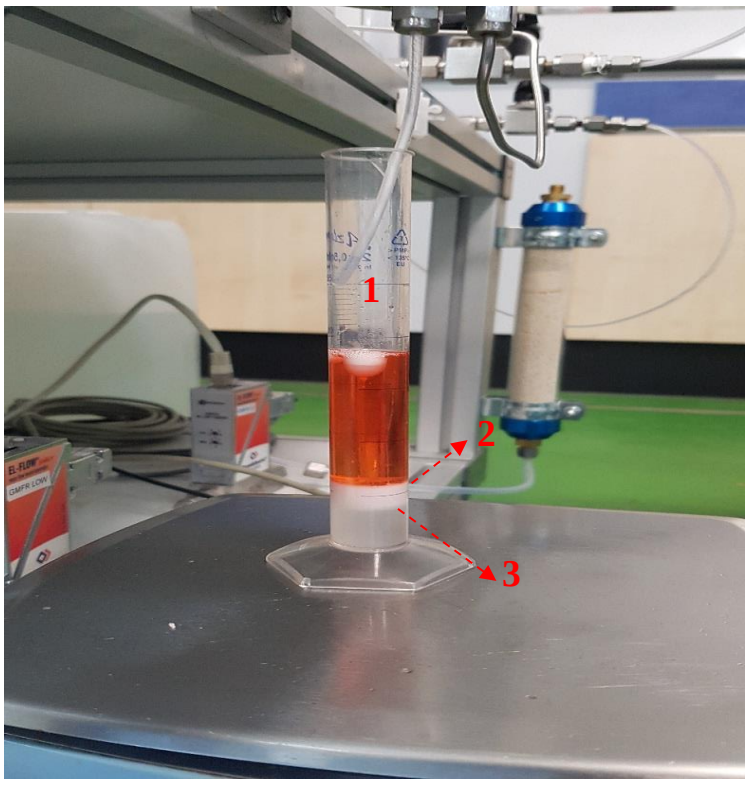

1 Graduated measuring cylinder **2** Oil-polymer contact **3** Polymer-water contact

Figure 3.39 Effluent recovery for analysis

The schematics of the core flooding equipment assembly is shown in Figure 3.40. It illustrates the major components of the coreflooding equipment with the control and flow lines.

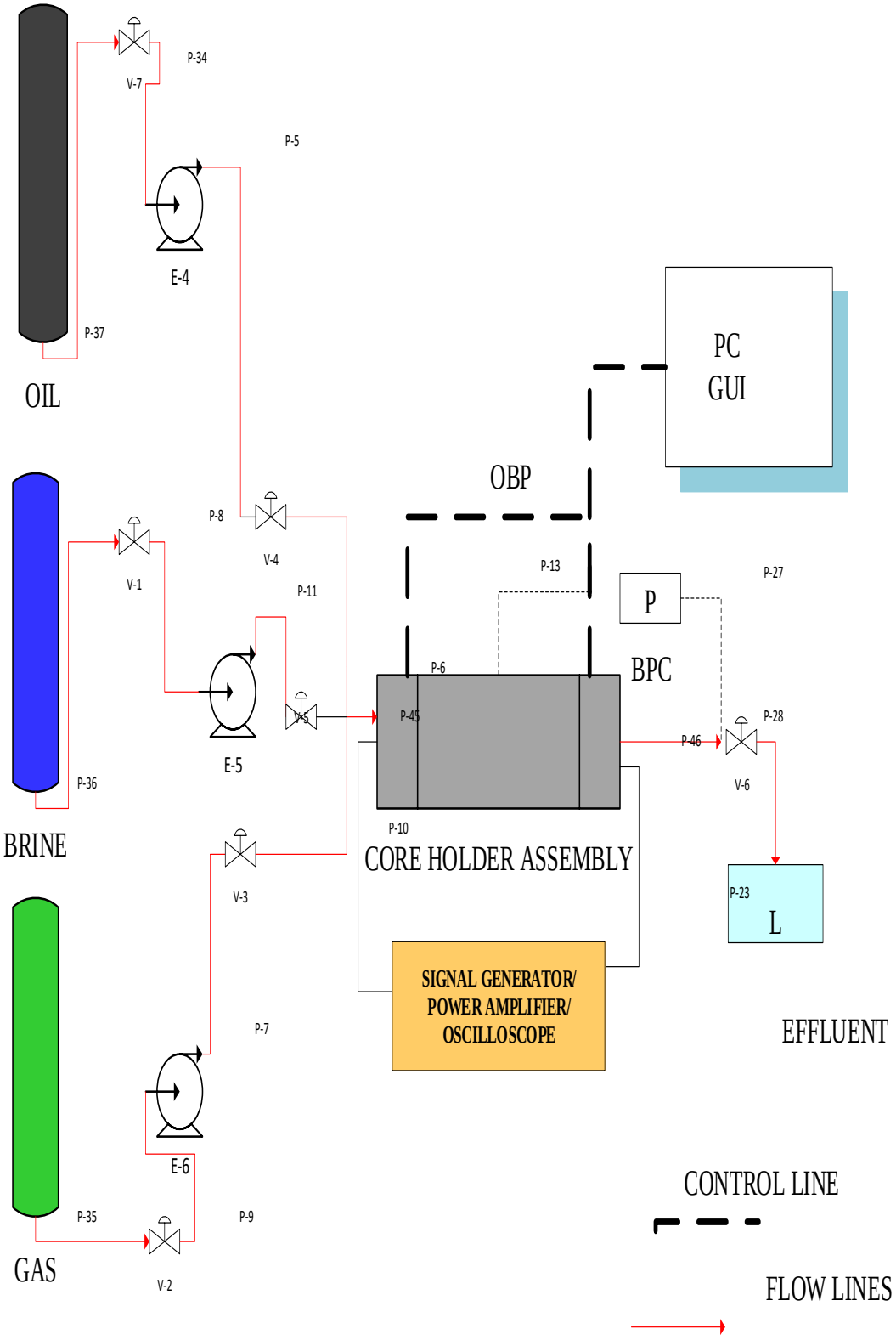

Figure 3.40: Schematics of the coreflooding assembly

3.4.4 Ultrasound application Methodology

3.4.4.1 Ultrasound equipment and mode of data collection

The three major devices for the generation and monitoring of the ultrasound and its transmission are the acoustic core holder, the signal/power amplifier and the oscilloscope. The devices are shown in Figure 3.41

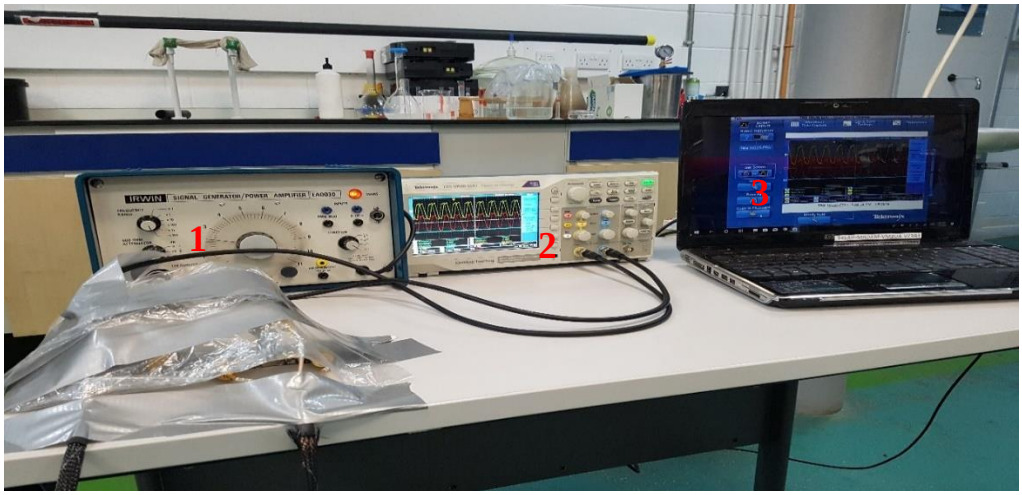

1 Signal generator/amplifier **2** Oscilloscope **3** Graphic use interface

Figure 3.41: Ultrasound generation, amplification and Graphic user interface

3.4.4.1.1 The acoustic core holder

The acoustic core holder illustrated in Figure 3.42 houses the transducer assembly. The transducers assembly in the acoustic core holder comprises of the transmitter and receiver. Though utilised for 2-inch core length, it can accommodate shorter lengths. The specification of the acoustic core holder is in Table 3:10 The design is based on ASME specifications for high-pressure vessels. It utilises hydraulic fluid for core and pressure confinement enabling pressures to be raised to 5000psi. The pressure confinement provides overburden pressure on the core sample. A sleeve jacket medium separates the hydraulic fluid from the pressurised core sample. The pore pressure can be raised to 4,500 psi, which is 500 psi less for safety considerations. The measurements of the pressure were observed on the control panel of the coreflooding equipment.

The waves generated by the ultrasonic transducers are compressional P-waves and Shear S-waves. The ultrasonic waves, sequentially propagated, travel down the axes of the core sample along its cylindrical length. The acoustic velocity core holder used for this ultrasound enhance oil recovery can also be used for determination of the dynamic moduli and Young's

moduli as well as Poison's ratio. Other parameters measurable are bulk and shear modulus subject to additional software and hardware facilities for data acquisition. The presence of two inlet and outlet pore pressure ports enables flow of fluid in and out of the acoustic assembly. A one-inch diameter distribution plug on the circular portion of the core sample performs the injection of the fluid into the core.

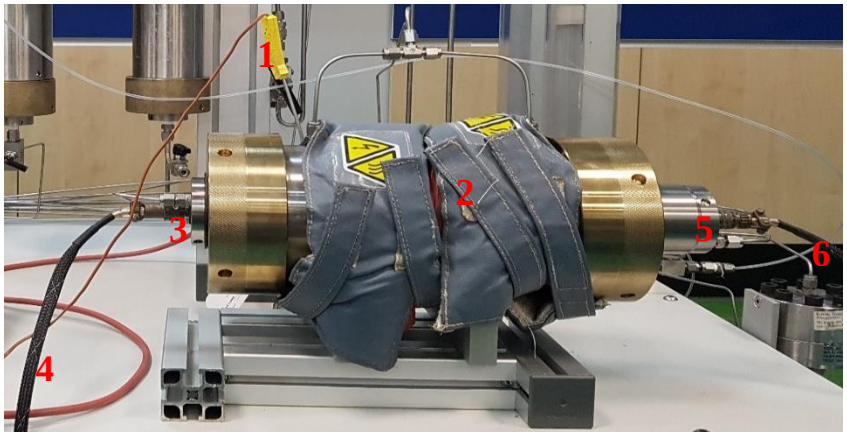

1 Thermometer
2 Jacket with heating coil
3 Transmitting transducer
4 Transmitting cable
5 Receiving transducer
6 Receiving cable

Figure 3.42 Acoustic velocity core holder

Table 3:9: Acoustic core holder specifications

Parameter	Magnitude	Units
Diameter of core/sleeve diameter	1	inch
Length of core/ sleeve length	0-2	inch
Maximum operating pressure	6000	psi
Maximum operating temperature	100^{o}	C
Material of Construction	Stainless steel sleeve	
Overburden port	Two 1/8 tubing	inch
Fluid inlet	One 1/8 tubing	inch
Fluid outlet	One 1/8 tubing	inch
Confining pressure loading	Tri-axial	
Wave transducers	Set of P &S2 wave transducers	
Frequency range	500	kilohertz

3.4.4.1.2 Signal generator/Power amplifier

The combined signal generator and power amplifier illustrated in Figure 3.43 is an IRWIN EA0030 Signal/Power Amplifier. It has a frequency range of 0.09Hz to 110KHz. The calibration has a graduation in multiples of 10. It has five control knobs: Frequency (main) range knob, Units (fraction) frequency range knob, Attenuator (600ohm) knob, Output level knob and a Function (waveform selection) knob. The IRWIN EA0030 Signal/Power amplifier provides sufficient frequency band width required for the experimental investigation - 20 to 100KHz.

1 Power output control
2 Power output port
3 Frequency regulator
4 Frequency unitary control
5 Signal waveform selector
6 Impedance output port

Figure 3.43: Combined IRWIN signal generator and power amplifier EA0030

The frequency range knob and the unit frequency knob provide avenue for regulation of the setting of the desired frequency value output. Though the main frequency knob provides the frequency in multiples of ten, the unit (fraction) frequency knob provides the frequency as fraction or tenth unit of the main.

The Attenuator knob has a maximum of 600-ohm impedance value. It is graduated on the main. The Unit or fraction knob provides the lower value(s) needed. This is similar to the setting of the frequency. However, the attenuator is not utilised in this study.

The function knob on the left-hand side of the Irwin Signal generator/power amplifier EA0030 has four waveforms. The desired waveform can be selected by adjusting the knob to the symbol on the display. However, waveform signals can be generated internally or

externally for the purpose of amplification. If an externally generated waveform is employed, connection via the banana socket adjacent to the mains switch is utilised. On the display, it is marked as INPUT.

3.4.4.1.3 Oscilloscope

The oscilloscope in Figure 3.44 is a Tektronix TBS 1052B-EDU Digital oscilloscope employed in the observation and measurement of the waveform signal and voltage properties. The properties are presented as a two-dimensional graphical plot of the signal versus time. From the oscilloscope, variation of the voltage at any instance either continuous or non-continuous can be determined. With adjustments, a continuous fast signal is captured, graphically as stationary image on the display for as long as desired to enable measurement being taken. The voltage variation also connotes acoustic or vibration changes.

The major sections of the oscilloscope are the display section, the vertical section, the horizontal section, the trigger section and menu section.

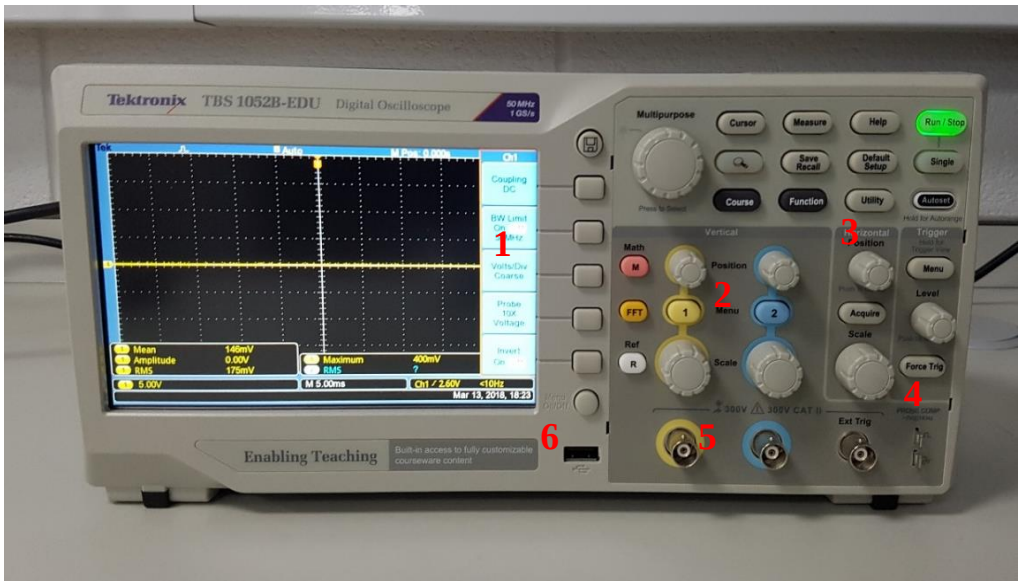

1 Display section
2 Vertical section control
3 Horizontal section control
4 Trigger controls
5 Channel coaxial port
6 USB port

Figure 3.44: Digital oscilloscope

From the display, numerous properties of the waveform such as frequency, amplitude, rise time, period, time interval and overall wave behaviour were determined.

The Display section is the graphic user interface (GUI). This section provides the desired representation of the signal or waveform for observation and measurement. The grid lines

on the display are set to indicate the interval for both the vertical and horizontal axis. The display section also provides visual exposure during setting selection as key functions are sighted simultaneously.

The vertical section provides the voltage control and regulation for each of the channels independently. The horizontal section controls the time scale for the two channels of the oscilloscope.

The trigger section enables instantaneous measurement of a signal once the trigger is set. Here, a signal tracer starts measurement once a part of the waveform or signal is in the view of the tracer cursor. The menu section encompasses all the various setting such as save image etc.

The two channels of the oscilloscope permit monitoring of input and output waveforms from the acoustic core holder during coreflooding or aging of the core sample.

3.4.5 Generation of signal (waveform)

The waveform signals were generated and amplified with the aid of an IRWIN EA0030 Signal/power amplifier. The sinusoidal waveform was selected from the function control knob, which had the three waveforms: sinusoidal, square and saw respectively. The selection of the sinusoidal waveform was based on the energy transfer efficiency of sinusoidal waves being the highest when the input energy is fixed (Song et al., 2019) and therefore greater potential to displace fluid and transverse across the formation with least attenuation and higher mechanical energy.

3.4.6 Signal amplification

The wave signals generated were amplified to maximum with an IRWIN EA0030 signal/power amplifier with desired adjustments of the Output level facilitated by the control knob. Similarly, the regulation and alteration of the frequency applied to the desired values by controlling frequency range knob displayed as multiple of ten. The amplification of the signal increased the wave amplitude of the signal, providing more pressure and reducing attenuation. The maximum current and Voltage obtainable for peak-to-peak is18A and 20V, respectively. Therefore, the total power available for transducer excitation and wave amplification, based on the designed and manufacture capacity of the signal generator/power amplifier 360 watts. Scientifically, power is the product of current and voltage. Therefore, this implies that power supplied peak to peak is 18A multiplied by 20V which is 360Watts.

3.4.7 Signal/ Waveform monitoring and graphic user interface

Each signal or waveform selected was channelled through the oscilloscope to determine its properties and measurement taken prior to transmission to the acoustic core holder. After transmission through the acoustic core holder and subsequent excitation of the transducer, the signal was measured at the exit or receiver transducer. The Channel 1 on the oscilloscope was set to measure transmitted waveform to transducer and Channel 2 was set to measure receiver transducer waveform. The net changes of the waveform are measured on the oscilloscope. The graphical representation of the waveform variation is shown on the display and both the reduction of amplitude and reduction in voltage as well as time variation were recorded.

3.4.8 Data acquisition of waveform properties

The waveforms and their characteristic properties were acquired from visual display of the oscilloscope. The oscilloscope was connected to a HP Laptop with software that enabled data to be saved to the laptop computer via a USB cable connected to the USB port on the oscilloscope. The data was saved as an excel spreadsheet and reconstructed to provide graphical representation that were replica of the visual display on the oscilloscope.

3.4.8.1 Data analysis

The data obtained from the two waves; transmitted and received were analysed with the aid of the graphical representations of the plots for amplitude versus time. Comparison of the graphs of the various waveforms for both transmitted and received (exit) was carried out. This was with a view to establish the level of attenuation of the waveform. Vibrational potential using Fast Fourier transform (FFT) were observed.

3.5 Evaluation of EOR strategy

In each enhanced oil recovery (EOR) experimental run, measured recovered oil was compared for the sandstone and carbonate reservoir rocks. The oil displacements were carried out in an ordered sequence: waterflooding oil recovery, polymer flooding oil recovery and polymer flooding with ultrasound oil recovery. The basis of displacement was core sample pore volume. Polymer was injected into the saturated core samples with the aid of a core flooding equipment. The recovery from saturated core samples measured and evaluated to determine the production over a period of injection for optimisation of the

overall production. Horizontal and vertical core assembly orientations were adopted to observe whether gravity had impact on the recovery.

3.5.1 Production and oil recovery

During the period of ultrasound stimulation and the continuous flooding of the core sample with the core flood equipment, the effluent and output were monitored. The recovery was monitored for the applied frequency based on pore volume.

Precautions: During the assemblage and running of the ultrasound numerous precautions were taken:

i) The connections between the core holder and the signal generator were properly fastened and secured to ensure adequate passage of ultrasound waves into the core holder and subsequent contact with the core sample.

ii) The power generation from the amplifier was maintained high to ensure enough power to excite the ultrasound transducers in the core samples.

iii) The oscilloscope wave data were acquired when flow through the core sample indicated steady state behaviour. The wave forms obtained at steady state gave mean properties and characteristics of the wave at any instant across the core sample.

3.6 Chapter summary

In chapter three, the selection of appropriate reservoir conditions for experimentation ensured laboratory experiments were within actual oil field conditions. The petrophysical analysis of injection fluids and the procedure for preparation of polymer solution was explained. The methodology for geophysical analysis of the reservoir rocks used for coreflooding including computed tomography for pore sizes and pore distribution was detailed. Ultrasound signal generation and amplification and mode of data acquisition were extensively discussed.

CHAPTER FOUR
RESULTS AND DISCUSSIONS

4.1 Introduction

In this chapter, results obtained from experiments conducted are presented and extensively discussed. The first case was the consideration of the petrophysical properties such as interfacial tension (IFT) of reservoir fluids, viscosity, viscoelasticity and hysteresis analysis of hydrolysed polyacrylamide polymer solutions. The geophysical analysis involved core pore analysis with computed tomography (CT) scan. The third section is the oil recovery stage. Here, the results of oil recovery with different drive mechanisms for enhanced oil recovery are presented. The results, in most cases, are presented in tabular, graphical or imagery forms.

4.2 Petrophysical results

4.2.1 Interfacial tension measurements

Interfacial tension, as mentioned earlier, is a petrophysical property that shows the cohesive energy existing between two fluids at the interface which arises as a result of the imbalance of forces between the molecules of the two fluids. As ultrasound has been shown to reduce interfacial tension, it was, therefore, significant to determine the interfacial tension existing in the conditions to which the experiment is conducted. The preliminary results obtained from the experiment in the determination of the interfacial tension properties of oil and brine with changes in reservoir pressure at reservoir condition (77^{o}C) is illustrated in Figure 4.1. This shows a curve that depicts rise and fall behaviour with similarity to an unstable system. The pressure range was 773psi with the highest pressures at commencement of 2643psi and the lowest at 1870psi. Similarly, the IFT ranged from 15.54 dyne/cm to 14.89 dyne/cm. This profile depicts a reservoir which is declining in production. The fluctuations can be attributed to the forces of Van der Waals that exist between the two surface molecular layers of oil and brine as the cohesive forces attempt to maintain stability and reach equilibrium. This is noticeable due to the range utilised and intervals set for taking measurements which are very close to each other allowing the behaviour to be illustrated.

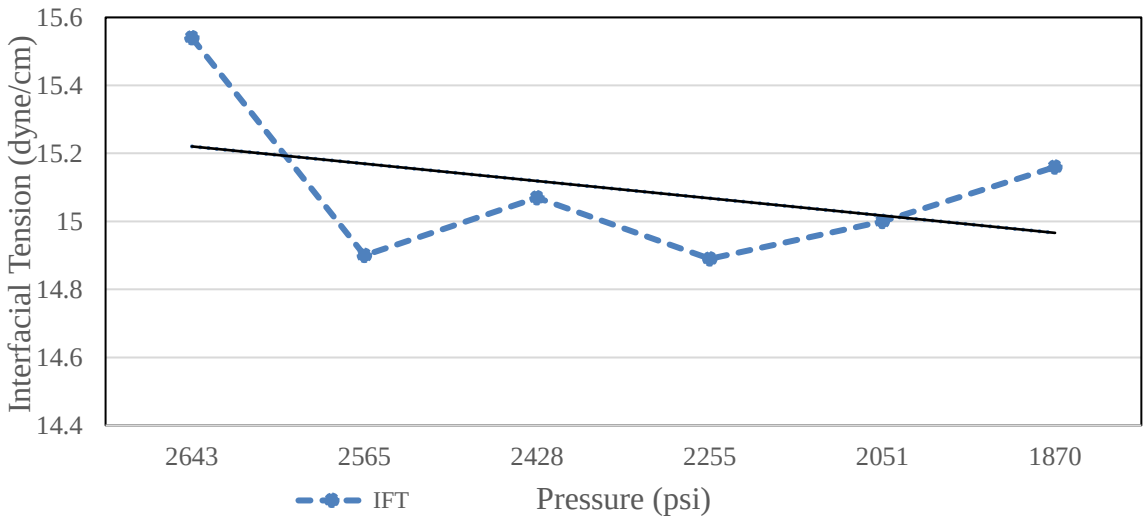

Figure 4.1: Interfacial tension measurement for maturing reservoir

In Figure 4.2 the measurements of the interfacial tension were obtained with increasing pressure. The purpose was to observe the effects of increasing reservoir pressures on interfacial tension. The pressure range had an initial reservoir pressure set at 780 psi and the final pressure set at 4,400psi. From the graph, the interfacial tension increased steadily from 780 psi to 1435 psi. Once this pressure was attained, the system became stable, as there was no change in IFT behaviour depicting equilibrium status of the surface forces between the fluids. However, when the pressure attained 3300psi there was a step increase in IFT. This could be attributed to the fall in the stable state attained by the surface molecules. Hence, the Van der Waals forces that had attained equilibrium were subsequently disrupted as pressure increased resulting in a sharp increase in IFT. This clearly shows that certain thresholds of pressure are required to increase or alter the stability of an IFT system in a reservoir. Upon further increase in pressure to 3700 psi, it was observed that the interfacial tension dropped. A visual inspection of the oil drop from the camera on the IFT measuring equipment showed the bubble had shrunk in size. The bubble images are shown in Appendix B. The understanding from this behaviour was that as pressure was increased to a certain threshold, the IFT decreased. The advantages of knowing how the IFT behaves at reservoir pressures as well as within coreflooding pressures in enhanced oil recovery is that it facilitates reservoir pressure maintenance and therefore aids the maximisation of the oil recovery through a more efficient recovery strategy and methodology. In the context of this research, since ultrasound affects reservoir pressure and interfacial tension, the investigation of the interaction of IFT and reservoir pressure would provide deeper understanding of the role of ultrasound on reservoir fluid behaviour.

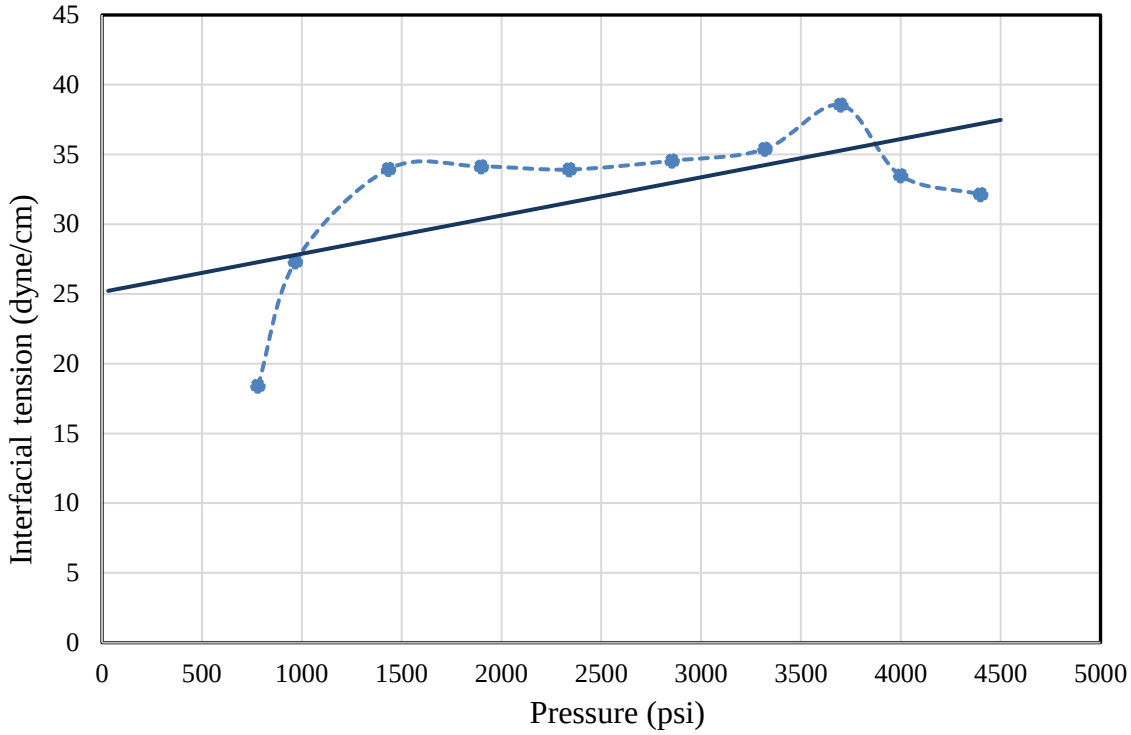

Figure 4.2: Interfacial tension profile for pressure increasing well

4.2.2 Viscosity, viscoelasticity and hysteresis of polymer solution

The viscosity and viscoelasticity of polymer solution was determined with OFITE Model l100 pressurised viscometer. It enabled characterisation of the polymer solutions at different concentrations and ensured optimum selection of appropriate polymer solution concentration for injection. The viscometer was calibrated prior to utilisation. This ensured that shear stress reference and shear stress raw data were proportional. Without a constant of proportionality data obtained from the graphic user interface, the subsequent results would be flawed. With the aid of the OFITE viscometer calibration fluid from manufacturer, the calibration curve in Figure 4.3 was obtained. Evidently, values generated with the calibration fluid gave R^2c as 0.9991 which is greater than 0.9990. As a rule, expressed by the manufacturer of the viscometer, the value of R^2c must exceed 0.9990. Therefore, this implies that the calibration was accurate and the instrument fully calibrated. Figure 4.3 is the calibration curve. The plot of shear stress reference versus shear stress raw is a straight-line graph.

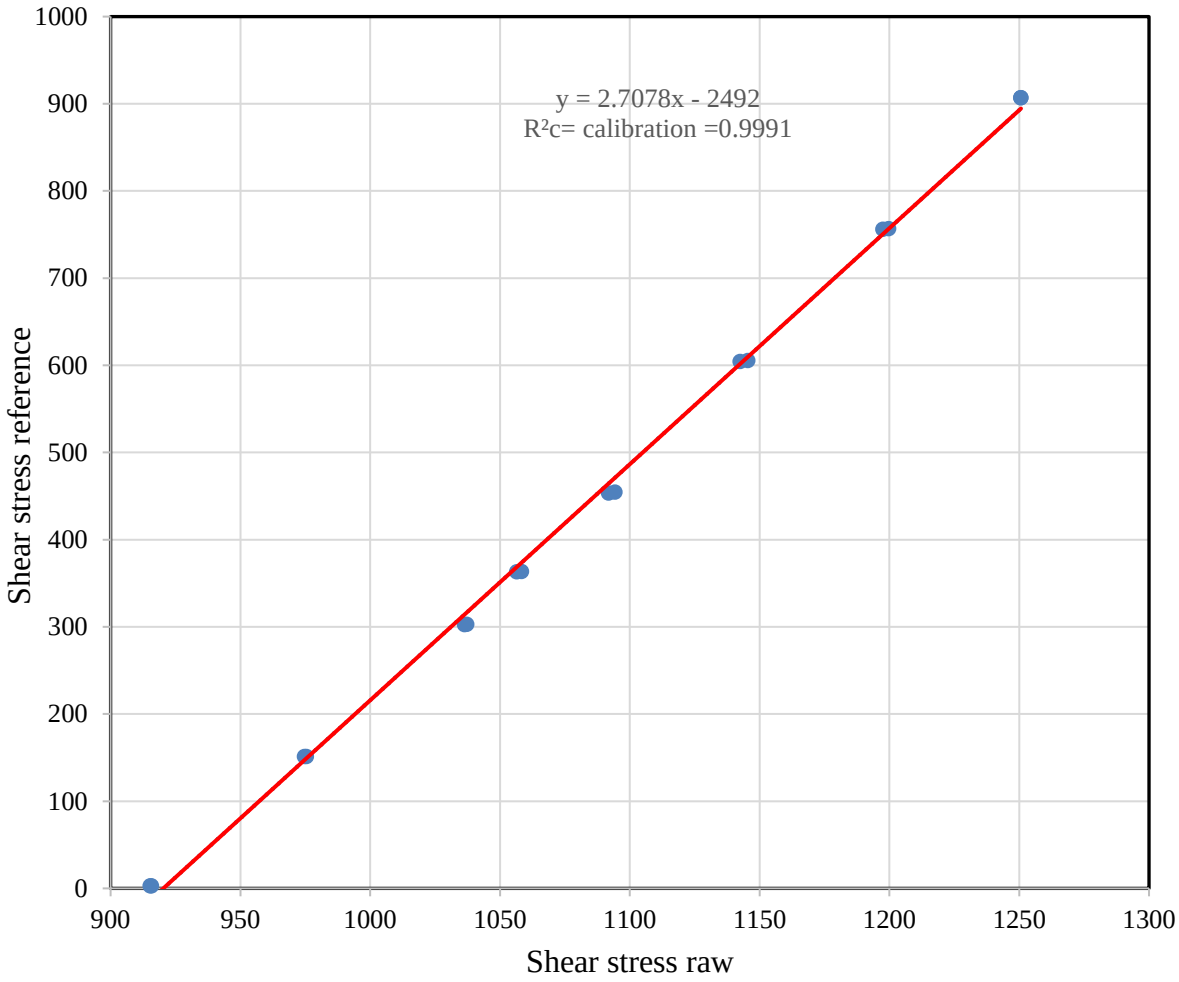

Figure 4.3: Viscometer calibration showing shear stress reference versus shear stress raw

Figure 4.4 shows the graph of consistency factor (K) versus fluid flow behaviour index (n) for a 2000ppm polymer concentration curve. The graph illustrates the highest and lowest values of K as 1.83cp and 1.71cp respectively. Similarly, the highest and lowest values of the flow behaviour indices, n, are 0.259 and 0.275 respectively. The consistency factor, a measure of the viscosity of the fluid, is an important tool in predicting the behaviour of polymer during injection and EOR operations as well as determines the ability of the displacing fluid to displace oil. The n values, commonly referred to as fluid flow index, is a dimensionless number, which characterises the deviation of the fluid from Newtonian behaviour. When n is less than 1 (one) the fluid's response to shear stress is pseudoplastic.

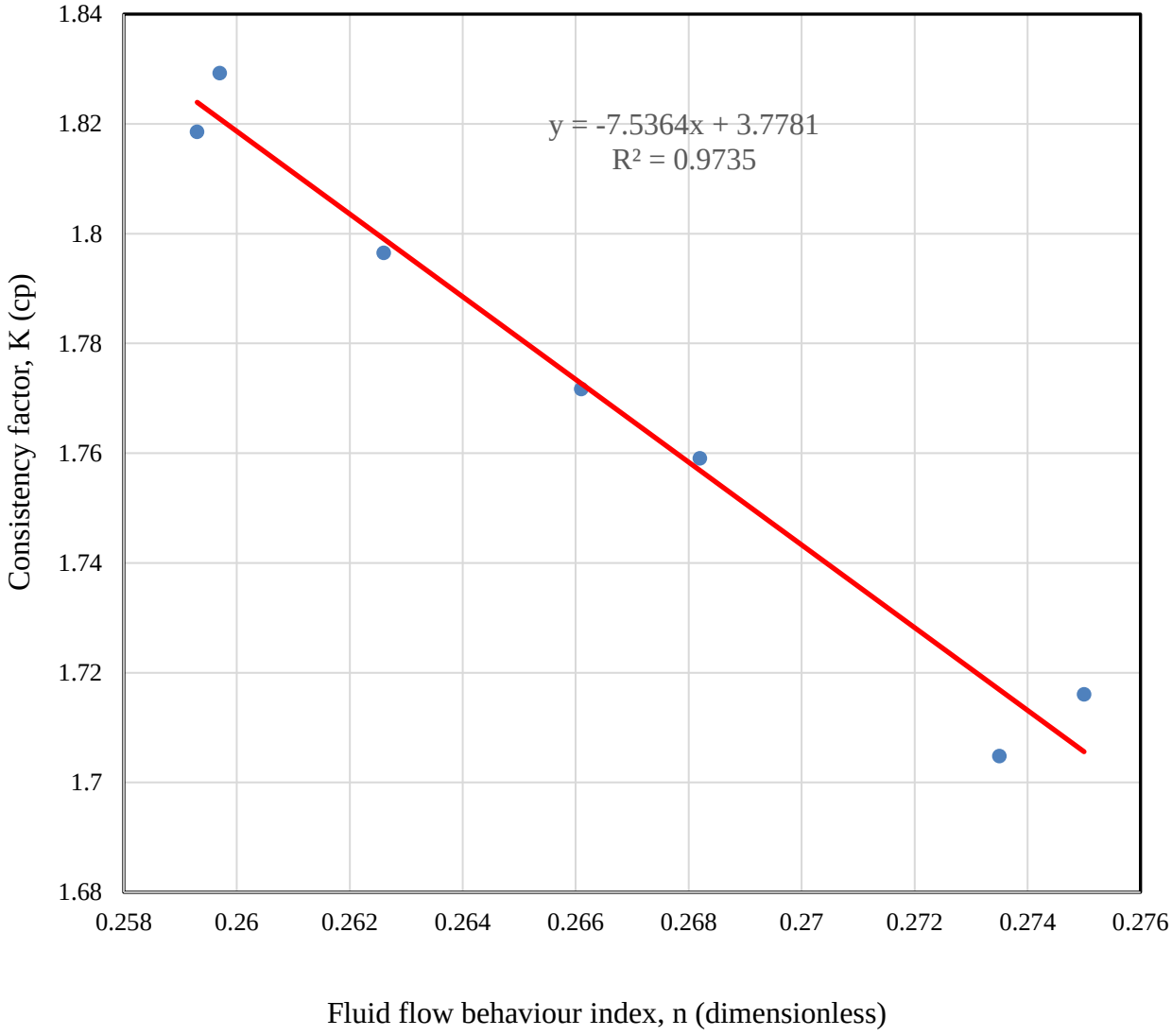

Figure 4.4: Consistency factor versus flow index behaviour at 2000ppm

The hysteresis behaviour of HPAM at 2000ppm concentration was obtained by monitoring the change in shear stress with shear rate in the forward direction and in the reverse direction. The settings selected on the graphic user interface enabled the viscometer to generate hysteresis data during visco-metering of the polymer fluid, in addition to the regular viscosity measurements. Figure 4.5 shows hysteresis behaviour for HPAM at 2000ppm. The envelope commences at 4.3 to 6.4lb/100ft^2 on the shear stress axis and 20 to 100s^{-1} on the shear rate axis. In the graphical illustration, the envelope depicts the change in energy of the polymer due to the spinning bob of the viscometer to reverse mode from forward. If there were no hysteresis, the envelope would not have existed, and a straight line would have developed.

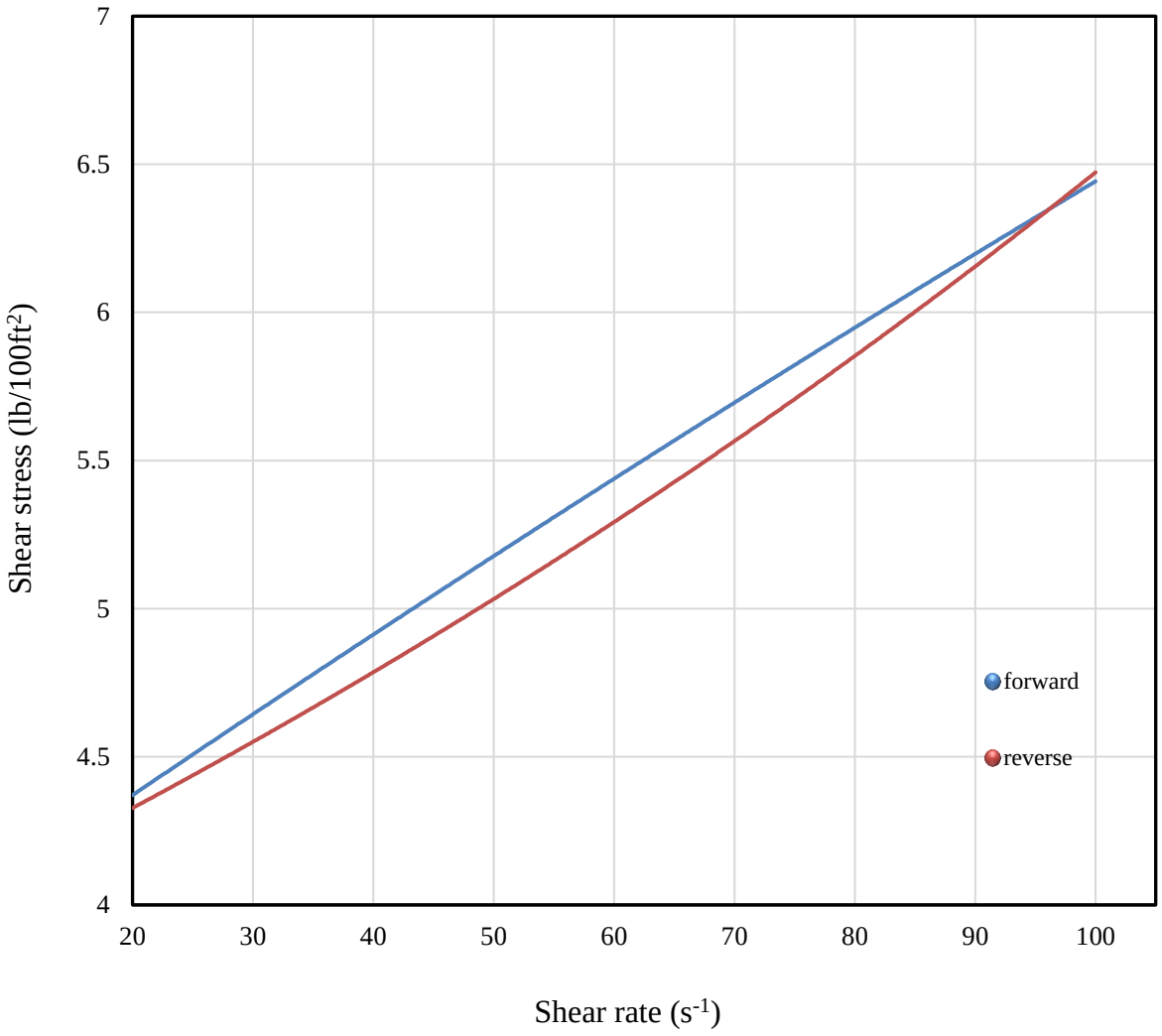

Figure 4.5: Hysteresis behaviour of HPAM at 2000ppm concentration

The characteristic flow behaviour of HPAM at concentrations of 2000ppm indicates that the viscoelasticity was greater than at lower concentrations. Figure 4.6 shows the shear stress versus shear rate characteristics of HPAM at 2000ppm concentration. The maximum value for viscosity was 85cp at low shear rate of $25s^{-1}$. When the shearing rates were increased to $100s^{-1}$ the viscosity decreased to 37cp. However, when the subsequent cycle was applied to the polymer, the viscosity decreased to 36cp. This indicates a slight and gradual decrease in the viscosity of the polymer because of shearing by the viscometer. The small decrease in elasticity of the polymer implies that during coreflooding it would exhibit high stability and viscosity within the reservoir. However, the stability of the polymer is associated to its high viscoelasticity. At 2000ppm, it was almost gel-like in nature. The measurement of the

samples size of the polymer was challenging due to viscous and continuous flow nature of the polymer exhibiting resistance to permanent deformation. The trendline viscosity was approximately 50cp. This was an indication that a fluid of 50cp or less can readily be displaced by HPAM at 2000ppm concentration.

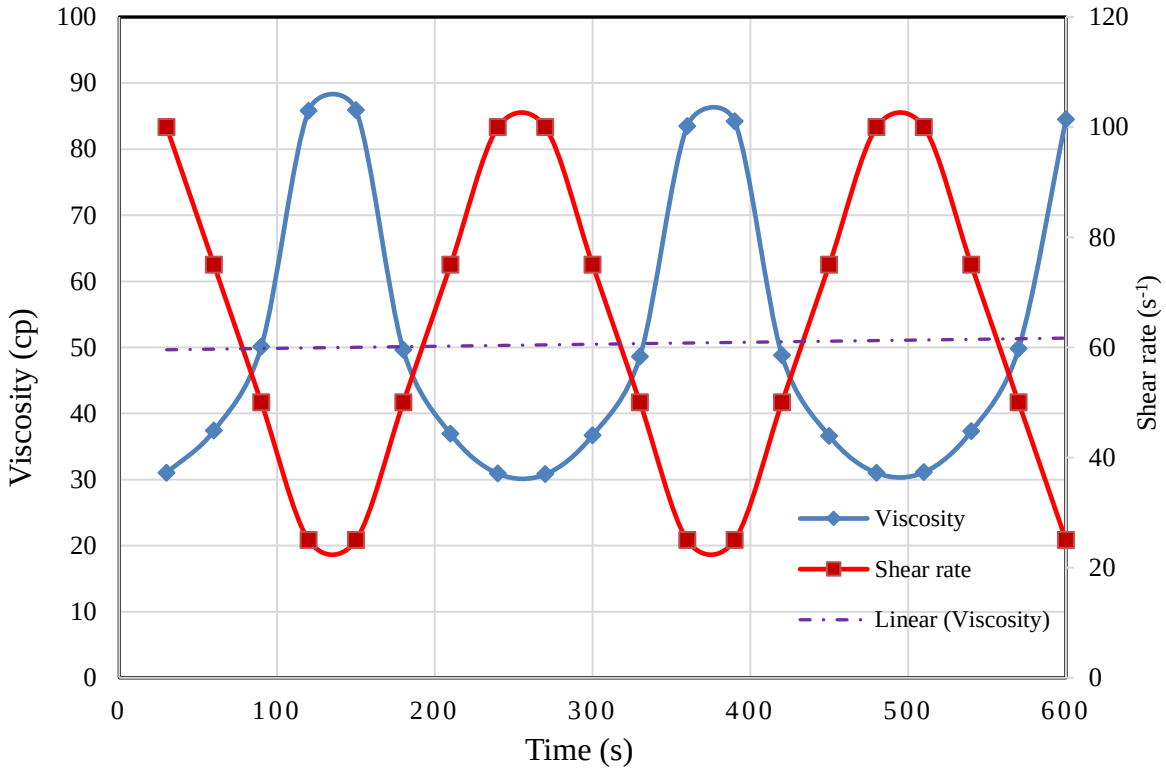

Figure 4.6: Shear stress versus shear rate characteristics of HPAM at 2000ppm concentration

The hysteresis behavioural phenomenon of HPAM @1600ppm is shown in Figure 4.7. As the polymer underwent shearing and extensional forces applied on the coil formation of the molecular chains of the polymer, the hysteresis envelope was observed. The region enclosed by the forward and the reverse curves depicts the loss of viscosity or change of viscoelastic properties of the polymer. In terms of energy loss, it can be expressed as change of energy between the extensional and contractional forces of the polymer molecular chains associated with the hysteresis. When the shear rate was at $25s^{-1}$ the shear stress was as high as $3.2lb/100ft^2$. The shear stress reduced as shear rates increased until it reached $50s^{-1}$. Ordinarily, expectations are that the shear stress would increase, however at shear rates of 50 to 60 s^{-1} the shear stress rose from 2.5 to 3.1 $lb/100ft^2$ and was tensile in nature. This was

associated with the extensional forces associated with the polymer chain. The viscoelastic properties, clearly seen in the hysteresis envelope, provided favourable consideration as a viscoelastic fluid for polymer flooding operations in enhanced oil recovery (EOR).

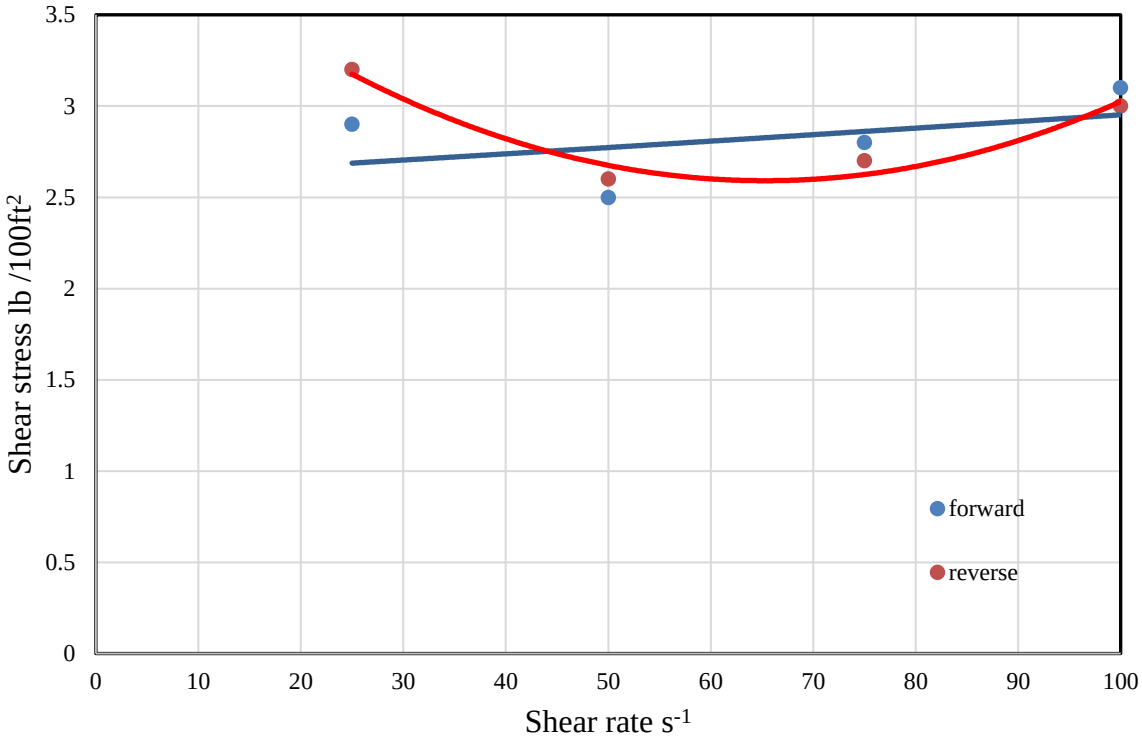

Figure 4.7: Hysteresis behaviour of HPAM at 1600ppm concentration

In Figure 4.8 the viscoelastic properties of HPAM were evident with the viscosity alternating between 64cp to 15cp as the shearing rate was gradually increased and decreased from 25 to 100s^{-1} over a period of 600 seconds. The shear rate, though maintained at a regulated interval, indicated, from close observation, the occurrence of the gradual reduction of the viscoelasticity with continuous shearing applied to the polymer solution. Although the reduction in viscoelasticity was considerably small, it did, however, indicate that when subjected to continuous shearing there was likelihood that over the span of a flooding operations in the reservoir during injection and pore transport, polymer potential to displace oil could be reduced.

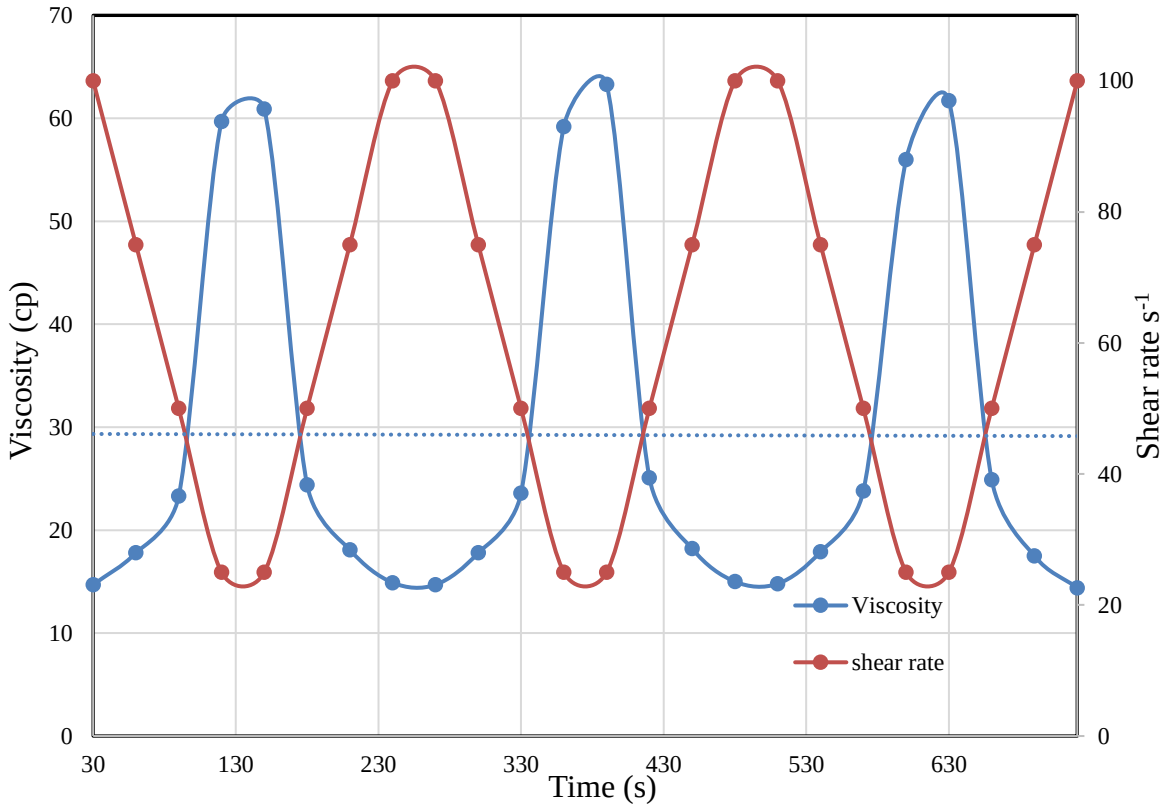

Figure 4.8: Shear rate and viscosity characteristics of HPAM at 1600ppm concentration

Figure 4.9 provides a graphical illustration of the consistency factor, K, versus fluid flow index, n, for a polymer solution with a concentration of 1200ppm. Although 2 points are far off the linear trendline, the remaining 4 points approach the trendline. The consistency factor, K, ranges from 0.47 to 0.55cp. The fluid flow index, n, ranged from 0.30 to 0.3. The entire values of n are much less than 1, hence a completely pseudoplastic fluid.

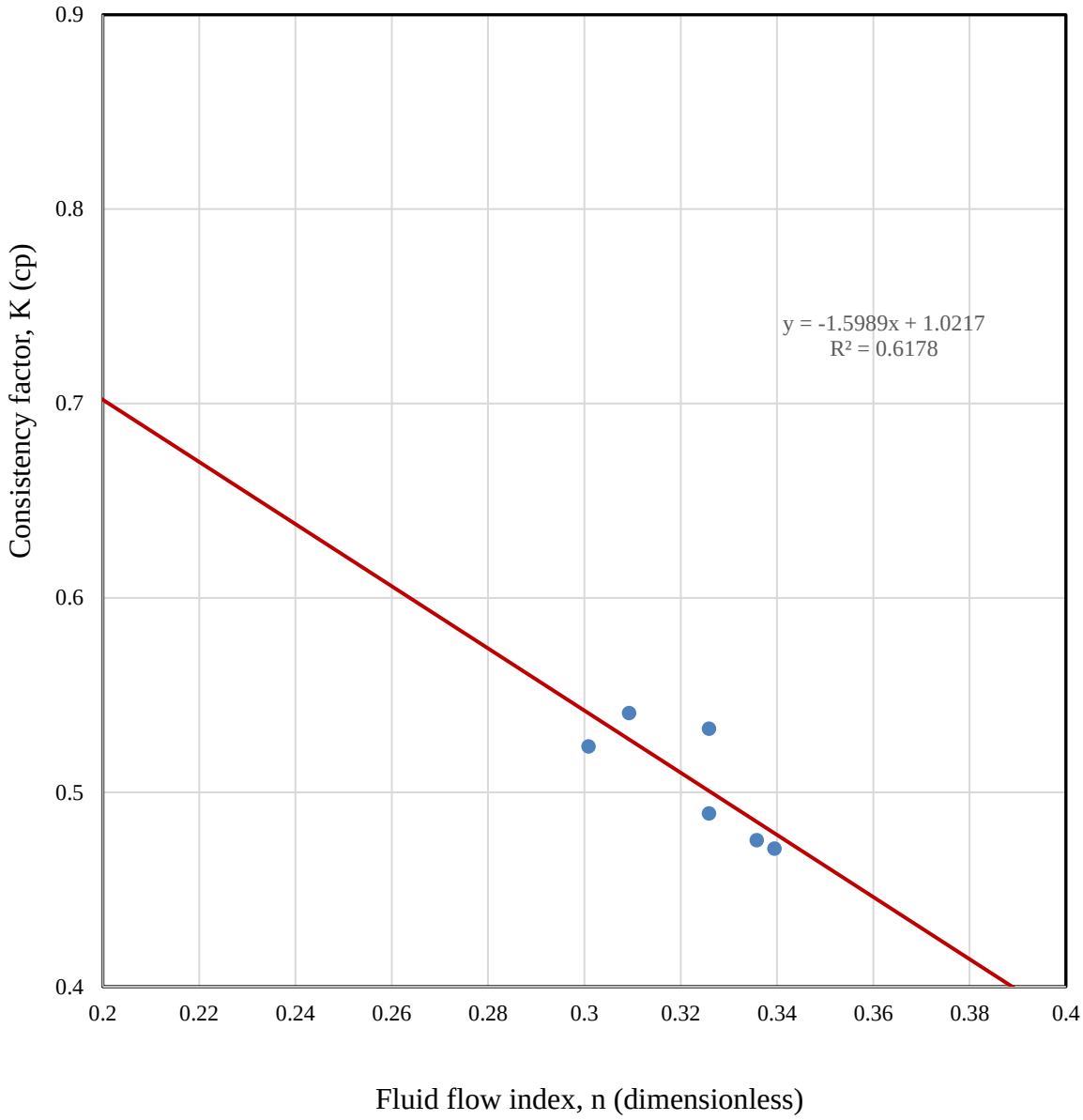

Figure 4.9: Consistency factor versus fluid flow characteristic of HPAM at1200ppm concentration

Figure 4.10 for the hysteresis behaviour of HPAM at 1200ppm concentration shows the large envelope of the forward and reverse cycle on the shear stress versus shear rate ordinates. The envelope encloses a shear stress of 1.5lb/100ft^2 to 2.7lb/100ft^2. The shear rate spans from 25 to 125s^{-1}. The smooth fitting curve and the large envelope behaviour of the curve shows a lot of energy released through hysteresis. This could have positive impact on oil displacement. It also showed that the ability of the polymer to drag residual oil and facilitate oil displacement is highly increased with the hysteresis envelope exhibited.

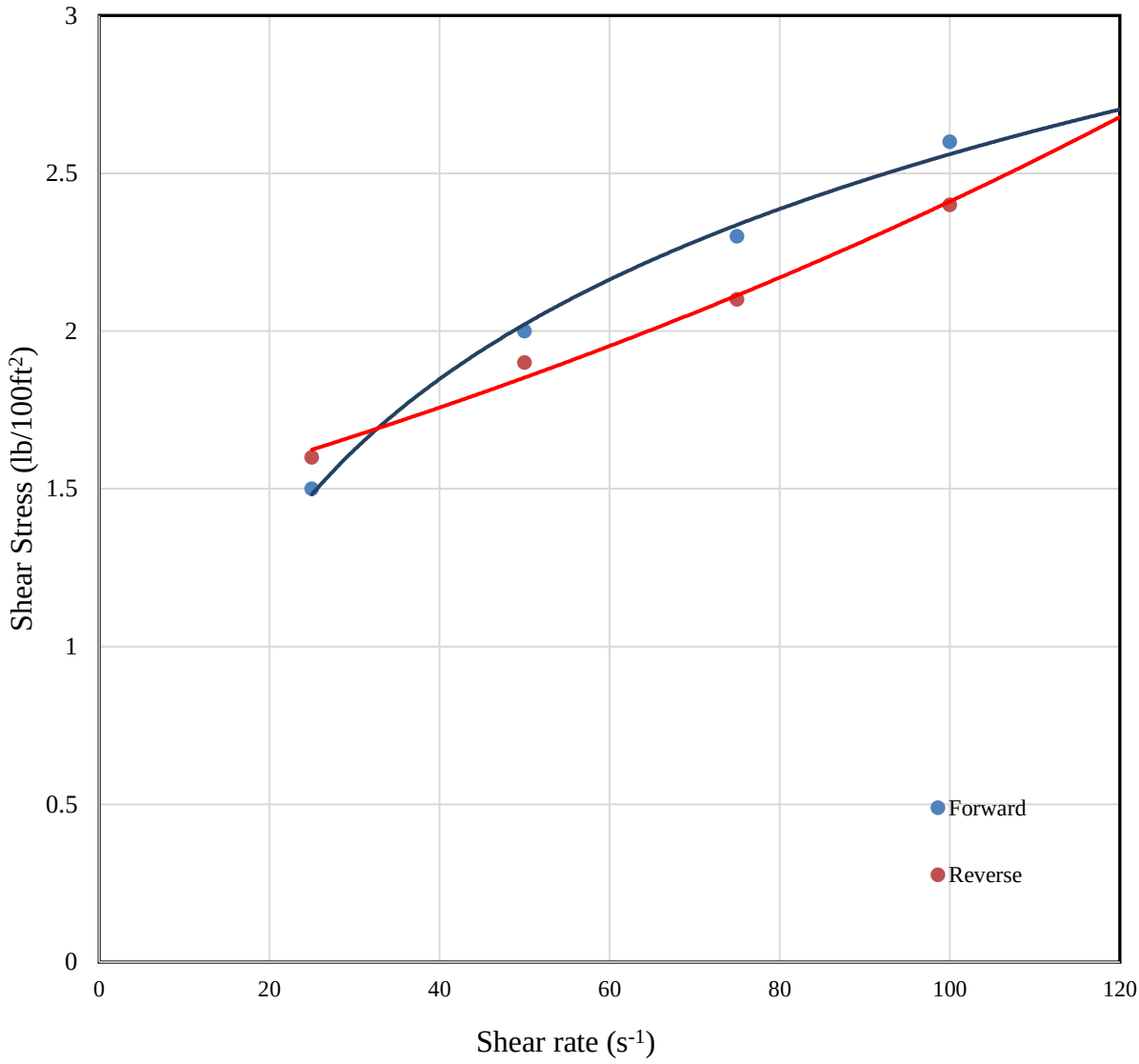

Figure 4.10: Hysteresis behaviour of HPAM at 1200ppm concentration

The viscoelastic properties of HPAM at 1200ppm concentration showed a highly viscoelastic fluid with viscosity ranging from 12cp to 32cp as shown in Figure 4.11 The trendline can clearly be seen to decline with time. This is an indication of viscoelastic reduction of the polymer with continuous shearing with time. The viscosity trendline reduced from 19cp to 17cp. This illustrates that with continuous shearing in field applications in the oil reservoir, there is bound to be reduction in viscosity. However, from the graph for 1200ppm concentration it can inferred that the polymer is appropriate for displacing oil of 10cp viscosity conveniently (the trendline at 18 -17cp).

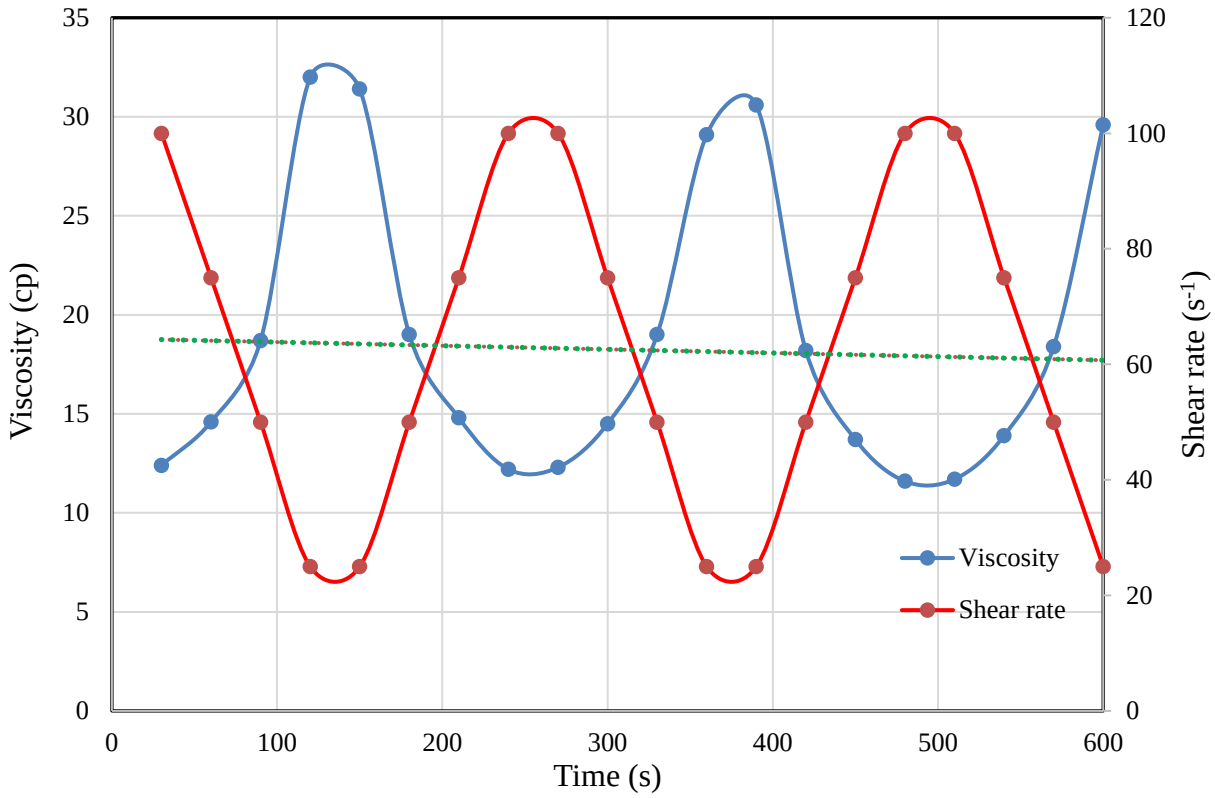

Figure 4.11: Viscosity and shear rate characteristics of HPAM at 1200ppm

In Figure 4.12, the consistency factor versus fluid flow characteristic index curve is illustrated. The k values ranged from 0.24 to 0.46cp and the fluid flow characteristic, n, has values ranging from 0.27 to 0.43. The fluid is pseudoplastic from the n values, which are all less than one (1). The lower the n value, the higher the consistency factor.

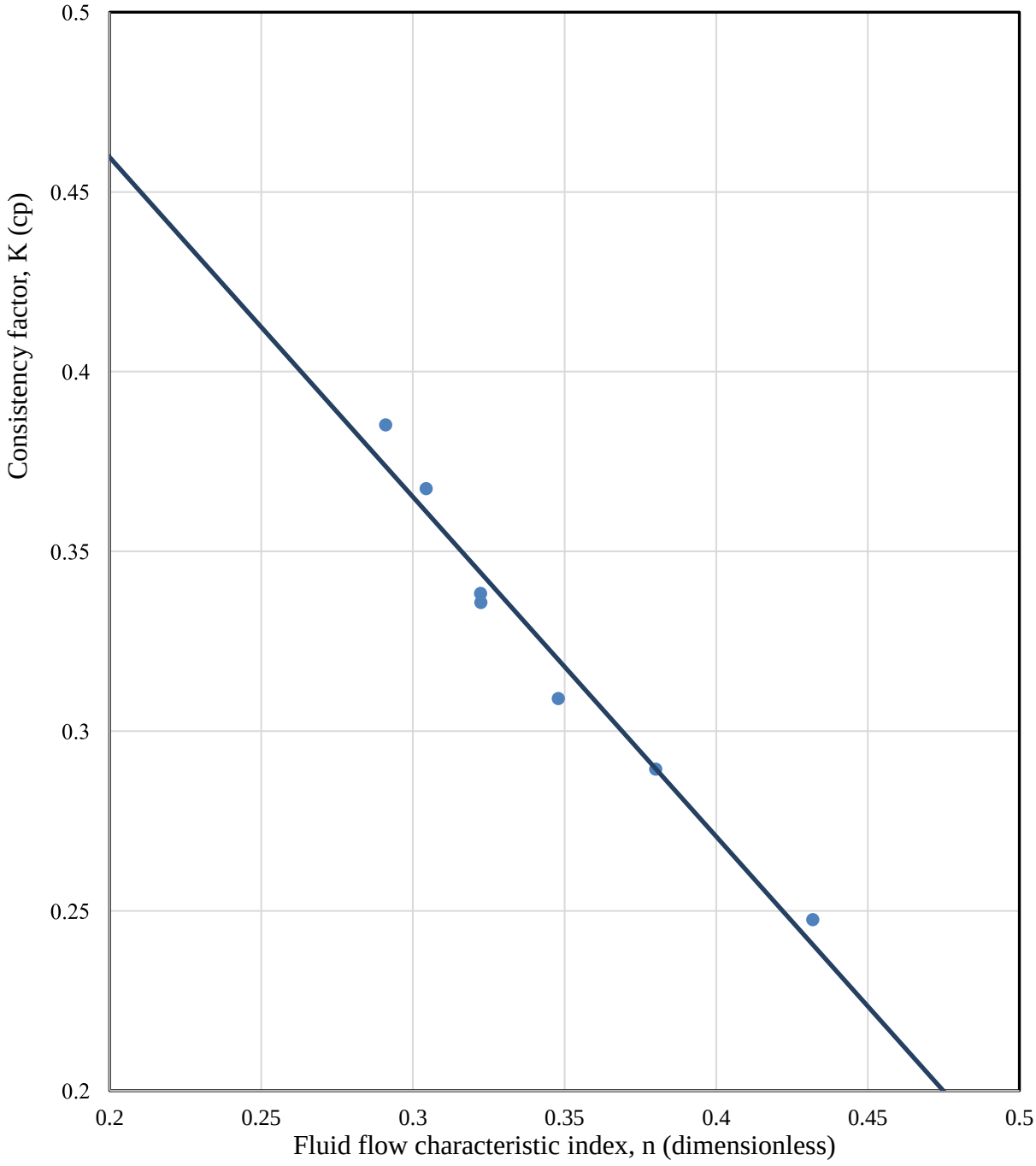

Figure 4.12: Fluid flow behaviour index at 800ppm concentration

Similarly, Figure 4.13 illustrates the hysteresis behaviour of HPAM at 800ppm concentration. The hysteresis envelope in Figure 4.13 has shear stress values ranging from 2.0 to 1.2 lb/100ft^2 within shear rate range of 25 to 100s^{-1} respectively. The loss of energy it exhibits during a cycle, which is marked by the envelope, show some proportionality associated with the concentration of hydrolysed polymer solution. The coil stretch-coil cycle

phenomenon associated with polymer chains at stagnation points for 800ppm concentration is beneficial for enhanced oil recovery operations during flooding.

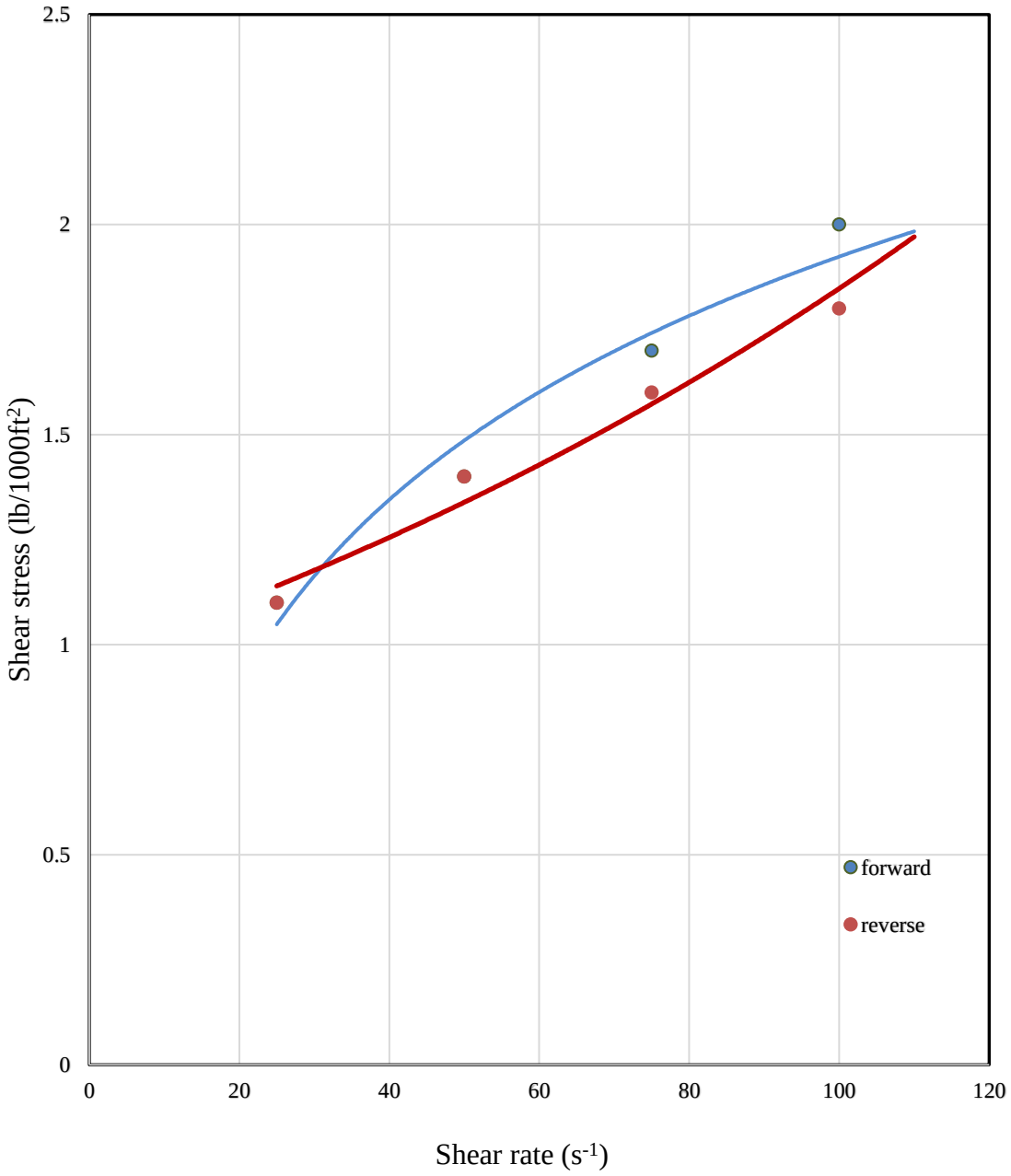

Figure 4.13: Hysteresis behaviour of HPAM at 800ppm concentration

The viscoelasticity graph of hydrolysed polyacrylamide shown in Figure 4.14, which highlights the viscosity and shear characteristics for HPAM at 800ppm concentration has viscosity ranging from 9 to 21cp with shearing rates of 25 to 100^{-1}. The total time for viscoelasticity measurement spans 600seconds. The trendline indicates a decreasing

viscoelastic fluid with time as result of shearing. From the graph the shearing has adverse effect on the polymer solution viscosity.

With time, the coil stretch –coil cycle stagnation will cause the polymer solution to lose its ability to remove residual oil, as it loses viscosity. However, given the slope of the trendline which is quite small, it is observable that a lengthy period of time is required for the polymer to disintegrate completely. Hence, its application at 800ppm is, from the results, appropriate for EOR.

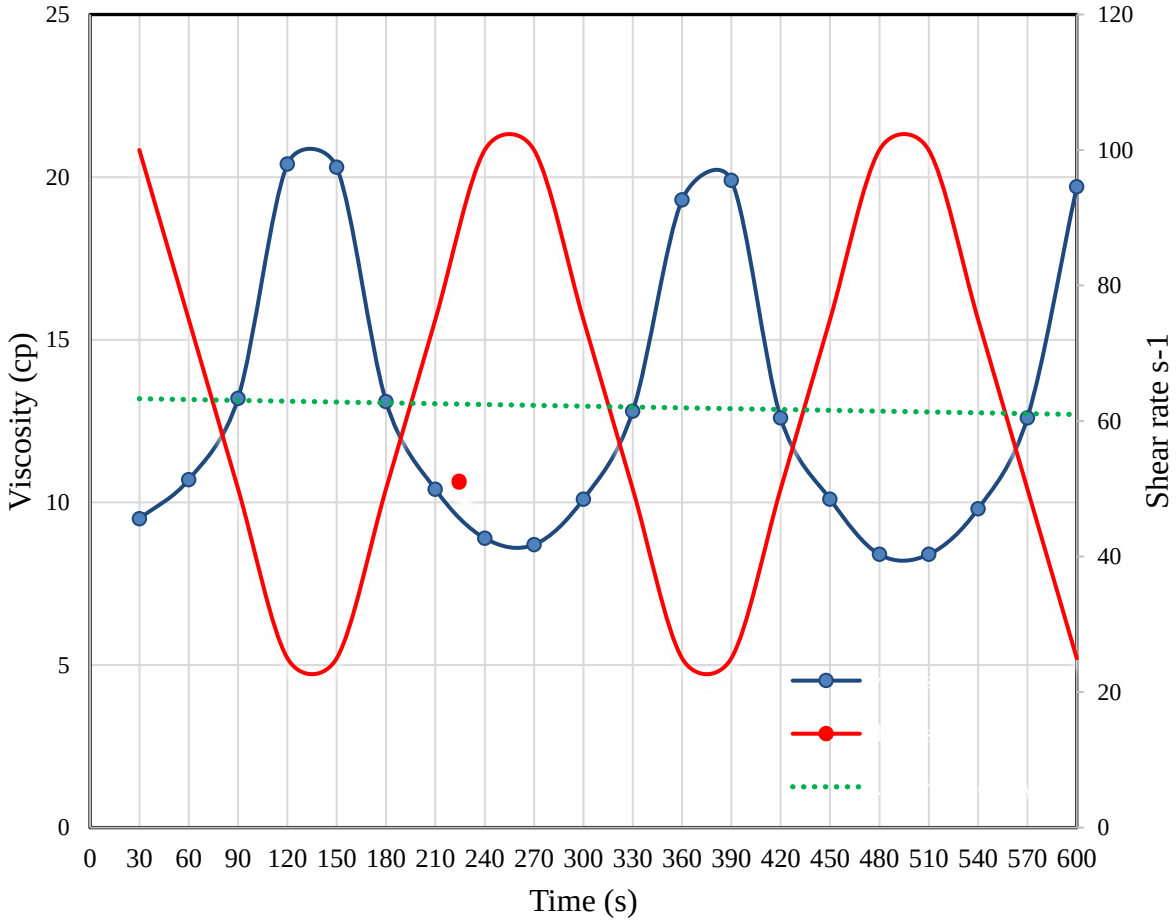

Figure 4.14: Viscosity and shear characteristics for HPAM at 800ppm concentration

Figure 4.15 shows the hysteresis behaviour of HPAM at 400ppm. The solution of 400ppm concentration of HPAM equally exhibits hysteresis envelope with the forward and reverse sweeps respectively on a plot of a single cycle shear stress-shear rate graph. The hysteresis envelope constitutes a defining property for the elasticity of the polymer solution. The single envelope spans from a shear stress range of 0.8 to 1.2 Ib/100ft^2 with a shear rate of 30 to

$85s^{-1}$. The size of the hysteresis envelope is small compared to higher concentrations of polymer solutions.

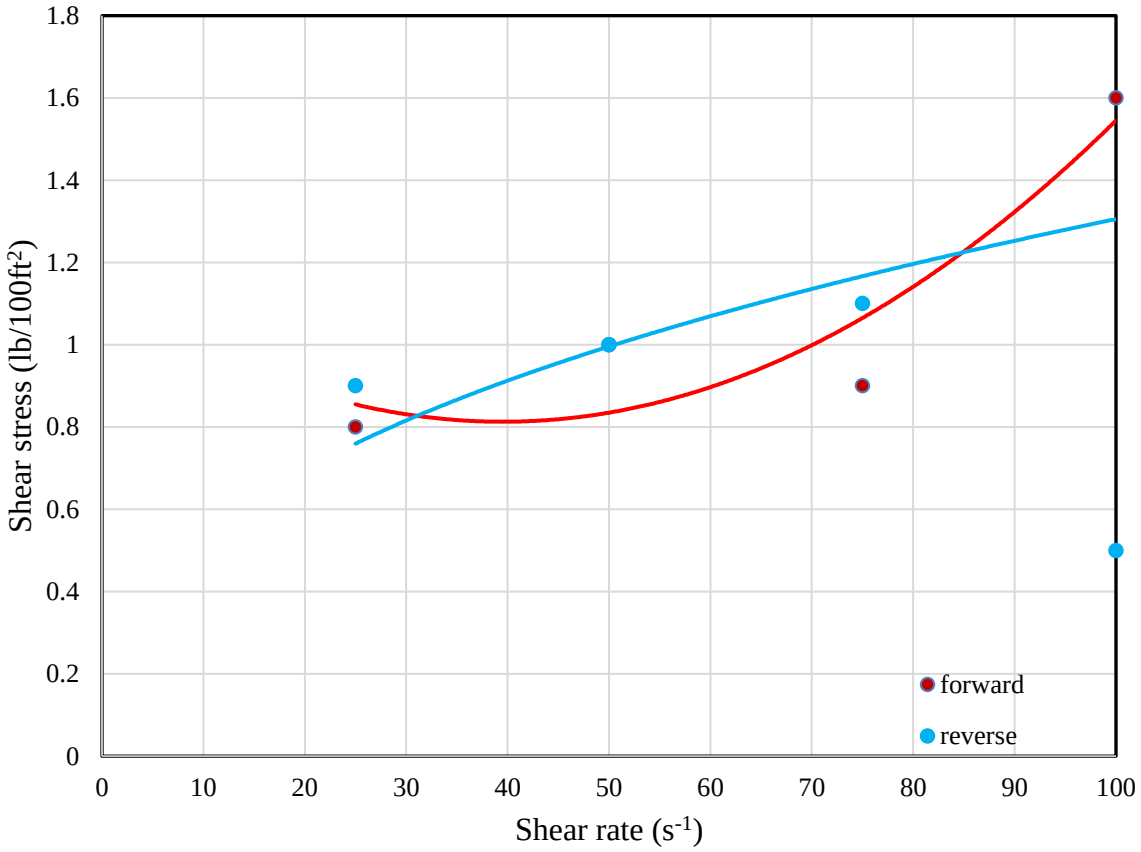

Figure 4.15: Hysteresis behaviour of HPAM at 400ppm concentration

The viscoelastic behaviour of a 400ppm concentration is illustrated in Figure 4.16. The trendline line graph (dotted line) in Figure 4.16 shows that the viscosity is increasing with increasing shear. This is typical of a dilatant fluid and not common in pseudoplastic fluids. The trend of the viscosity with shear is rather beneficial in core flooding where dilatancy can increase displacement efficiency of the displacing fluid. However, the total fluid behaviour is pseudoplastic from the low values of n obtained. The molecular structure of HPAM enables it to expand when in contact with water thereby increasing overall volume of solution formed.

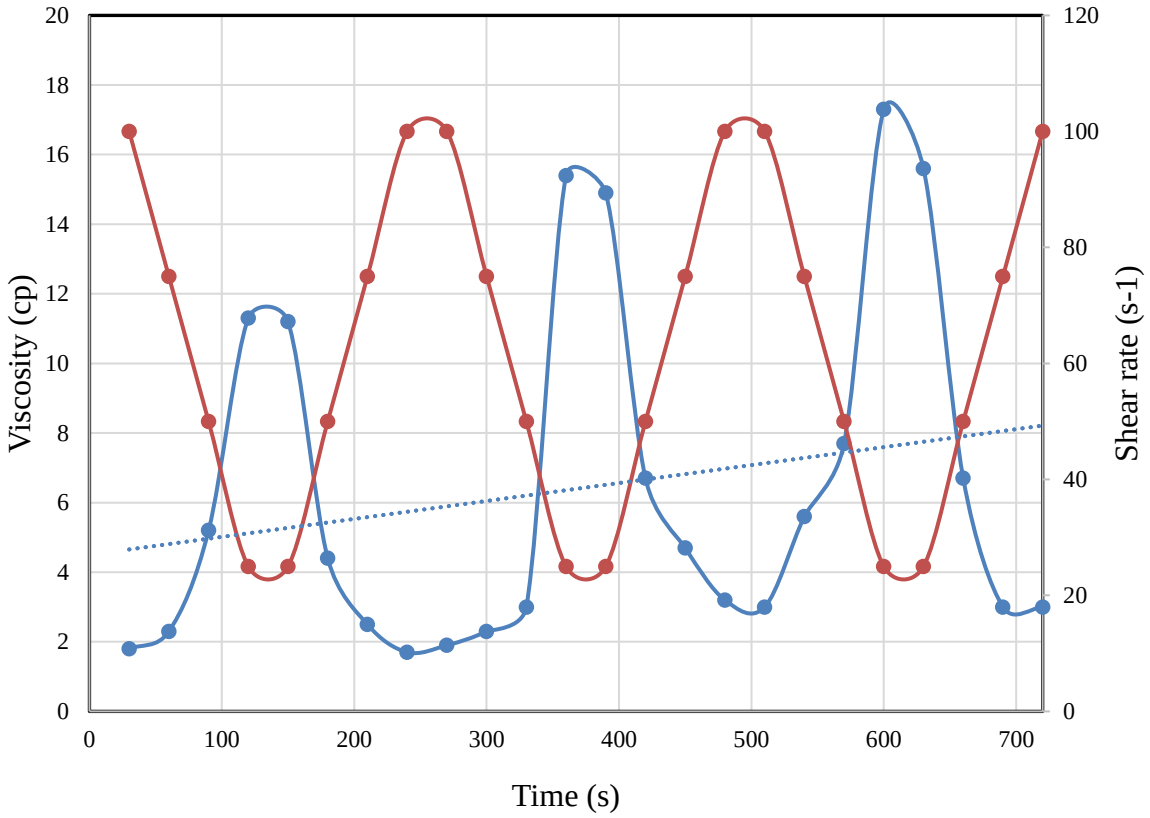

Figure 4.16: HPAM viscosity and shear pseudoplastic characteristic at 400ppm concentration

The increasing viscosity and viscoelasticity are associated with low concentration of the polymer in solution that gives the polymer a higher degree of freedom and large space for expansion of the coil molecular chains of the polymer. Therefore, the final fluid has a good potential for exhibiting molecular viscoelasticity and dilatancy in the tortuous pores of the reservoir.

Figure 4.17 clearly illustrates the impact of concentration of polymer on overall viscosity and viscoelasticity of solution formed. The higher the concentration, the higher the viscosity as well as the higher the viscoelasticity. The lower the polymer concentration, the lower the viscosity and viscoelasticity. However, the utilisation of higher polymer concentration should be with some caution due to the impact of pore blockage and permeability reduction. Therefore, a trade off should be considered to maximise recovery and production.

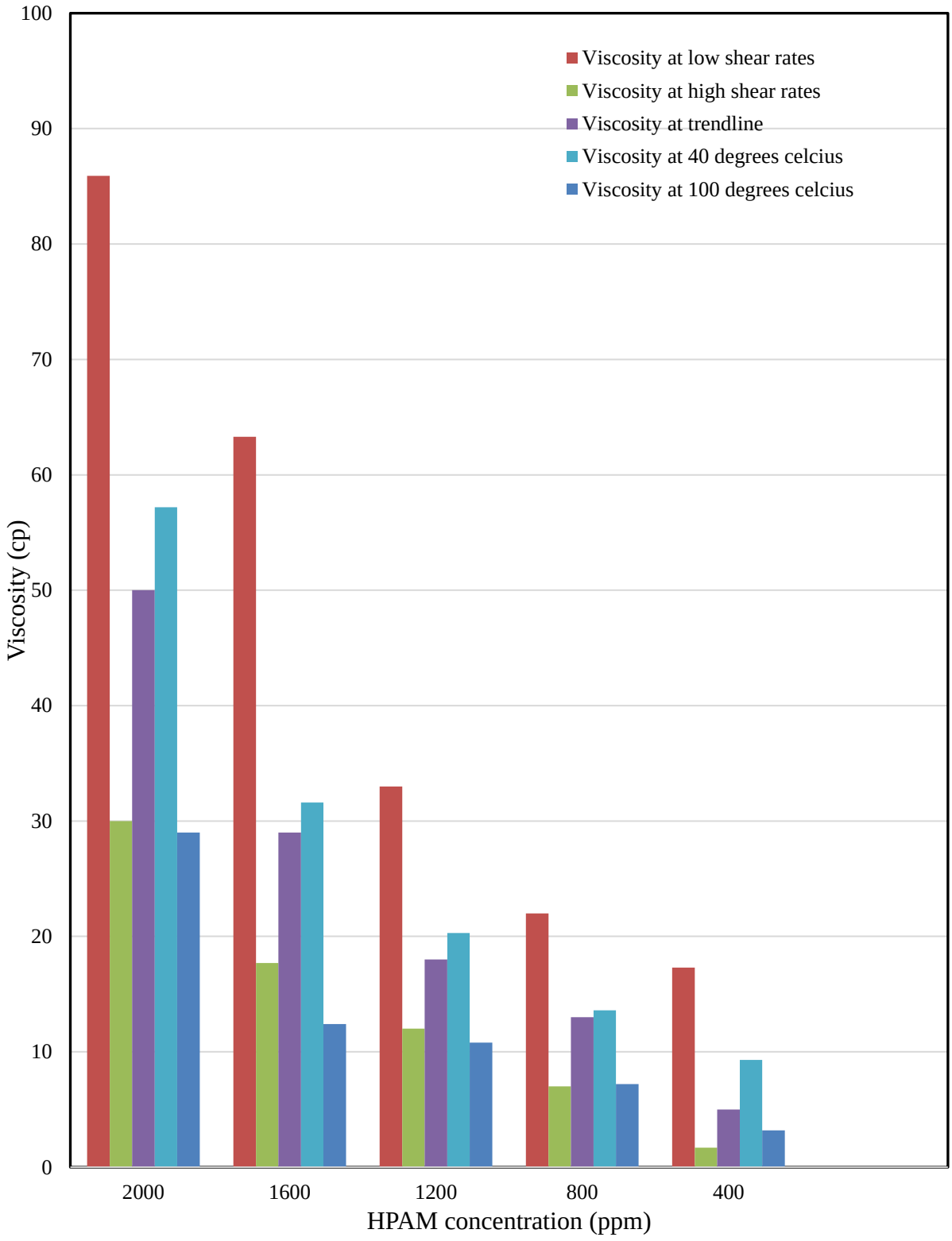

Figure 4.17: Viscosity profile at varying shear rates for several HPAM polymer solution concentrations

4.2.3 Mobility ratio and HPAM polymer solution viscosity at elevated temperatures

The mobility ratio for the displacing polymer based on the operating temperature of 40°C and HPAM polymer injection characteristics at elevated temperature is shown in Table 4.1.

$$M_{mobility} = \left[\left(\frac{K_w}{K_o}\right)\left(\frac{\mu_o}{\mu_w}\right)\right]$$

Table 4:1: Mobility ratio, Fluid behavioural index, Consistency factor and viscosity at elevated temperatures

HPAM Concentration (ppm)	$M_{mobility}$	n	K (cp)	Viscosity @40°C (cp)	Viscosity @100°C (cp)	Viscosity cp@170°C (cp)
400	0.874	0.0207	0.86019	11.1	4.5	2.7
800	0.688	0.3801	0.28942	14.1	8	5.8
1200	0.478	0.3093	0.54079	20.3	10.8	7.5
1600	0.307	0.0565	1.90411	31.6	12.4	7.2
2000	0.169	0.2597	1.82928	57.2	29	19.6

The mobility ratios for all the polymer concentrations decreased as the concentration of the polymer increased as detailed in Table 4.1.

4.2.4 Power law and HPAM polymer solution at elevated temperatures

The Newtonian behaviour of the HPAM polymer solution at displacement temperature of 40°C using the power law shows pseudoplasticity even at elevated temperatures. The Power law which provides the relationship between shear rate and shear stress (Silva et al., 2018) is shown Equation 2.15

$$\tau = K\gamma^n \qquad 2.15$$

When the value of n is greater than 1, the fluid is dilatant, when n is equal to 1 the fluid is Newtonian and when n is less than 1 the fluid is pseudoplastic. In Table 4.1, the values of n were all less than 1 indicating pseudoplasticity of all the prepared polymer concentrations.

4.3 Geophysical analysis

4.3.1 Reservoir core sample porosity and pore distribution

The core samples were scanned to generate images showing the structure of the core sample at the microscale level. The geometry of all the core samples were cylindrical. The dimension of the core samples was 1inch by 2 inches. This section reveals the volume reconstruction at different settings. The highest setting is 200 and the least is 0 (zero). At high transparency, the surface structure and geometry of the core sample is shown in its complete physical appearance with all its surface features while at zero setting the core sample inclusion and voids are revealed. Figure 4.18, Figure 4.19, Figure 4.20, Figure 4.21, Figure 4.22, Figure 4.23, Figure 4.24, Figure 4.25, Figure 4.26, Figure 4.27, Figure 4.28 and Figure 4.29 illustrate the various transparency setting images obtained for the volume reconstruction.

Similarly, the volume graphics statistical results for voids (porosity) and inclusion (foreign matter) are shown in Table 4.2, Table 4.3, Table 4.4, Table 4.5, Table 4.6, Table 4.7, Table 4.8, Table 4.9, Table 4.10 and Table 4.11. respectively.

In Figure 4.18, computed tomography volume reconstruction of Edward brown at 200 transparency setting of the volume graphics user interface shows relatively large surface pores. The numerous pores on the core surface, upon close visual observation, are an indication of high porosity potential.

Figure 4.18: CT volume reconstruction of Edward brown at Transparency setting of 200

In Figure 4.19, the Edward brown computed tomography volume reconstruction at zero setting has a pore distribution ranging from 9mm^3 to 1mm^3. These pores are fairly interconnected based on the reconstructed imagery. Large voids of 5mm^3 can be seen centrally located in the core sample. The large pores are significant in aiding the permeability of the core sample and enhancing fluid flow during core flooding operations. The pockets of 9mm^3 voids located on the edges of this particular Edward brown core sample not only increases the propensity of fluid flow but maximises the interconnectivity of the micropores of the core sample.

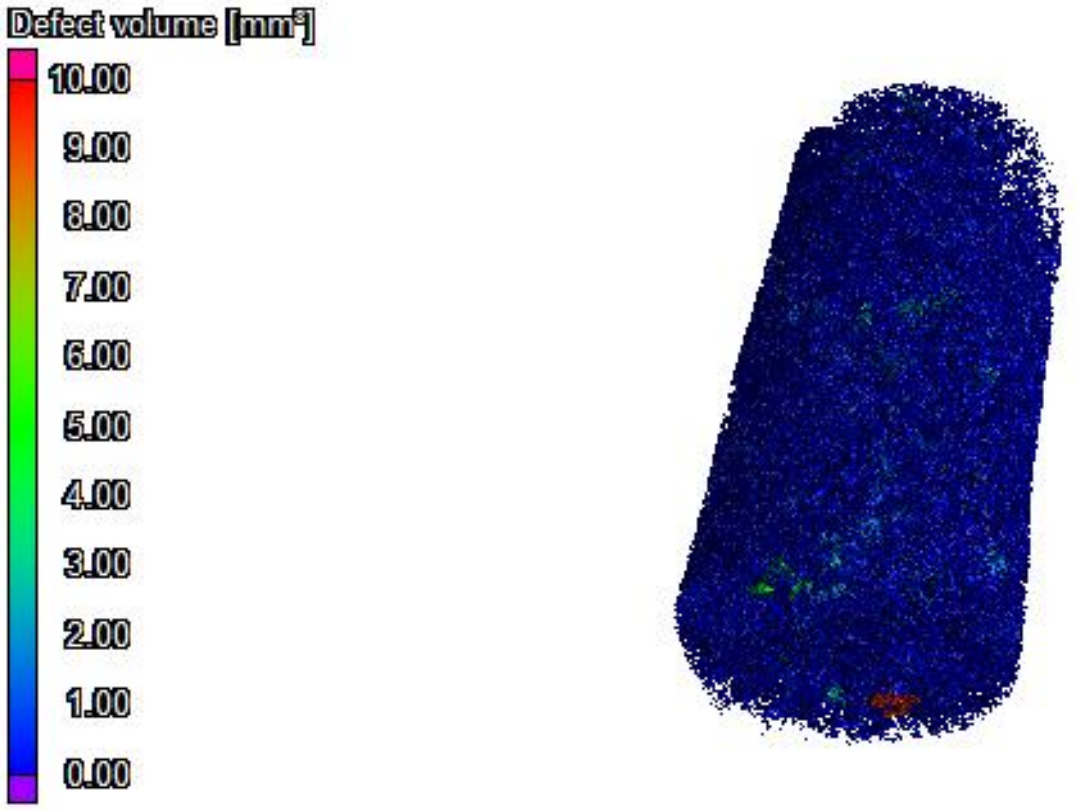

Figure 4.19: CT volume reconstruction of Edward brown at Transparency setting of zero showing pores and pore size distribution

Table 4:2: Edward brown porosity (voids) statistical results

Parameter	Magnitude	Units
∑Voxel	19543804	Dimensionless
∑Volume	4117.01	mm^3
∑Surface	134571.77	mm
∑Px	20057.94	mm^2
∑Py	20099.55	mm^2
∑Pz	20536.24	mm^2
Material	Iso value using surface determination	mm^3
Voids	4117.01	mm^2
Voids	16.08	%

The circular plane view of the Edward core sample has pores of up $5mm^3$ in the pore distribution. Comparing the images in Figure 4.19 and Figure 4.20 it is evident that this large pore is interconnected and linked across to its cylindrical end. Similarly, the slice view of the Edward brown further buttresses the high pore interconnectivity of core sample. The large voids stretch across the cylindrical core sample. The central and edge to edge location of large pores observed contributes significantly in enhancing fluid flow dynamics in the complex pore structure. The micropores are interconnected to a large extent, but there are pockets of isolated pores that have no connectivity to other adjacent micropores.

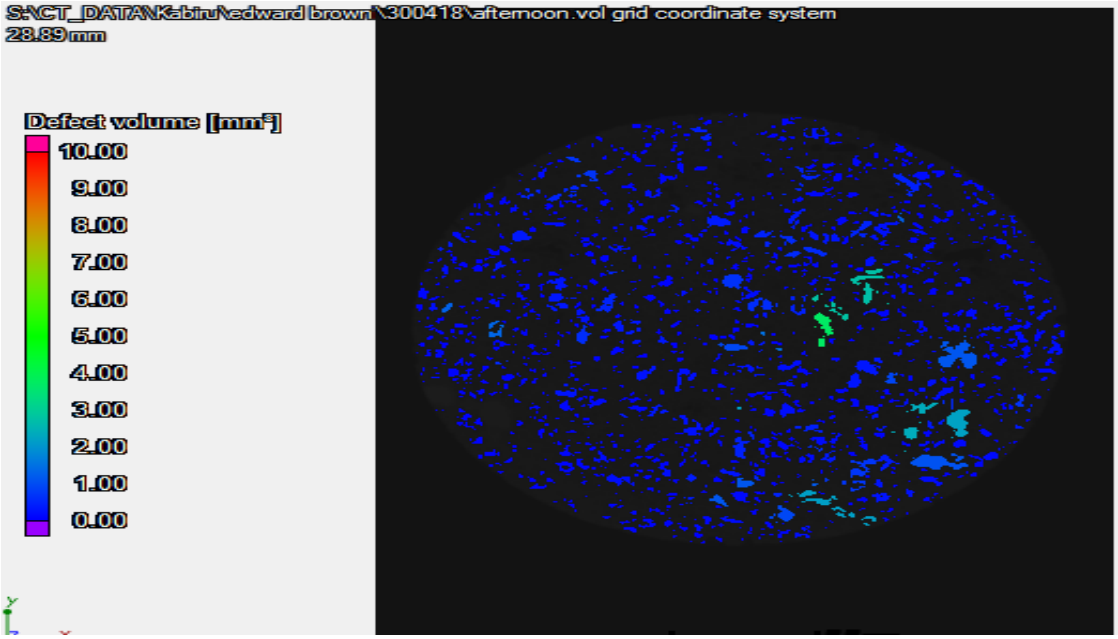

Figure 4.20: Volume reconstruction of Edward brown core sample showing pores and pore size distribution (Top view)

In Table 4.2 it is evident that Edward brown core sample volume graphic statistics shows the existence of inclusions or foreign matter up to 3.42 %. This is quite small and thus the rock can still be viewed to be relatively homogeneous due to the size of the inclusions.

Table 4:3: Edward brown core sample inclusion statistical results

Parameter	Magnitude	Units
∑Voxel	4037091	Dimensionless
∑Volume	850.44	mm^3
∑Surface	53727.93	mm
∑Px	8695.01	mm^2
∑Py	8920.13	mm^2
∑Pz	8775.75	mm^2
Material	Iso value using surface determination volume is 240117.2	mm^3
Inclusions	850.44	mm^2
Inclusions	3.42	%

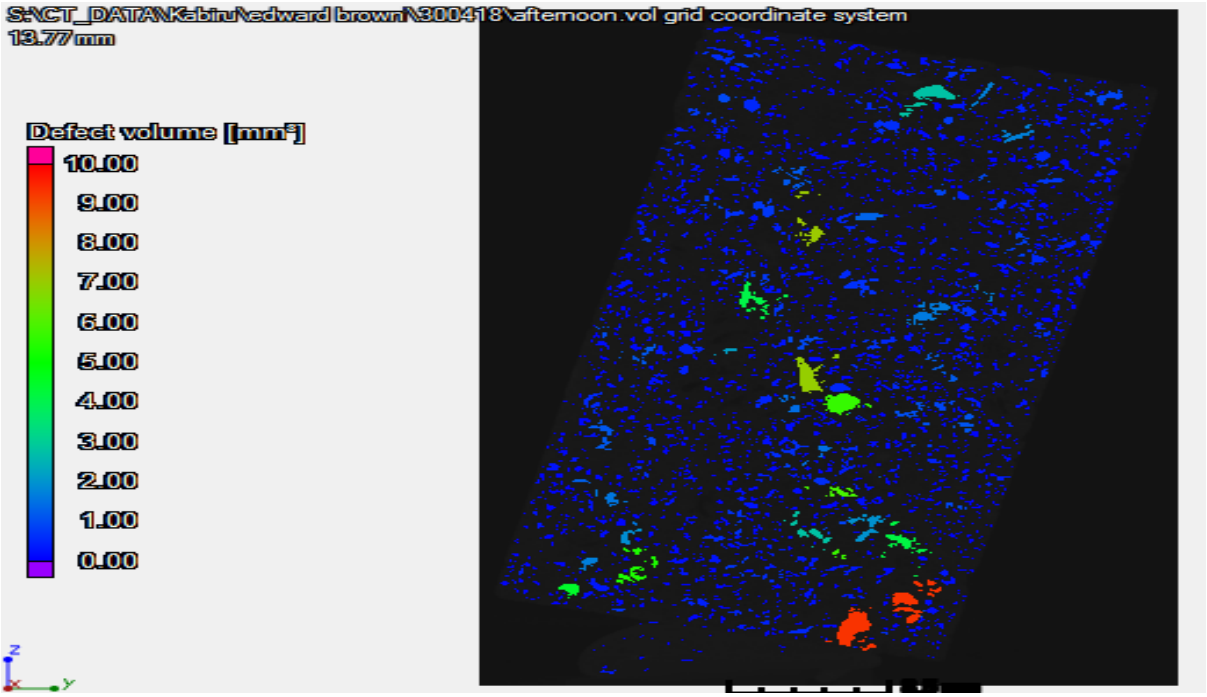

Figure 4.21: Volume reconstruction of Edward grey sandstone core sample showing pore and pore size distribution (Side view)

The grey Berea core sample in Figure 4.22 at volume graphic transparency setting of 200 illustrates a uniformly grained sandstone core sample. When Berea core sample at transparency setting of 200 is compared with its transparency setting of zero image the internal pores are matched with surface pores.

Figure 4.22: CT volume reconstruction of Grey Berea at Transparency setting of 200

Table 4.4 details the pore statistics for Grey Berea and Figure 4.23 shows the volume reconstruction at zero setting. The pores are mainly within 0.5mm^3 and are uniformly distributed. Though visual observation shows relatively high pore interconnectivity, a significant proportion of unconnected pores exist.

Table 4:4: Grey Berea core sample Pore statistical results

Parameter	Magnitude	Units
∑Voxel	11598172	Dimensionless
∑Volume	2443.22	mm^3
∑Surface	133126.86	mm
∑Px	21799.06	mm^2
∑Py	21102.65	mm^2
∑Pz	21922.69	mm^2
Material	Iso value using surface determination volume is 23373.24	mm^3
Voids	2442.22	mm^2
Voids	9.46	%

Figure 4.23: CT volume reconstruction of Grey Berea at Transparency setting of zero showing pore and pore size distribution.

In terms of homogeneity, the Grey Berea sandstone indicated is highly homogeneous due to its low value of inclusions as detailed in Table 4.5.

Table 4:5: Grey Berea core sample Inclusions statistical results

Parameter	Magnitude	Units
∑Voxel	4577867	Dimensionless
∑Volume	964.35	mm^3
∑Surface	58048.23	mm
∑Px	9502.26	mm^2
∑Py	9355.22	mm^2
∑Pz	9778.86	mm^2
Material	Iso value using surface determination volume is 24850.1	mm^3
Inclusions	964.35	mm^2
Inclusions	3.74	%

In Figure 4.24 the computed tomography scan of Guelph dolomite shows the surface structure of the core sample at a transparency setting of 200. The surface appears to have large voids with potentials for pore interconnectivity by the depth of visible surface pores. Figure 4.25 reaffirms the pore interconnectivity of Guelph dolomite with the transparency setting set at 0 (zero).

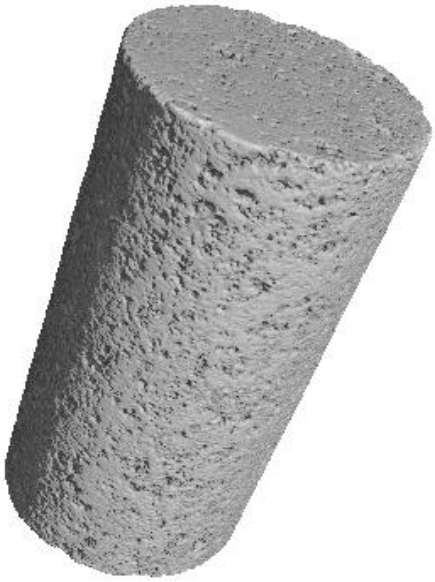

Figure 4.24: CT volume reconstruction of Guelph dolomite at Transparency setting of 200

Guleph dolomite based on the pore statistical results in Table 4.6 indicates an almost 12% void percentage. The corresponding pore size and pore distributions in Figure 4.25 for Guleph dolomite indicate pore sizes mainly less than 5mm^3. However, there are pores of up to 20mm^3 distributed across the core sample. The inclusions are minimal standing at 3.41% as shown in Table 4.7.

Table 4:6: Guelph dolomite Pore statistical results

Parameter	Magnitude	Units
∑Voxel	14547993	Dimensionless
∑Volume	3064.62	mm^3
∑Surface	98460.05	mm
∑Px	13879.30	mm^2
∑Py	14135.40	mm^2
∑Pz	13890.80	mm^2
Material	Iso value using surface determination volume is 22817.45	mm^3
Voids	3064.62	mm^3
Voids	11.84	%

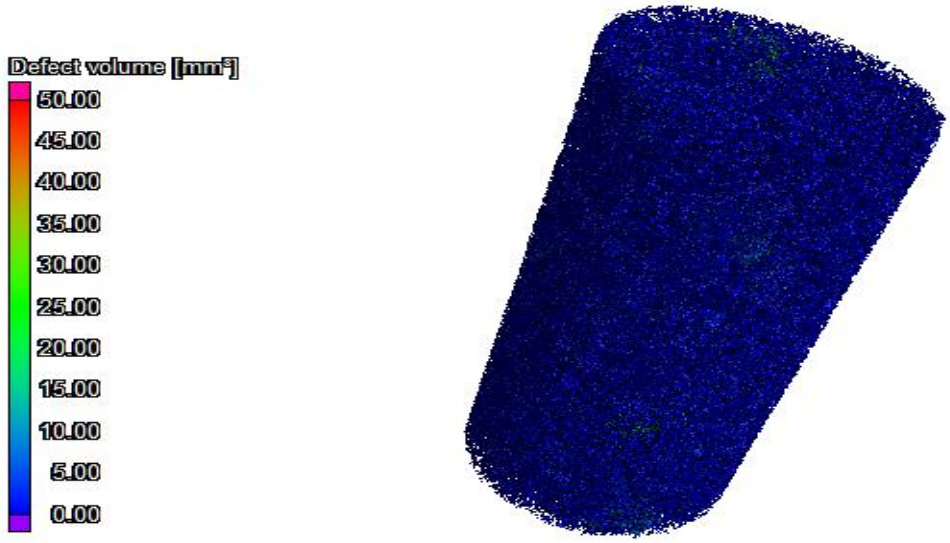

Figure 4.25: CT volume reconstruction of Guelph dolomite at Transparency setting of zero showing pore and pore size distribution

Table 4:7: Guelph dolomite inclusions statistical results

Parameter	Magnitude	Units
∑Voxel	4091886	Dimensionless
∑Volume	861.98	mm^3
∑Surface	57029.78	mm
∑Px	9472.66	mm^2
∑Py	9474.01	mm^2
∑Pz	8992.80	mm^2
Material	Iso value using surface determination volume is 24850.1	mm^3
Inclusions	861.98	mm^2
Inclusions	3.41	%

The surface structure of Indiana 70 Limestone shown in Figure 4.26 indicates numerous surface pores. This indicates potential for surface pore interconnectivity with interior pores.

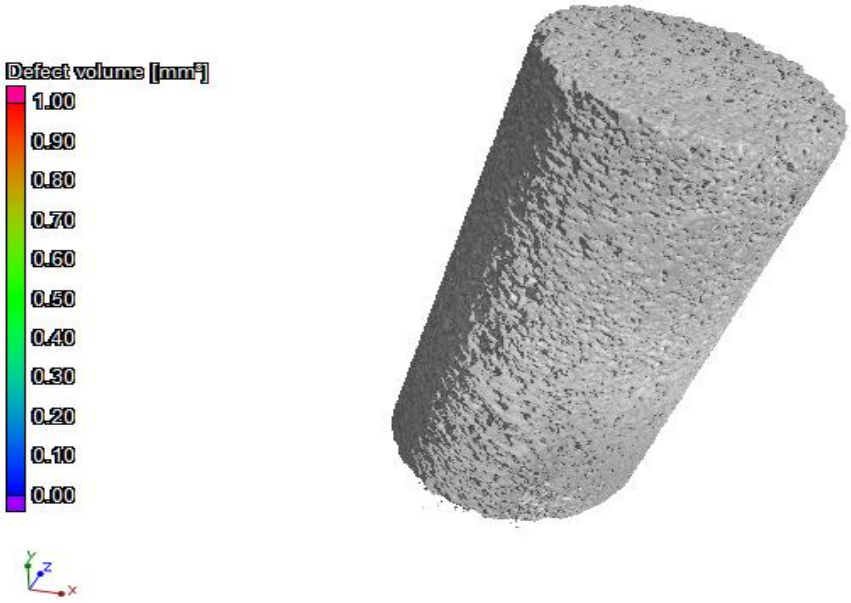

Figure 4.26: CT volume reconstruction of Indiana 70 Limestone at Transparency setting of 200

The percentage of voids is 5.56% in Indiana 70 limestone as shown in Table 4.8. These voids are observed in Figure 4.27. Though most of the pores are less than 0.2mm^3, there are a small quantity of pores in the region of 0.4 to 0.6mm^3. In addition, a few pores of 0.9mm^3 are there.

Table 4:8 Indiana 70 limestone voids statistical results

Parameter	Magnitude	Units
∑Voxel	4220388	Dimensionless
∑Volume	889.05	mm^3
∑Surface	48934.78	mm
∑Px	7985.10	mm^2
∑Py	7720.73	mm^2
∑Pz	7846.17	mm^2
Material	Iso value using surface determination volume is 15109.71	mm^3
Voids	889.05	mm^3
Voids	5.56	%

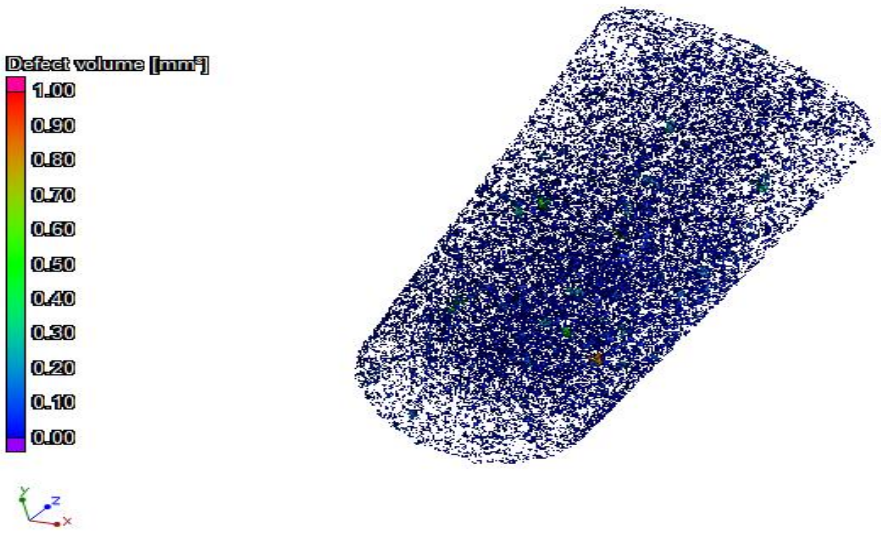

Figure 4.27 CT volume reconstruction of Indiana 70 Limestone at Transparency setting of zero showing pores and pore size distribution in Indiana Limestone core sample

The foreign matter in the Indiana limestone is 3.47% of the entire core sample as indicated in Table 4.9.

Table 4:9: Indiana Limestone core sample inclusions statistical results

Parameter	Magnitude	Units
∑Voxel	2622765	Dimensionless
∑Volume	552.50	mm^3
∑Surface	35120.67	mm
∑Px	5703.68	mm^2
∑Py	5767	mm^2
∑Pz	5734.72	mm^2
Material	Iso value using surface determination volume is 15360.94	mm^3
Inclusions	552.50	mm^2
Inclusions	3.47	%

Silurian dolomite has highly non uniform surface pores as can be seen in Figure 4.28. the presence of large and small surface voids is a characteristic of carbonate reservoirs.

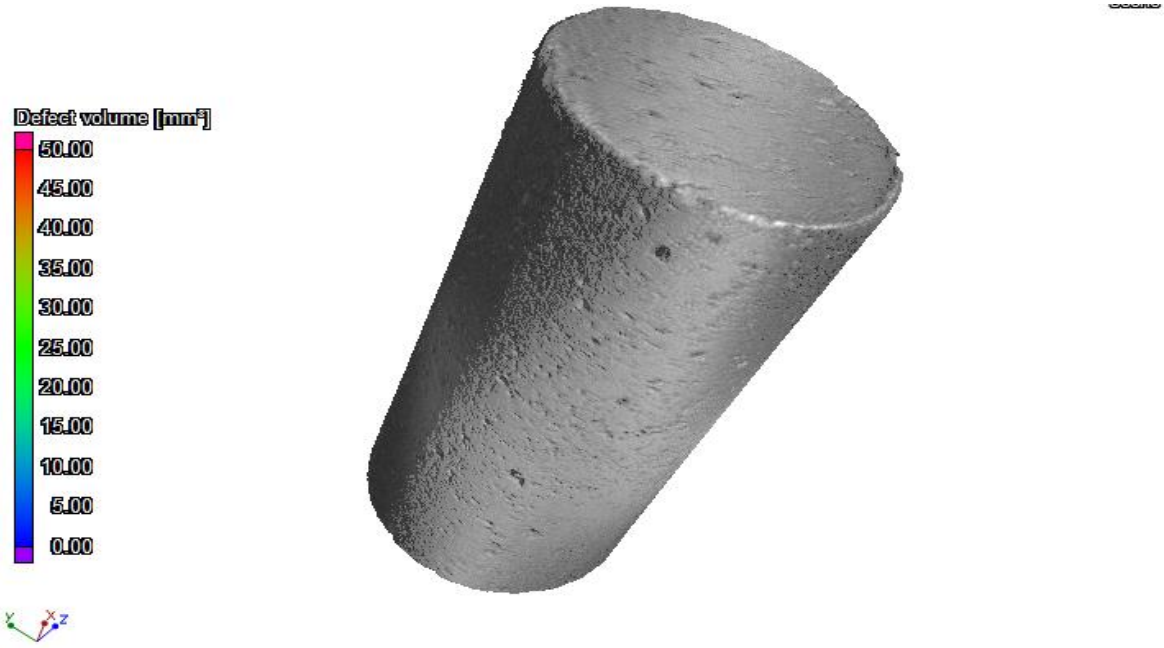

Figure 4.28: CT Volume reconstruction Silurian dolomite at Transparency setting of 200

The volume graphics reconstruction indicates 9.32% voids in Silurian dolomite as shown in Table 4.10. This is an indication for potentials for favourable porosity. A close observation of Figure 4.29 shows the high interconnected pores 5mm^3 and a few embedded pores of 25 to 35mm^3 in the Silurian dolomite.

Table 4:10: Silurian Dolomite core sample pore statistical results

Parameter	Magnitude	Unit
∑Voxel	11514209	Dimensionless
∑Volume	2425.53	mm^3
∑Surface	86863.34	mm
∑Px	14209.71	mm^2
∑Py	12685.95	mm^2
∑Pz	12647.16	mm^2
Material	Iso value using surface determination volume is 23595.11	mm^3
Voids	2425.53	mm^3
Voids	9.32	%

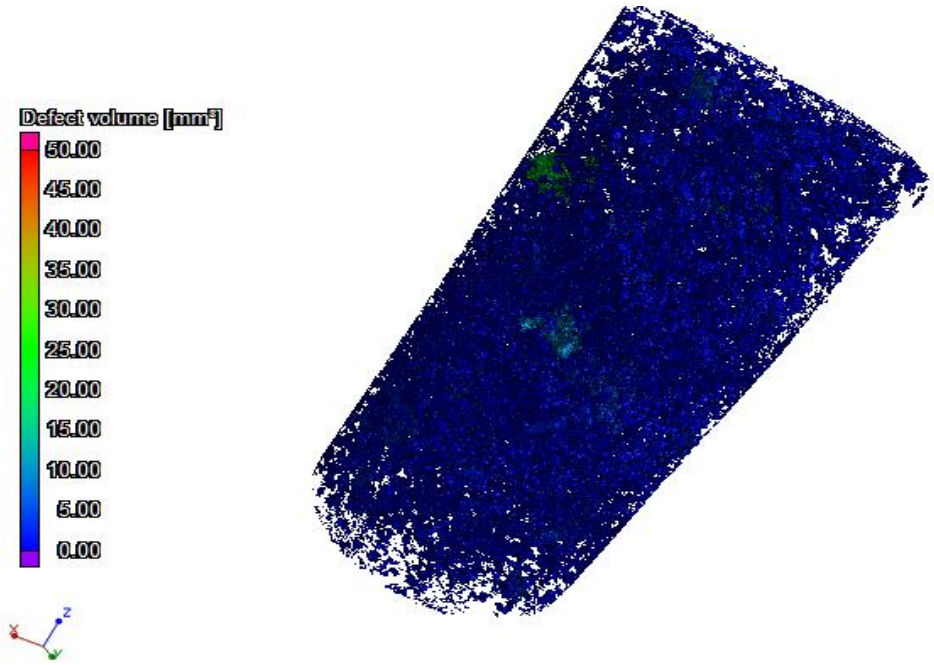

Figure 4.29: CT Volume reconstruction of Silurian dolomite at Transparency setting of zero showing pore and pore size distribution

The foreign matter in Silurian dolomite is 3.95% of the core sample as detailed in the inclusion statistical results in Table 4.1.

Table 4:11: Silurian dolomite inclusions statistical results

Parameter	Magnitude	Units
∑Voxel	4856938	Dimensionless
∑Volume	1023.14	mm^3
∑Surface	64654.47	mm
∑Px	10652.33	mm^2
∑Py	10689.78	mm^2
∑Pz	10269.79	mm^2
Material	Iso value using surface determination volume is 24867.55	mm^3
Inclusions	1023.14	mm^2
Inclusions	3.95	%

All the core samples subjected to computed tomography (CT) scanning and subsequent volume graphics reconstruction showed varying degree of interconnected pores. Therefore, the CT provided porosity confirmation as detailed in Table 4.12

Table 4:12: Summary of rock properties and porosity confirmation

S. N	Rock type	Core sample porosity (%)	Porosity confirmation with CT Scanner voids (%)	Pore volume (cm^3)
1	Edward brown	39	16	10.28
2	Grey Berea Upper	21	9	5.40
3	Grey Berea lower	19	4	4.88
4	Guelph dolomite	10	12	2.75
5	Indiana limestone	18	6	4.63
6	Silurian Dolomite	16	9	4.11

4.4 Oil recovery

4.4.1 Oscilloscope ultrasound waveform

The oscilloscope wave form graphs illustrated from Figure 4.30 to Figure 4.56 are the sinusoidal waves observed on the oscilloscope for the input transmitter Channel 1 (CH1), output signal receiver channel 2 (CH2) and the Fast Fourier transform (FFT) for 20KHz, 30KHz, 40KHz, 50KHz, 60KHz, 70KHz, 80KHz, 90KHz and 100KHz.

4.4.1.1 Transmitter and receiver waveform

The sinusoidal signal from the transmitting transducer indicates high amplitude waveform and has maximum power. Only maximum power provides excitation and desired vibration. As the frequency is increased the amplitude of the waves decreases. The oscilloscope's voltage capacity was exceeded, hence the waveform appeared to have ridges. Therefore, reference voltage was used as a yard stick. A close observation of the 20KHz sinusoidal wave shown in Figure 4.30 indicates peak to peak values of 1.92mV (Reference voltage) and period 5.35ms. On the other hand, in Figure 4.31, the signal received at the receiver

transducer is highly attenuated. The maximum wave amplitude is 0.256mV and period $1.51x10^{-3}$ms. These two properties at the receiving transducer (CH2) are much smaller than their corresponding transmitter values.

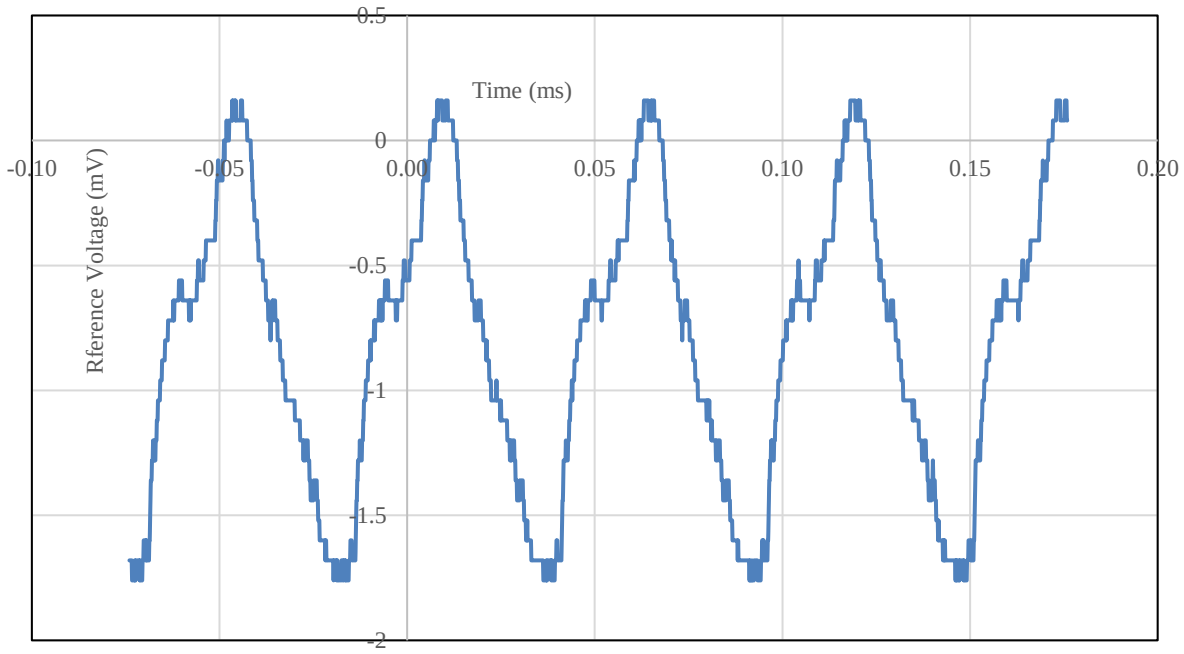

Figure 4.30: Ultrasound at 20KHz and maximum power setting (Transmitter)

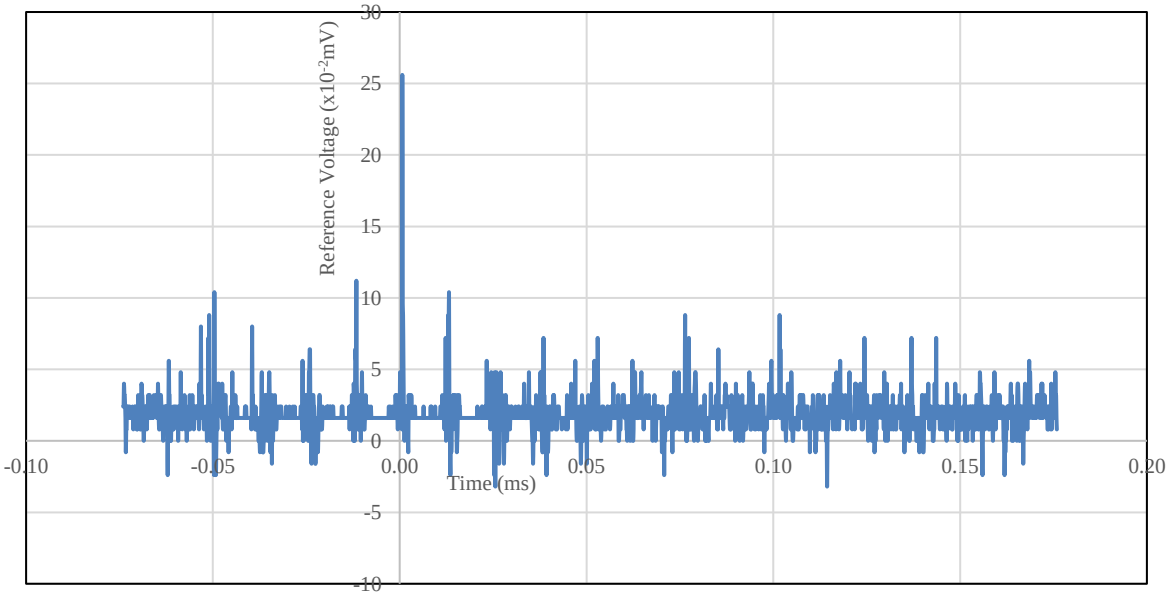

Figure 4.31: Ultrasound at 20KHz at maximum power setting (Receiver)

4.4.1.2 Vibrations and Fast Fourier Transforms

The Fast Fourier Transform (FFT), which is the discretised sinusoidal wave form, provides the algorithm needed to interpret vibrations being transmitted in the rock sample during ultrasound enhanced oil recovery. In Figure 4.32 the spectral component of 20KHz frequency domain is smaller than the spectral view of 30KHz in Figure 4.35. Similarly, the spectral component of 40KHz is larger than the spectral component of 30KHz.

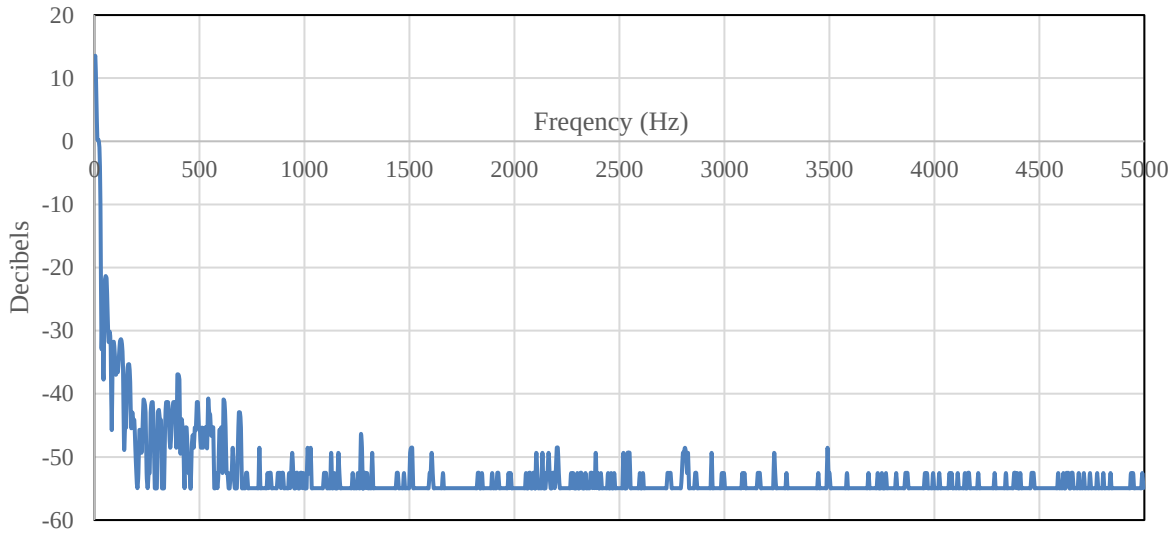

Figure 4.32: Fast Fourier Transform (FFT) showing Spectral view of 20KHz frequency domain for vibration analysis

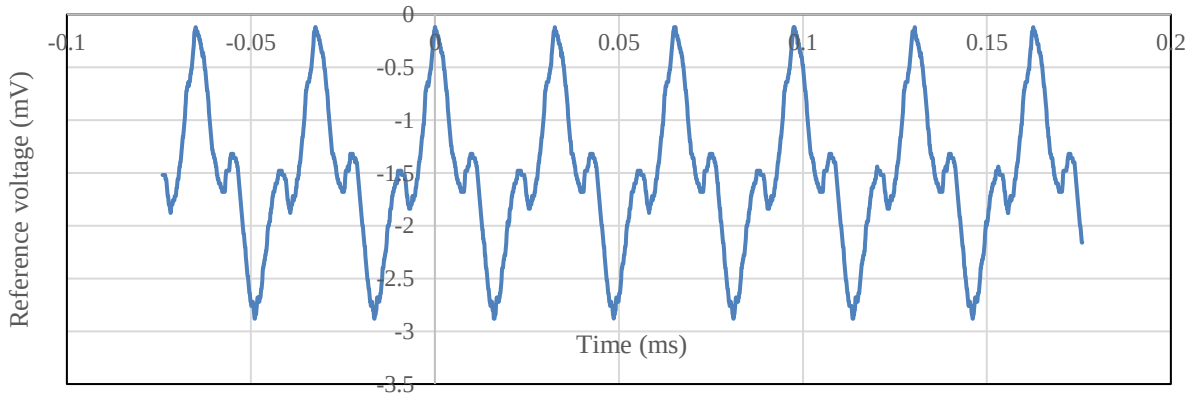

Figure 4.33: Ultrasound at 30KHz and maximum power setting (Transmitter)

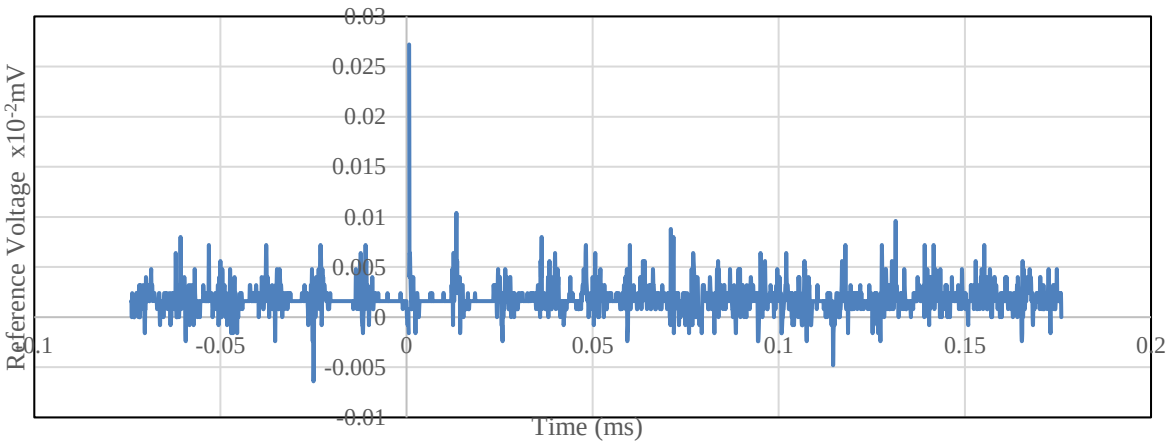

Figure 4.34: Ultrasound at 30KHz at maximum power setting (Receiver)

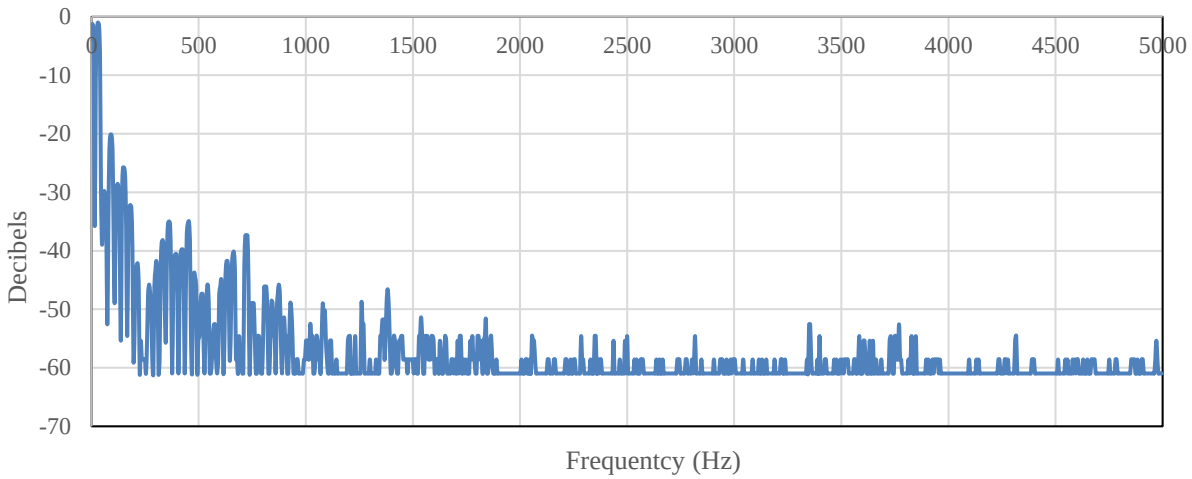

Figure 4.35: Fast Fourier Transform (FFT) showing spectral view of 30KHz frequency domain for vibration analysis

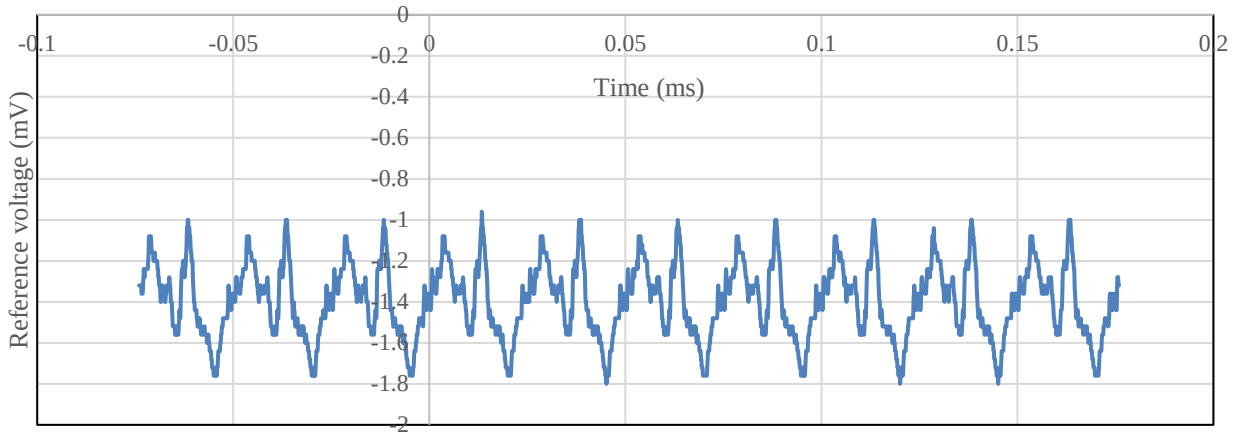

Figure 4.36: Ultrasound at 40KHz and maximum power setting (Transmitter)

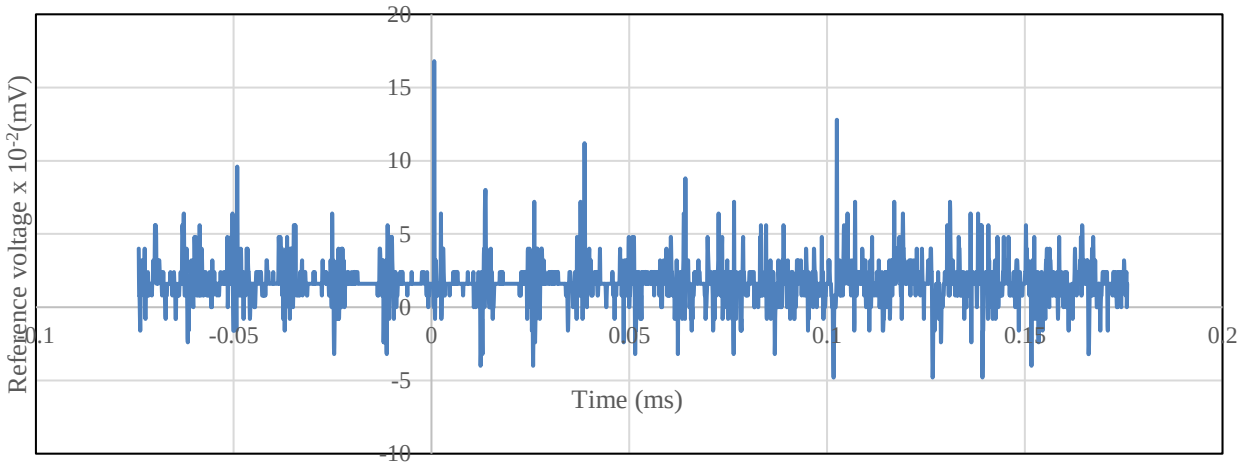

Figure 4.37: Ultrasound at 40KHz at maximum power setting (Receiver)

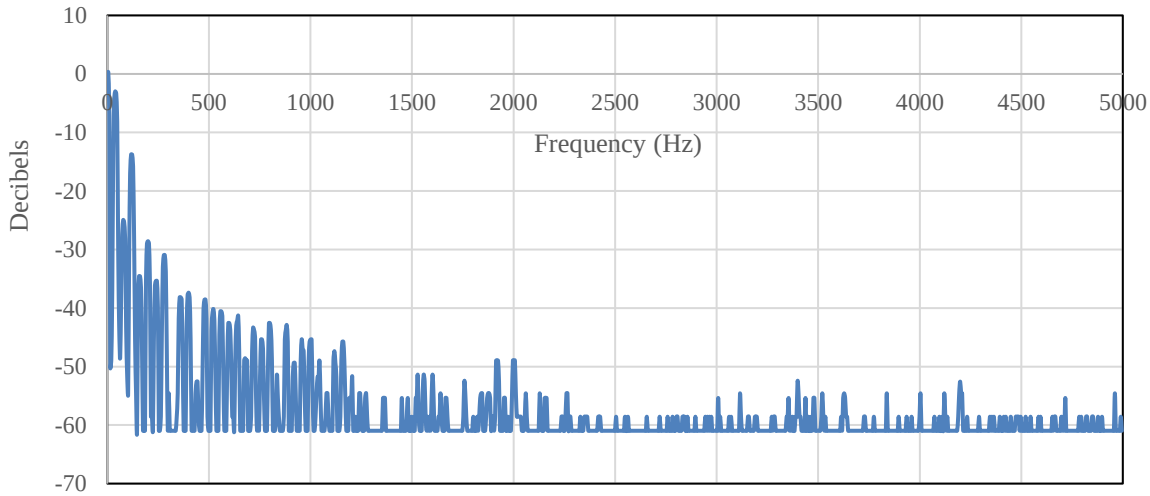

Figure 4.38: Fast Fourier Transform (FFT) showing spectral view of 40KHz frequency domain for vibration analysis

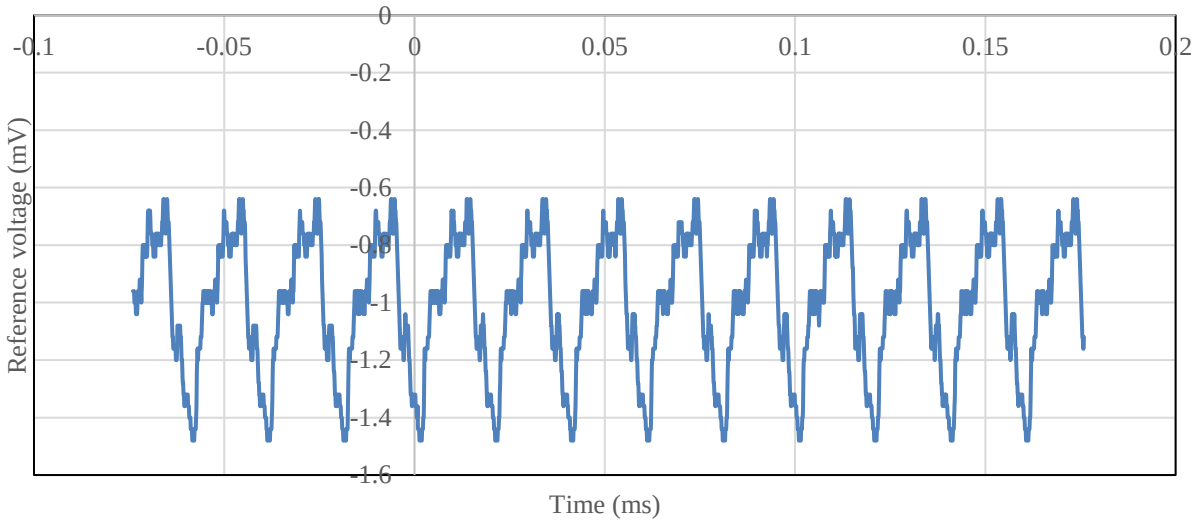

Figure 4.39: Ultrasound at 50KHz and maximum power setting (Transmitter)

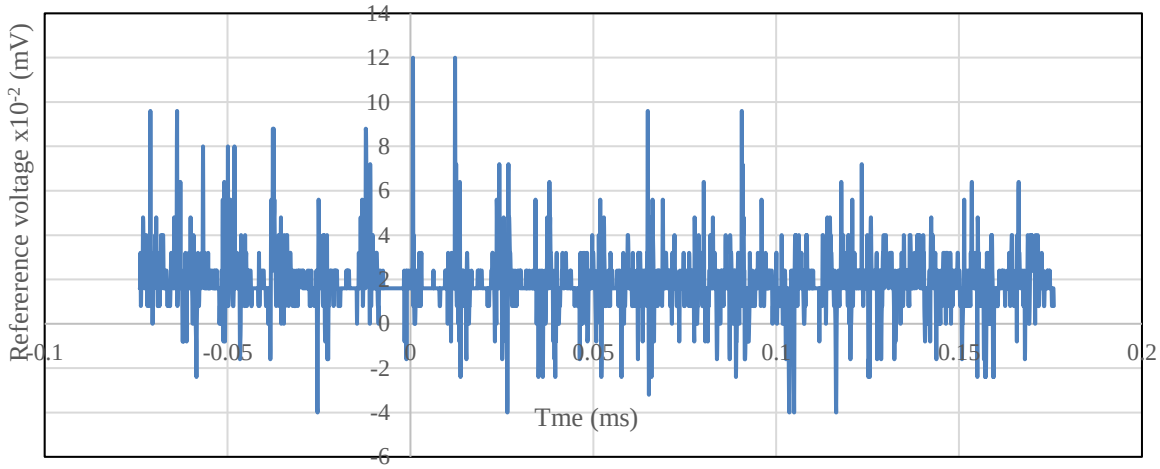

Figure 4.40: Ultrasound at 50KHz at maximum power setting (Receiver)

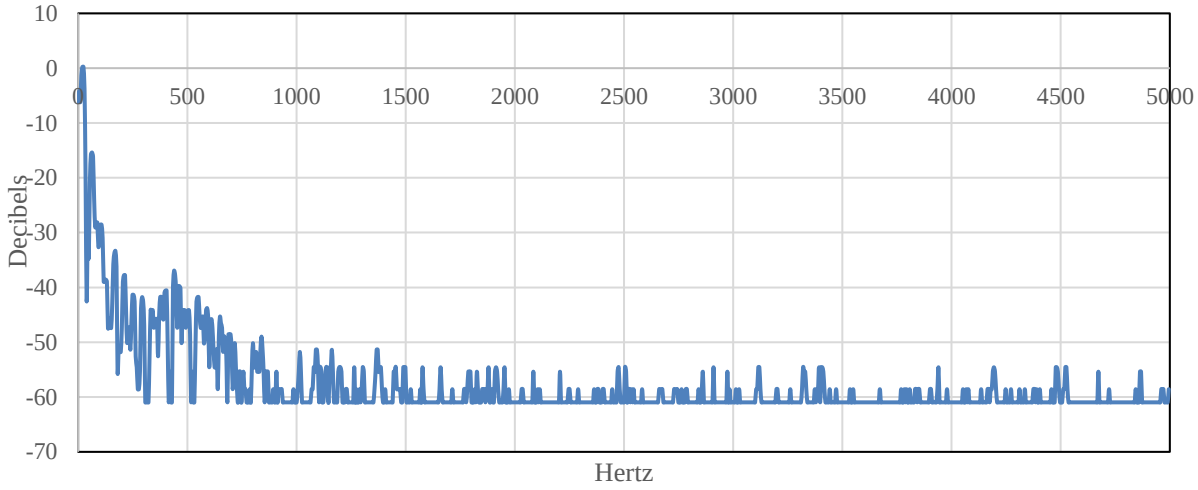

Figure 4.41: Fast Fourier Transform (FFT) showing spectral view of 40KHz frequency domain for vibration analysis

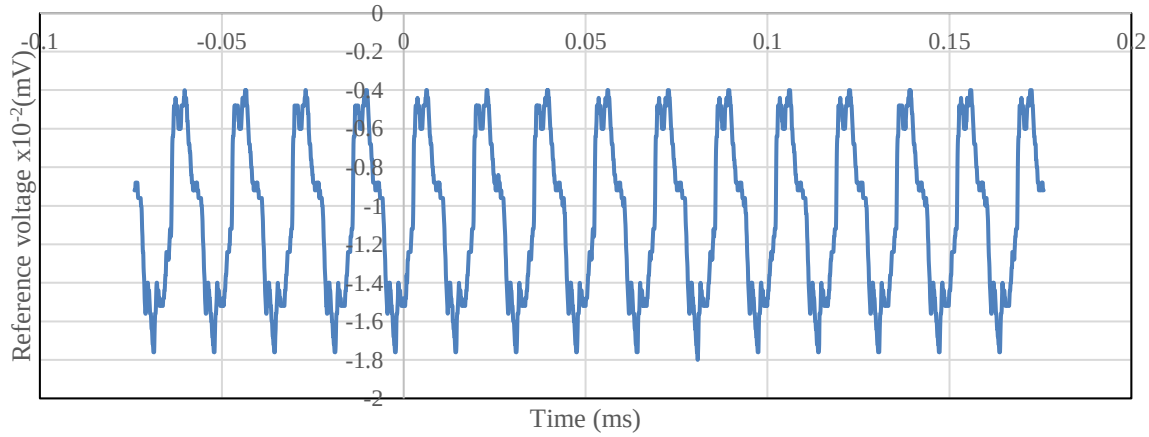

Figure 4.42: Ultrasound at 60KHz and maximum power setting (Transmitter)

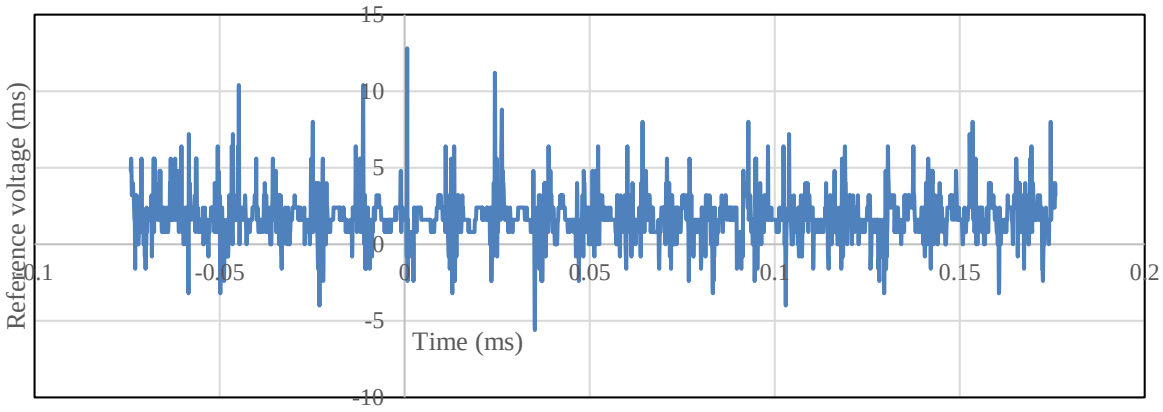

Figure 4.43: Ultrasound at 60KHz at maximum power setting (Receiver)

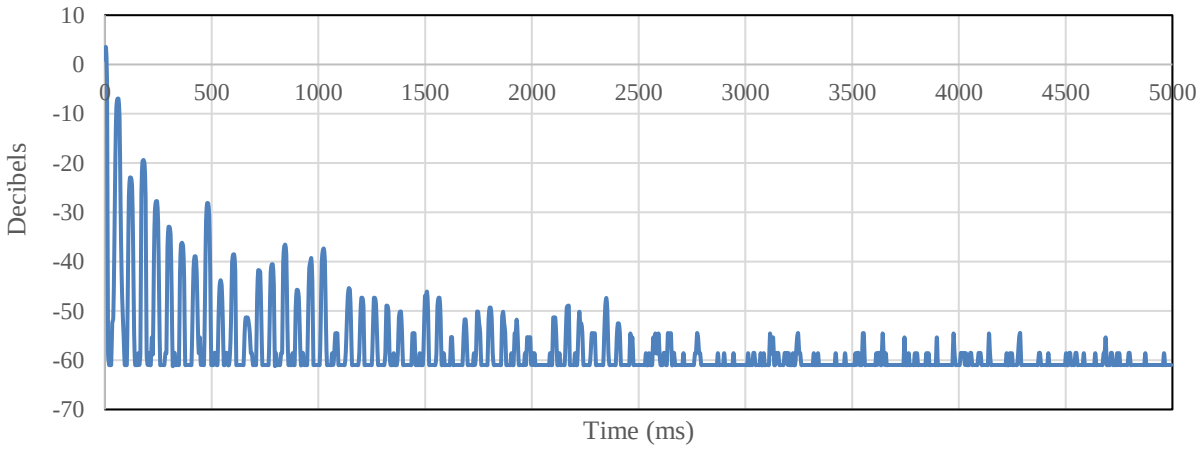

Figure 4.44: Fast Fourier Transform (FFT) showing spectral view of 60KHz frequency domain for vibration analysis

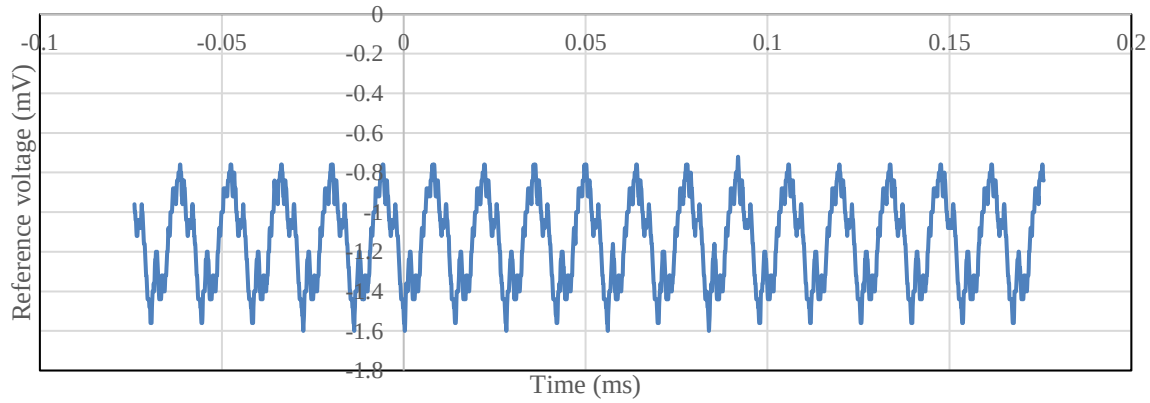

Figure 4.45: Ultrasound at 70KHz and maximum power setting (Transmitter)

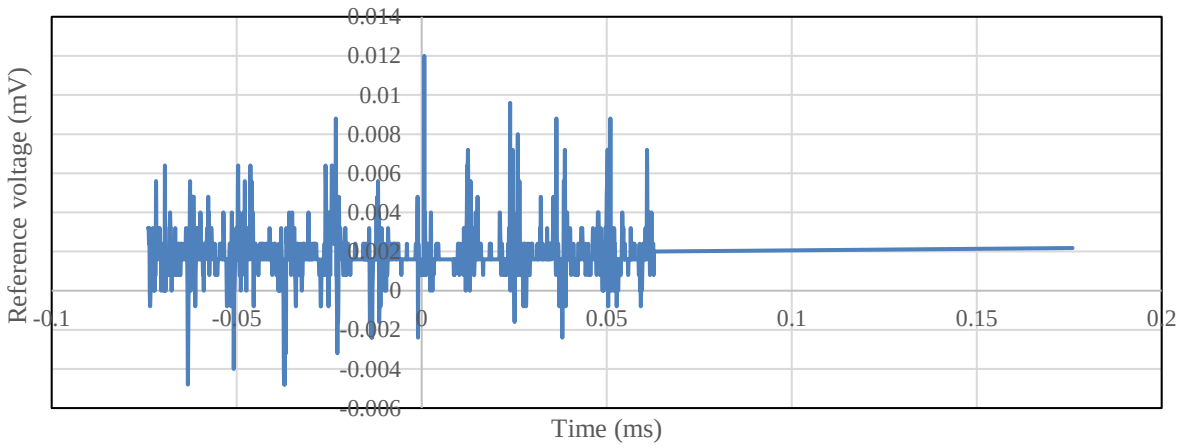

Figure 4.46: Ultrasound at 70KHz at maximum power setting (Receiver)

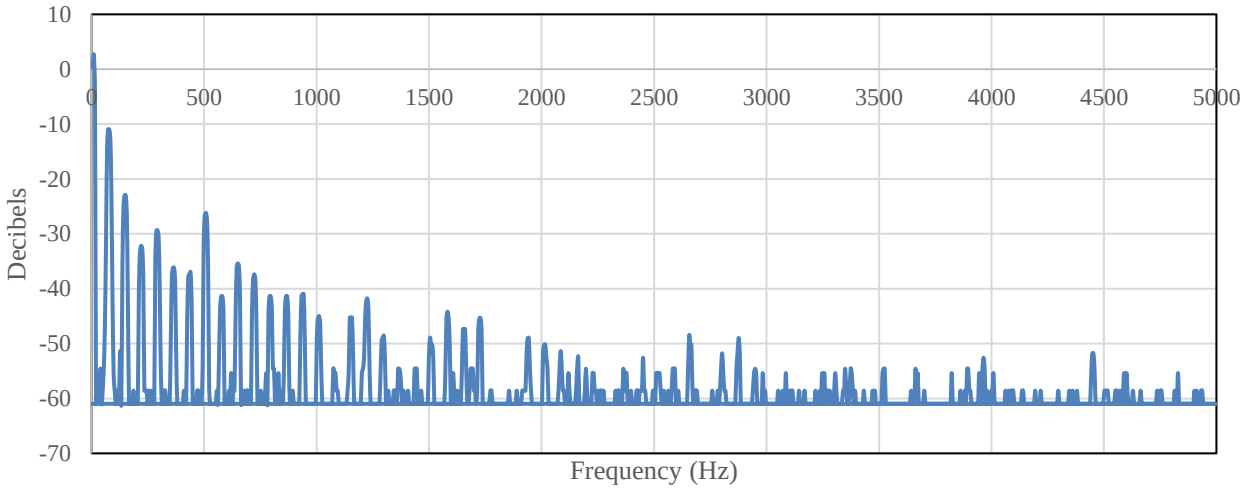

Figure 4.47: Fast Fourier Transform (FFT) showing spectral view of 70KHz frequency domain for vibration analysis

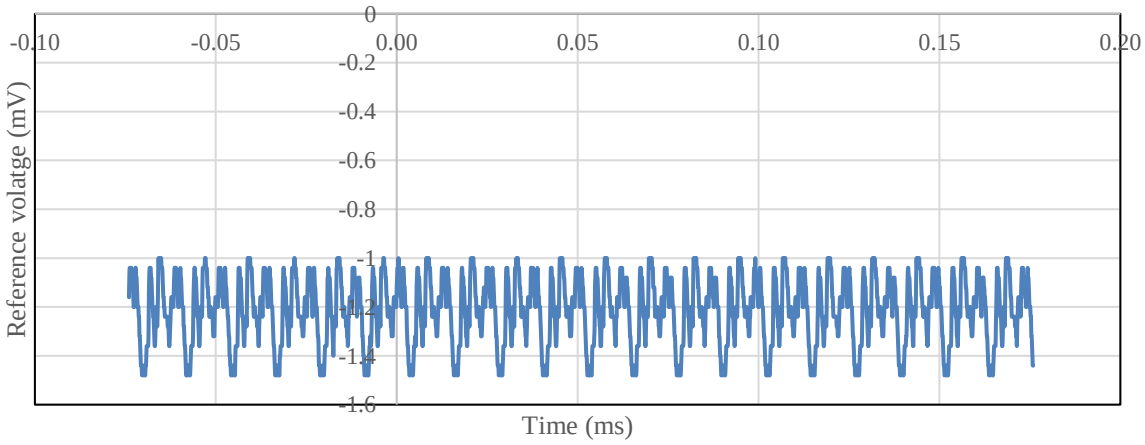

Figure 4.48: Ultrasound at 80KHz and maximum power setting (Transmitter)

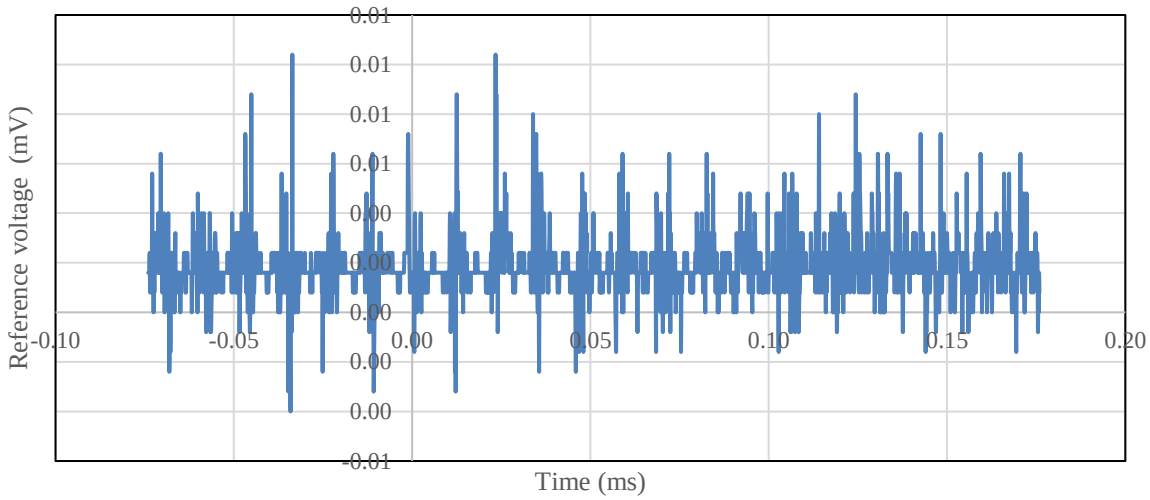

Figure 4.49: Ultrasound at 80KHz at maximum power setting (Receiver)

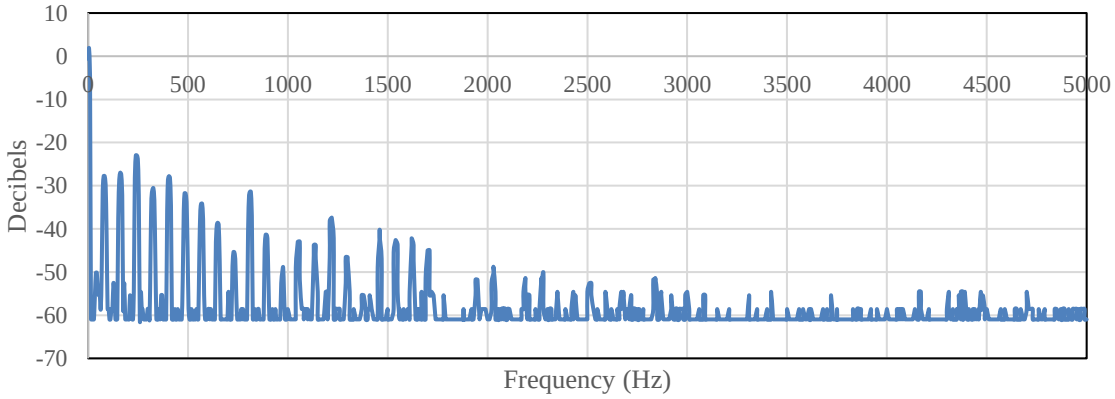

Figure 4.50: Fast Fourier Transform (FFT) showing spectral view of 80KHz frequency domain for vibration analysis

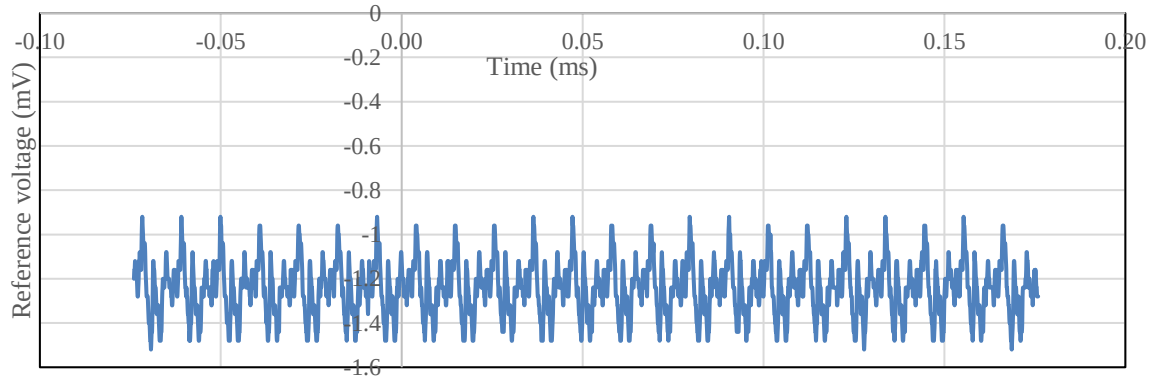

Figure 4.51: Ultrasound at 90KHz and maximum power setting (Transmitter)

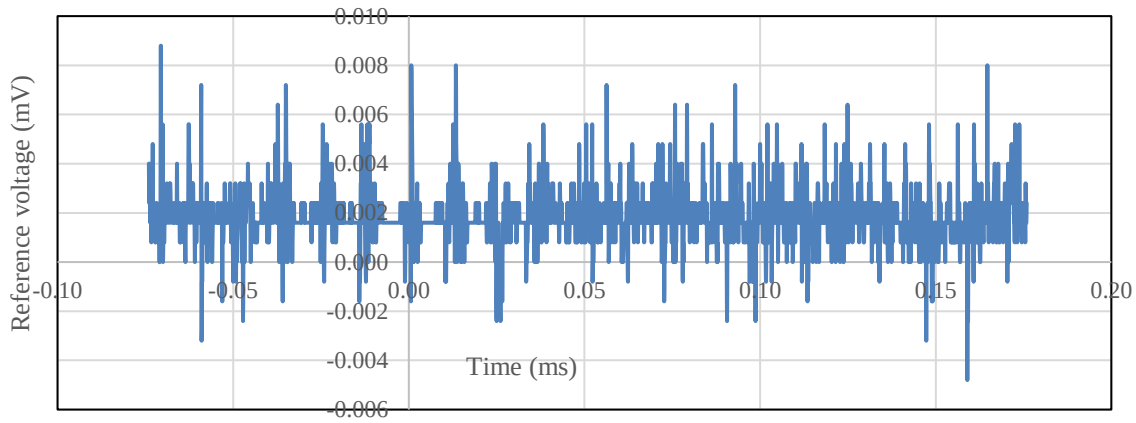

Figure 4.52: Ultrasound at 90KHz at maximum power setting (Receiver)

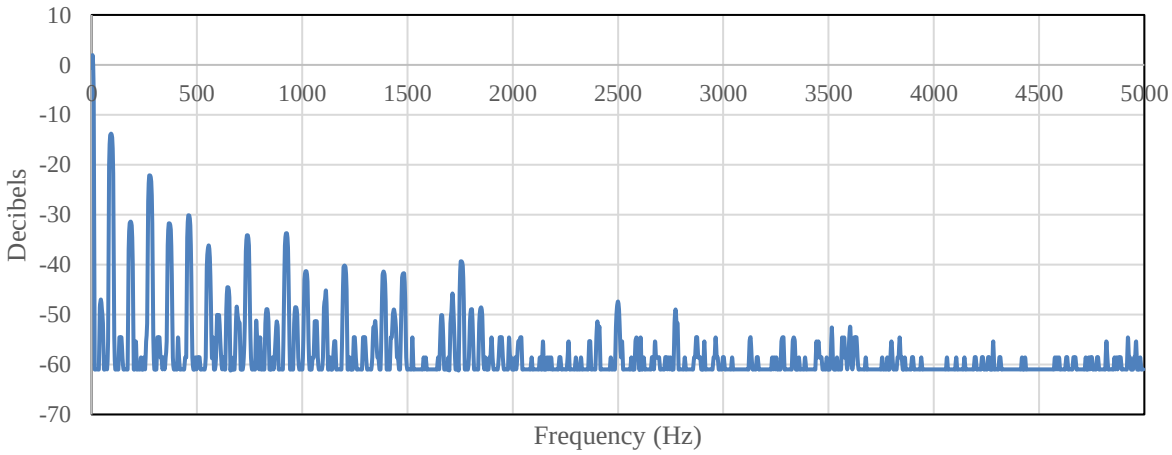

Figure 4.53: Fast Fourier Transform (FFT) showing Spectral view of 90KHz frequency domain for vibration analysis

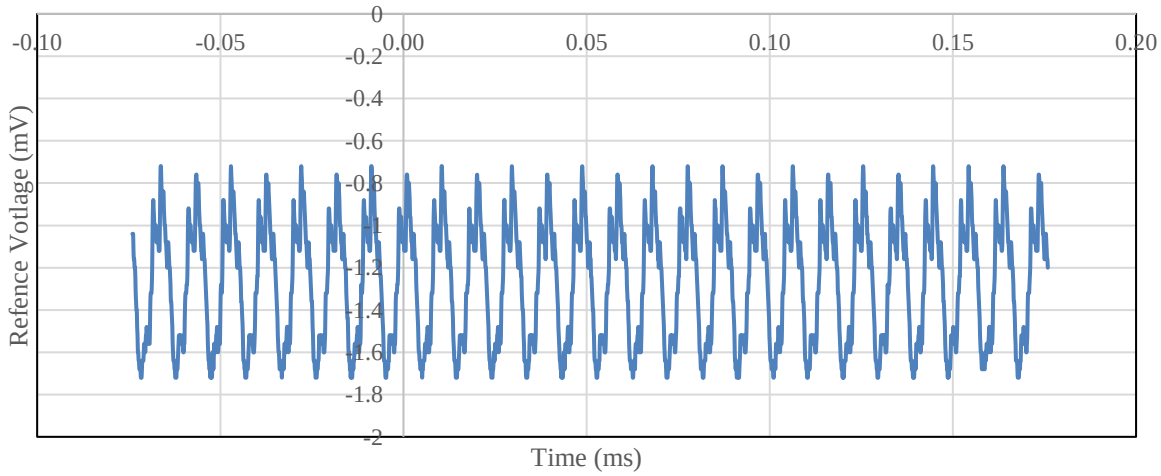

Figure 4.54: Ultrasound at 100KHz and maximum power setting (Transmitter)

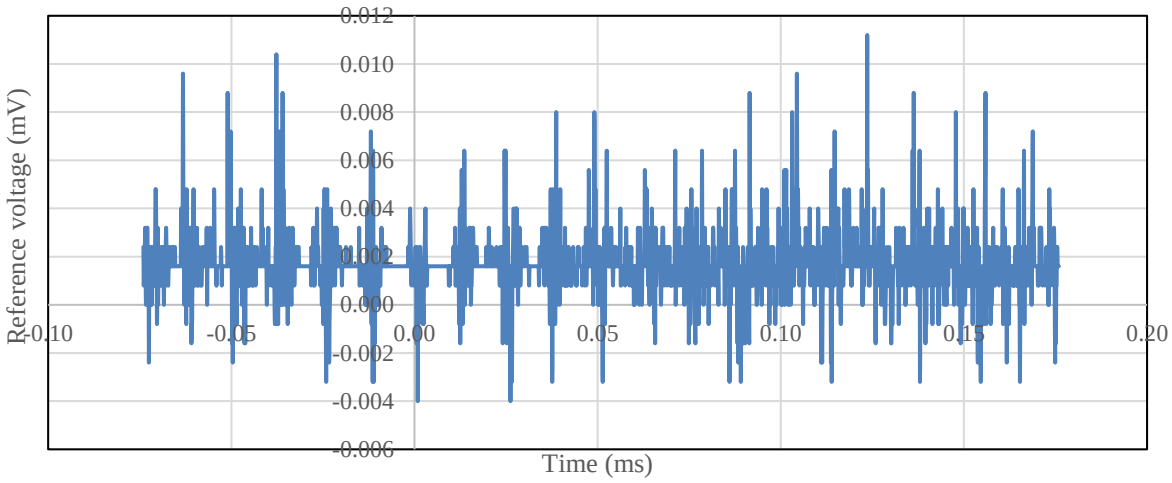

Figure 4.55: Ultrasound at 100KHz at maximum power setting (Receiver)

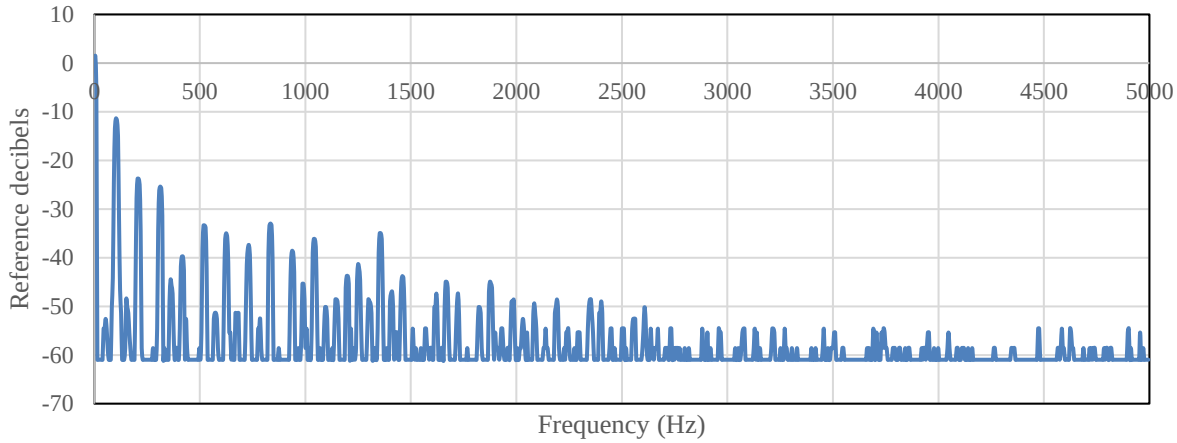

Figure 4.56: Fast Fourier Transform (FFT) showing spectral view of 100KHz frequency domain for vibration analysis

4.4.2 Ultrasound fluid displacement in of porous media

One of the major characteristics of acoustic waves is the mechanical energy transmitted which is dependent on wave amplitude. A high amplitude wave provides and transmits greater energy than a low amplitude wave of the same power. In this section, the power transmitted by the wave across the core samples is graphically presented in terms fluid displacement and ultrasound wave frequency.

In Figure 4.57, the highest fluid displacement is at the 20KHz frequency with a total of 29.5mL of fluid displaced and the lowest was at 100KHz with 27.5mL displaced over a period of 30minutes. The fluid injection rate was 2mL per minute. This further reaffirms the greater power of lower frequency waves to provide greater mechanical vibrations on reservoir cores. The difference of 2mL obtained in favour of 20KHz frequency might appear

small, but over a long period of oil production in a reservoir is significant. It is, in view of this, that subsequent coreflooding operations in this research were based on 20KHz frequency ultrasound waves, which is also the minimise the threshold for ultrasound waves, to maximise the recovery process.

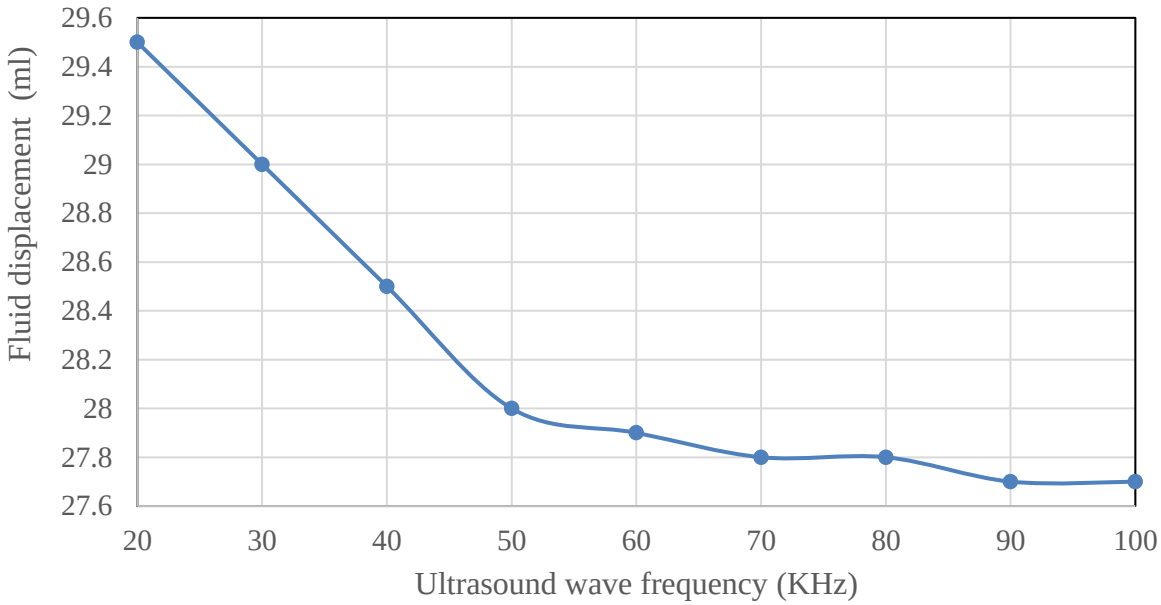

Figure 4.57: Fluid displacement versus ultrasound wave frequency over a period of 30minutes from one-inch diameter by two-inch core sample

4.4.3 Pressure differential during Core flooding

Pressure drop (differential pressure) across the core sample is the difference between the inlet pressure and the outlet (exit) pressure of injected fluid as it passes through tortuous pores of the core sample. It usually varies depending on the viscosity of the injected fluid, the rock's permeability and the fluid flow rate. Accordingly, the larger the pressure drop across a core sample the greater the resistance to fluid flow and vice versa. In this section, the pressure drop behaviours of the injected fluids in the core sample of Berea upper sandstone, Berea lower sandstone, Guleph dolomite carbonate, Silurian dolomite, Edward brown and Indiana are graphically illustrated and discussed.

The differential pressure (dP) profile graphs presented in this section are in accordance to natural petroleum reservoir creation (formation) and development and subsequent production. In this regard, the first stage was the saturation of the reservoir with water, followed by the displacement of water by oil to occupy the space of water in the pores generating a water wet reservoir. The next stage was water flooding to displace the oil in the

reservoir until most of the oil in place had been recovered. The enhanced oil recovery stage was the application of polymer flooding and ultrasound to displace the residual oil and produce more oil. Horizontal and vertical displacement scenarios were conducted to determine the impact gravity drainage on the performance of integrated ultrasound and polymer flooding

4.4.3.1 Horizontal displacement

The acoustic core holder was stationed in the horizontal position. Figure 4.58, Figure 4.59, Figure 4.60, Figure 4.61, Figure 4.62 and Figure 4.63 illustrate the differentials pressures of Berea upper sandstone, Berea Lower sandstone, Guleph dolomite, Silurian dolomite, Edward brown and Indiana limestone during flooding operation respectively. These fluid flow behaviours and patterns plotted at the point of breakthrough can be seen to vary across the core samples.

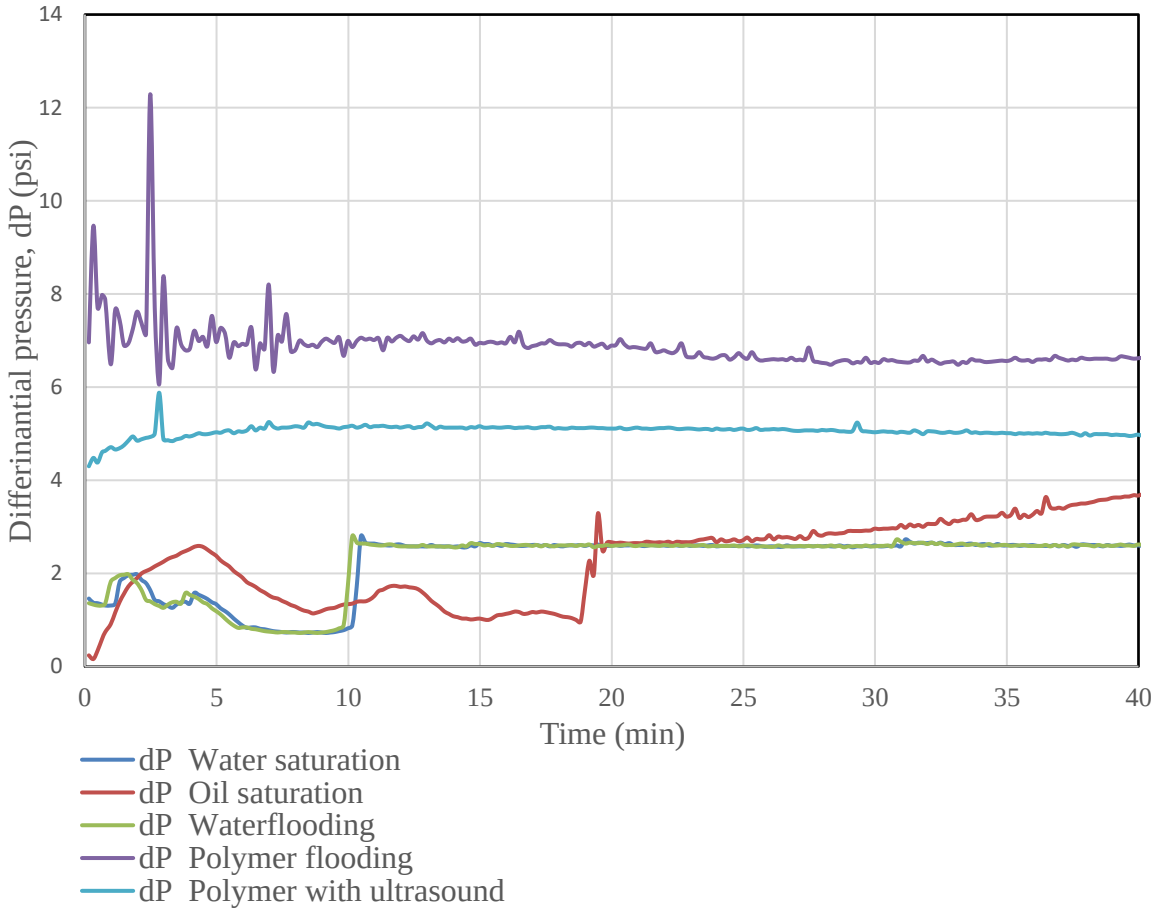

Figure 4.58 Differential pressure in Berea upper sandstone during flooding for horizontal displacement

In Figure 4.58, the differential pressure, dP curves for water saturation and water flooding are unstable prior to breakthrough but stabilise once breakthrough is attained. The water saturation and water flooding curves are relatively the same. The dPs profiles for polymer flooding and polymer with ultrasound across the Berea upper sandstone are also similar. However, it is evident that pressure differential is lowered when ultrasound is introduced. This can be attributed to decreased oil viscosity from the mechanical wave vibration of ultrasound resulting in decrease in flow resistance. Hence, increase in flow is observed.

The characteristic behaviour of the differential pressure across a Berea lower sandstone core sample is illustrated in Figure 4.59. Here, in the first five minutes leading to breakthrough all the pressure curves show instability with exception of the oil saturation curve. The spike in the polymer flooding curve is attributed to the pressure build-up from polymer stripping and penetration into the tortuous pores of the Berea lower sandstone. Once, penetration reaches the breakthrough point, the pressure steadily remains stable. The breakthrough is observed about 7 minutes as fluid is injected.

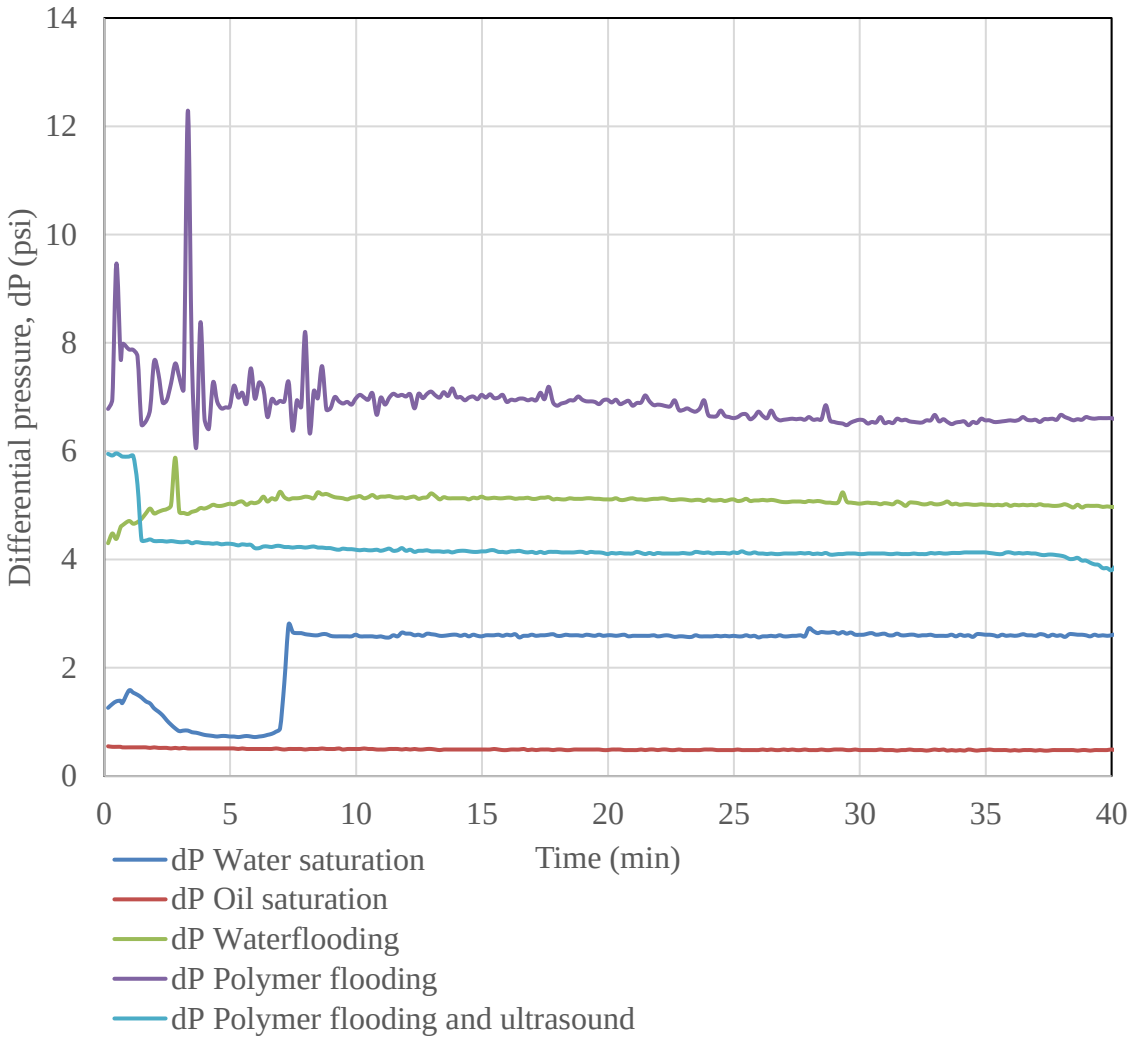

Figure 4.59: Differential pressure in Berea Lower sandstone during flooding for horizontal displacement

In Figure 4.60 the pressure differential across the Guelph dolomite core reaches up to 1,800 psi. The high pressures are associated with the tight and low permeability of the Guelph dolomite formation. Comparing the Guelph dolomite differential pressures with Berea sandstone differential pressure values, it is evident that the pressures of Berea with highest peak of 12psi is quite small in relation to Guelph with 1800psi. The breakthrough took longer for fluid injection. Average breakthrough was seen at 20 to 25 minutes. The pump (injection) pressure had to rise to adequate level to be able to penetrate the micropores of the core sample. A steep rise in differential pressure is attributed to tight pores and constrictions encountered during injection. These tight pores could widen with continuous fluid injection as small sediments are pushed through the pore channels. Subsequently, additional injections would be smoother and the curve more linear as seen in the curve for polymer flooding, oil saturation, and polymer with ultrasound.

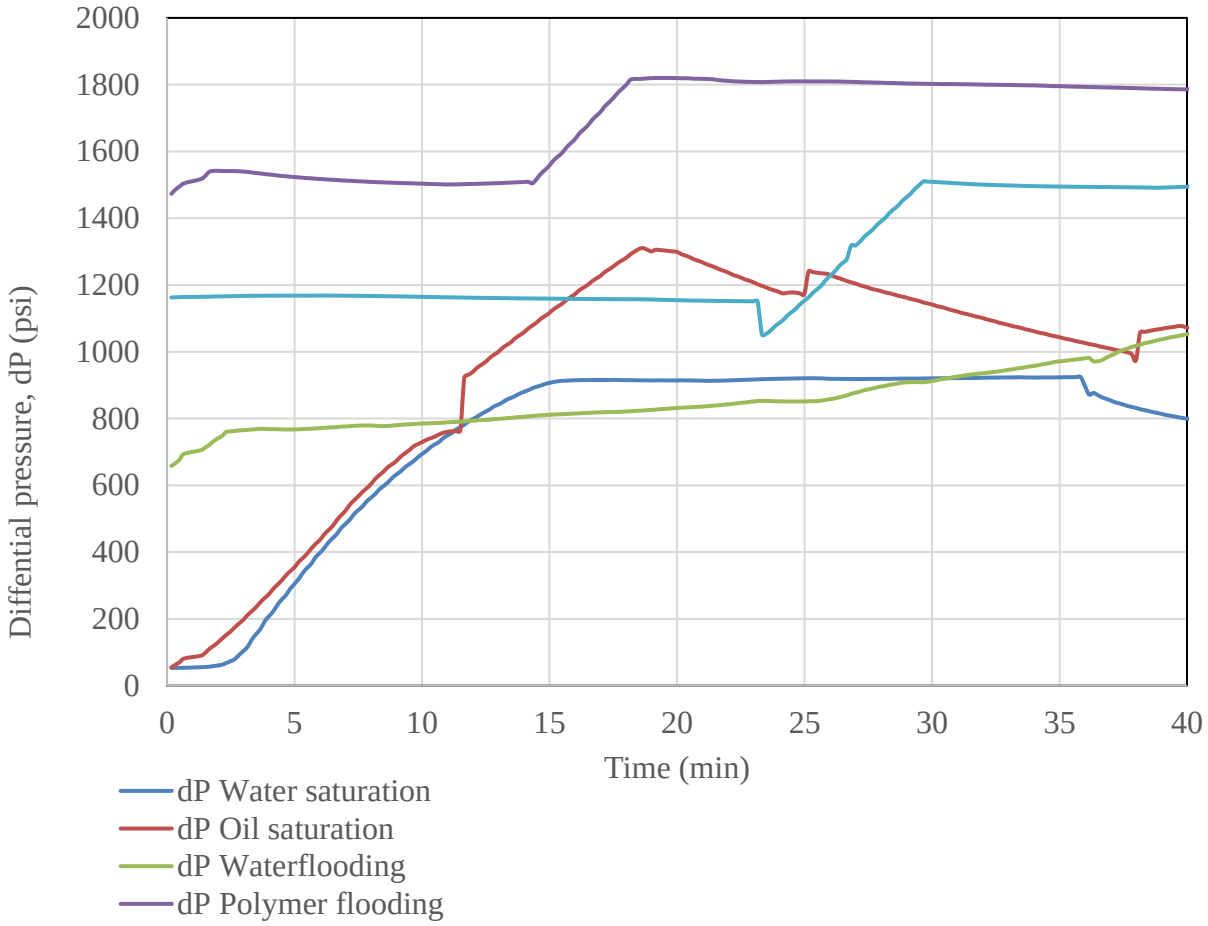

Figure 4.60: Differential pressure in Guelph dolomite during flooding for horizontal displacement

In Figure 4.61 the differential pressures (dP) for Silurian dolomite fluctuates with steep and low points. The dP values are high. This is a characteristic of tight reservoirs. The breakthrough occurs from 25 to 35 minutes of fluid injection depending upon the flooding operation being conducted. The maximum differential pressure was at 1,850psi observed during polymer flooding. Evidently, the application of ultrasound to polymer flooding lowered the pressure differential profile.

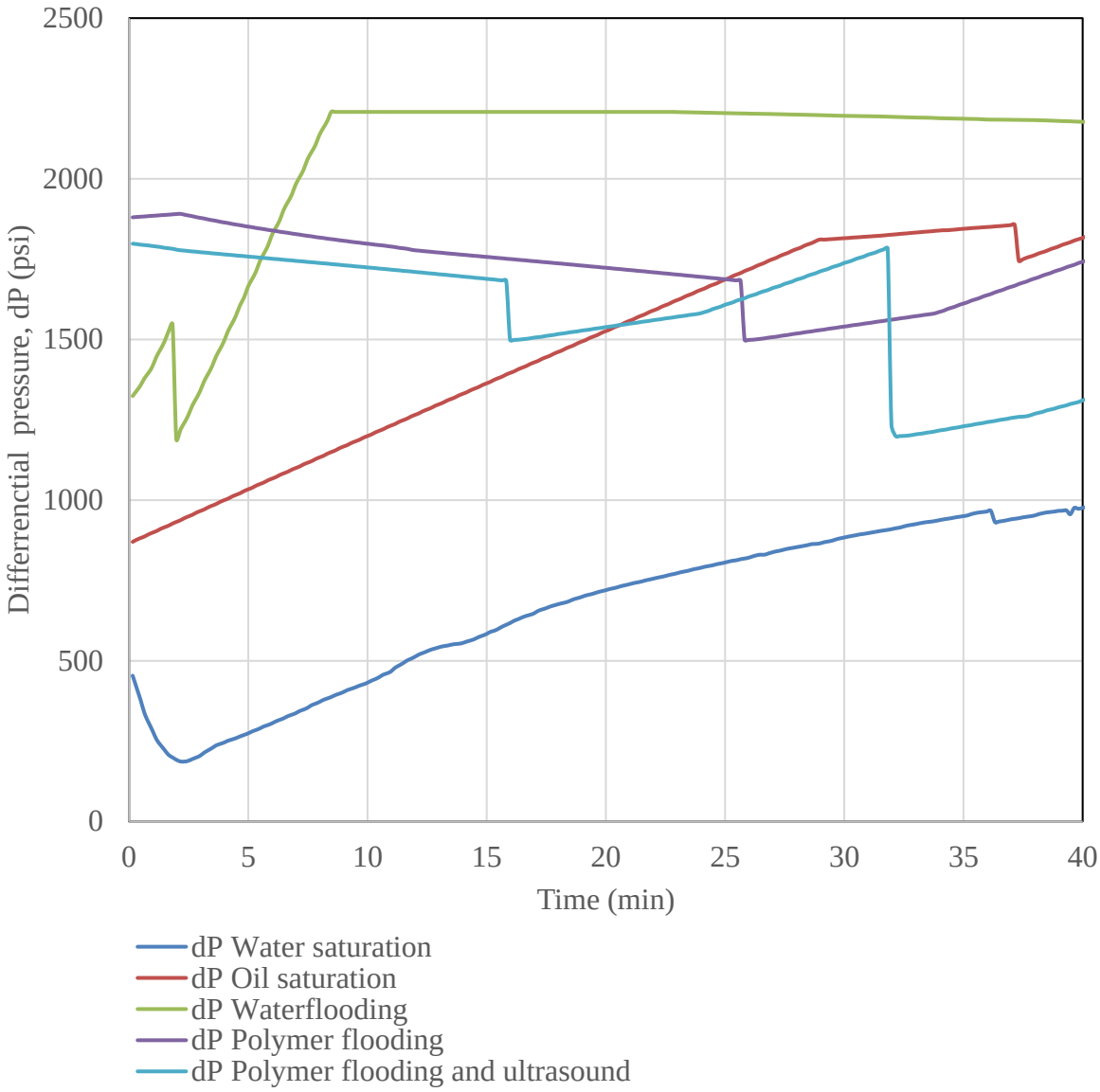

Figure 4.61: Differential pressure in Silurian dolomite during flooding for horizontal displacement

In Figure 4.62 the differential pressures of Indiana limestone are unique but share some common characteristics with previous coreflooding pressure differentials. The major similarity is the lowering of the dPs of polymer flooding when ultrasound is applied. This is a consistent trend. The differential pressures attained a maximum at 330 psi. The oil saturation differential pressure curve has multiple peaks. This is a characteristic of flow through tortuous micropores of Indiana limestone.

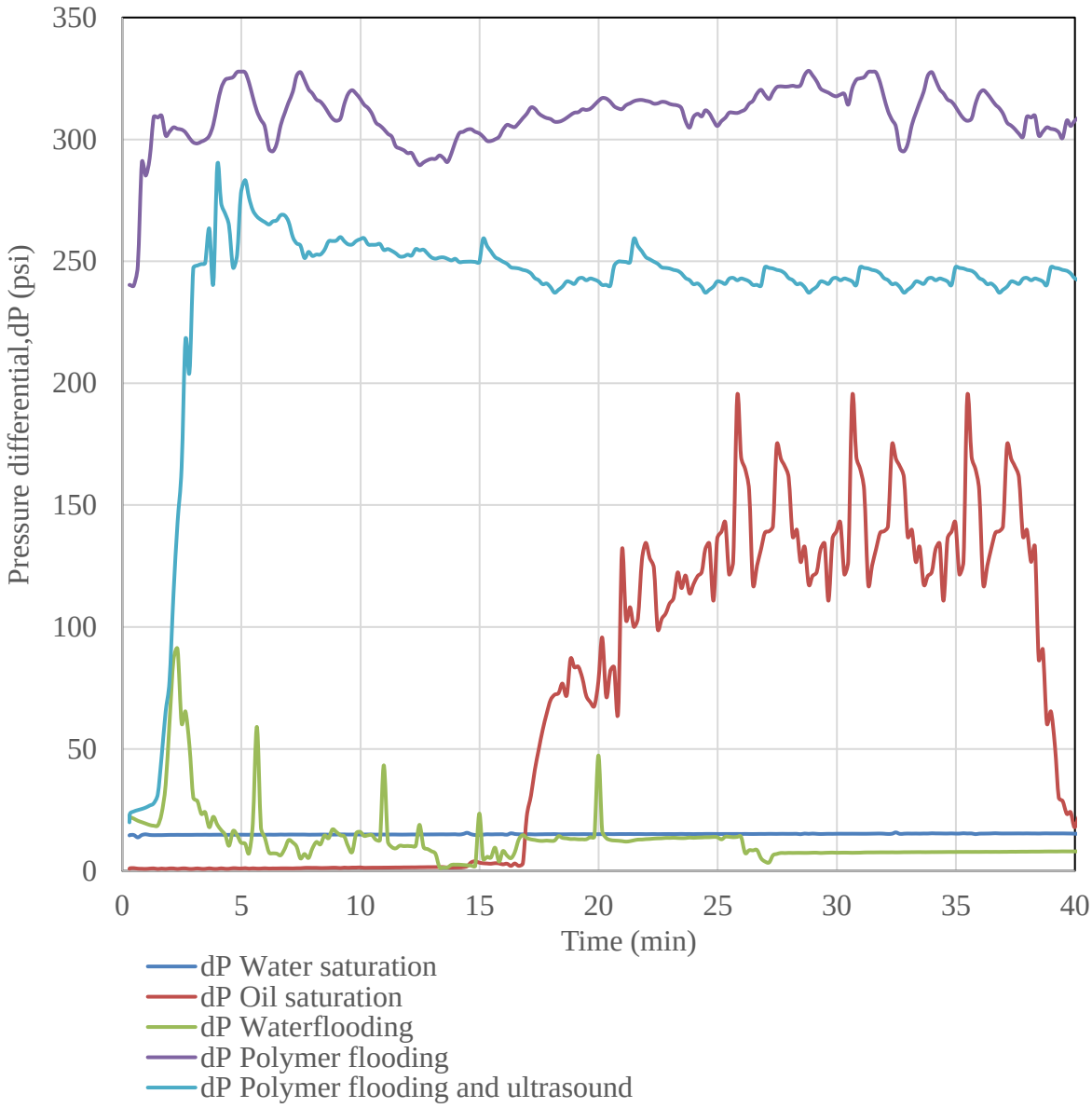

Figure 4.62: Differential pressure in Indiana Limestone during flooding for horizontal displacement

In Figure 4.63 the differential pressure curve for Edward brown limestone ranged within 100 to 800psi except the oil saturation curve which apparently rises steeply to 800psi and declines to 88psi almost instantly. In the first 7 minutes the oil and saturation curves were highly unstable, but afterwards rose and linearised respectively.

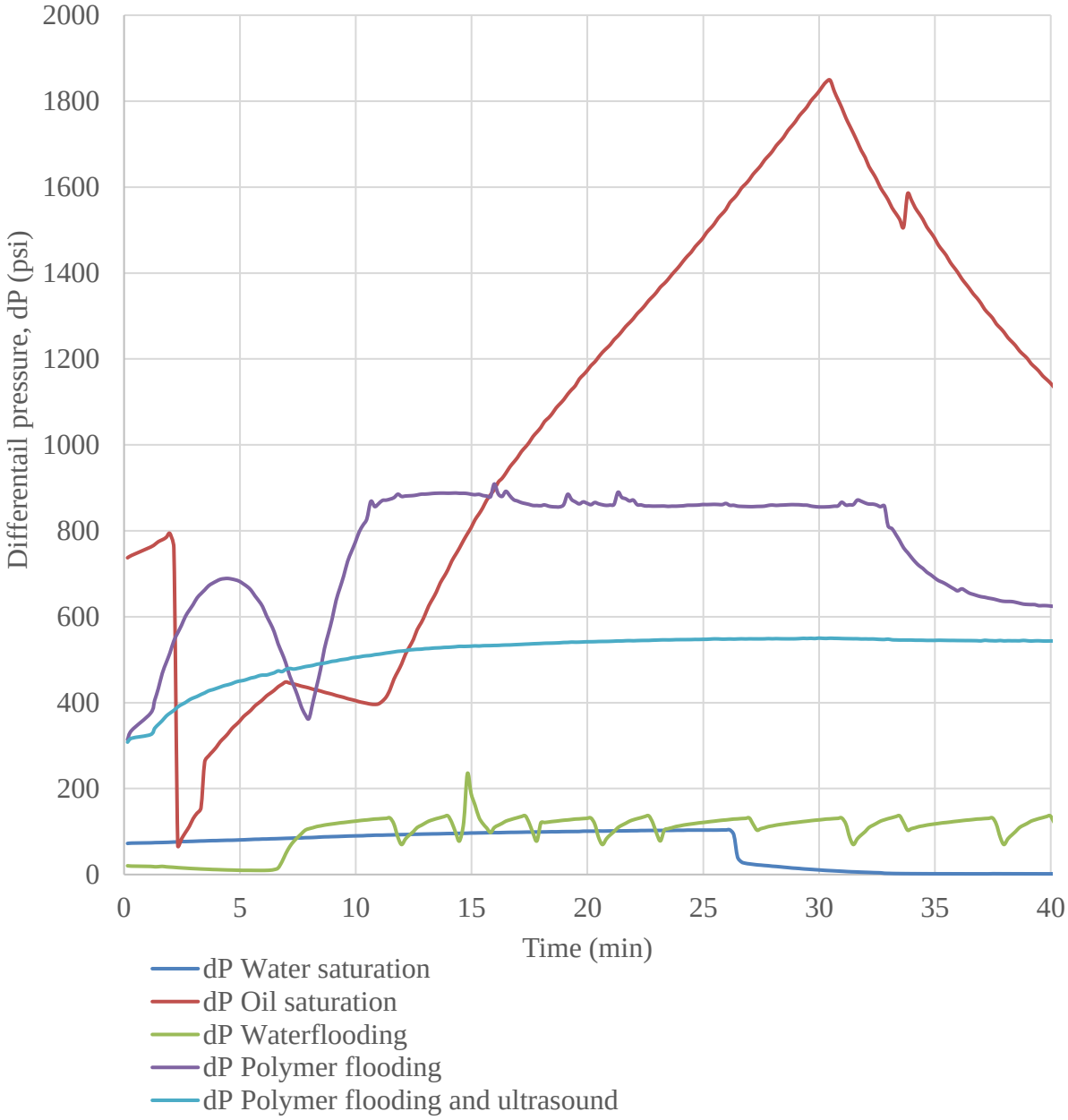

Figure.4.63: Edwards brown limestone differential pressure during flooding for horizontal displacement

4.4.3.2 Vertical displacement

With the acoustic core holder firmly fixed in the vertical position, core saturation and flooding were carried out. In Figure 4.64, Figure 4.65, Figure 4.66, Figure 4.67, Figure 4.68 and Figure 4.69 the differentials pressures (dP) graphs for Berea upper sandstone, Berea

Lower sandstone, Guleph dolomite, Silurian dolomite, Edward brown and Indiana limestone during vertical flooding operation are shown respectively.

In Figure 4.64, the water and oil saturation differential pressure curves are lowest (5 to 80psi). The implication of this is that the rock exhibits unsteady state in the first 10mins and last 10minutes of injection. But within a period of 20minutes exhibits steady state flow. The differential pressure curve of polymer flooding and polymer with ultrasound rose up to 240psi. This was attributed to reduced flow and high pressure build up during polymer injection.

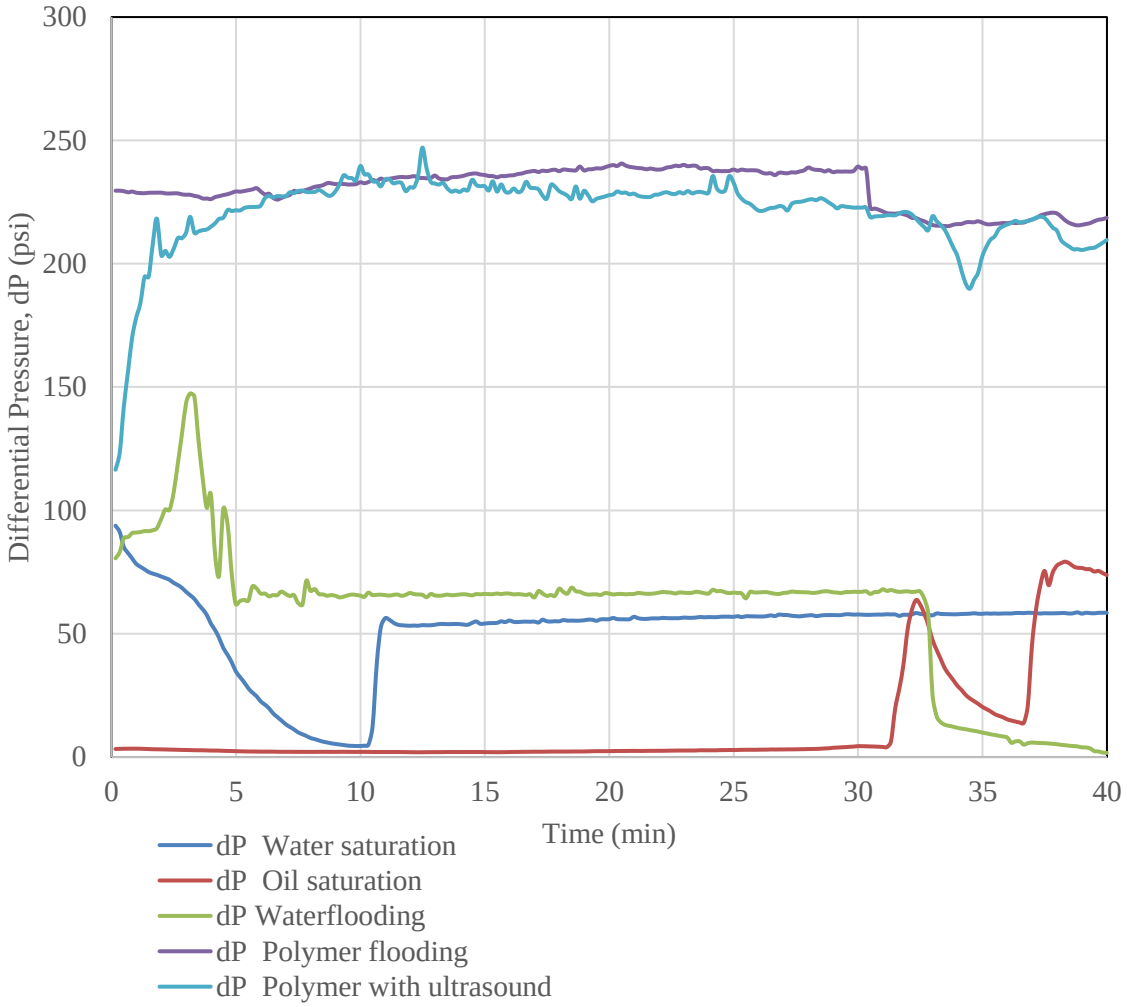

Figure 4.64: Berea Upper sandstone differential pressure during flooding for vertical displacement

However, the differential pressure curves of polymer flooding were lowered when ultrasound was applied. This further reaffirms the ability of ultrasound to increase fluid flow potentials in the reservoir.

The differential pressure of the Berea lower sandstone, in Figure 4.65, peaks to 2300psi for water saturation. This clearly indicates that there is tremendous resistance to flow and low permeability to water of the Berea lower sandstone. Though the pressure differential curve for all subsequent floods were much lower than 2300psi, one significant observation was the steep reduction of the differential pressure of injected polymer when ultrasound was applied from 700psi to 40 psi over a period of 40minutes.

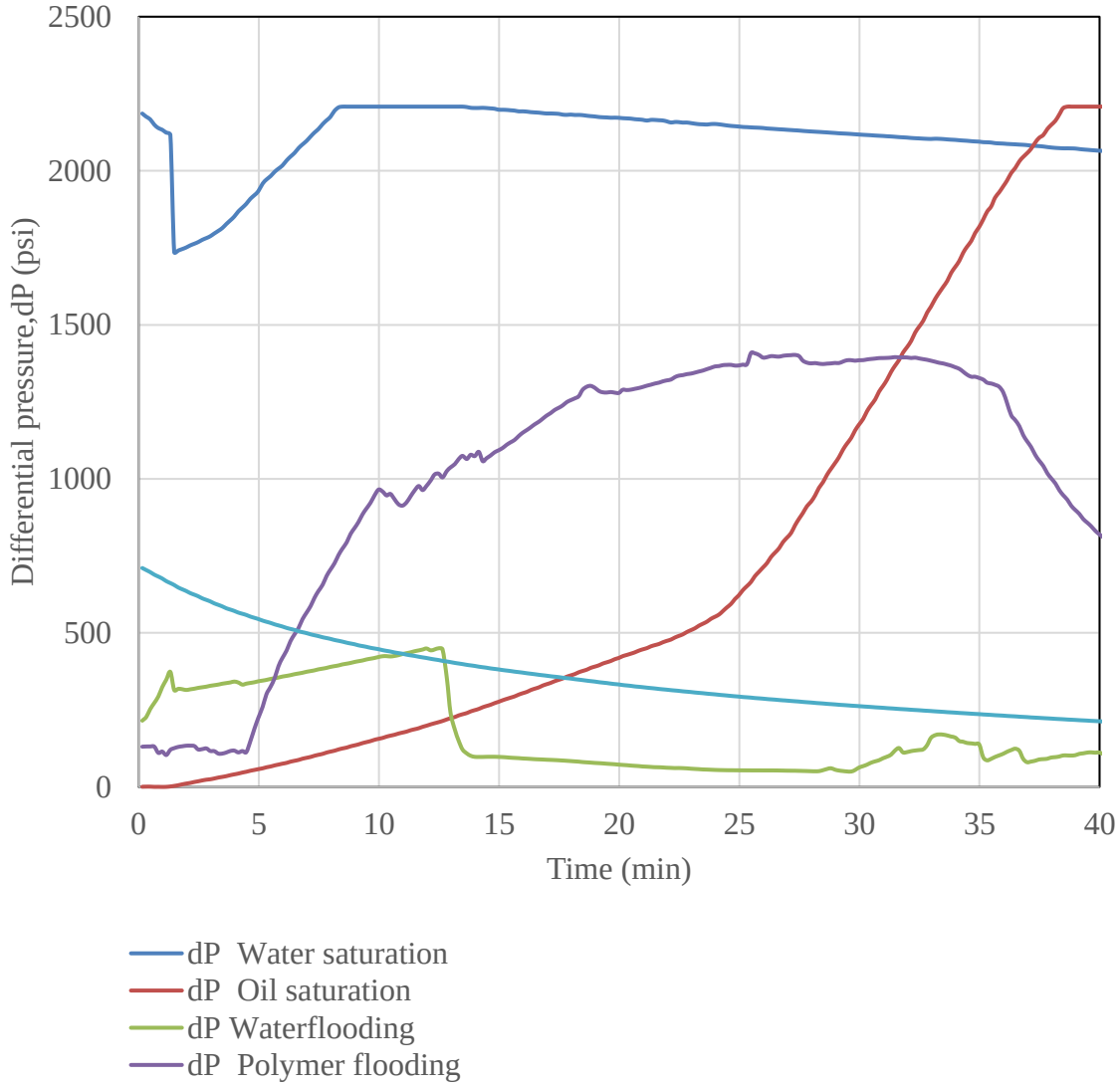

Figure 4.65: Berea Lower sandstone differential pressure during flooding for vertical displacement

As mentioned earlier, one of the characteristics of resistance to fluid flow in a reservoir rock is high differential pressure. When the curves are steep, similar to the Guelph graph in Figure 4.66, it implies that injections be stopped to allow the pressure to reduce below 2400 psi. Here, like previous similar trends the water saturation pressure differential peaks curves are

greater than the peaks for oil saturation. This implies that the permeability to water is lower than permeability to oil. The low permeability to water was attributed to water lining the reservoir rock pore surfaces and enabling ease of micropore penetration. The lowering of the polymer flooding differential pressure by the introduction of ultrasound was also observed in the Guelph oil recovery operation.

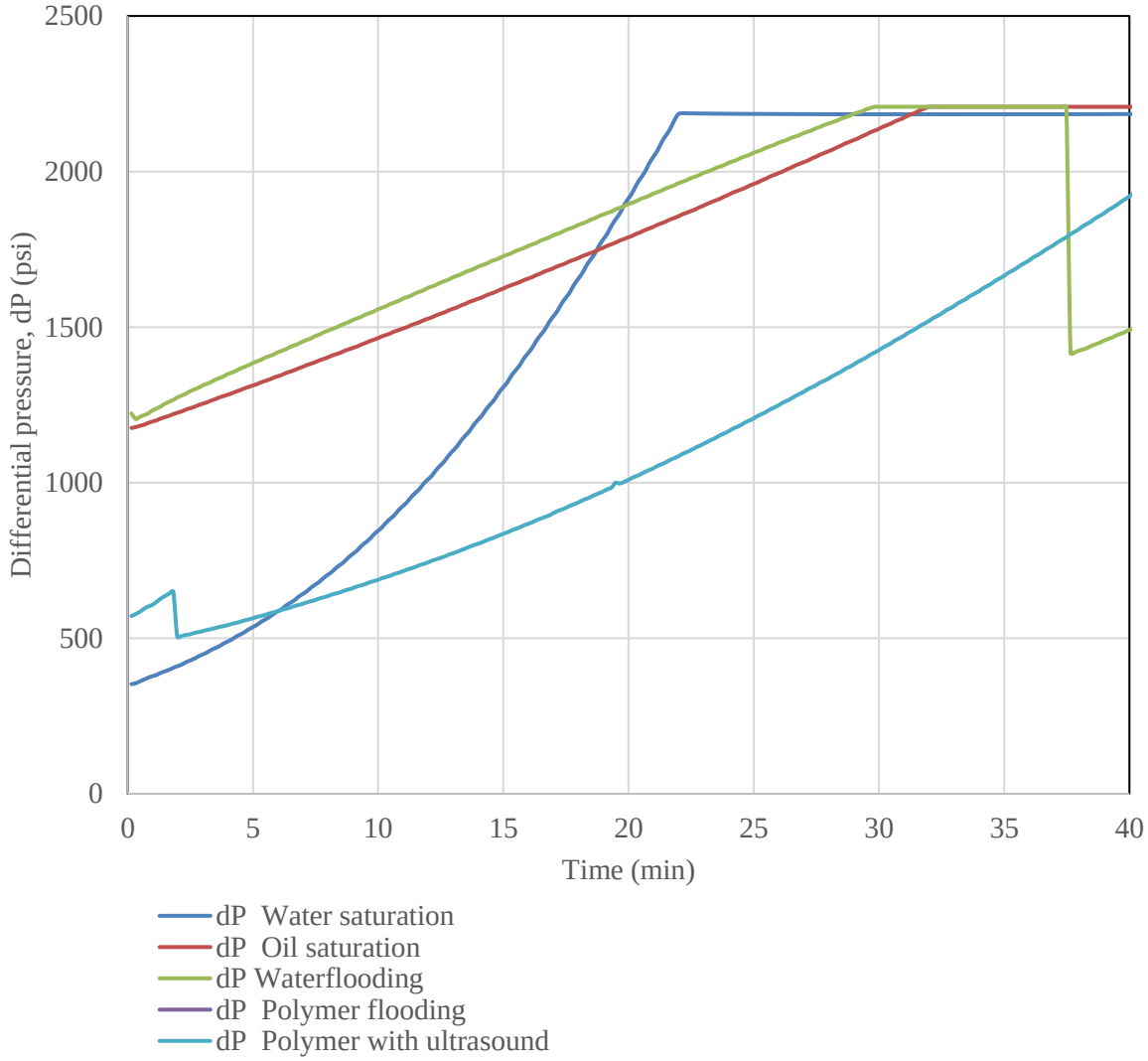

Figure 4.66: Guleph differential pressure during flooding for vertical displacement

Silurian dolomite is another tight reservoir rock with low permeability given the high values of differential pressures with peaks up to 2200psi during vertical oil displacement. The permeability to oil, during the saturation period, is much lower than during water saturation. Silurian dolomite has high tendency to have regions with large pores followed by smaller pores creating constrictions. This scenario leads to uneven pressure fluctuations in the

reservoir rock. The general trend observed in previous applications of polymer flooding with ultrasound are also evident in Figure 4.67. The differential pressures of polymer flooding were high (1700 to 2200psi) while polymer with ultrasound were slightly lower (230 to 1940 psi). This clearly indicates the ability of ultrasound to increase fluid flow by reducing the resistance to flow. The outcome observed was increased oil recovery.

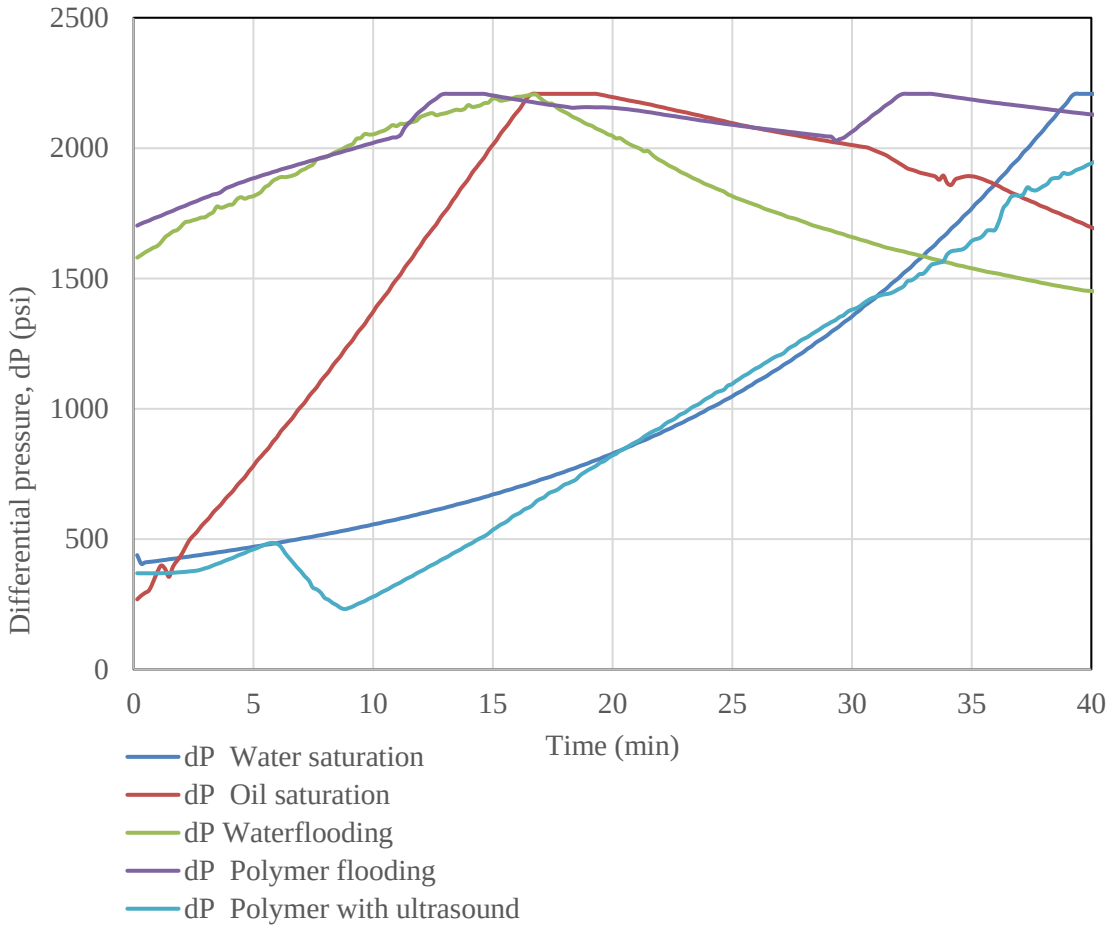

Figure 4.67: Silurian dolomite differential pressure during flooding for vertical displacement

The differential pressures of Indian limestone, shown in Figure 4.68, illustrates high pressures up 2200psi. The low permeability to water during the water saturation was attributed to the pore surface geometry and structure. The least differential pressure for water saturation was 1420psi whereas oil saturation had least differential pressure of 70psi and maximum pressure differential of 2190 psi. All differential pressures of polymer with

ultrasound were lower than the corresponding differentials pressures of polymer flooding alone.

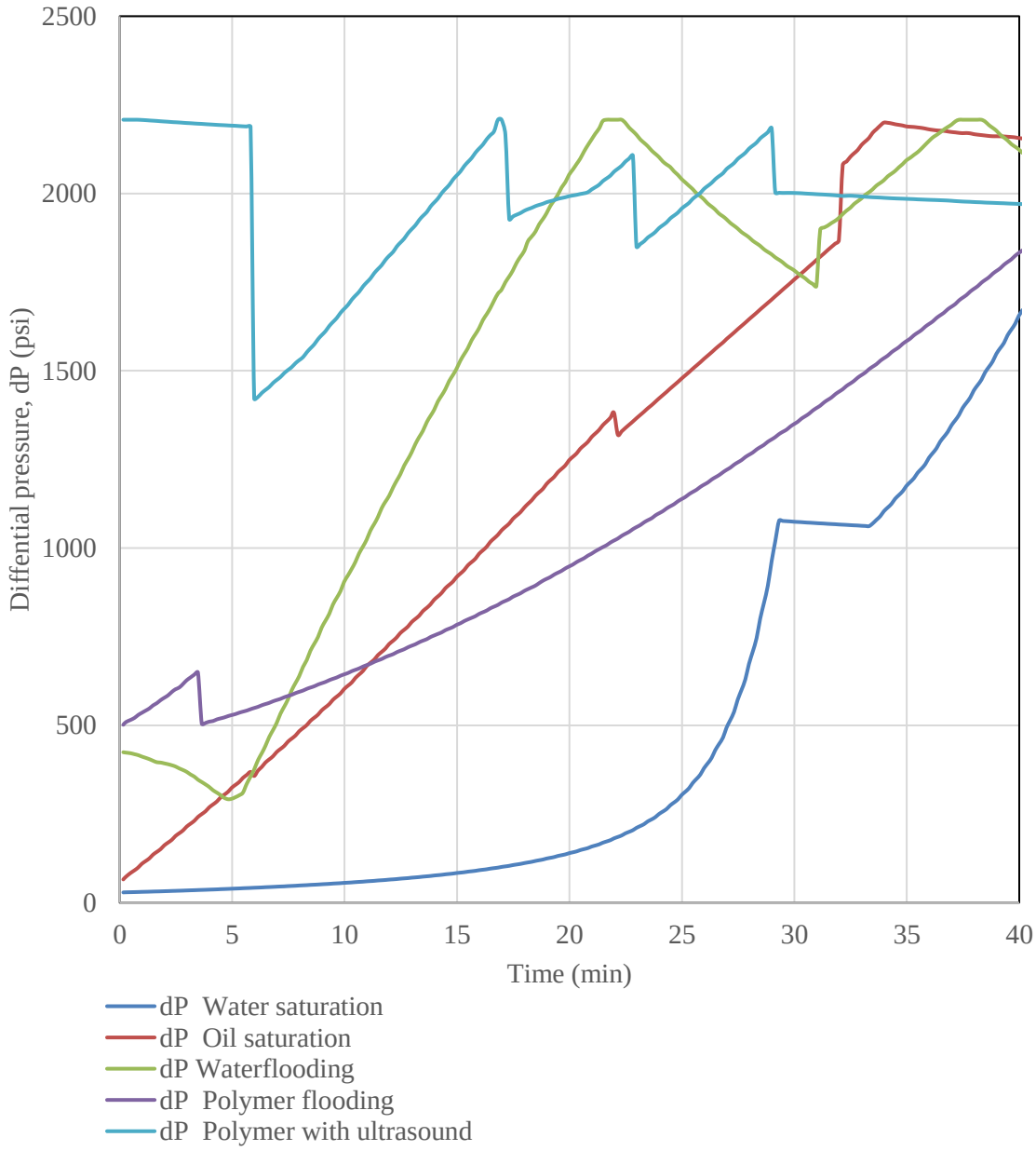

Figure 4.68: Indiana differential pressure during flooding for vertical displacement

In Figure 4.69, Edward brown core sample rock underwent failure after the first 10 minutes of water flooding. This is similar to reservoir formation damage. The polymer flooding and polymer with ultrasound stages were not attained due to collapse of the core sample. In the 11th minutes of injection, the pressure differential instantly dropped to -2240psi. The overburden pressure was maintained at 500psi higher than the UCS of Edward brown rock. The collapse was attributed to wash out and loose grains of Edward brown as well as the low compaction and consolidation of the rock.

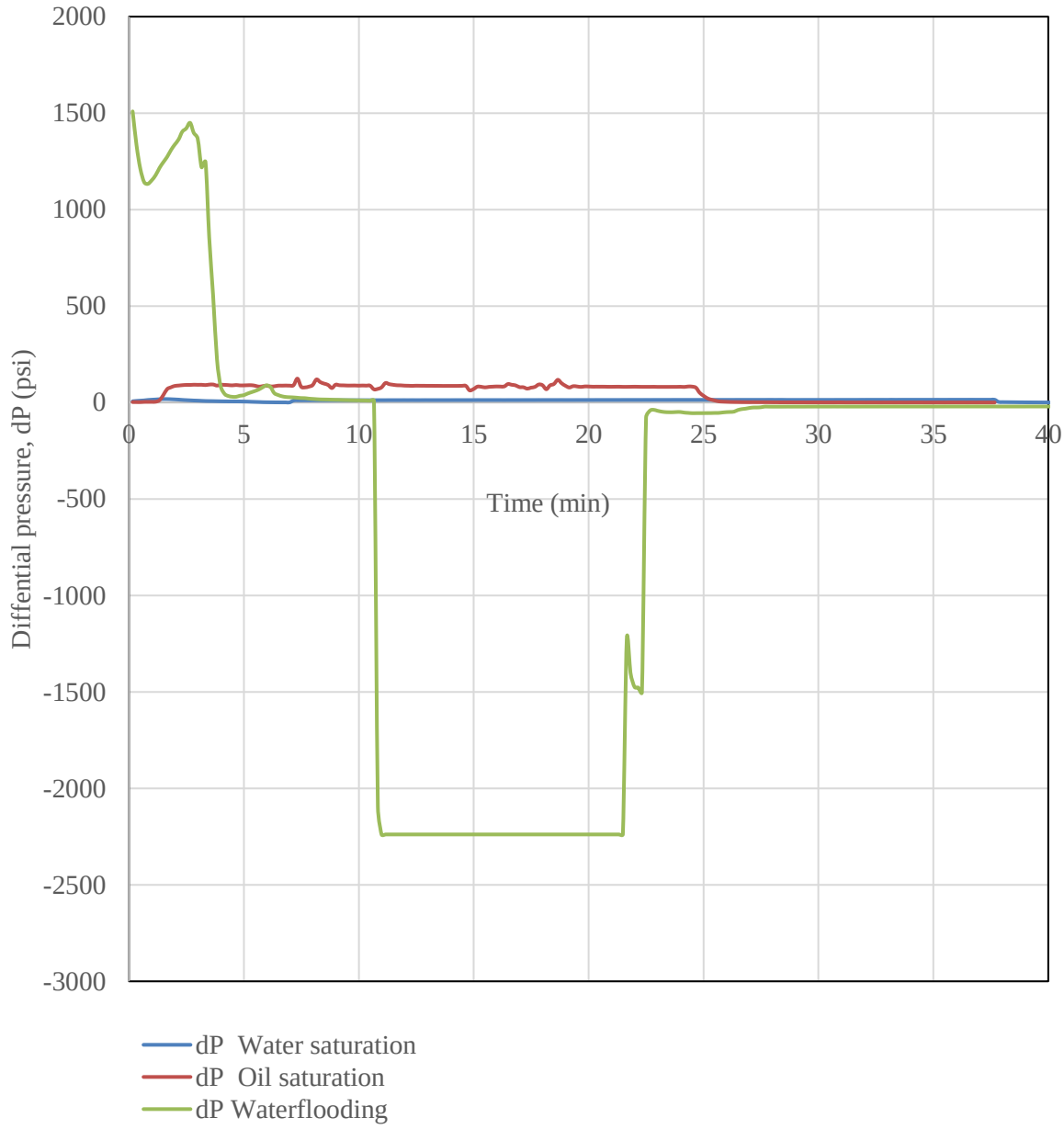

Figure 4.69: Edward brown differential pressure during flooding for vertical displacement indicating collapse of the core sample.

4.4.3.3 Core flood system pressures

With the aid of the UFS-200 coreflooding equipment, a saturated core sample of sandstone was desaturated, and oil recovered using waterflooding and polymer flooding. Figure 4.70 is a clear illustration of the fluid flow behaviour and pressure during coreflooding.

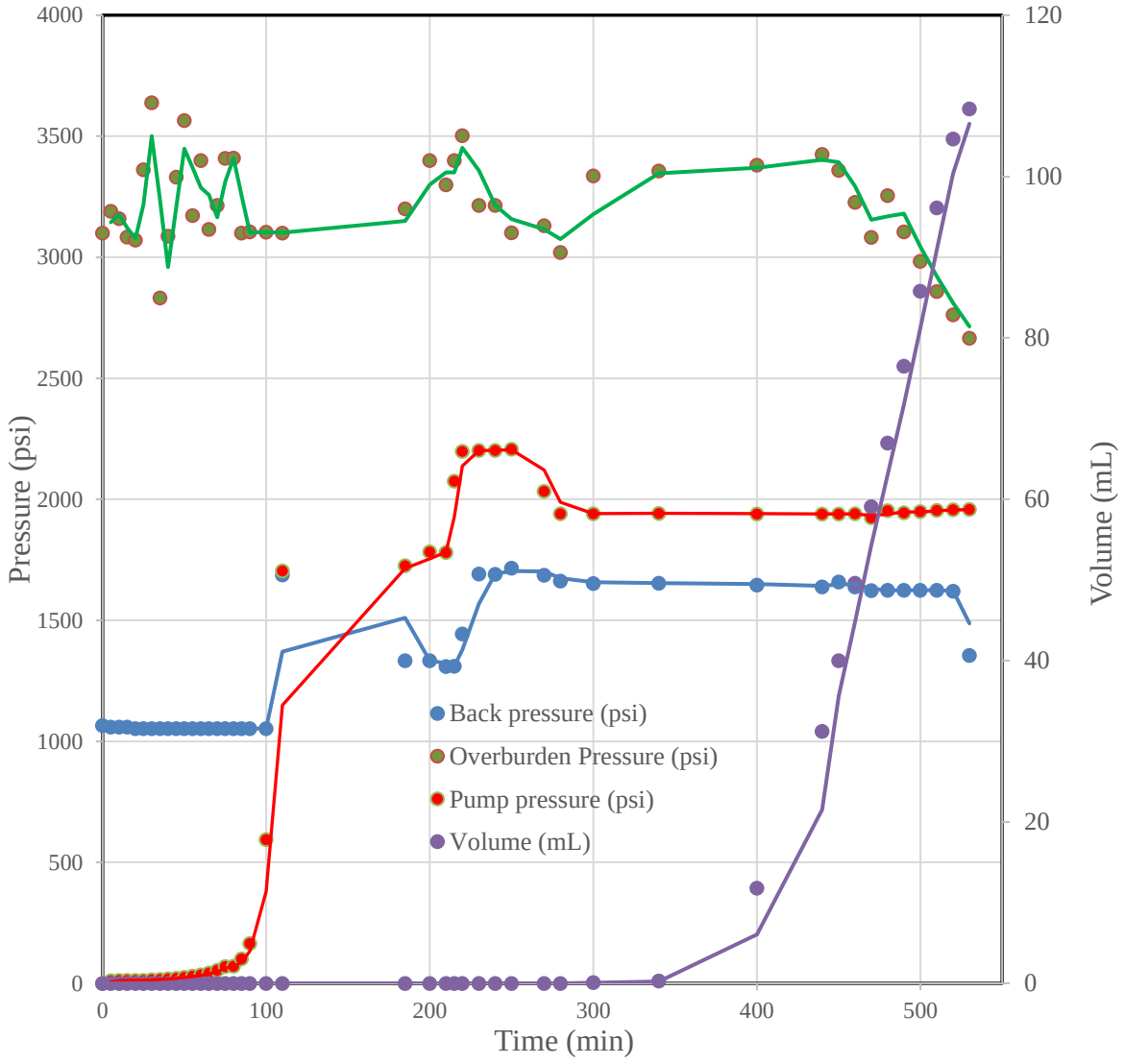

Figure 4.70: Coreflooding system pressures, fluid injection and oil recovery

The overburden pressure fluctuated from its 3000psi initial settings. This was attributed to the change in temperature as heating of the core holder was carried out to take the core environment to reservoir conditions. The overburden pressure rose steadily with increase in core temperature, as seen by the zigzag nature of the overburden curve. Instances, however, abound where need to regulate the pressure arose to forestall the overburden pressure from exceeding the allowable safety margin. The regulation of overburden pressure was done by slightly adjusting the drain overburden pump valve to lower the overburden pressure. This action could have been one of the reasons for the downward trend component of the zig zag curve. It is evident that after a while when the temperature had stabilised at the 44^{o}C mark, the overburden curve became steady. The temperature curve is illustrated in Figure 4.71.

Another significant activity took place near 200min of pumping reservoir fluid into the core sample; the pump pressure steadily rose to surpass the backpressure paving way for fluid to flow to the effluent chamber and the core saturation to take effect. It is evident that by the 300min mark, the flow of fluid had percolated the core and all capillary forces that could prevent flow of fluid neutralised to enable flow obtained at the outlet - effluent collection chamber.

Another interesting phenomenon is the backpressure that rose to accommodate the increasing pump pressures set at constant flow mode. This illustrates the impact of capillary forces resulting from the tortuous pore spaces, coupled with the rising pump pressure as fluid percolates the micropores of the reservoir. A seemingly increasing fluctuation occurred between the pump pressure and backpressure, the pressure increase must be in favour of the pump pressure for flow to the effluent to occur.

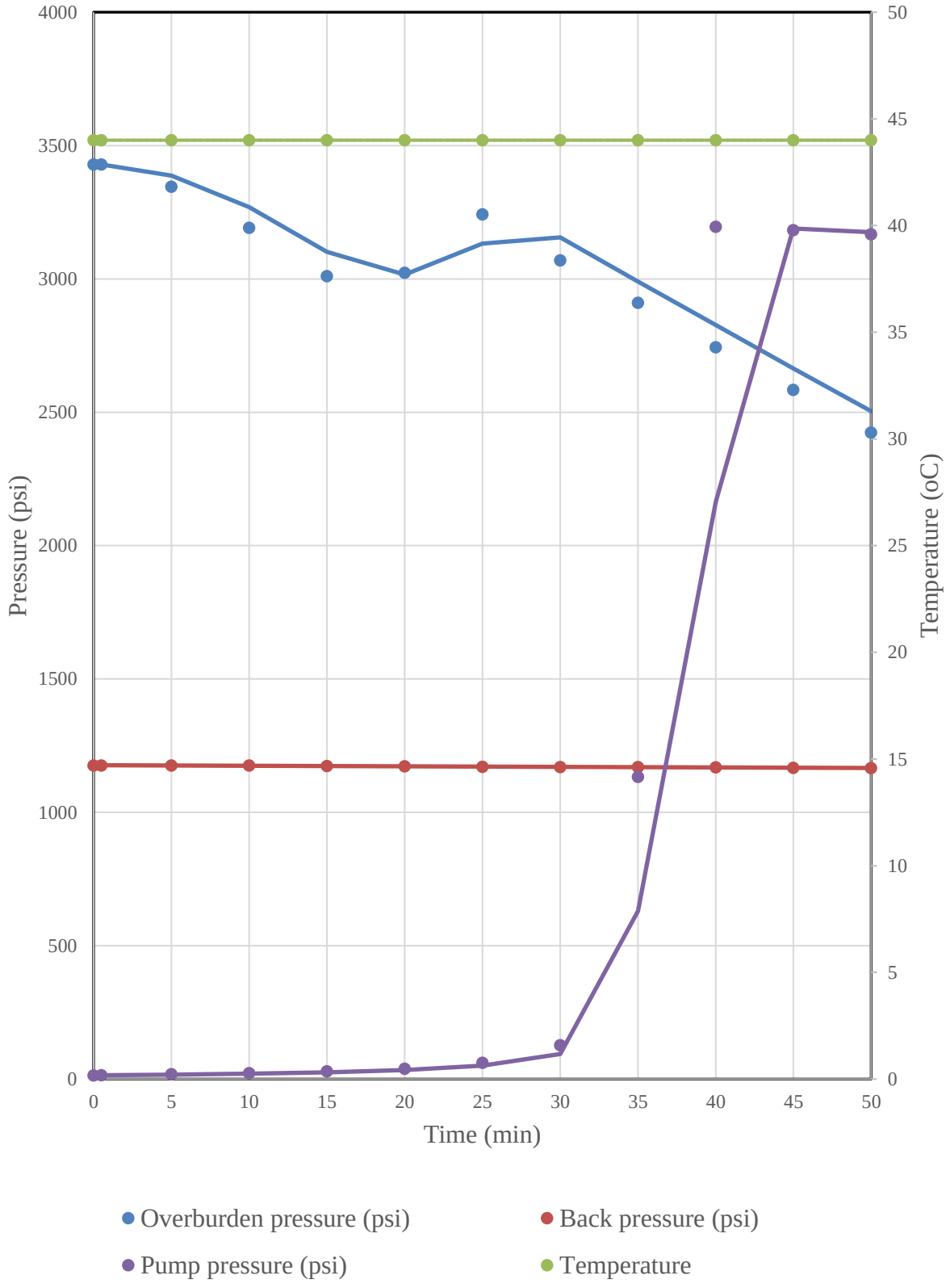

Figure 4.71: Coreflooding formation damage

Looking at Figure 4.72, an interesting phenomenon occurs when the pore spaces of the sandstone core sample clogged, and the rock permeability reduced considerably to the extent that the pump pressure exceeded the overburden pressure. In an effort for the pump to sustain constant flow mode setting and continuous flow of fluid across the tortuous pores of the rock, a pressure build-up occurred. This pressure-build up lead to the eventual collapse of the sleeve, which is due to the collapse of the rock, commonly referred to as formation damage. The overburden pressure gradually falls, and flow stops. One major cause of this pump pressure build-up exceeding overburden pressure is the low permeability of the rock. To forestall future occurrence, higher permeability formations were employed in subsequent enhanced oil recovery applications. Another reason for clogging is the limiting unconfined compressive strength (UCS) of the rock, which is less than 5,000psi. The lower the UCS the greater the potentials for the rock to collapse when subjected to high pressure or any pressure near its UCS.

Figure 4.72 clearly depicts the recovery of oil with an appearance of a steady state profile. Through the continuous injection of multiple pore volumes of displacing fluid, it was evident that once the pump flow rates were optimum the entire coreflooding system became stable and steady. The backpressure and pump pressure maintained a constant pressure differential. The constant pressure differential profiles in Figure 4.72 starts at the 250 minutes mark.

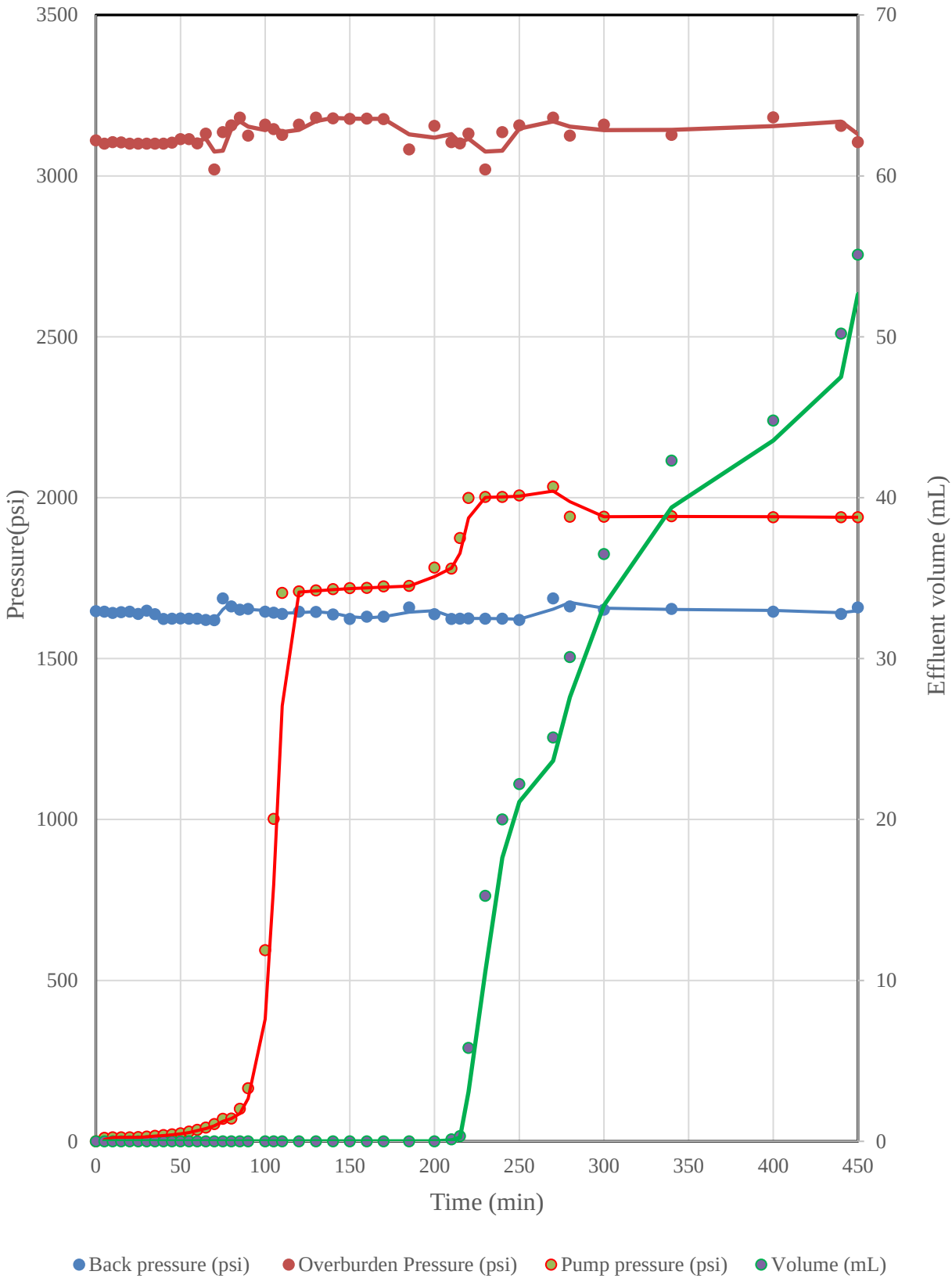

Figure 4.72: Oil recovery curve

4.4.4 Oil production

The delivery of effluent leading to oil recovery from saturated core samples is illustrated in Figure 4.73. Here, oil produced can be seen at the top floating on the thick polymer effluent as oil was continuously being displaced from the core sample. In Figure 4.74, volume of oil collected during a complete recovery process is shown.

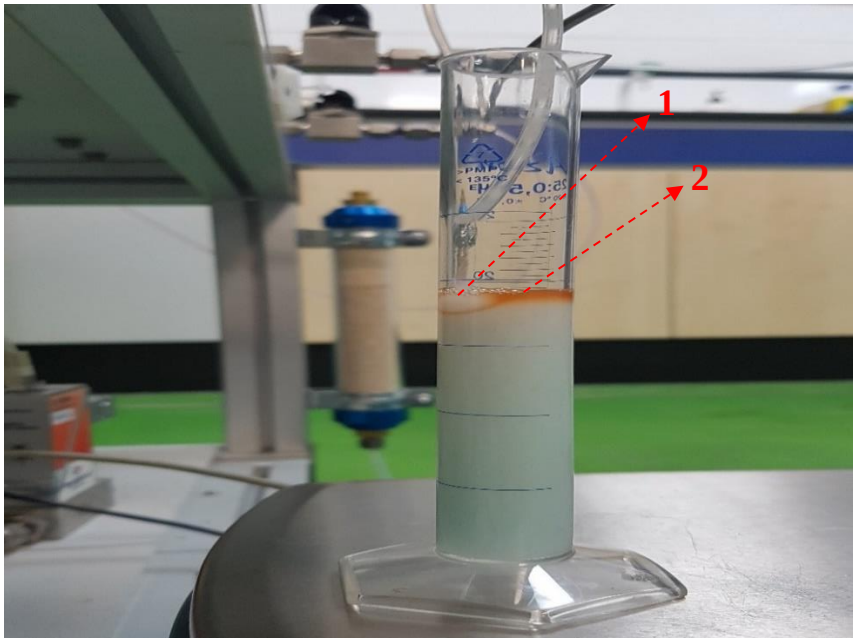

1 Effluent droplet **2** Oil separated from effluent droplet

Figure 4.73: Effluent oil being recovered

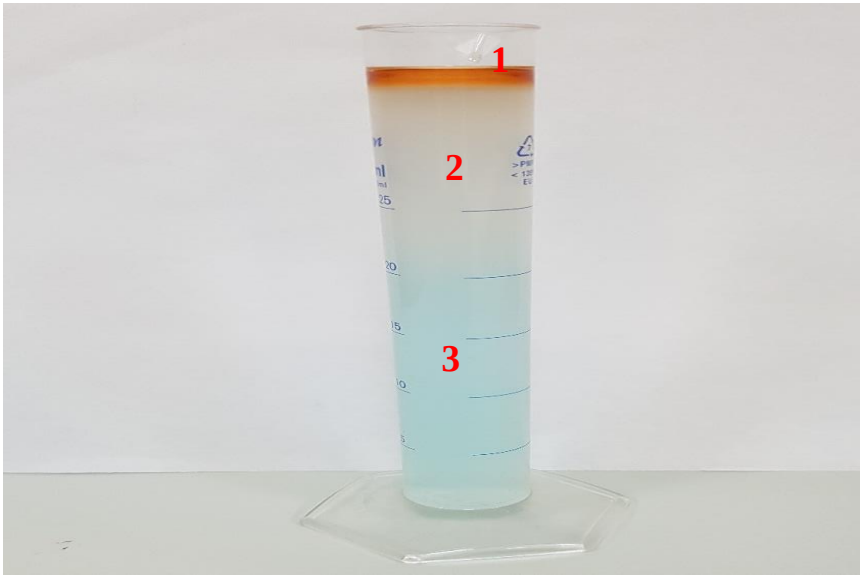

1 Oil **2** Water **3** HPAM

Figure 4.74: Profile of effluent after core flooding

Figure 4.75 and Figure 4.76 show the up-close thin layer of polymer precipitate laying between oil and water. The precipitate formed was attributed to the stripping and mechanical damage as the polymer passed through the pore spaces. Nevertheless, the precipitate pushes the oil upwards easing the separation and measurement of recovered oil volume.

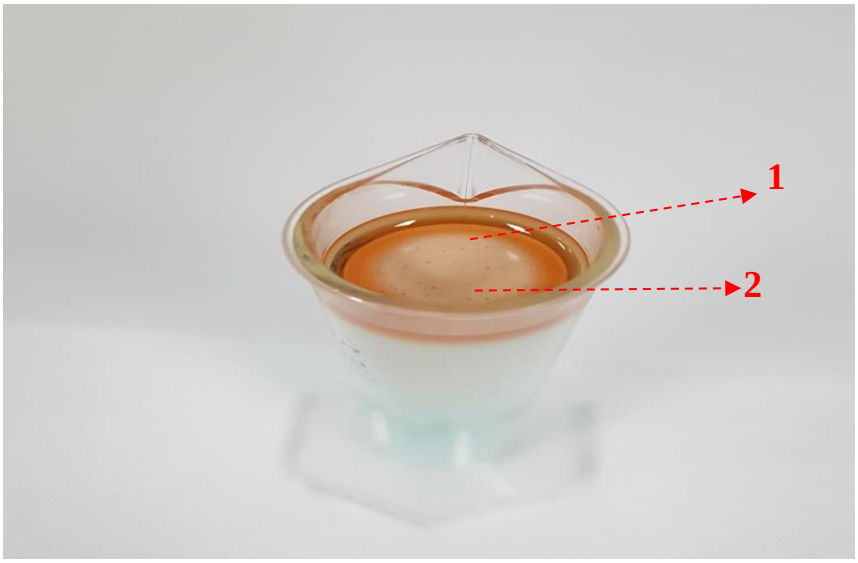

1 Oil layer **2** HPAM Layer

Figure 4.75: Top view of effluent showing oil and polymer precipitate from coreflooding

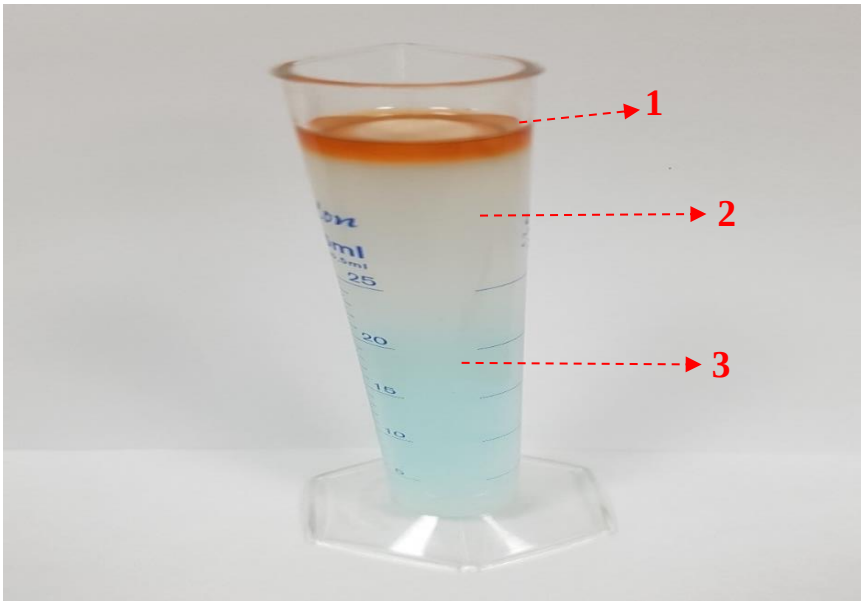

1 Oil layer **2** HPAM layer **3** Water

Figure 4.76: Effluent profile showing polymer precipitate from core flooding

4.4.4.1 Horizontal core oil production

In this section, the oil recovered from the sandstone and carbonate rocks based on horizontal orientation of the core samples are presented. With the horizontal core displacement arrangement,

The oil recovered at various stages from each of the core samples used in this research are illustrated graphically. In each of the cases, there was significant increase in oil recovery with the application of ultrasound and polymer. The incremental oil displaced with ultrasound from the one by two-inch core samples are shown in Figure 4.77, Figure 4.79, Figure 4.81, Figure 4.83 and Figure 4.85 respectively. Similarly, the oil recovered with injection of polymer without ultrasound are shown in Figure 4.78, Figure 4.80, Figure 4.82, Figure 4.84 and Figure 4.86 respectively.

In each of the charts the incremental oil obtained were determined based on waterflooding, polymer flooding and polymer with ultrasound. It is evident that additional increments were obtained with each additional pore volume injection. Based on the increments in Figure 4.77 the total oil recovered for Grey Berea Upper, Grey Berea lower, Indiana limestone, Guelph dolomite, Silurian dolomite and Edward brown are 3.67ml (5.40ml PV), 3.17ml (4.88ml PV), 2.68ml (4.63ml PV), 1.52ml (2.57ml PV), 2.39ml (4.11ml PV) and 5.96ml (10.28ml PV) respectively. Three pore volumes were injected.

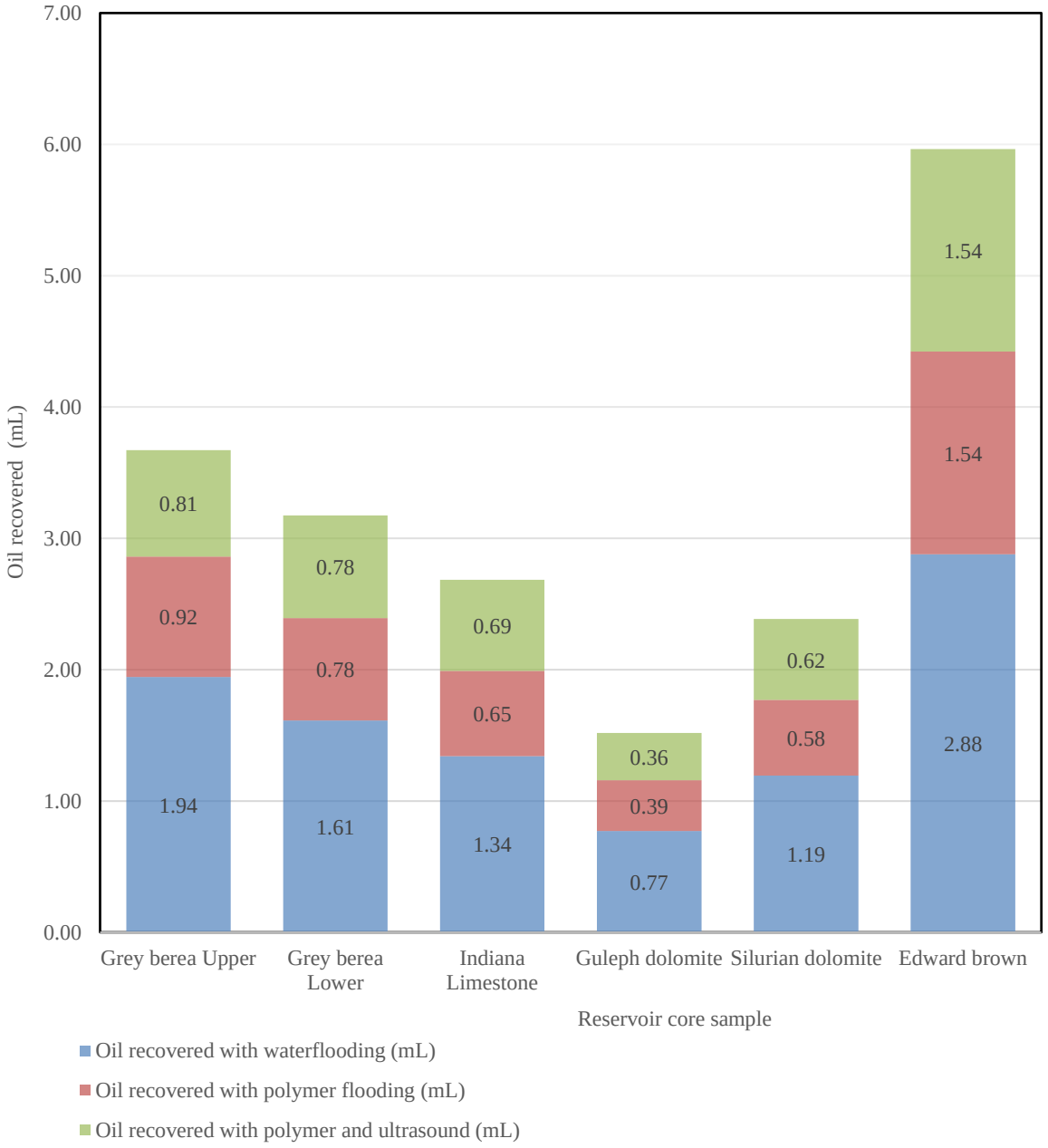

Figure 4.77: Incremental oil recovery with different recovery methods Stage 1 (three pore volume injected with ultrasound) horizontal core assembly

In Figure 4.78 the incremental volumes of oil recovered with injection of one pore volume of water and 2 pore volumes of polymer are shown.

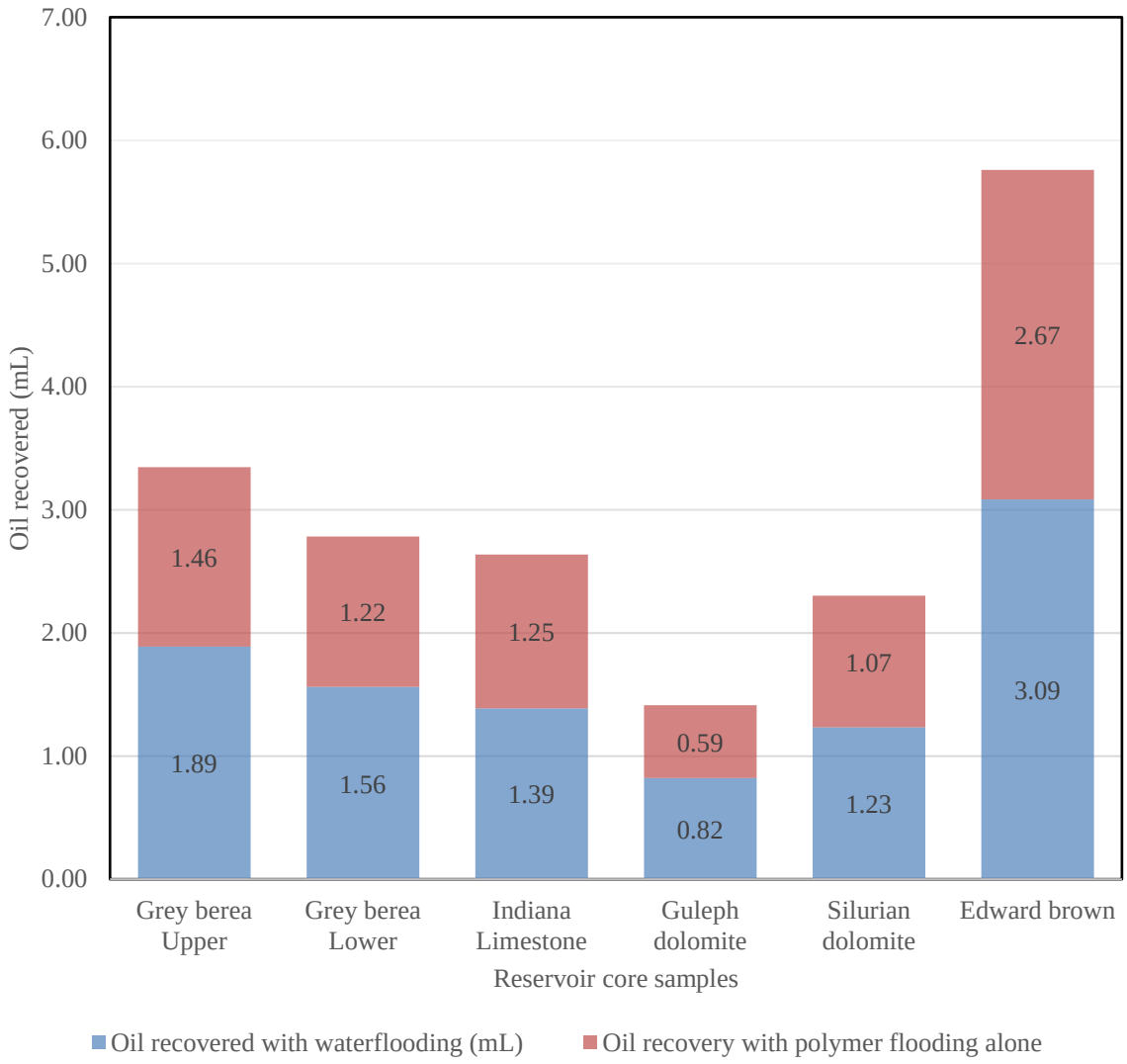

Figure 4.78: Incremental oil recovery with water and polymer flooding stage 1 (three pore volumes injected without ultrasound) horizontal core assembly

Summing up of the numeric figures in Figure 4.79 shows that the total oil recovered for Grey Berea Upper, Grey Berea lower, Indiana limestone, Guelph dolomite, Silurian dolomite and Edward brown are 3.38ml (5.40ml PV), 3.32ml (4.88ml PV), 2.78ml (4.63ml PV), 1.57ml (2.57ml PV), 2.47ml (4.11ml PV) and 6.17ml (10.28ml PV) respectively with injection of four pore volume.

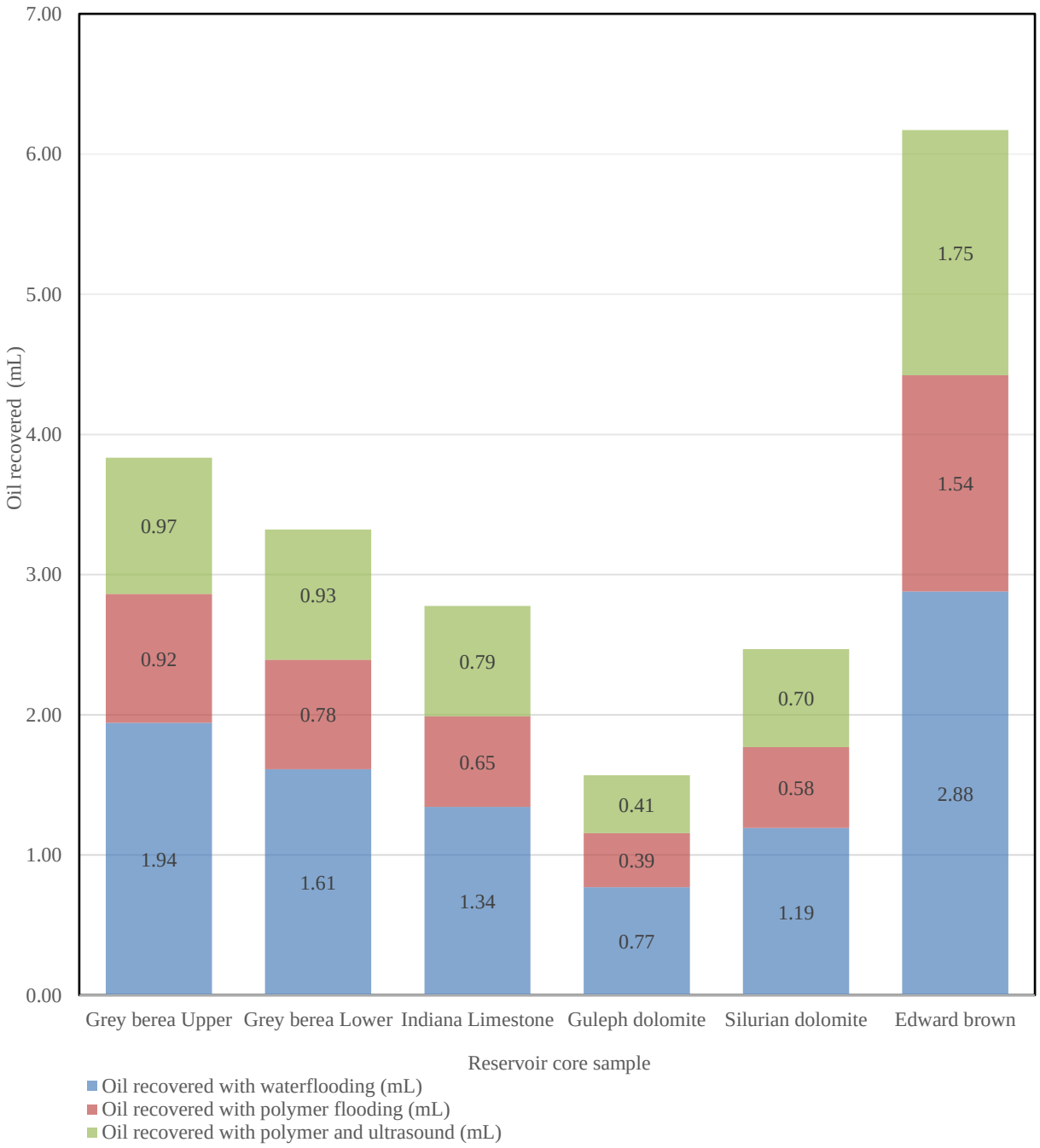

Figure 4.79: Incremental oil with different recovery methods stage 2 (four pore volumes injected) horizontal core assembly

In Figure 4.80 the incremental volumes of oil recovered with injection of one pore volume of water and 3 pore volumes of polymer are shown

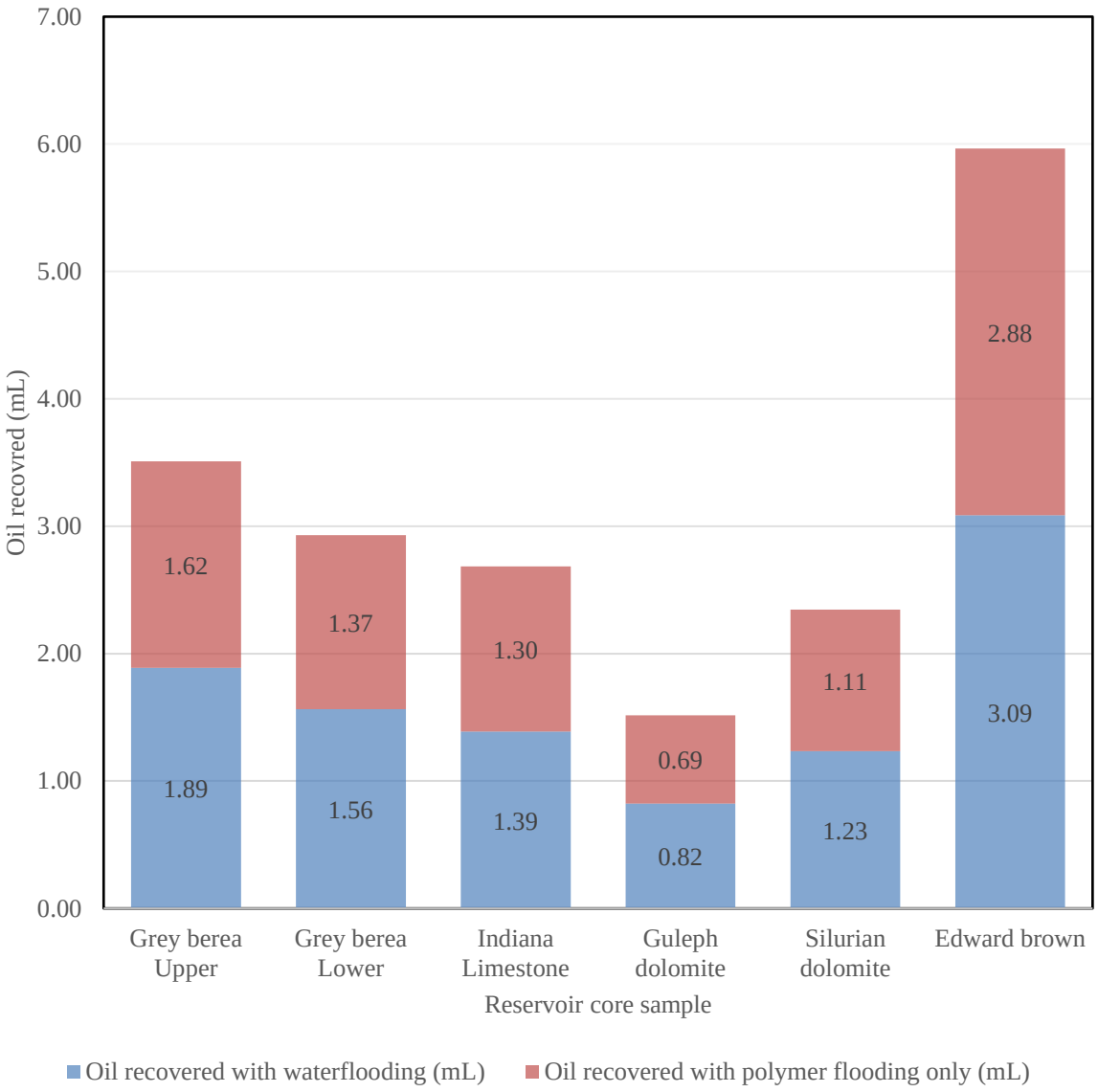

Figure 4.80: Incremental oil recovery with water and polymer flooding stage 2 (Four pore volumes injected without ultrasound) horizontal core assembly

In Figure 4.81 the sum total of incremental oil recovered from Grey Berea Upper, Grey Berea lower, Indiana limestone, Guelph dolomite, Silurian dolomite and Edward brown are 3.89ml (5.40ml PV), 3.37ml (4.88ml PV), 2.87ml (4.63ml PV), 1.60ml (2.57ml PV), 2.51ml (4.11ml PV) and 6.37ml (10.28ml PV) respectively are presented. At this stage five pore volumes were injected.

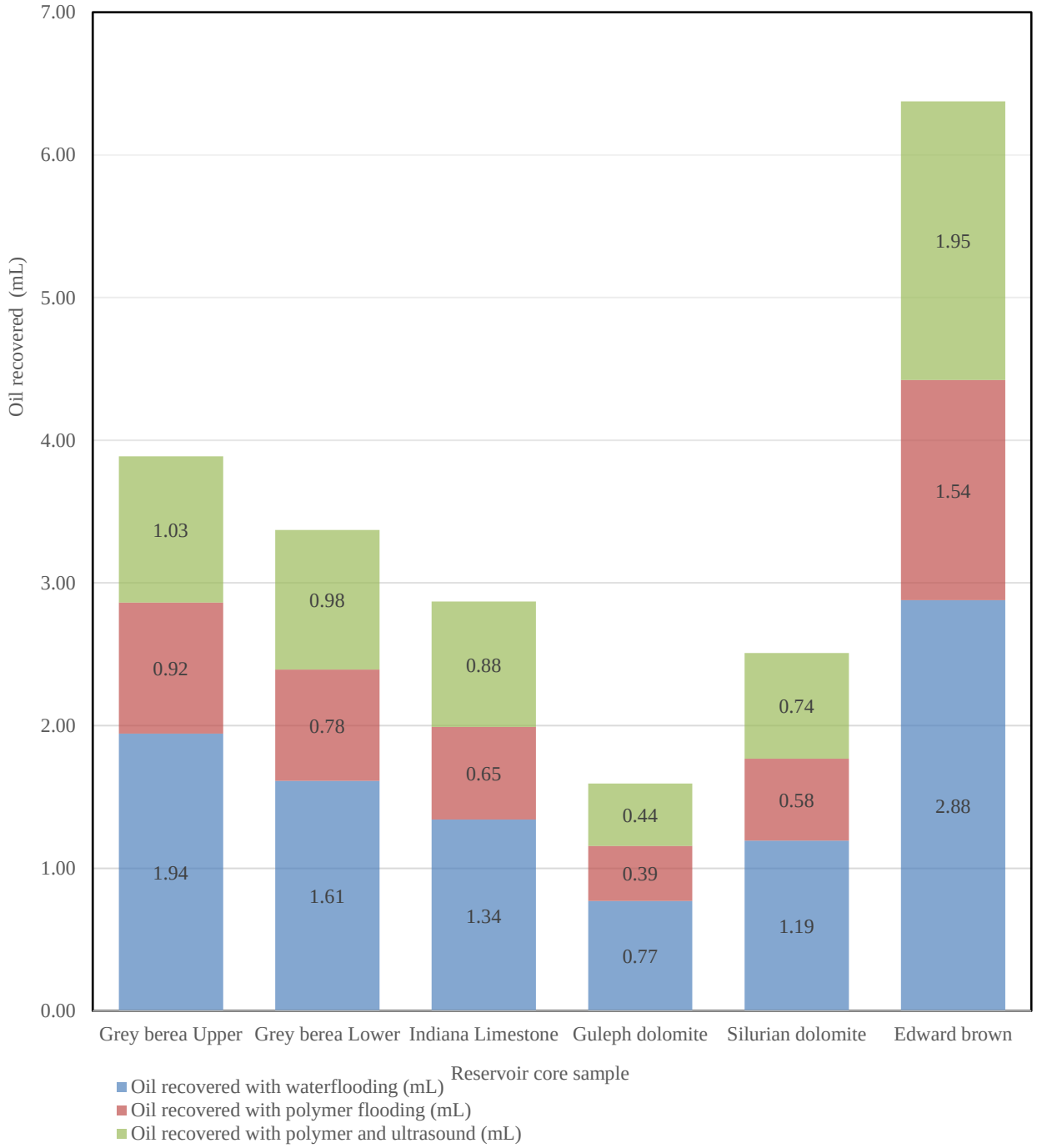

Figure 4.81: Incremental oil with different recovery methods stage 3(five pore volumes injected) horizontal core assembly

In Figure 4.82 the incremental volumes of oil recovered with injection of one pore volume of water and 4 pore volumes of polymer are shown

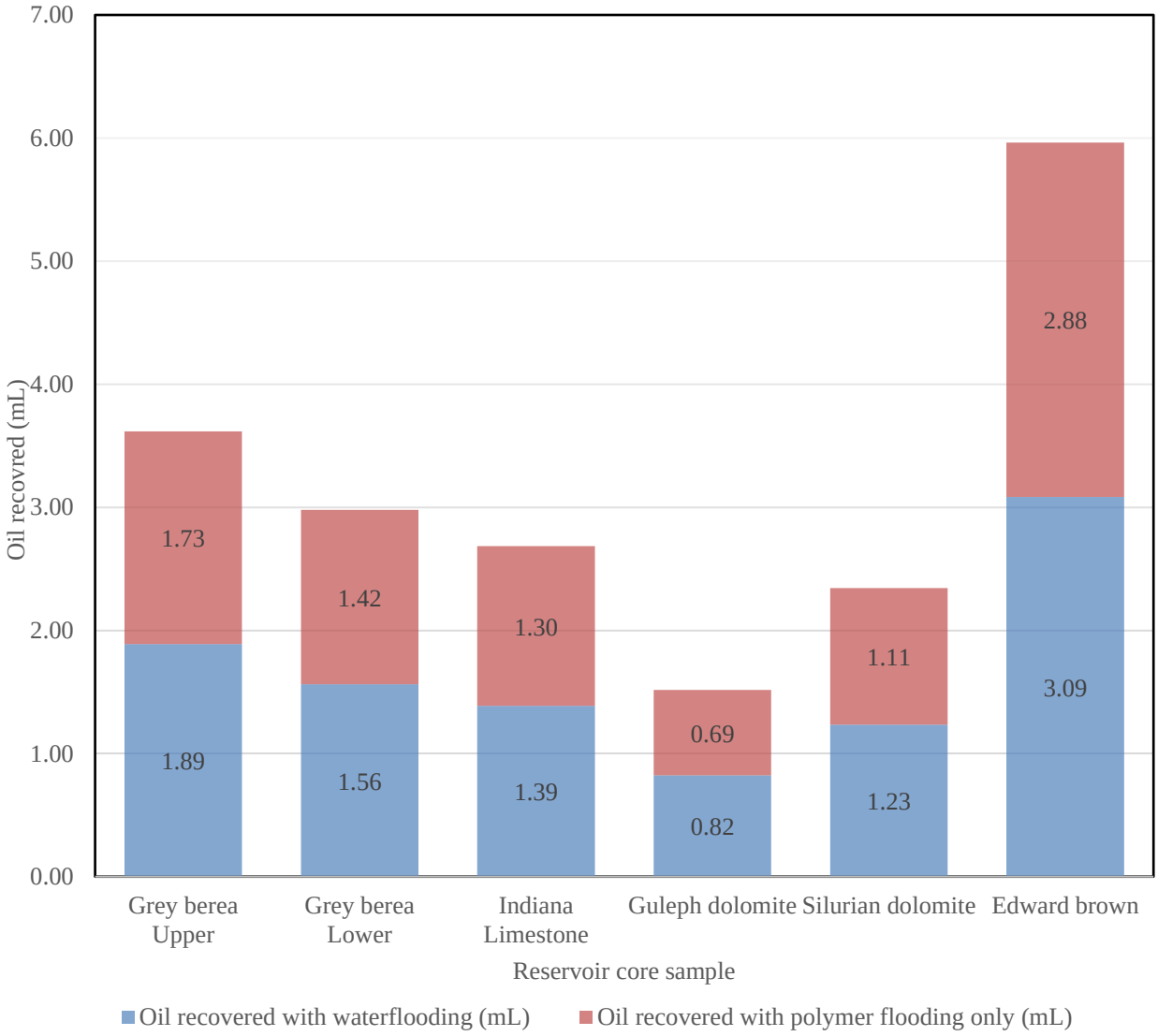

Figure 4.82: Incremental oil recovery with water and polymer flooding stage 3 (Five pore volumes injected without ultrasound) horizontal core assembly

Figure 4.83 provides the total oil recovery from Grey Berea Upper, Grey Berea lower, Indiana limestone, Guelph dolomite, Silurian dolomite and Edward brown as 4.64ml (5.40ml PV), 4.01ml (4.88ml PV), 3.42ml (4.63ml PV), 1.90ml (2.57ml PV), 3.00ml (4.11ml PV) and 7.71ml (10.28ml PV) respectively when six pore volumes were injected.

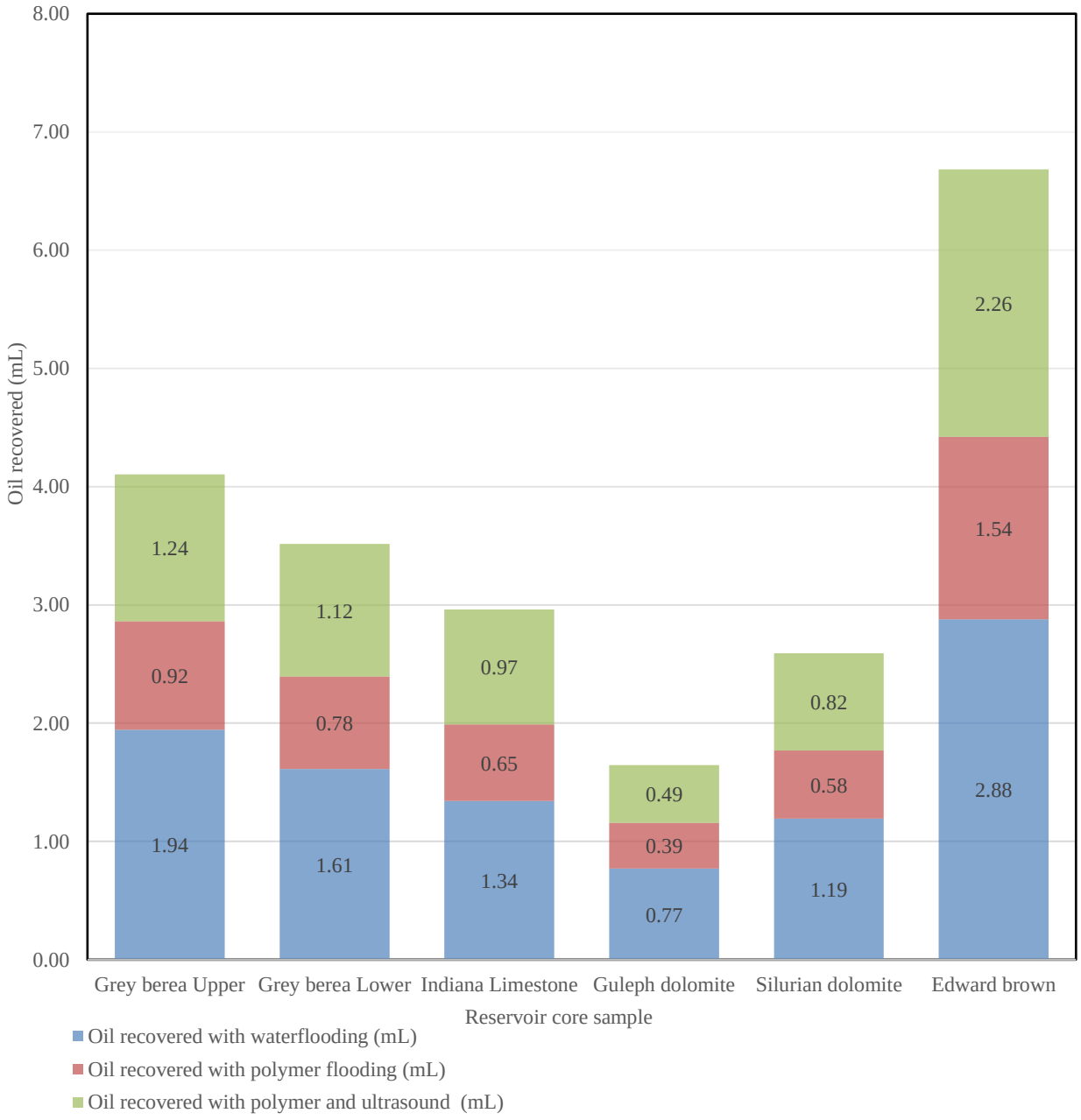

Figure 4.83: Incremental oil with different recovery methods stage 4 (six pore volumes injected) horizontal core assembly

In Figure 4.84 the incremental volumes of oil recovered with injection of one pore volume of water and 5 pore volumes of polymer are shown.

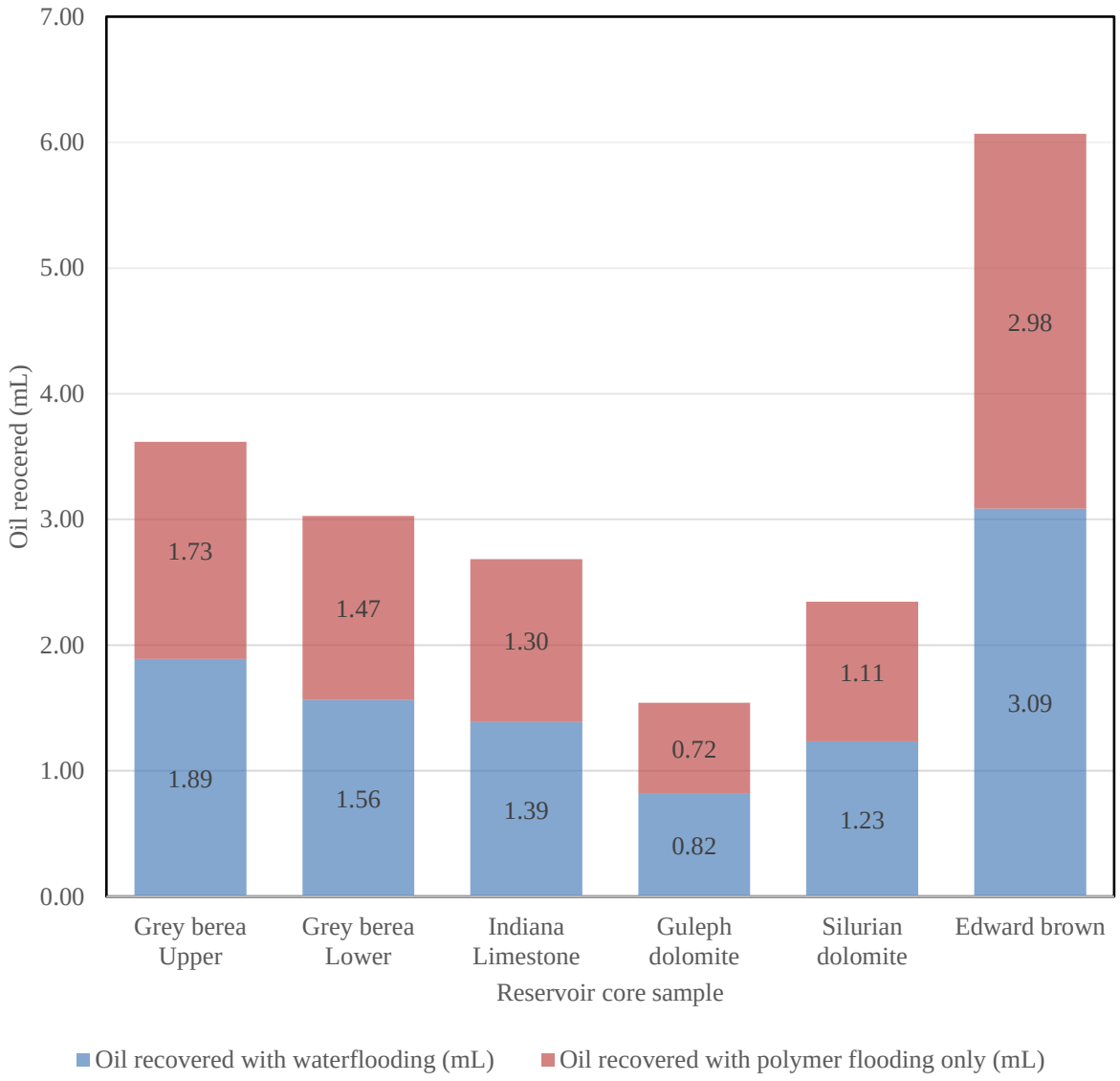

Figure 4.84: Incremental oil recovery with water and polymer flooding stage 4 (six pore volumes injected without ultrasound) horizontal core assembly

In Figure 4.81 the total recovery for Grey Berea Upper, Grey Berea lower, Indiana limestone, Guelph dolomite, Silurian dolomite and Edward brown are 4.21ml (5.40ml PV), 3.61ml (4.88ml PV), 3.19ml (4.63ml PV), 1.70ml (2.57ml PV), 2.67ml (4.11ml PV) and 6.79ml (10.28ml PV) respectively.

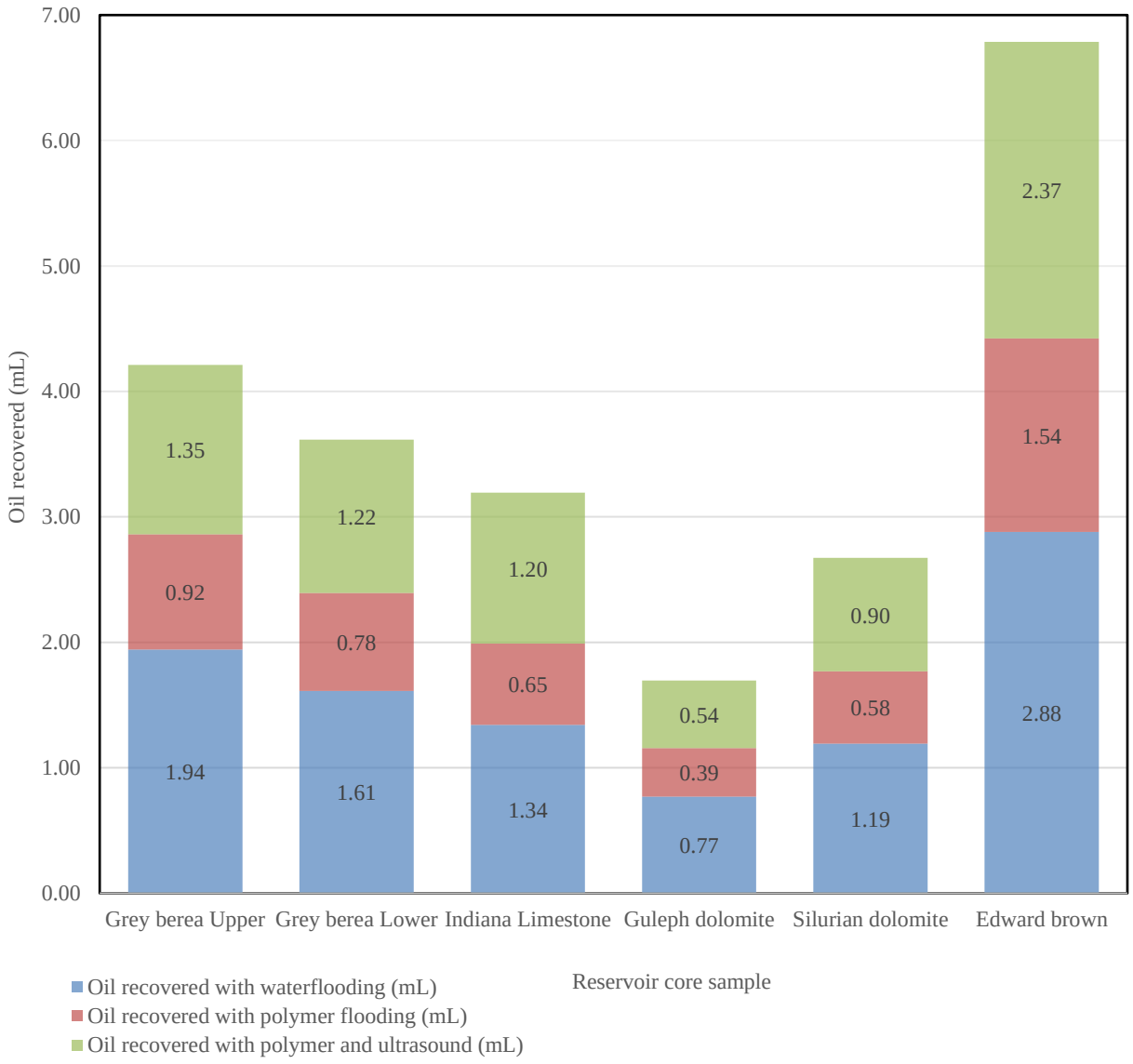

Figure 4.85: Incremental oil with different recovery methods stage 5 (seven pore volumes injected) horizontal core assembly

In Figure 4.86 the incremental volumes of oil recovered with injection of one pore volume of water and 6 pore volumes of polymer are shown

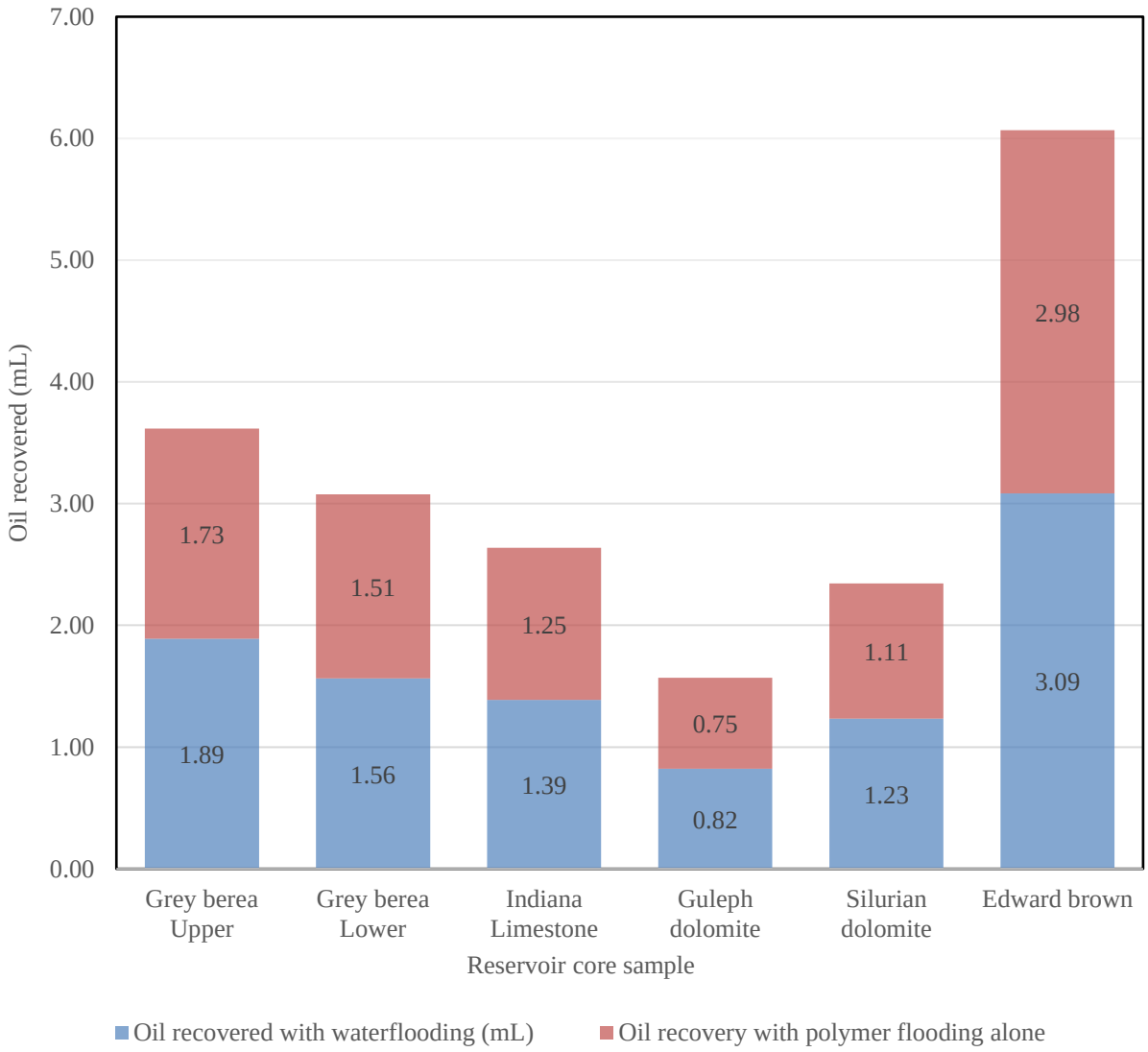

Figure 4.86: Incremental oil recovery with water and polymer flooding stage 4 (six pore volumes injected without ultrasound) horizontal core assembly

4.4.4.1.1 Overall oil recovery

The overall oil recovery as a percentage of recoverable original oil in place (OOIP) for various pore volume injections for six different core samples are shown in Figure 4.87, Figure 4.88, Figure 4.89, Figure 4.90 Figure 4.91, Figure 4.92, Figure 4.93, Figure 4.94, Figure 4.95 and Figure 4.96. Each of the graphs illustrates the incremental oil recovered based on pore volume injected. The main distinctions are injections with and without ultrasound which enabled comparison.

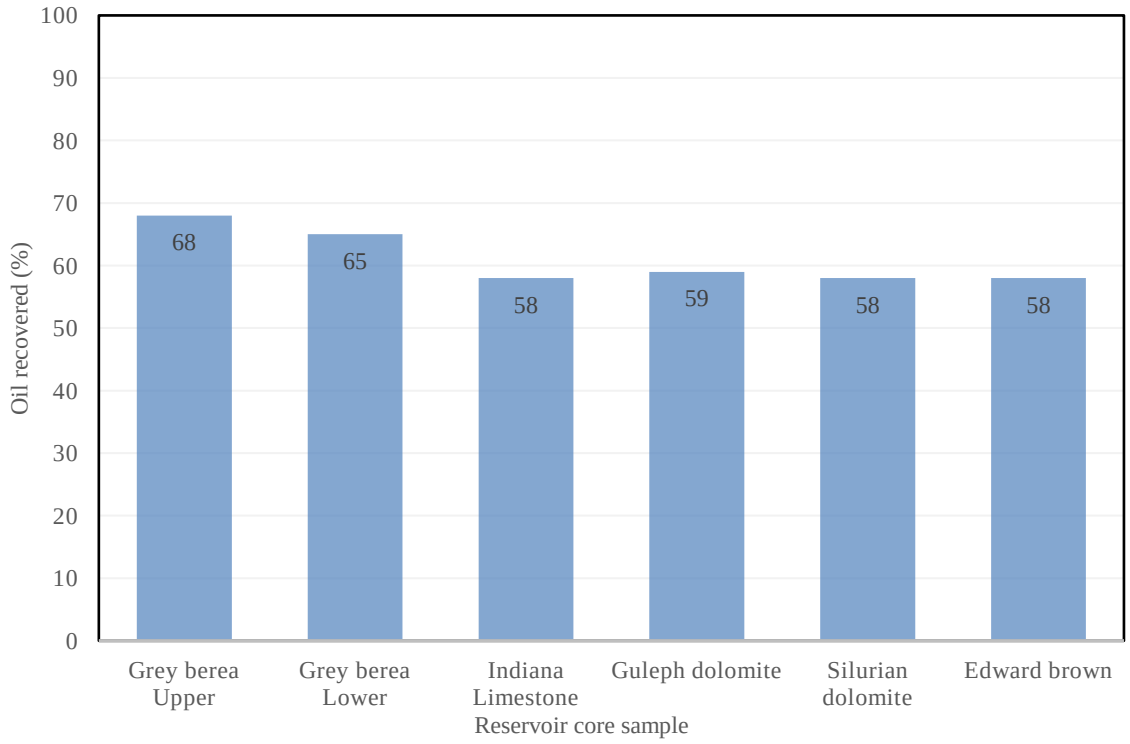

Figure 4.87: Percentage oil recovery at Stage 1 (with 3 pore volumes injected with ultrasound) horizontal core assembly

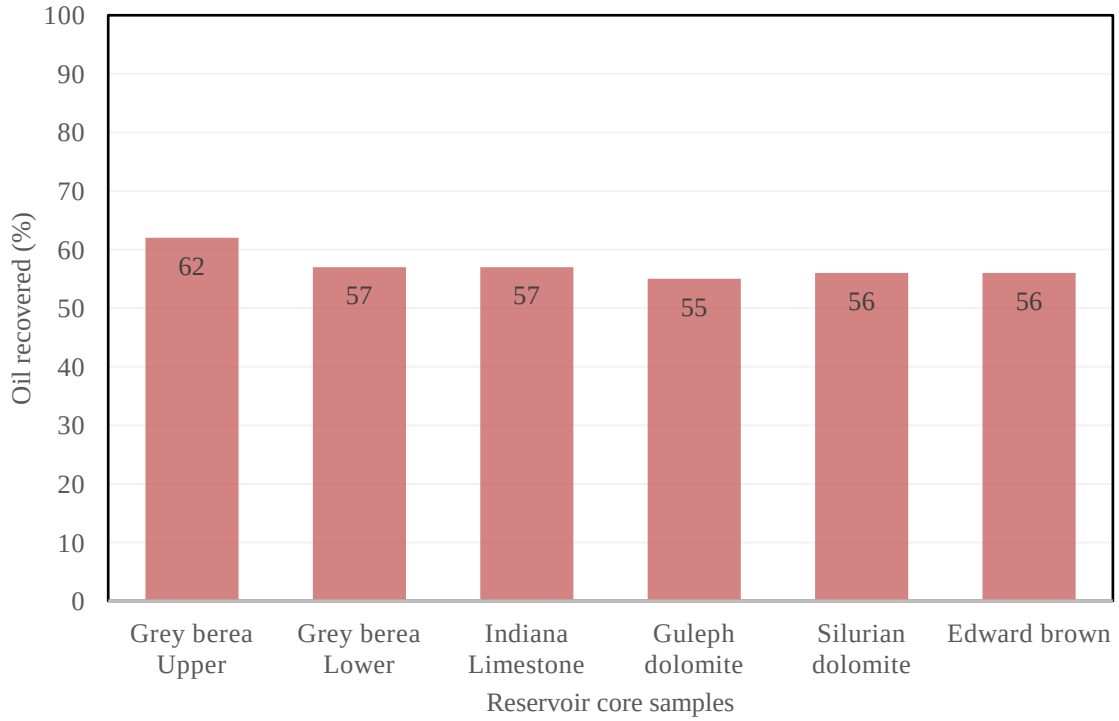

Figure 4.88: Percentage oil recovery at Stage 1 (with 3 pore volumes injected without ultrasound) horizontal core assembly

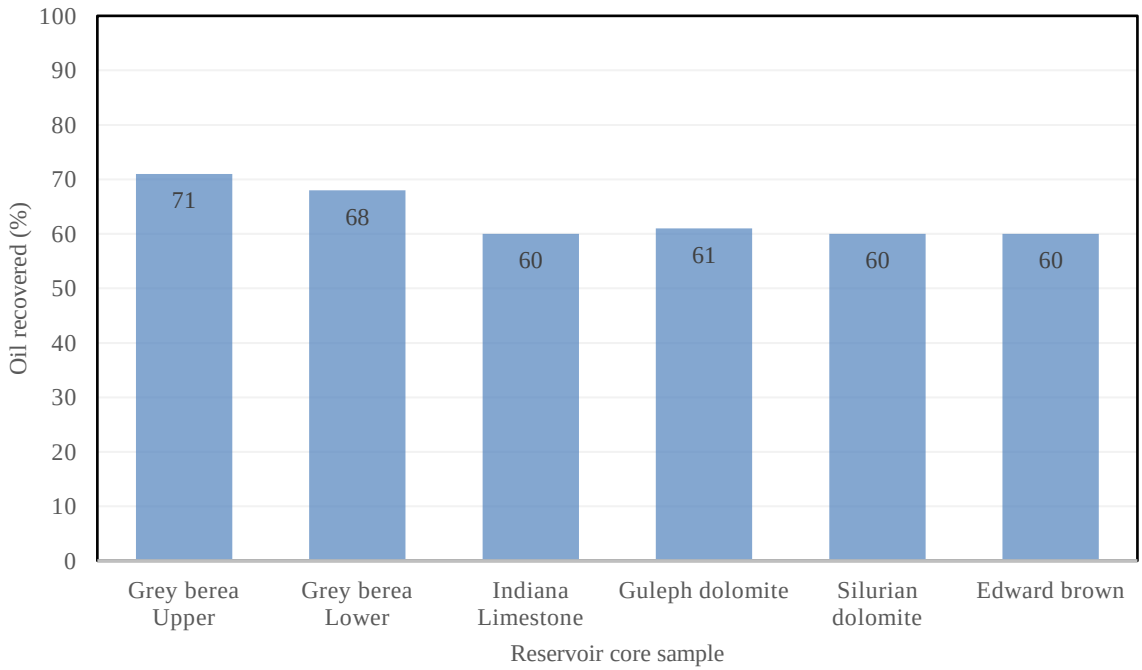

Figure 4.89: Percentage oil recovery at stage 2 (with 5 pore volumes injected with ultrasound) horizontal core assembly

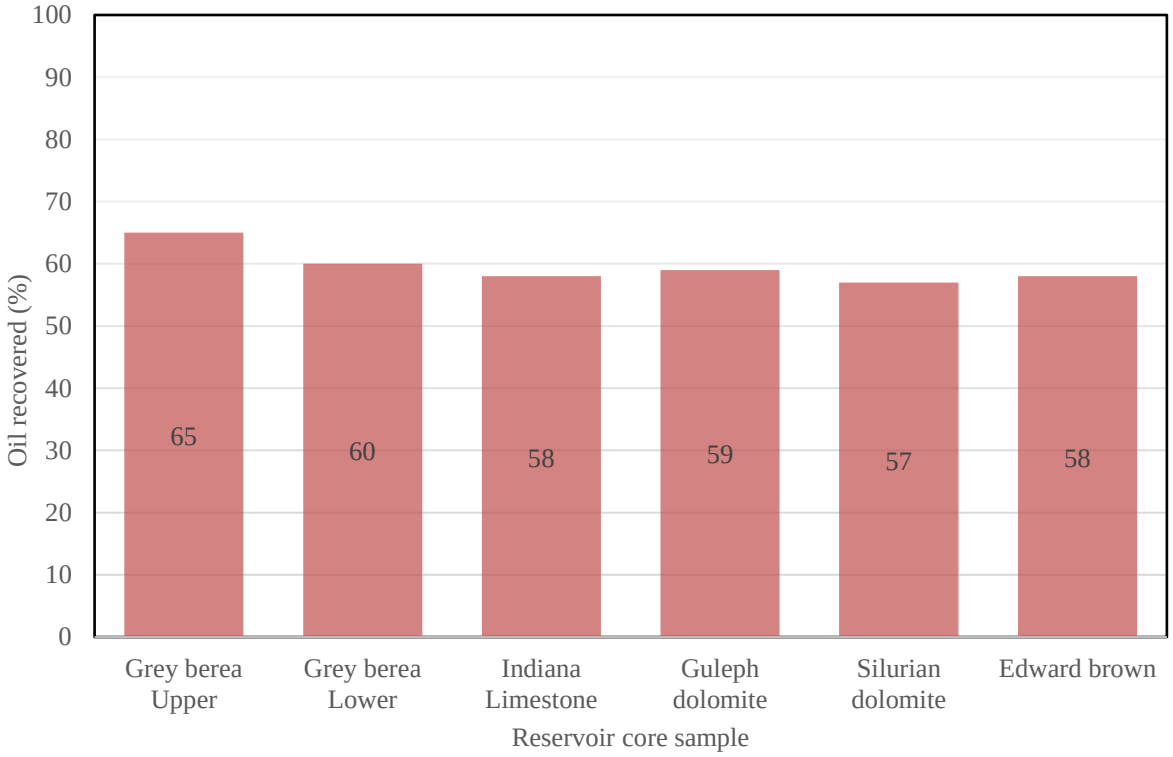

Figure 4.90: Percentage oil recovery at stage 2 (with 5 pore volumes injected without ultrasound) horizontal core assembly

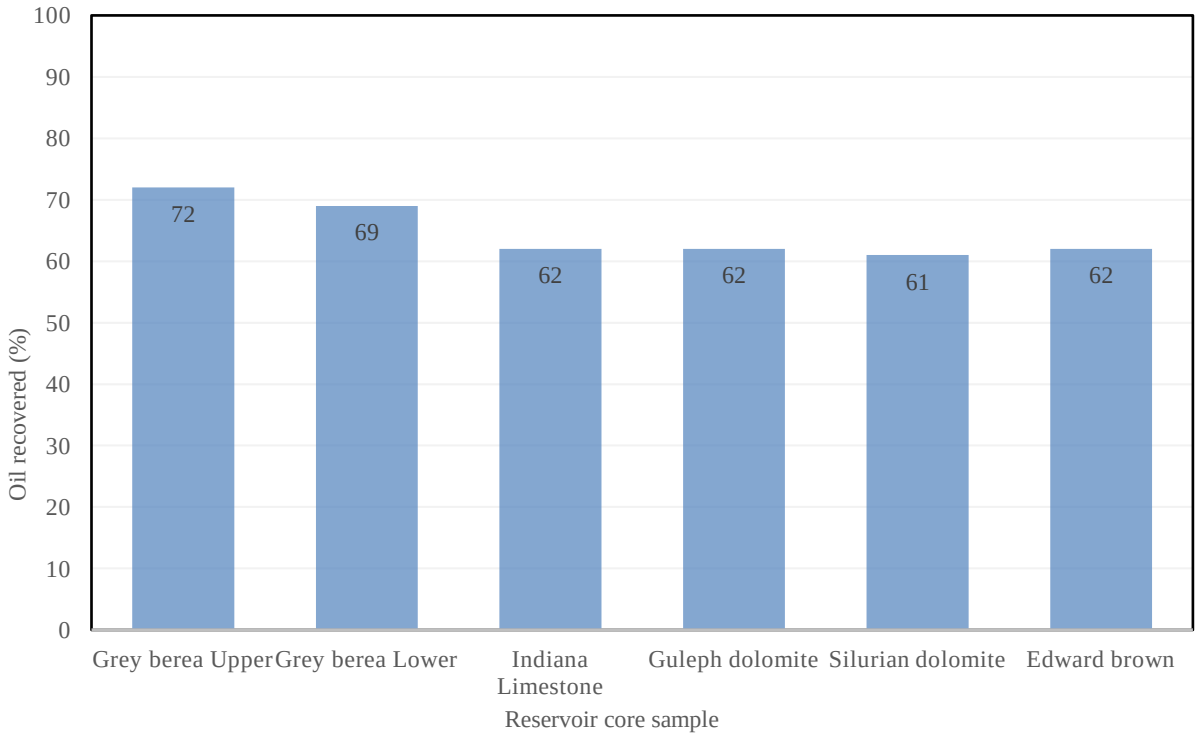

Figure 4.91: Percentage oil recovery at stage 3 (with 4 pore volumes injected with ultrasound) horizontal core assembly

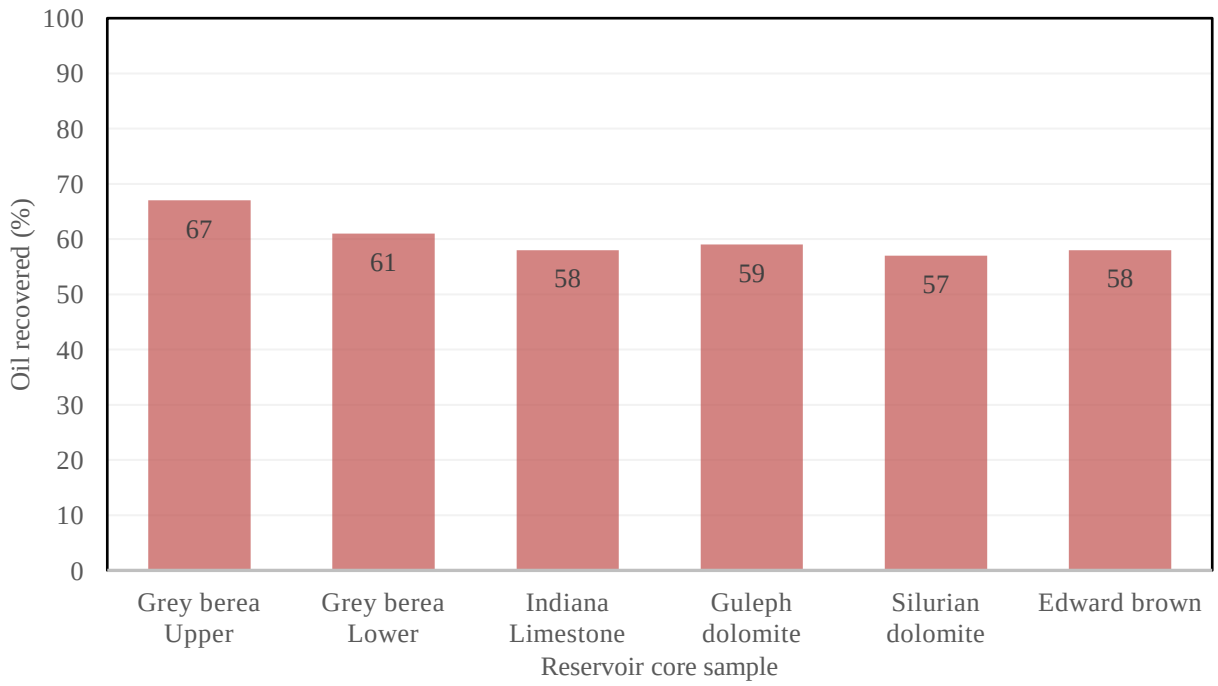

Figure 4.92: Percentage oil recovery at stage 3 (with 4 pore volumes injected without ultrasound) horizontal core assembly

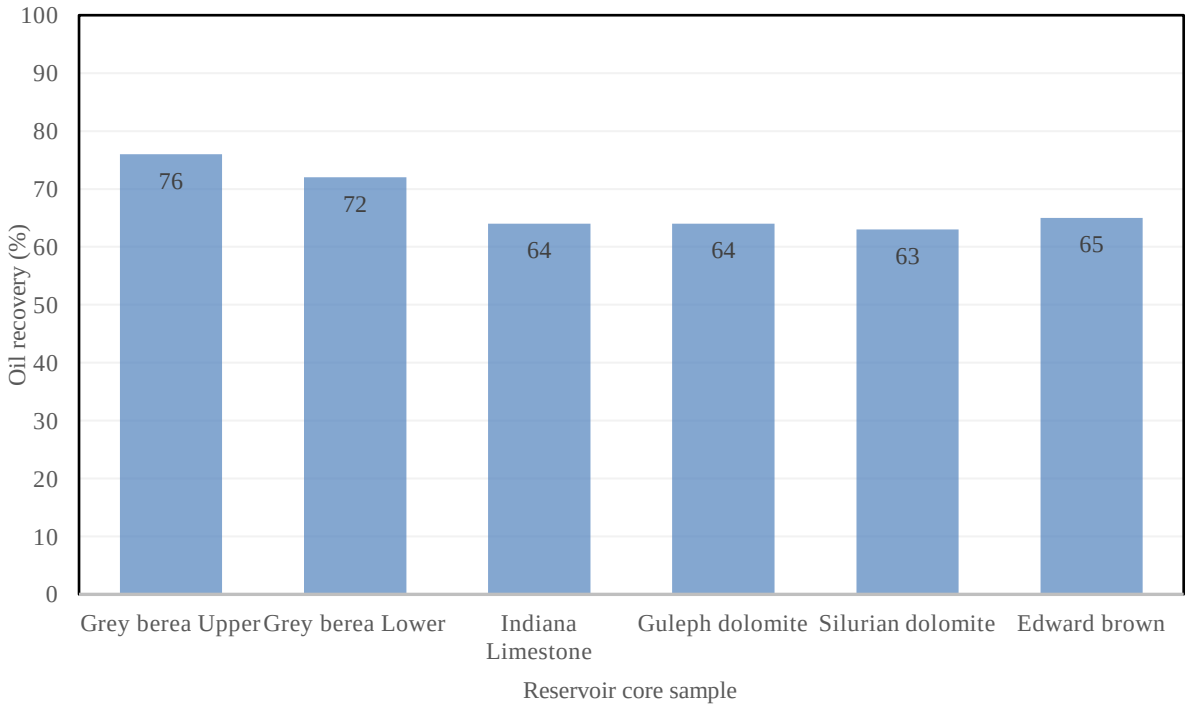

Figure 4.93: Percentage oil recovery at stage 4 (with 5 pore volumes injected with ultrasound) horizontal core assembly

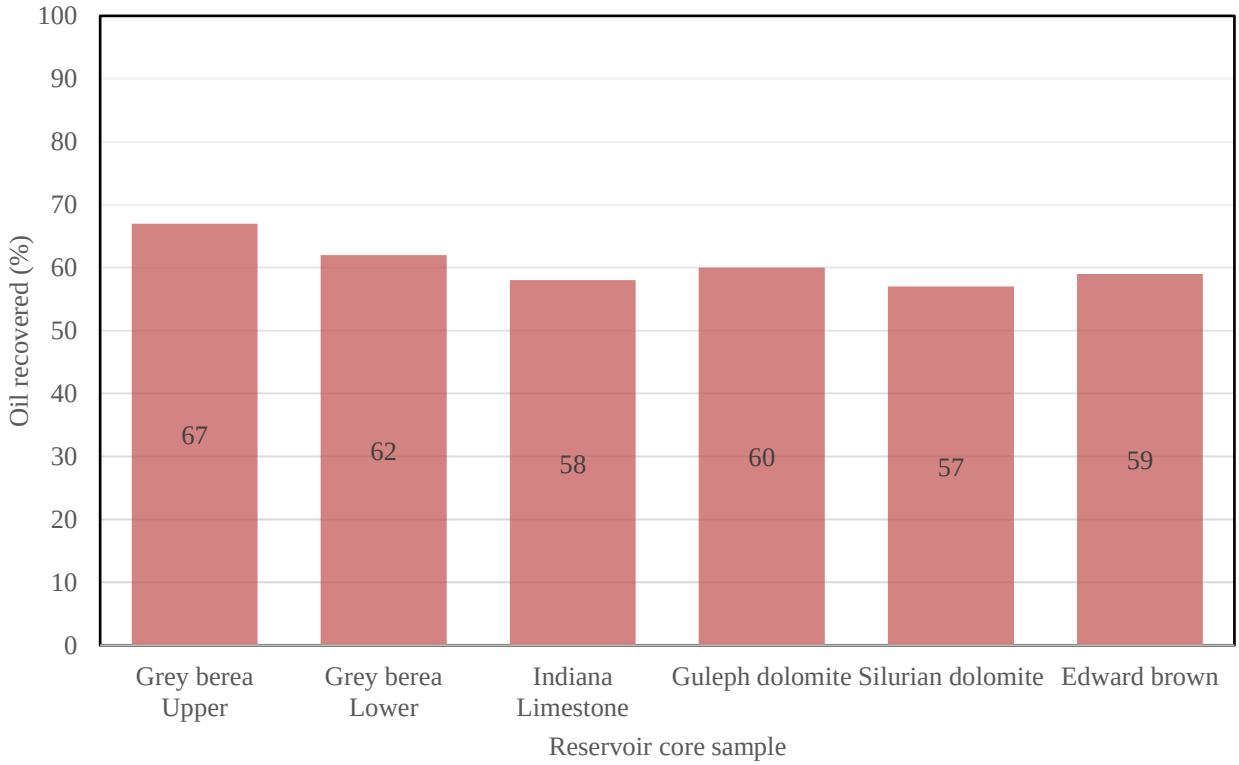

Figure 4.94: Percentage oil recovery at stage 4 (with 5 pore volumes injected without ultrasound) horizontal core assembly

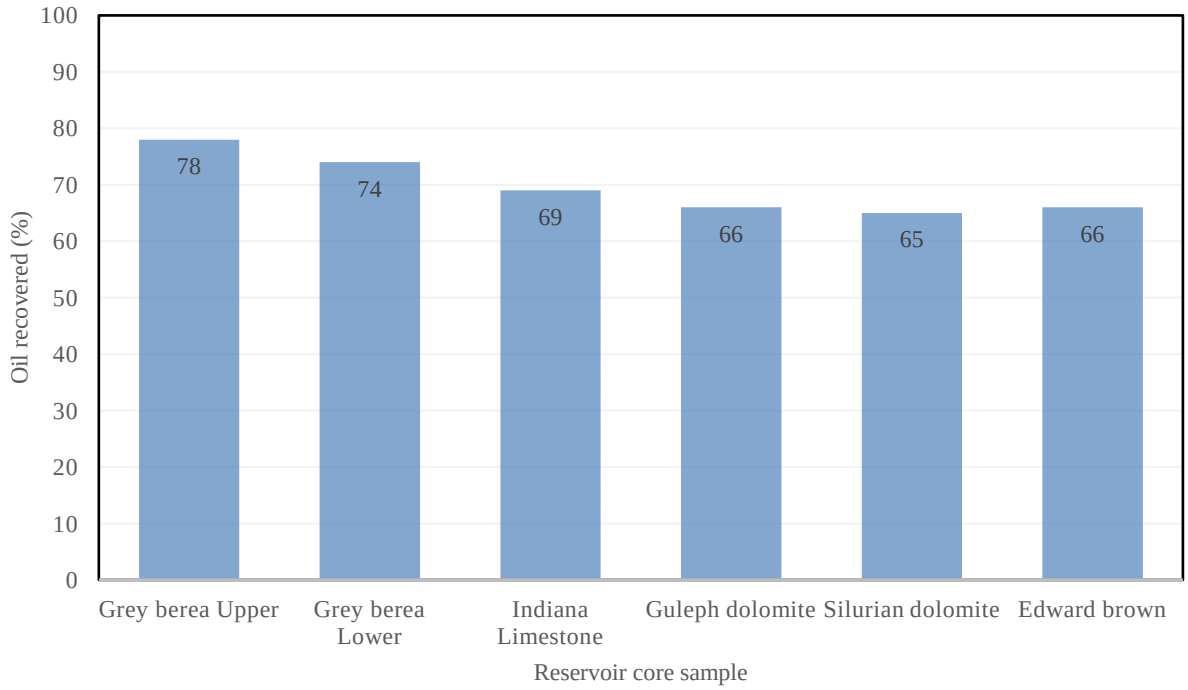

Figure 4.95: Percentage oil recovery at stage 5 (with 6 pore volumes injected with ultrasound) horizontal core assembly

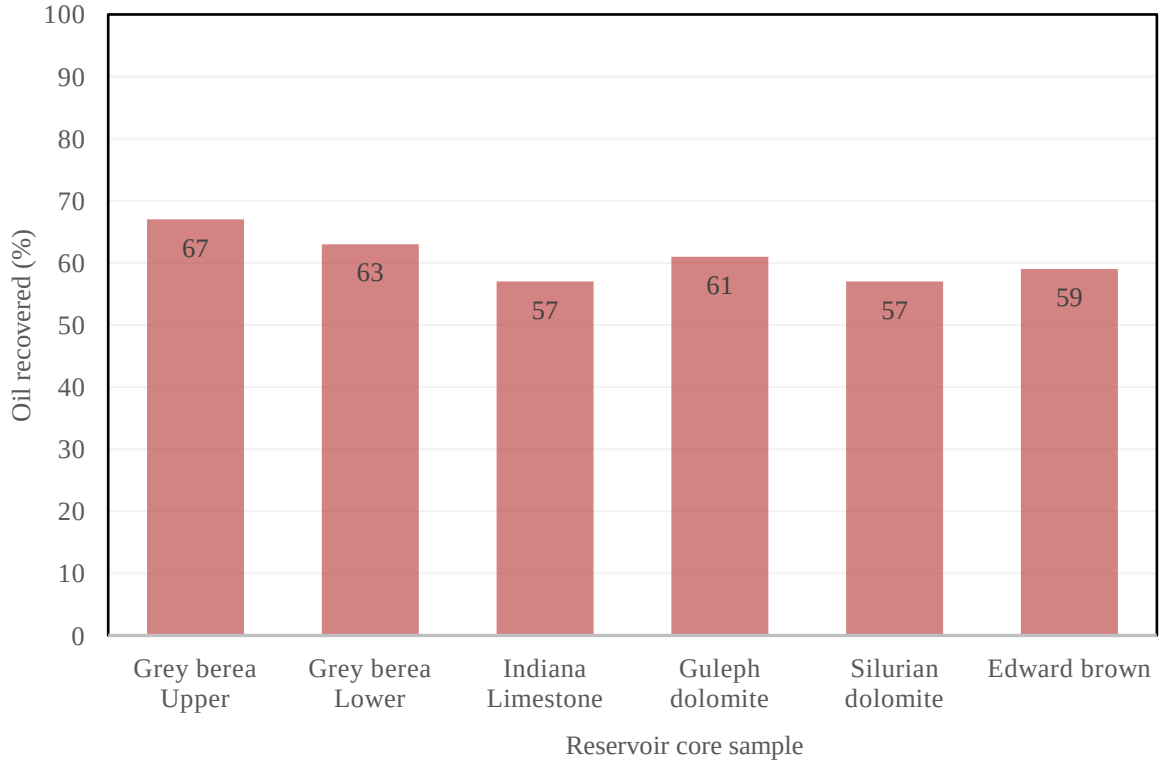

Figure 4.96: Percentage oil recovery at stage 5 (with 6 pore volumes injected without ultrasound) horizontal core assembly

4.4.4.2 Vertical core oil production

In this section, the oil recovered from the sandstone and carbonate rocks based on vertical orientation of the core samples are presented.

In Figure 4.97 the total recovery for Grey Berea Upper, Grey Berea lower, Indiana limestone, Guelph dolomite, Silurian dolomite and Edward brown are 3.83ml (5.40ml PV), 3.22ml (4.88ml PV), 2.87ml (4.63ml PV), 1.55ml (2.57ml PV), 2.26ml (4.11ml PV) and 6.38ml (10.28ml PV) respectively.

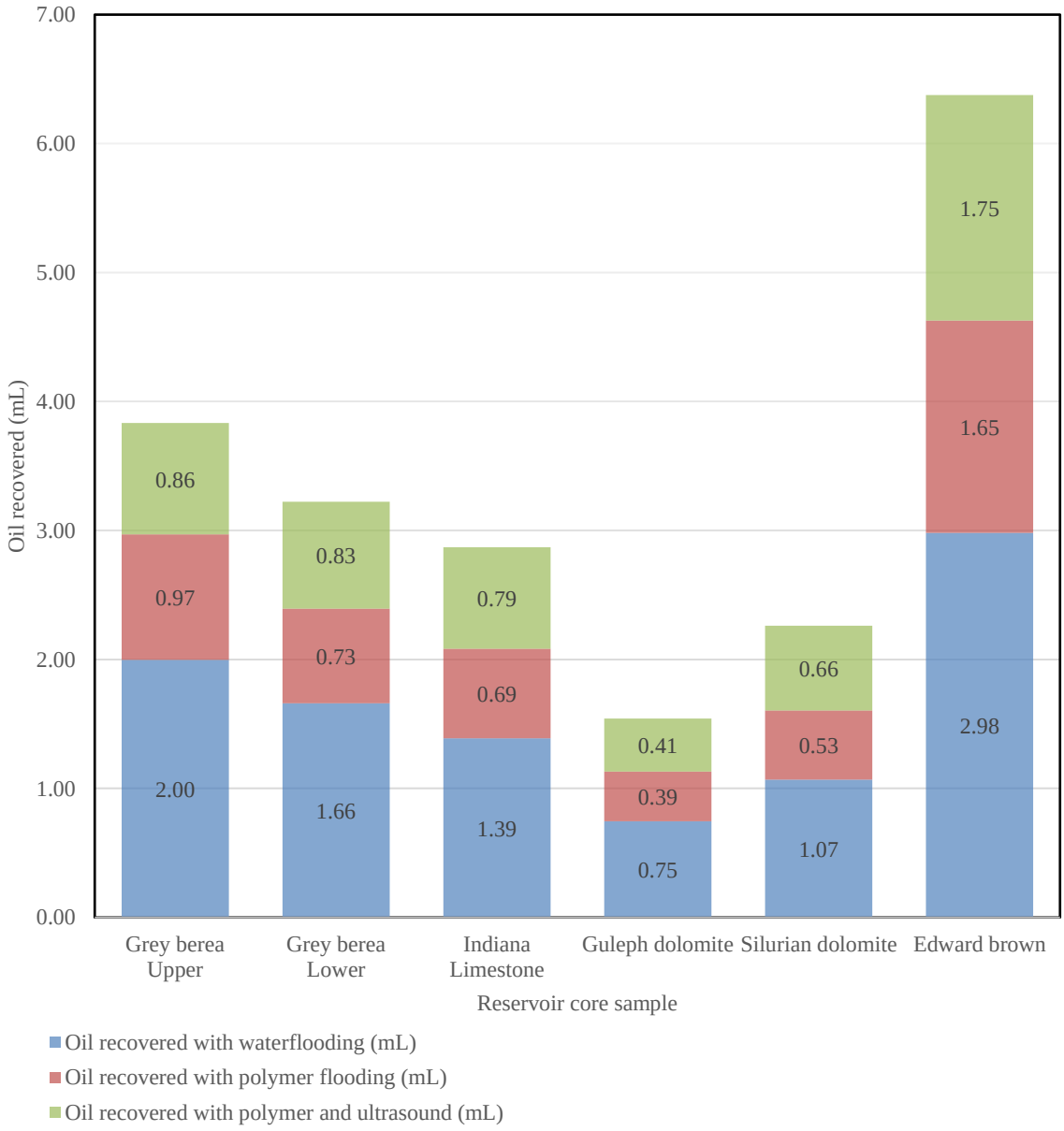

Figure 4.97: Incremental oil recovery with different recovery methods stage 1 (3 PV injected) vertical core assembly

In Figure 4.98 the incremental volumes of oil recovered with injection of one pore volume of water and 2 pore volumes of polymer are shown.

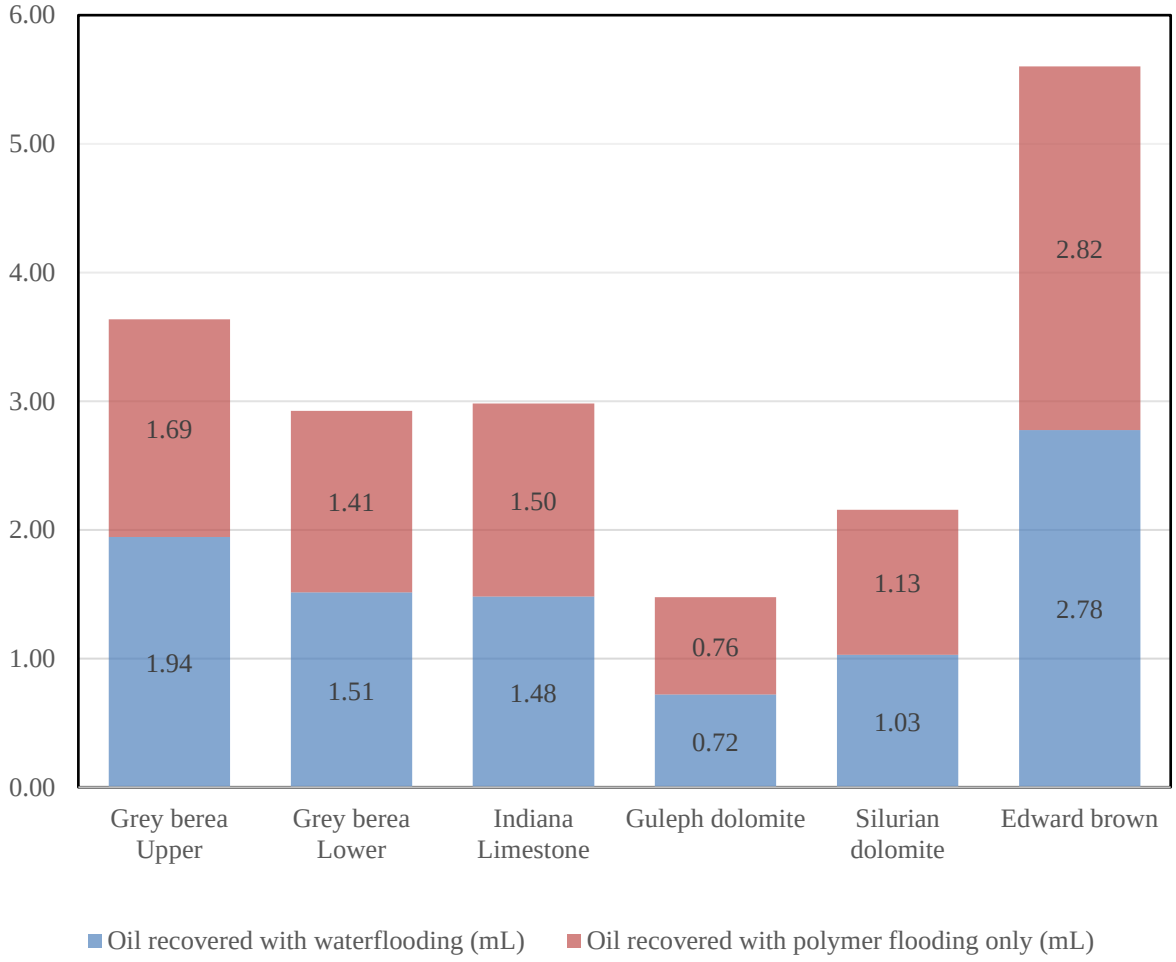

Figure 4.98: Incremental oil recovery with water and polymer flooding stage 1 (3 PV injected) vertical core assembly

In Figure 4.99, the total oil recovery for Grey Berea Upper, Grey Berea lower, Indiana limestone, Guelph dolomite, Silurian dolomite and Edward brown are 4.05ml (5.40ml PV), 3.32mL (4.88mL PV), 2.91mL (4.63mL PV), 1.60mL (2.57mL PV), 2.34mL (4.11mL PV) and 6.58mL (10.28mL PV) respectively.

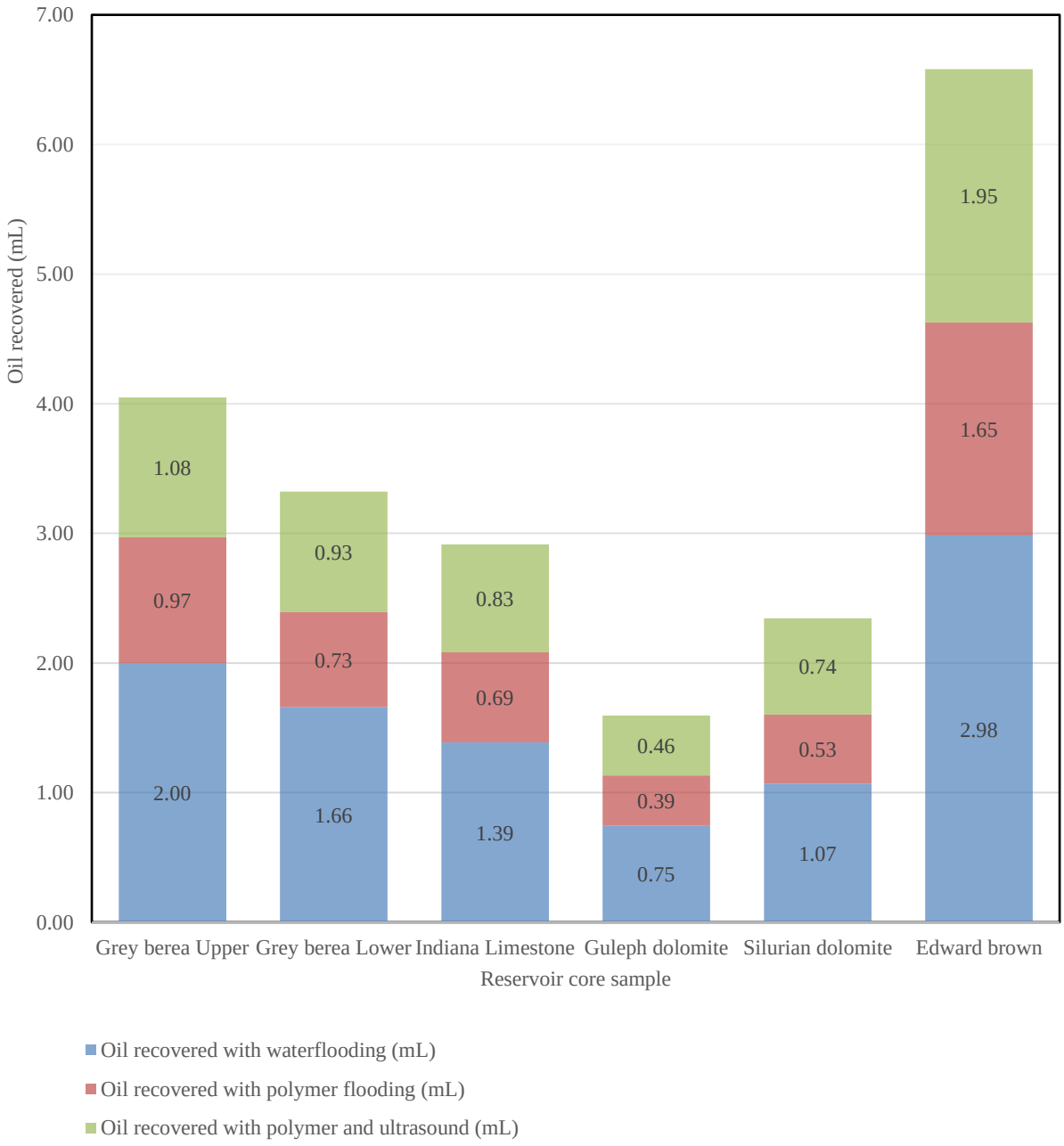

Figure 4.99: Incremental oil recovery with different recovery methods stage 2 (4 PV injected) vertical core assembly

In Figure 4.100 the incremental volumes of oil recovered with injection of one pore volume of water and 3 pore volumes of polymer are shown.

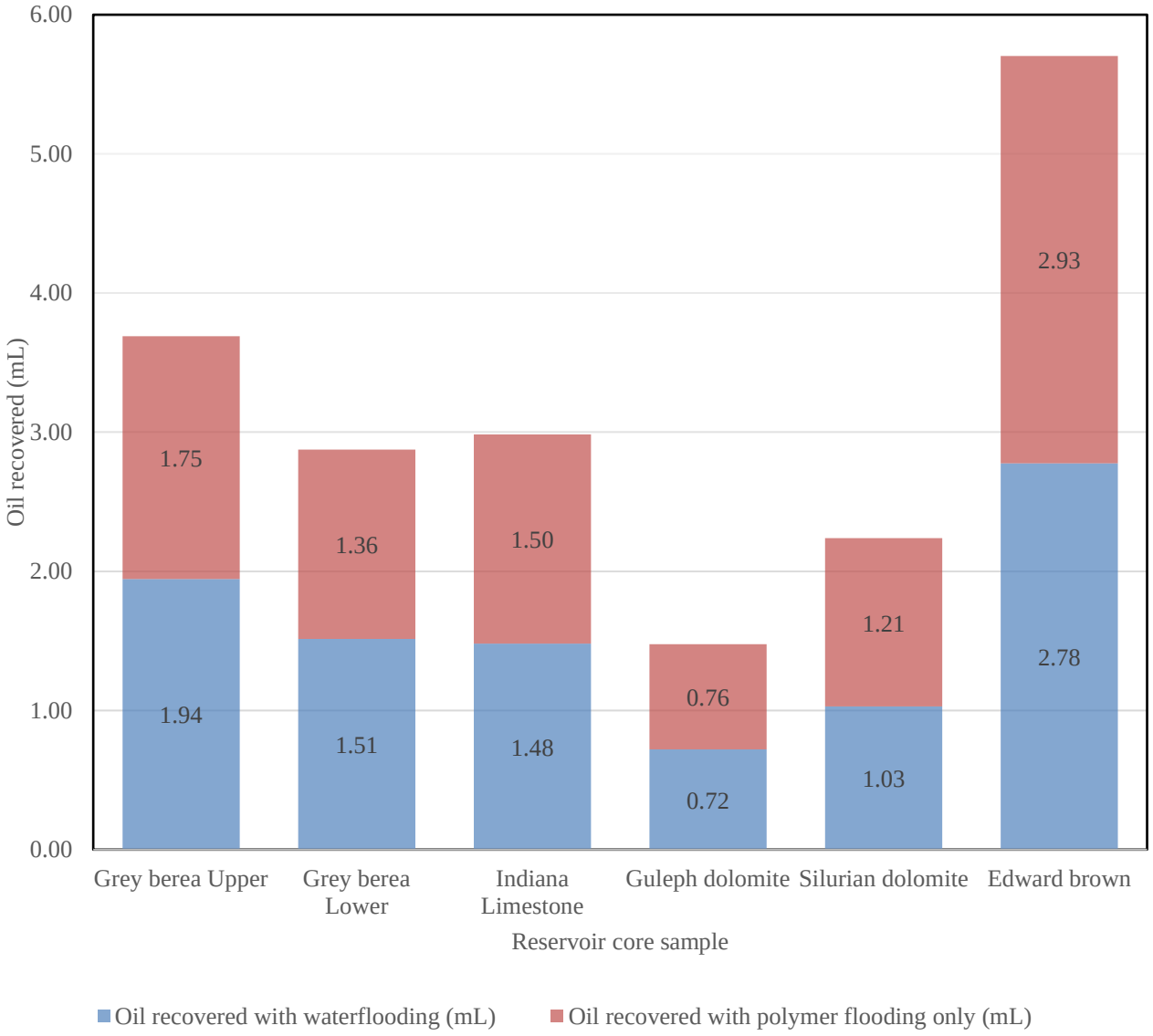

Figure 4.100: Incremental oil recovery with water and polymer flooding stage 2 (3 PV injected) vertical core assembly

In Figure 4.101, the total oil recovery for Grey Berea Upper, Grey Berea lower, Indiana limestone, Guelph dolomite, Silurian dolomite and Edward brown are 4.61ml (5.40ml PV), 3.42ml (4.88ml PV), 2.91ml (4.63ml PV), 1.63ml (2.57ml PV), 2.34ml (4.11ml PV) and 6.69ml (10.28ml PV) respectively.

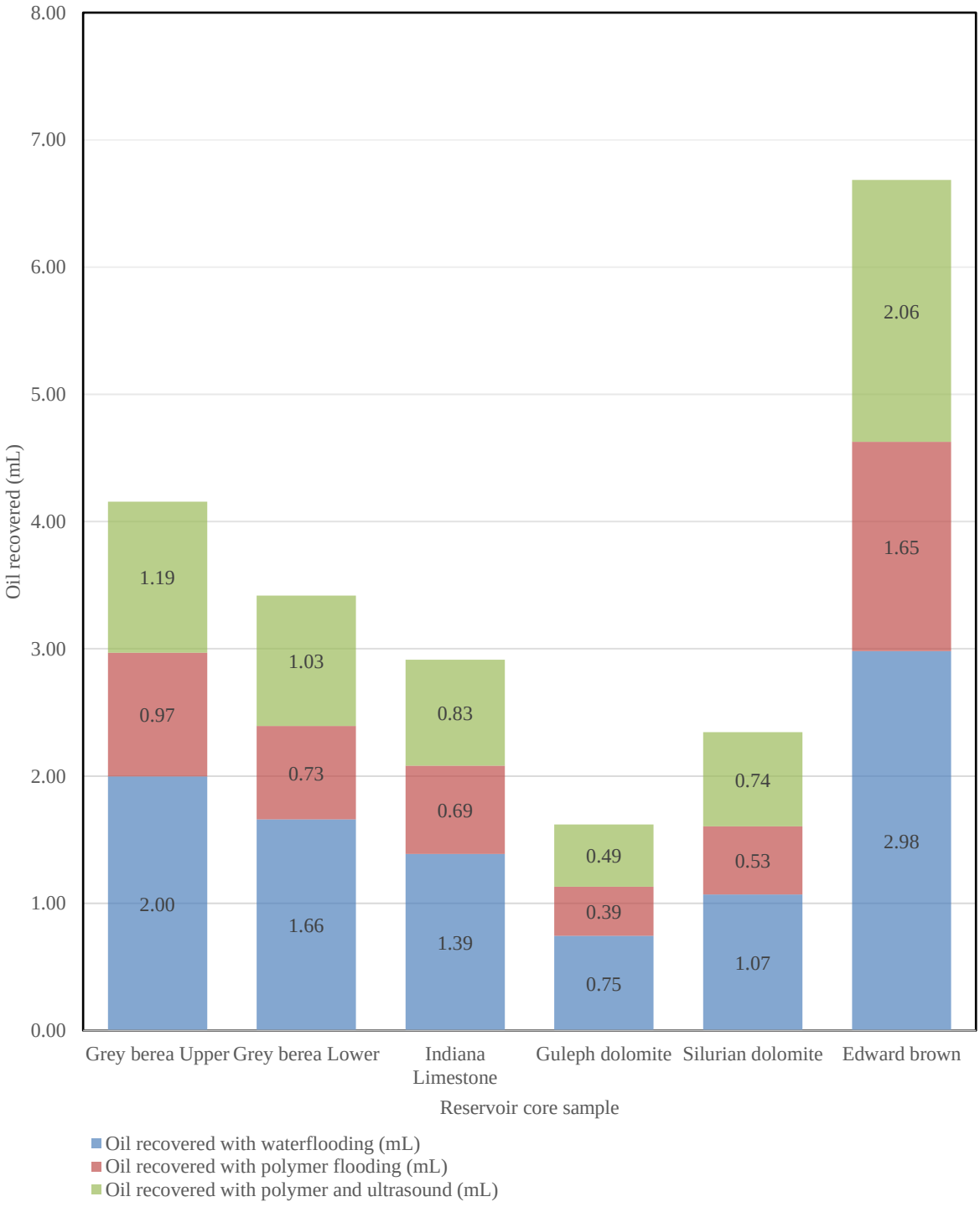

Figure 4.101: Incremental oil recovery with different recovery methods stage 3 (5 PV injected) vertical core assembly

In Figure 4.102 the incremental volumes of oil recovered with injection of one pore volume of water and 4 pore volumes of polymer are shown

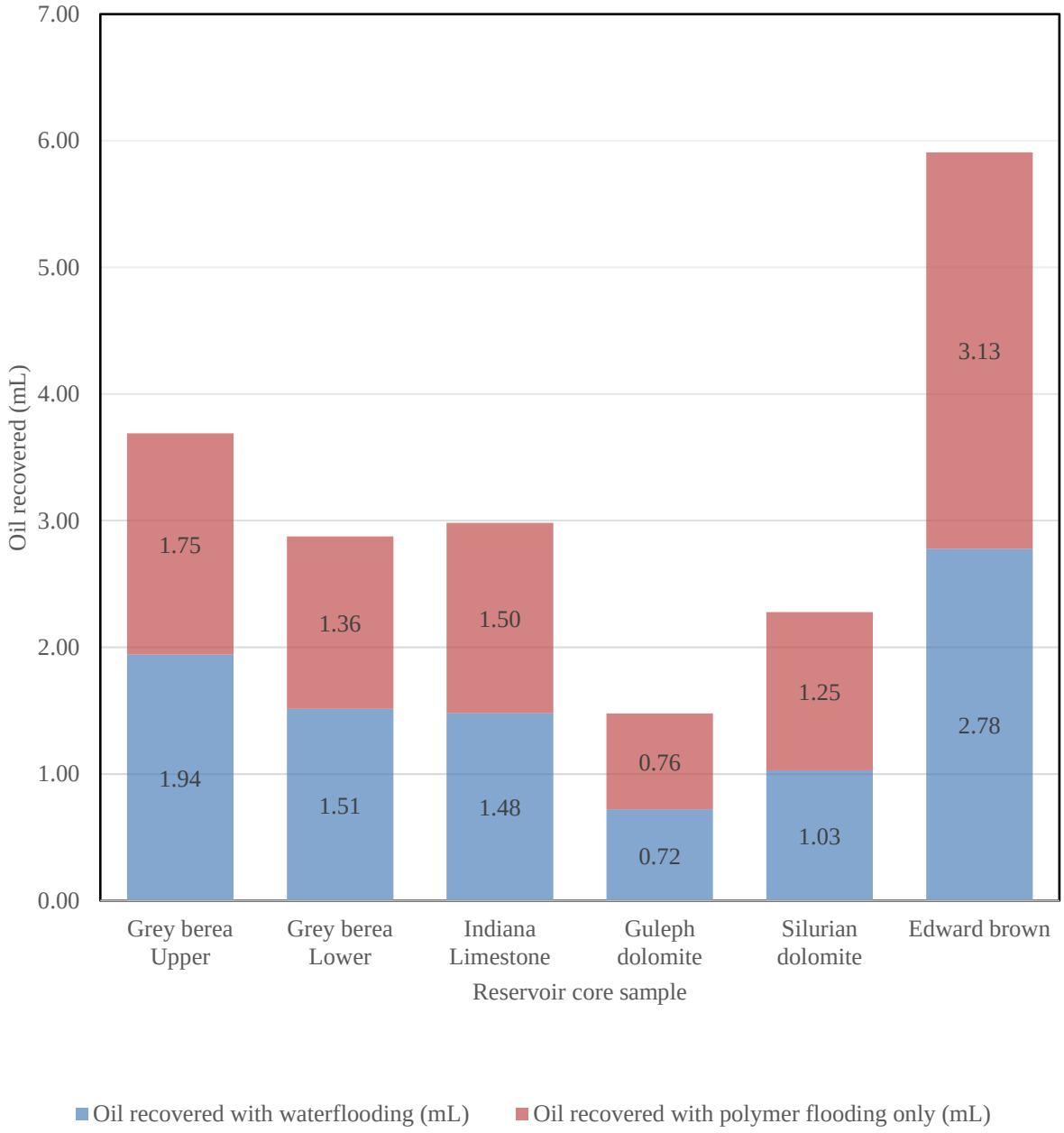

Figure 4.102: Incremental oil recovery with water and polymer flooding stage 3 (5 PV injected) vertical core assembly

In Figure 4.103, the total oil recovery for Grey Berea Upper, Grey Berea lower, Indiana limestone, Guelph dolomite, Silurian dolomite and Edward brown are 4.27ml (5.40ml PV), 3.51ml (4.88ml PV), 3.10ml (4.63ml PV), 1.68ml (2.57ml PV), 2.50ml (4.11ml PV) and 7.1ml (10.28ml PV) respectively.

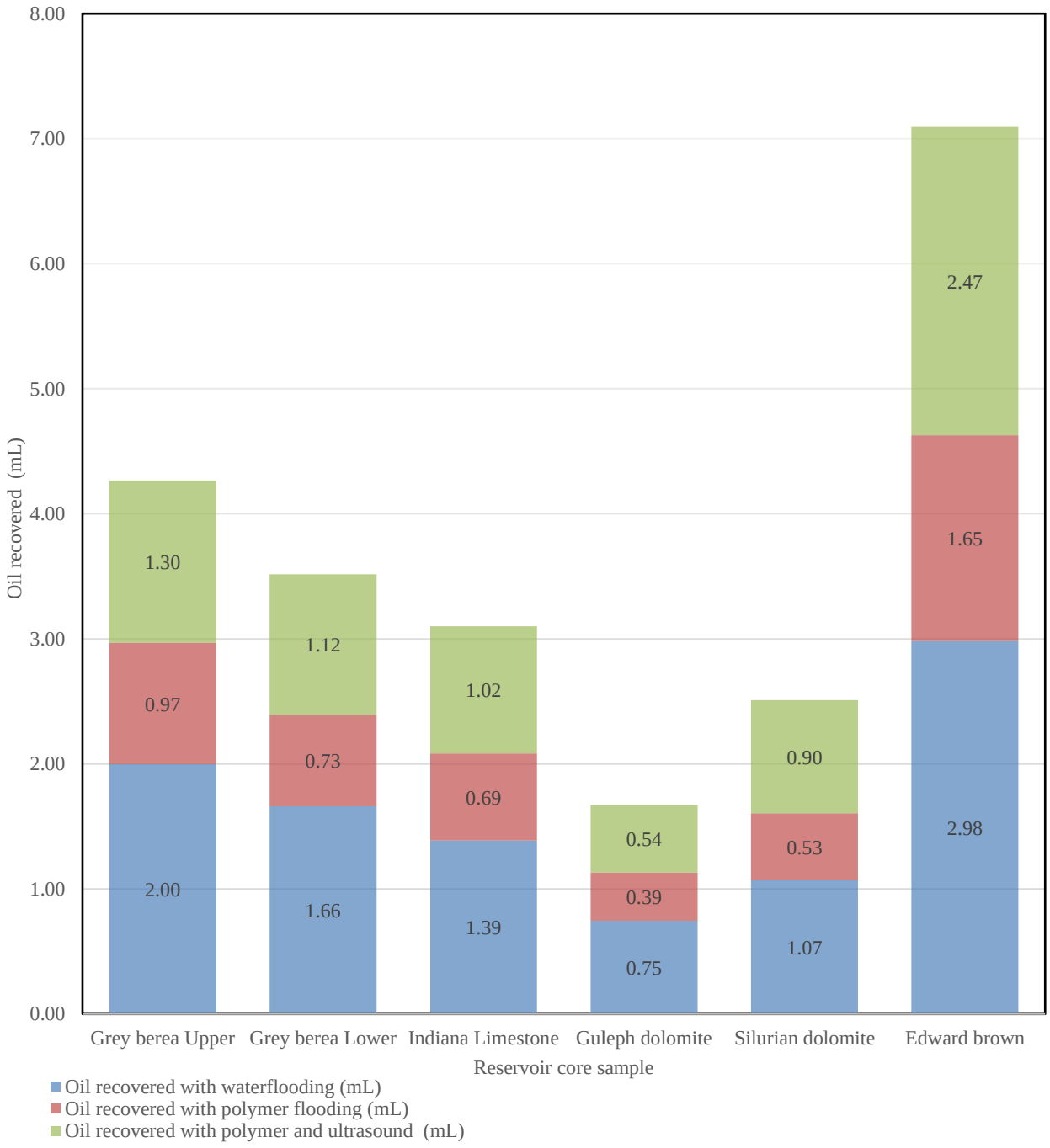

Figure 4.103: Incremental oil recovery with different recovery methods stage 4 (6 PV injected) vertical core assembly

In Figure 4.104 the incremental volumes of oil recovered with injection of one pore volume of water and 5 pore volumes of polymer are shown

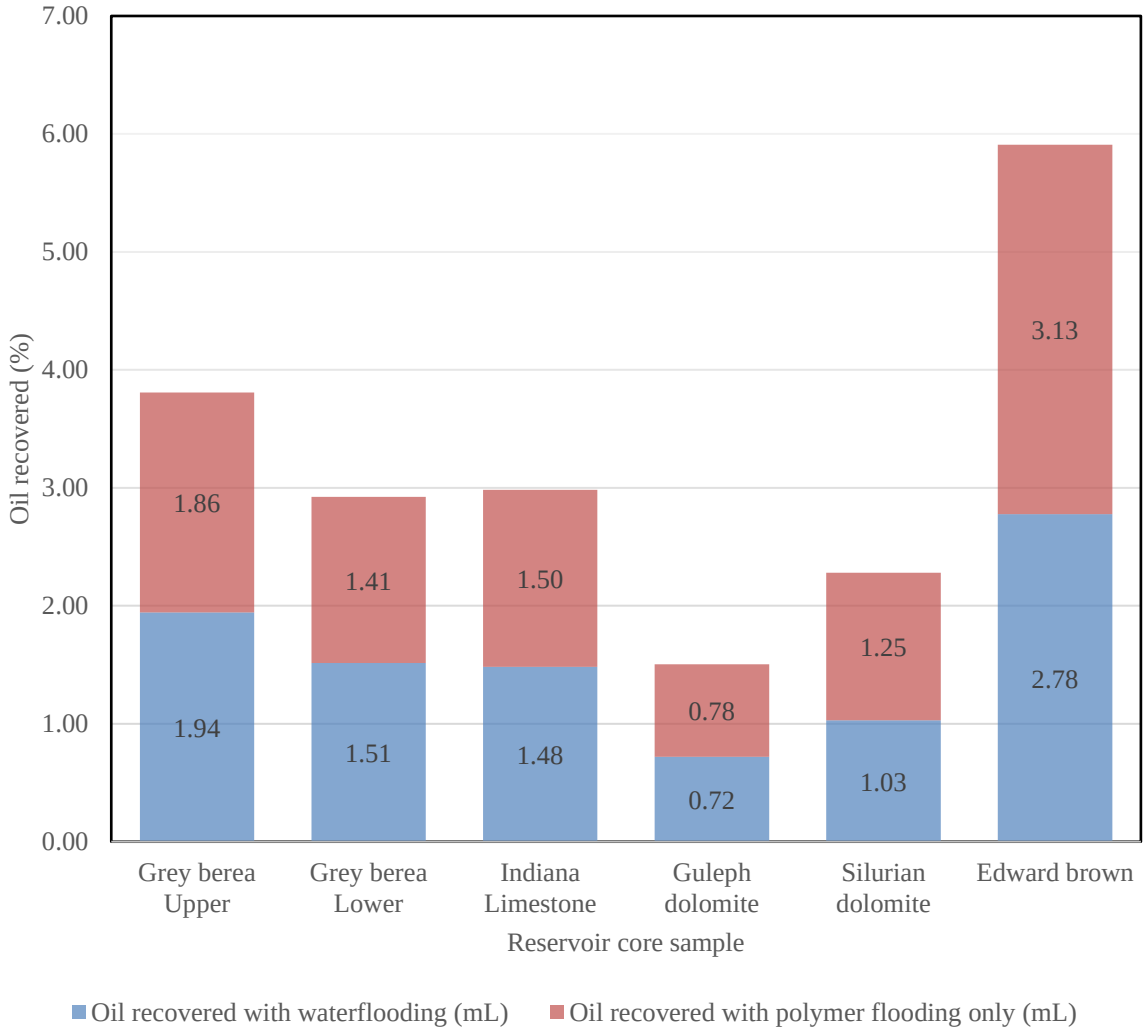

Figure 4.104: Incremental oil recovery with water and polymer flooding stage 4 (5 PV injected) vertical core assembly

In Figure 4.105, the total recovery for Grey Berea Upper, Grey Berea lower, Indiana limestone, Guelph dolomite, Silurian dolomite and Edward brown are 4.32ml (5.40ml PV), 3.66ml (4.88ml PV), 3.38ml (4.63ml PV), 1.73ml (2.57ml PV), 2.55ml (4.11ml PV) and 7.2ml (10.28ml PV) respectively.

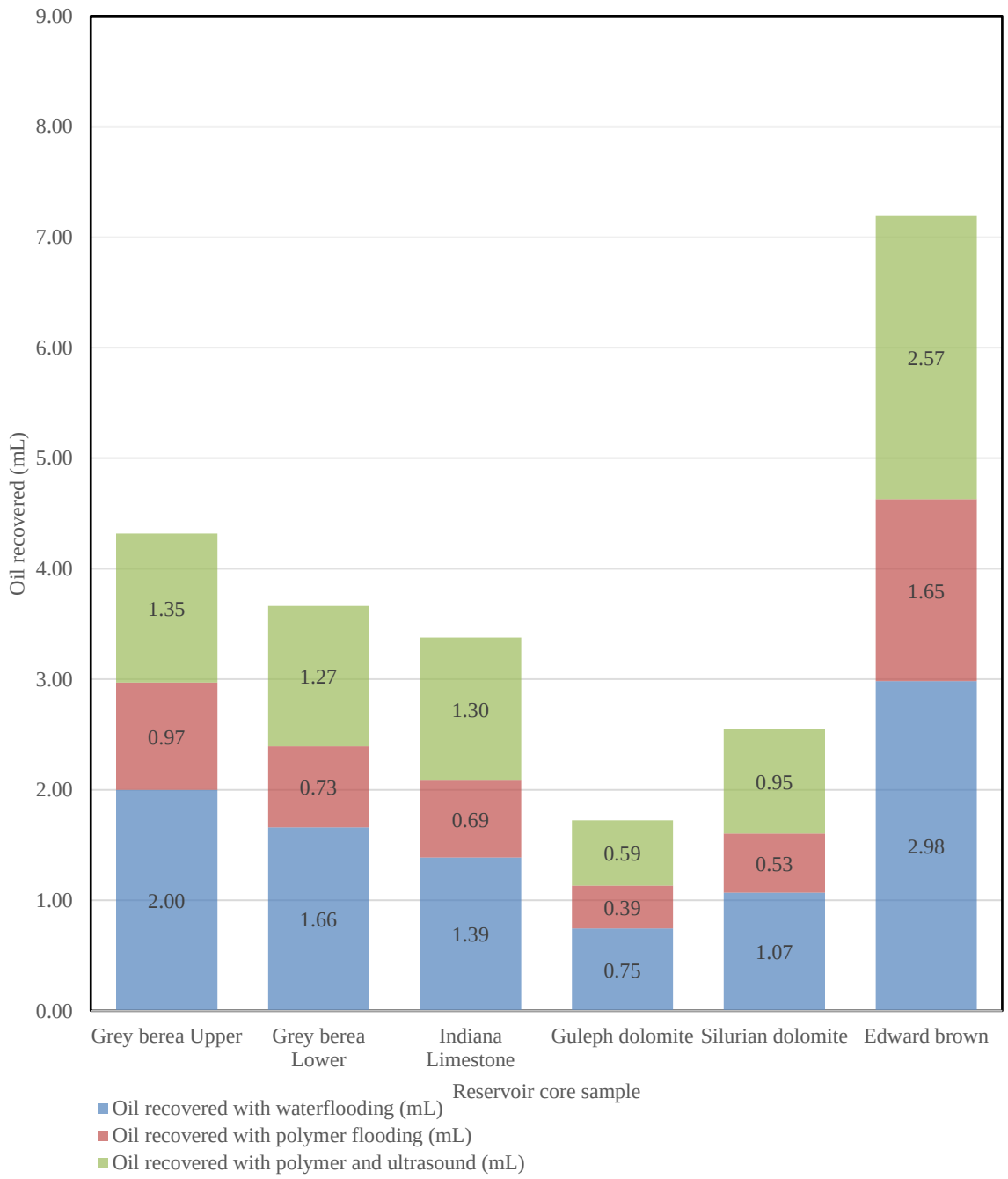

Figure 4.105: Incremental oil recovery with different recovery methods stage 5 (7 PV injected) vertical core assembly

In Figure 4.106 the incremental volumes of oil recovered with injection of one pore volume of water and 6 pore volumes of polymer are shown

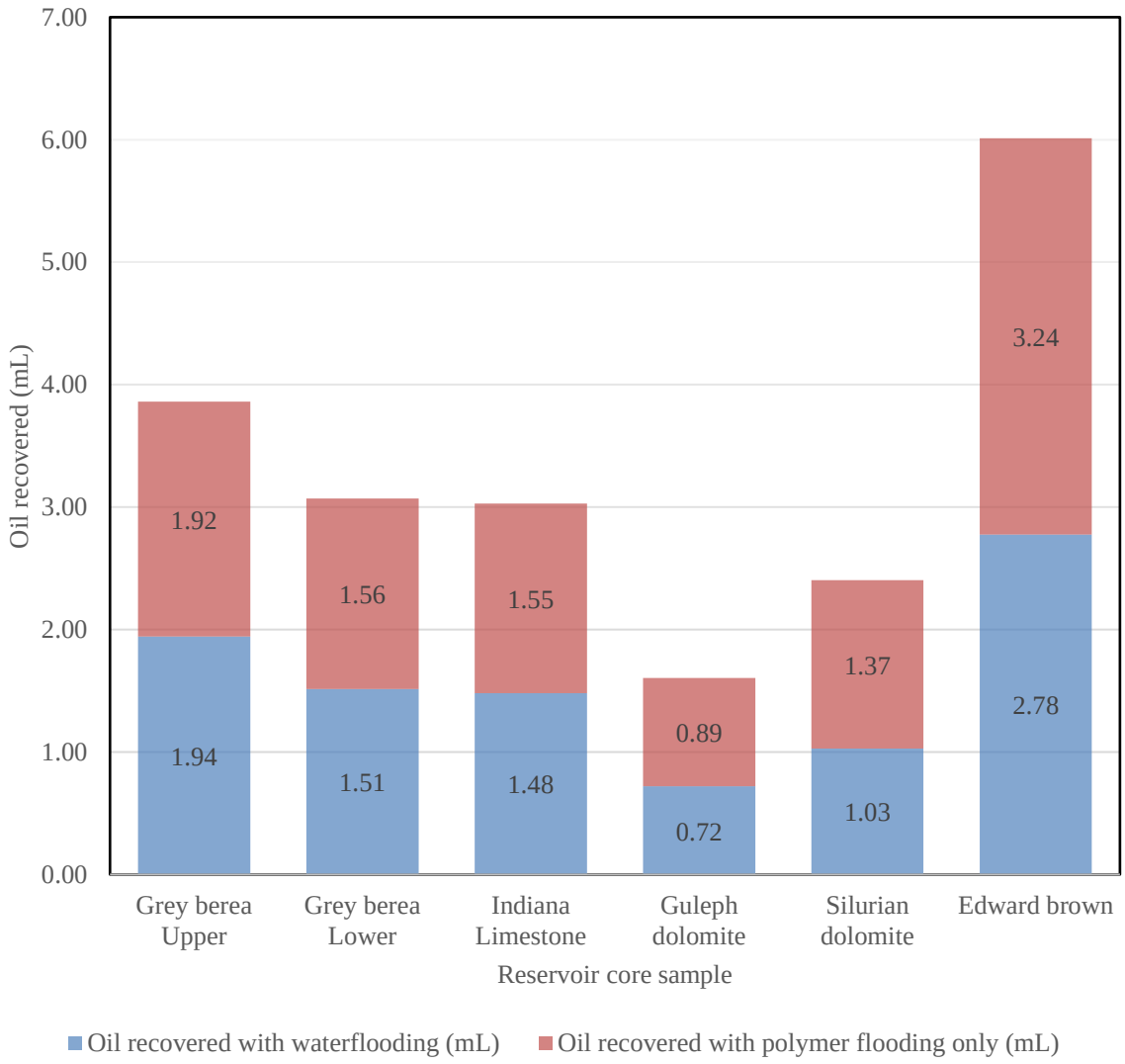

Figure 4.106: Incremental oil recovery with water and polymer flooding stage 5 (7 PV injected) vertical core assembly

4.4.4.2.1 Overall oil recovery

The overall oil recovered as a percentage of recoverable original oil in place (OOIP) for a three- pore volume injection for five different core samples are shown in Figure 4.107, Figure 4.109, Figure 4.111, Figure 4.113 and Figure 4.115. Each of the graphs illustrates the incremental oil recovered based on pore volume injected. Equivalent graphs for polymer injection are shown in Figure 4.108, Figure 4.110, Figure 4.114 and Figure 4.116 respectively.

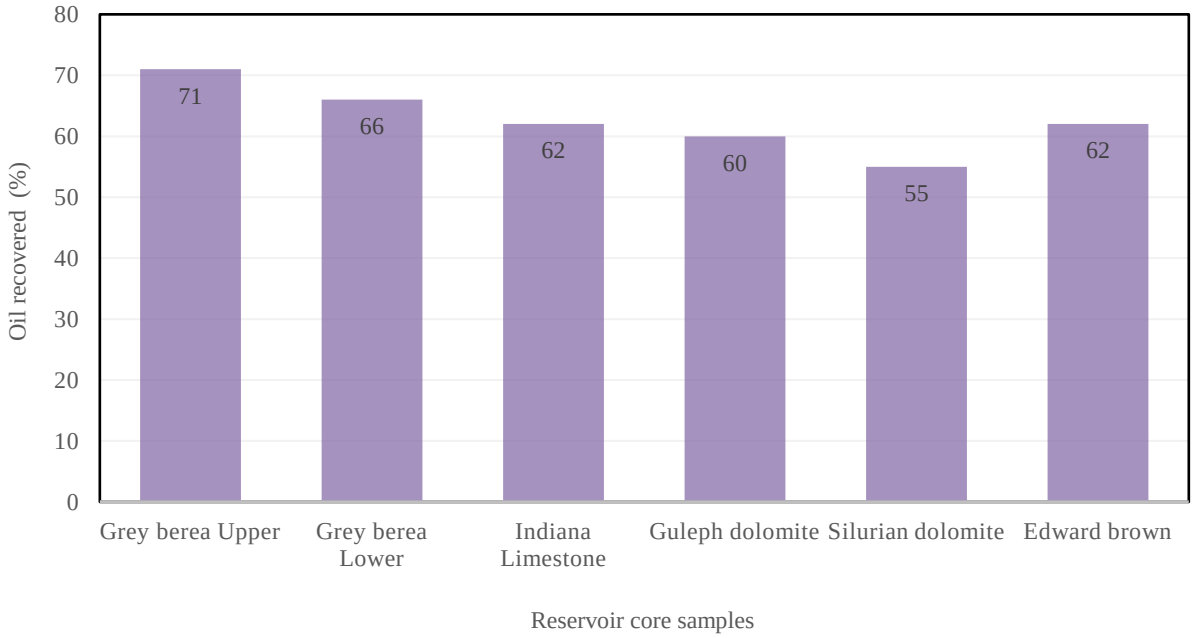

Figure 4.107: Percentage oil recovery at Stage 1 (with 3 pore volumes injected with ultrasound) and Vertical core assembly

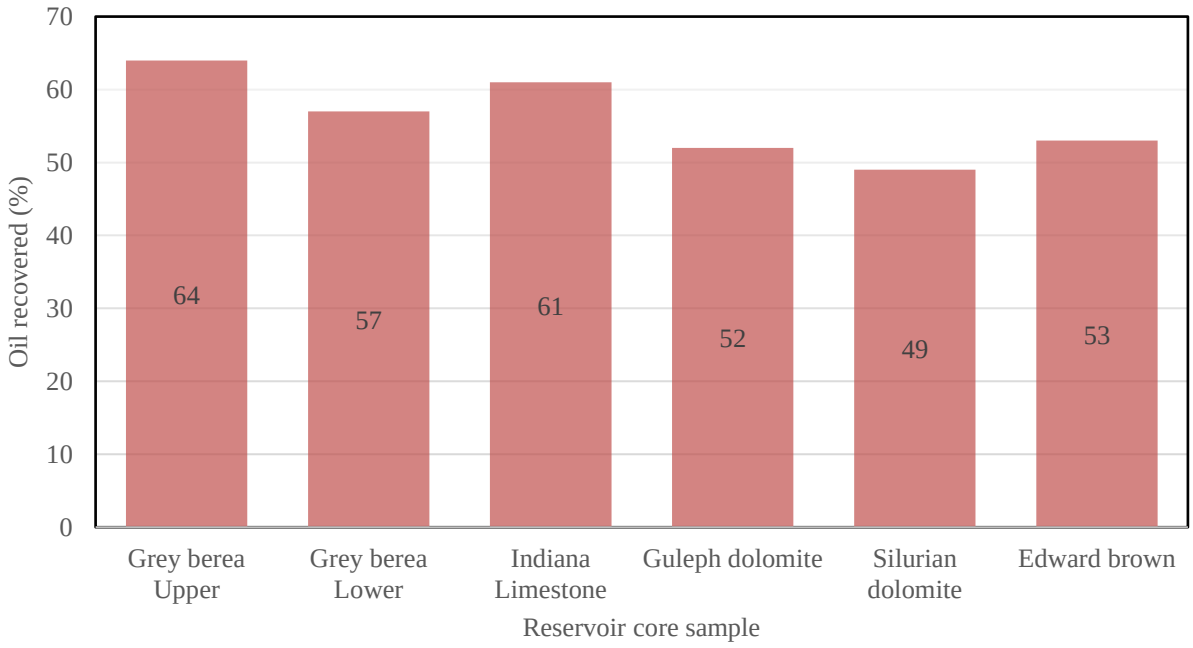

Figure 4.108 Percentage oil recovery at Stage 1 (with 3 pore volumes injected without ultrasound) and Vertical core assembly

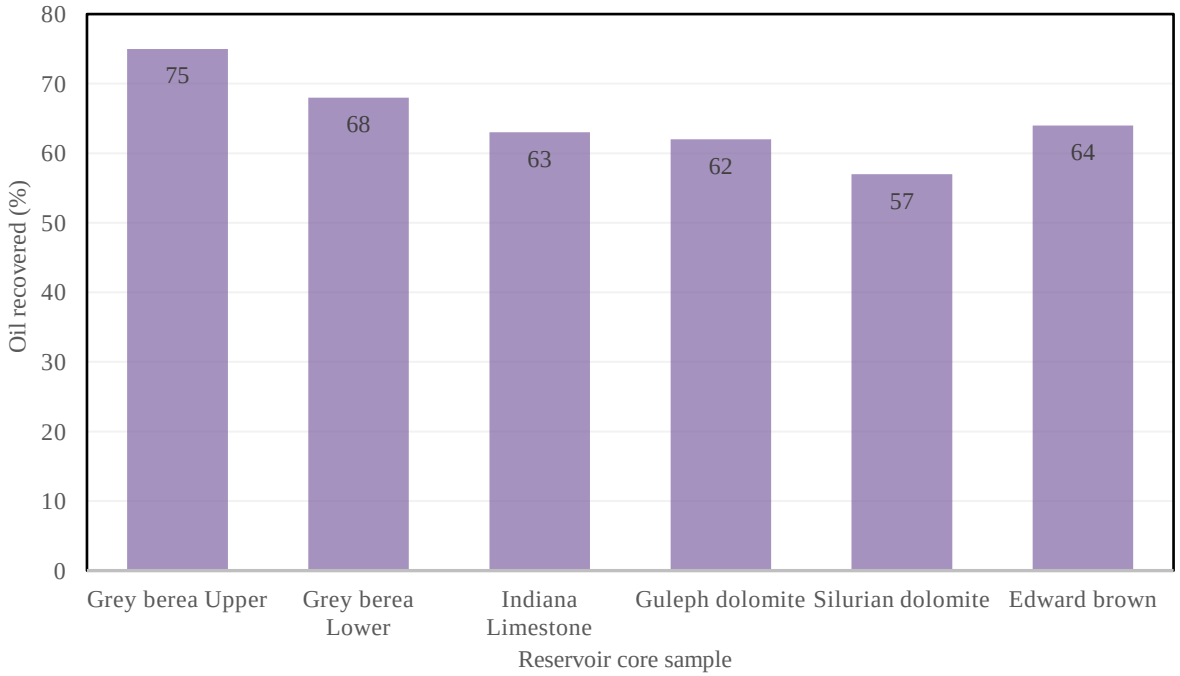

Figure 4.109: Percentage oil recovery at Stage 2 (with 4 pore volumes injected with ultrasound) and Vertical core assembly

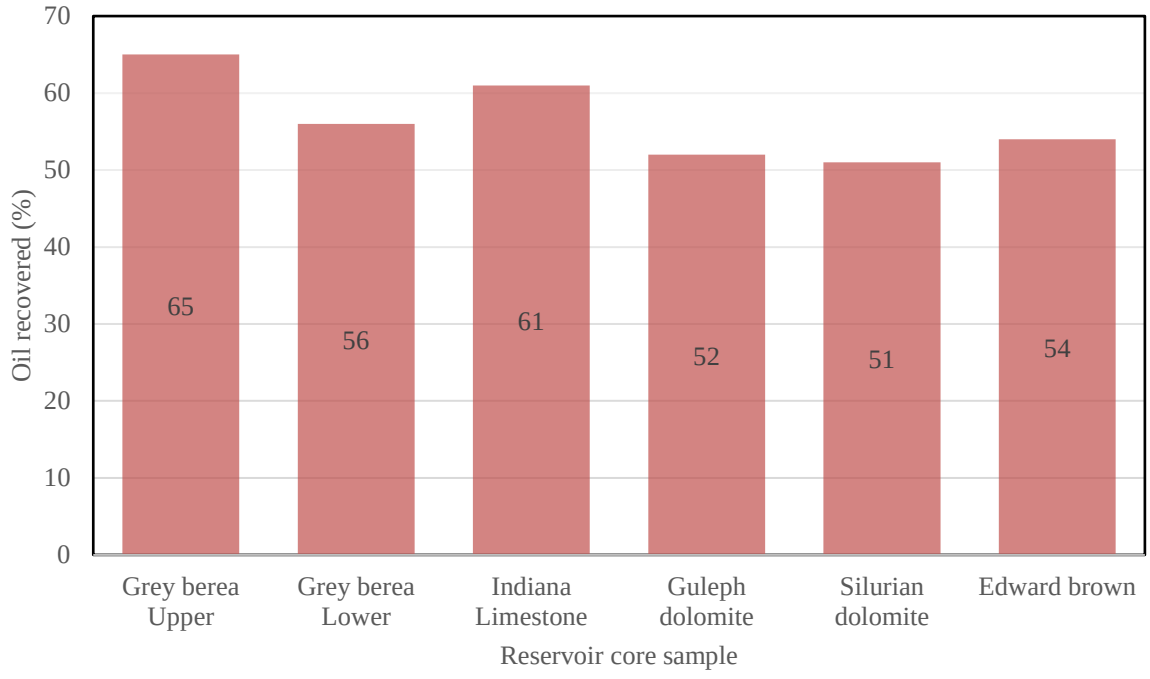

Figure 4.110: Percentage oil recovery at Stage 2 (with 4 pore volumes injected without ultrasound) vertical core assembly

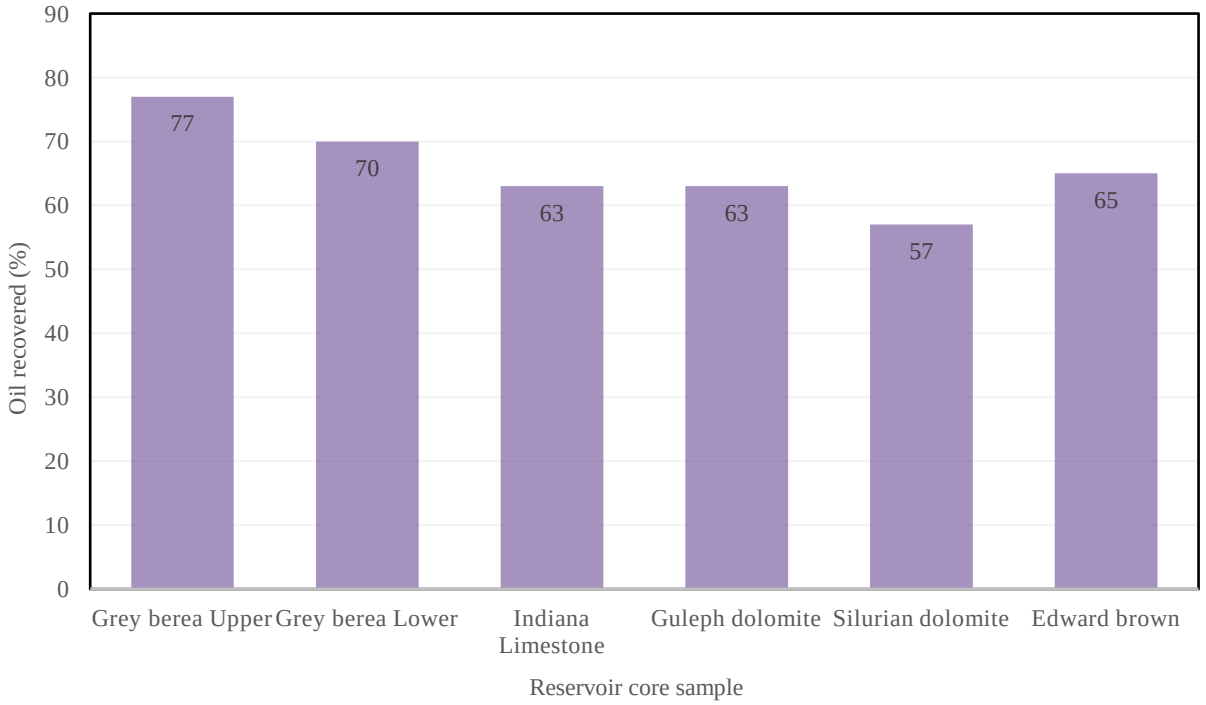

Figure 4.111: Percentage oil recovery at Stage 3 (with 5 pore volumes injected with ultrasound) vertical core assembly

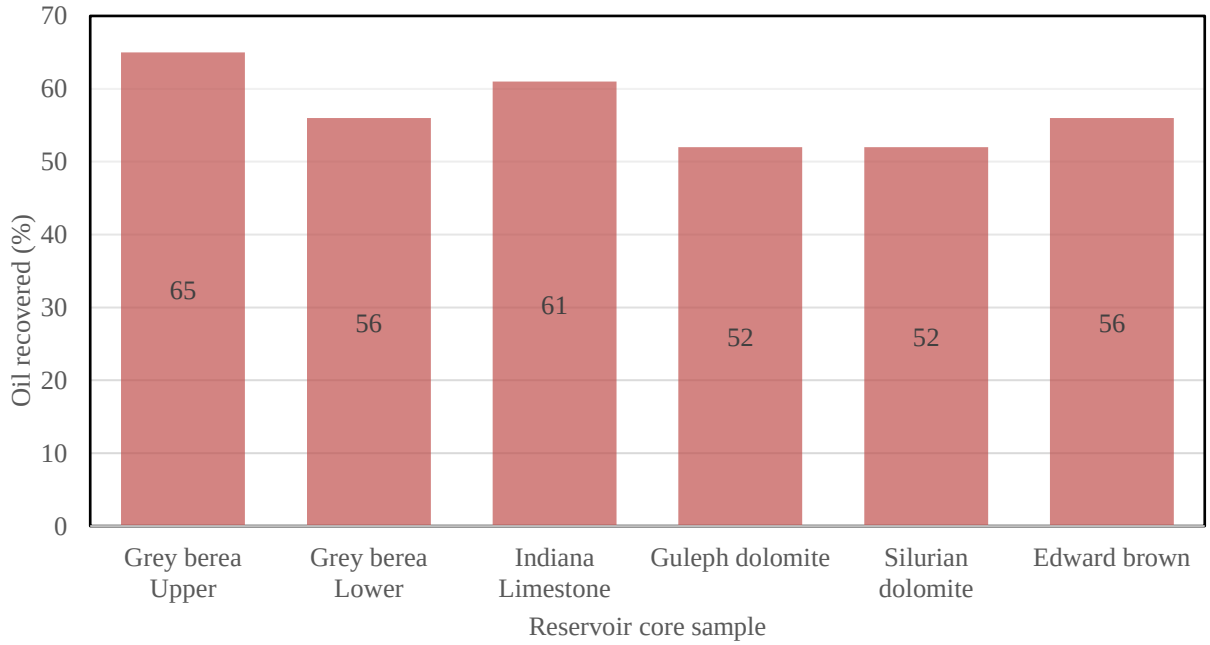

Figure 4.112: Percentage oil recovery at Stage 3 (with 5 pore volumes injected without ultrasound) vertical core assembly

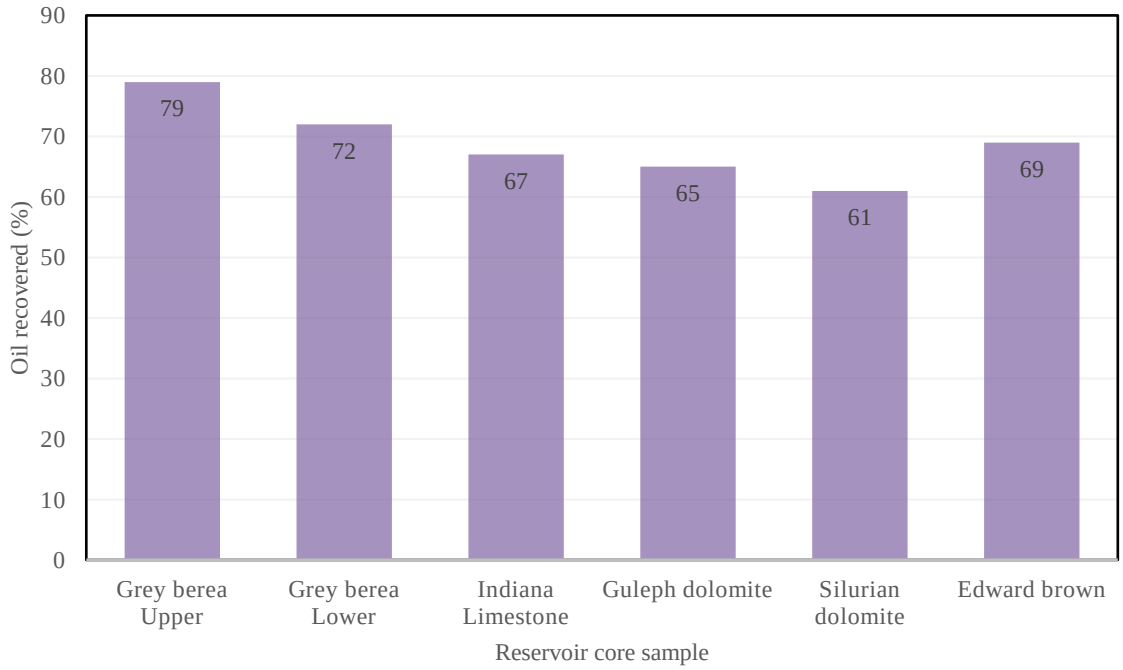

Figure 4.113: Percentage oil recovery at Stage 4 (with 6 pore volumes injected) vertical core assembly

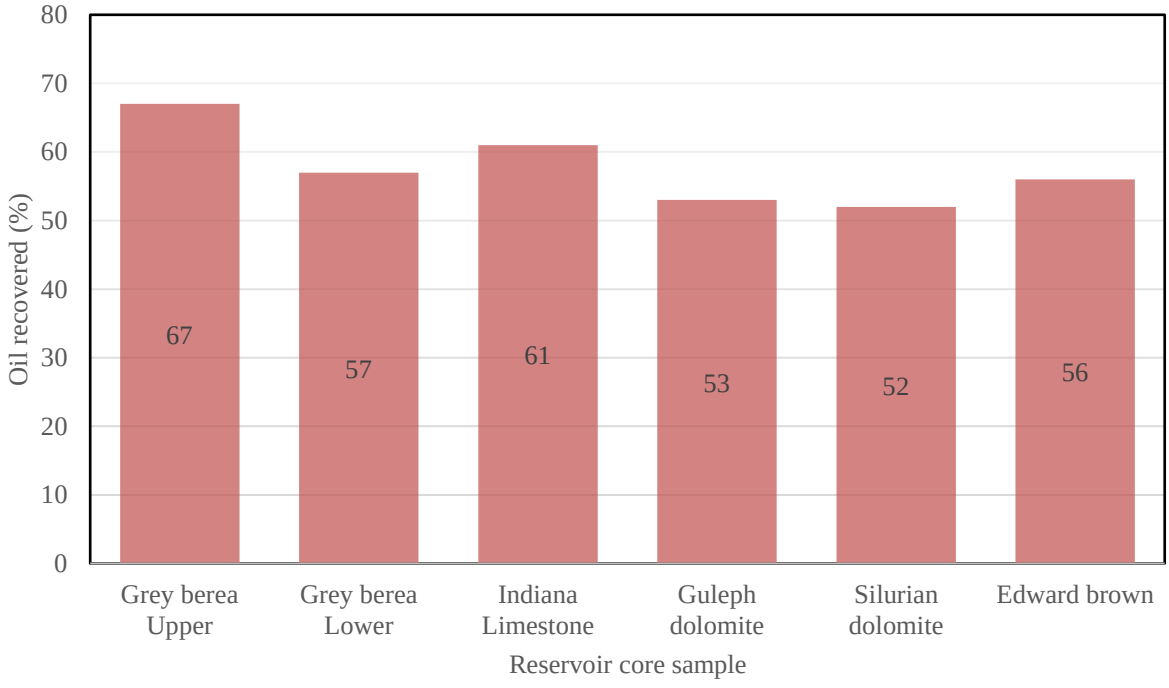

Figure 4.114: Percentage oil recovery at Stage 4 (with 6 pore volumes injected with ultrasound) vertical core assembly

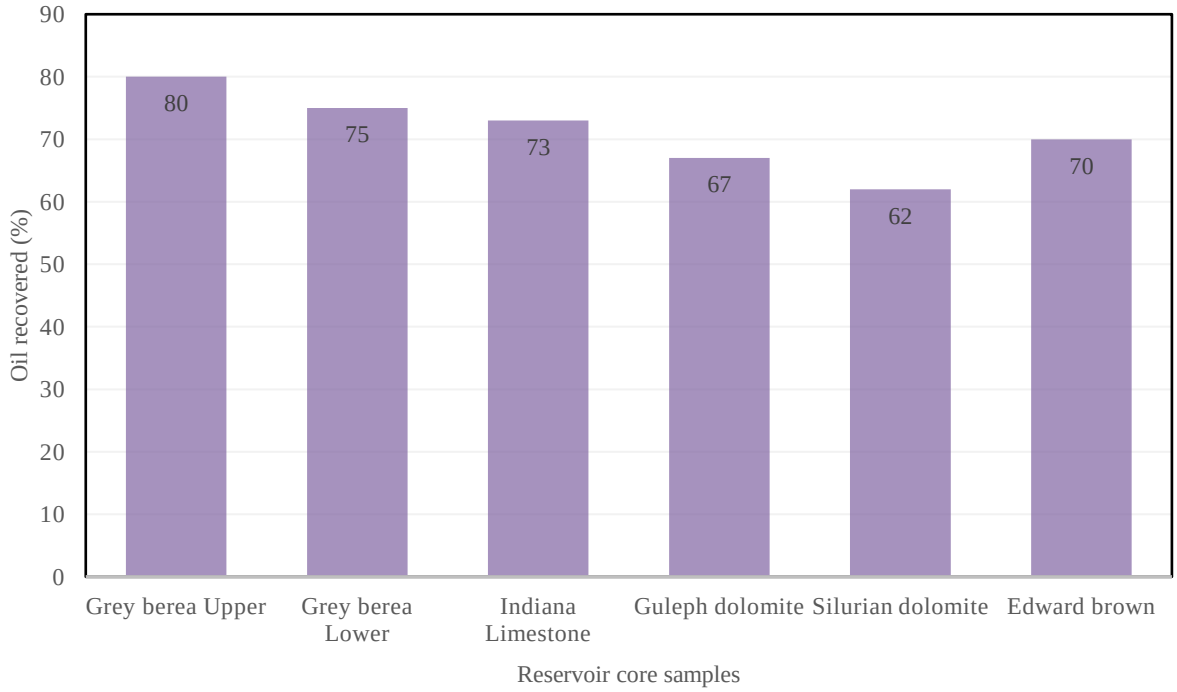

Figure 4.115: Percentage oil recovery at Stage 5 (with 7 pore volumes injected with ultrasound) vertical core assembly

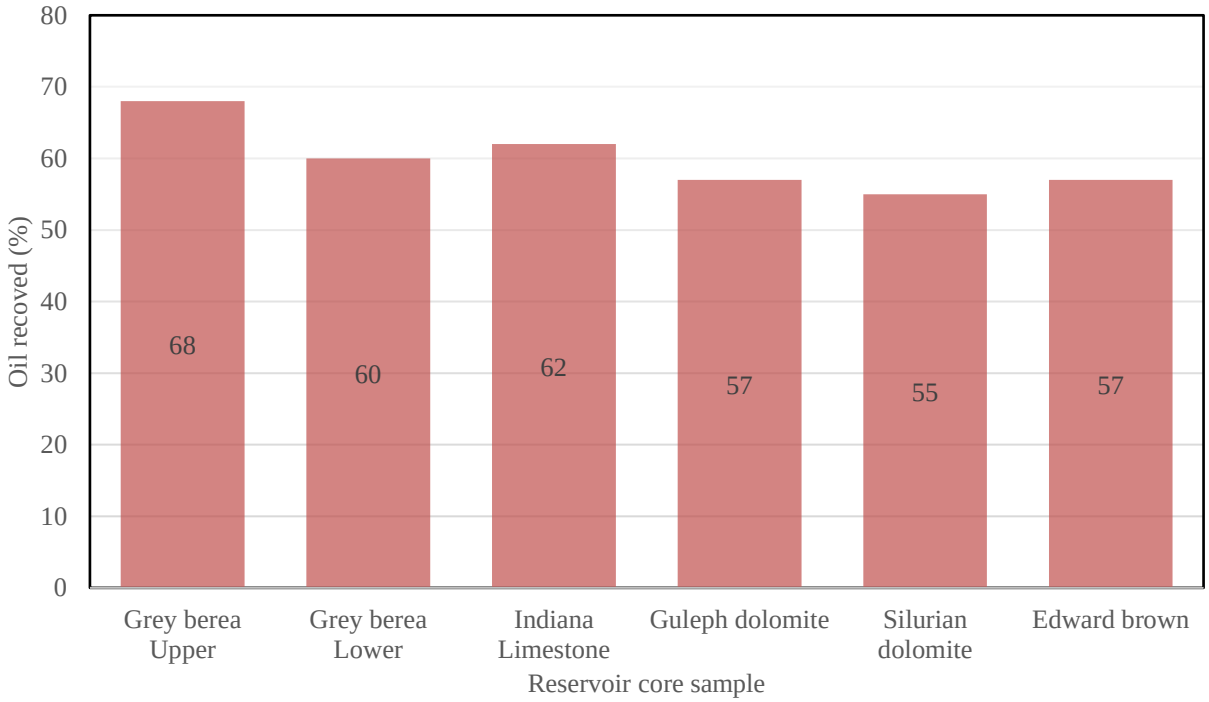

Figure 4.116: Percentage oil recovery at Stage 5 (with 7 pore volumes injected without ultrasound) vertical core assembly

4.4.4.2.2 Residual oil saturation

The residual oil saturation (ROS) is oil left in the pore space after enhanced oil recovery operations have been exhaustively conducted. The residual oil saturation can be defined as the ratio of the immobile residual oil volume divided by the porosity of the reservoir core. The ROS indicates the effectiveness and efficiency of the EOR method utilised. The lower the ROS, the more effective and efficient the recovery method adopted.

Here, the residual oil saturation obtained is presented in Table 4.13 and Table 4.14 for the horizontal and vertical assemblies, respectively. Each of the tables shows the ROS in two rows, one polymer flooding with ultrasound and the other polymer flooding without ultrasound. The displacing pore volume injected was 7PV.

The ROS values obtained when ultrasound was applied with polymer flooding were significantly lower for all scenarios: horizontal and vertical assemblies. This implies that the oil recovery is more efficient and effective when polymer flooding and ultrasound are integrated in enhanced oil recovery.

Table 4:13 Residual oil saturation for horizontal assembly

Reservoir Core sample	Grey berea Upper	Grey berea Lower	Indiana Limestone	Guleph dolomite	Silurian dolomite	Edward brown
ROS (with ultrasound)	0.22	0.32	0.40	0.39	0.40	0.40
ROS (without ultrasound)	0.33	0.37	0.43	0.39	0.43	0.41

Table 4:14 Residual oil saturation for vertical assembly

Reservoir Core sample	Grey berea Upper	Grey berea Lower	Indiana Limestone	Guleph dolomite	Silurian dolomite	Edward brown
ROS (with ultrasound)	0.20	0.25	0.27	0.33	0.38	0.30
ROS (without ultrasound)	0.32	0.40	0.38	0.43	0.45	0.43

4.5 Evaluation of enhanced oil recovery

In section 4.4.4 the oil recovery in both horizontal and vertical displacement core holder positions for sandstone and carbonate cores were presented. The sandstone core samples were Berea Upper sandstone and Berea lower sandstone. The carbonate core samples were Indiana limestone, Guelph dolomite, Silurian dolomite and Edward brown limestone. All the core samples underwent initial water saturation to create water-wet reservoir scenario. Oil injection into the core samples displaced the water saturation to oil saturated core samples. With the injection of one pore volume in waterflooding, an initial oil recovery was measured. Subsequently, polymer flooding was performed followed by polymer with ultrasound. However, during the polymer and ultrasound recovery a series of pore volumes of polymer were injected to determine extent of residual oil desaturation.

All the graphical representations in sections 4.4.4 showed incremental oil produced from both the sandstone and carbonate rocks. However, the incremental oil recovered from the sandstone core samples were in all instances higher than the incremental oil recovered from carbonate core samples, even though equivalent pore volumes of water, polymer, polymer and ultrasound were utilised on each core sample. Several factors were attributed to the higher oil recovery from sandstones reservoirs irrespective either vertical and horizontal displacement when compared with carbonate rocks. These factors are discussed in detail in the proceeding subsections.

4.5.1.1 Pore geometry and pore distribution

One of the unique characteristics of sandstone reservoirs was the greater uniformity of pore geometry and pore distribution when compared with carbonate reservoirs. During the period of diagenesis, when the sandstones are formed, depositions were often in layers in strata. Each section within strata had uniform properties and characteristics. A close observation of all the sandstone core samples: Berea upper and Berea Lower sandstones indicated a uniform pore geometry and pore distribution including uniform pore sizing. On the other hand, the carbonate rocks had large pores, and with some disproportionate size pores. The concentration of uniforms pores in the carbonate rock was a lot lower than observed in the sandstones. The computed tomography scan clearly illustrated this property in the transparency zero settings (Section 4.3.1) During injection and fluid flow through the tortuous micro and macro pore network of the carbonate rocks, the flow profile was highly distorted leading to the pressure dropping and variable fluid flow velocities due to non-

uniformity of the pore network. Because of the non- uniform pore network, the displacement potential of the displacing fluid was reduced in carbonate rocks. The flow profile of displacing fluid was distorted. Trapped oil is left in the crevices and restrictive micro pores of the rocks. The sweep efficiency of displacing fluid is lowered and overall oil recovery from the carbonate is lower. However, sandstone rocks exhibit greater uniformity of both micro and macro pore network. This was evident in the computed tomography scans of sandstone rocks produced at zero volume graphic transparency setting showing pore size and pore distribution of sandstones. This unique property of sandstone minimizes pressure drop and drawn downs as well as minimises micro crevices which the displacing fluid cannot reach. The uniform pore network structure of sandstone rocks allows fluid flow and penetration with least distortion. Steady state flow profile was readily observed. Because of the favourable flow conditions existing in the sandstone rocks, the displacing fluid displaces more oil as it experiences lower resistance to flow in the micropores of the rock. Therefore, in all instances the tendency for oil to be trapped in carbonate rocks after repeated flooding was greater than in sandstone rocks. This, perhaps, explains one of the reasons more oil was obtained from sandstone reservoirs in this experimental investigation irrespective of drive mechanism or displacing strategy adopted.

4.5.1.2 Permeability

The permeability of carbonate reservoir is non-uniform and can vary in inches. A two - inch length by one-inch diameter core sample of a carbonate rock could have variable permeability across length by a factor or multiple of 10 (Huang & Sun, 2015; Inês et al., 2015; Lucia et al., 2003). With this spatial variation in permeability of carbonate rocks, the tendency to produce less oil is further increased. However, sandstones are known to exhibit uniform permeability across a whole stratigraphic layer of the reservoir rock. This is attributed to both the deposition and the diagenesis as well as the its constituent minerals. Thus, the potential of having a two-inch length by one-inch diameter core sample with uniform permeability is high. Perhaps, the disproportionate lower pressure differentials observed during the saturation and flooding of the sandstone core samples can be attributed to carbonates having permeability variation.

4.5.1.3 Internal rock surfaces and the interior rock chemical activity

The nature and chemical behaviour of sandstone rock and carbonate rocks vary considerably. The surfaces of sandstone rocks have a net negative charge. Oil has a high

electronegative charge and tends to exhibit a repulsive behaviour on the surface of sandstones which also exhibits electronegativity. The repulsive tendency of oil-sandstone surfaces promotes water to form a surface layer in the interior crevices of the rock promoting water-wet conditions. The water-wet condition promotes displacement of oil from the reservoir and non-adhesion of oil to rock surface. On the other hand, in the case of carbonates, limestone and dolostone, where Calcium ion (Ca^{2+}) and Magnesium ion (Mg^{2+}) are the dominant active ionic sites the tendency of oil adhesion to the rock is greater. The electronegative oil and the electropositive rock surfaces create static forces of attraction which tends towards an oil wetness or mixed surfaces. Therefore, with the oil-wet condition more prevalent in the carbonate reservoirs, the displacement efficacy of a displacing fluid to enhance oil recovery is reduced. This perhaps explains the higher oil recovery obtained from all the sandstone core samples when compared to carbonate core samples in all the recovery methods adopted in this experimental research.

4.5.1.4 Polymer flooding and oil displacement

The utilisation of polymer flooding to displace oil from the micro-pores and macro-pores of both sandstone and carbonate reservoirs is to increase the efficiency of waterflooding by increasing the favourability of the mobility ratio. This is achieved by increasing the viscosity and viscoelasticity of the displacing front. Hydrolysed polyacrylamide (HPAM) used in this research work is anionic and therefore negatively charged. The negative charge of the hydrolysed polyacrylamide (HPAM) polymer solution could contribute to the slightly lower oil recovery obtained from the carbonate core samples. As earlier mentioned, carbonates rocks are electropositive and have tendency to cling on to electronegative substances. The electronegative HPAM polymer solution would be drawn to the carbonate rock surface and adhere. The fluid displacement efficiency of HPAM is therefore reduced in carbonate reservoir rock as polymer solution adherence increases with continuous injections. The impact of this adherence phenomenon is gradual reduction in carbonate rock permeability. Eventually, high pressure differential build-up would be observed leading to reservoir micro pore blockage and perhaps subsequent reservoir formation damage. This also explains the high pressures observed during recovery flooding of all the carbonate core samples. Differential pressures up to 2200psi were observed during polymer flooding. The adsorption of anionic hydrolysed polyacrylamide of carbonate rock is further supported by recent research (Saha, Uppaluri, & Tiwari, 2018). Sandstone reservoirs are generally electronegative with a high tendency to repel other electronegative substances. Because

HPAM polymer solutions are electronegative, adhesion to the rock pore surfaces is minimal. This therefore, improves the displacement efficiency of HPAM polymer solution as potential for oil displacement at micro and macro pore level is increased. An increase in displacement efficiency leads to more oil recovery. This could explain the reason behind the higher oil recovery from the sandstone core samples than in carbonate core samples.

4.5.1.5 Ultrasound

The propagation of ultrasound waves in the sandstone and carbonate core sample indicated increased oil recovery as seen in all the flooding operation results. The transport mechanism of ultrasound transmission is through a medium. In this case, the transmission is through a saturated porous medium. Carbonates, as mentioned earlier, have non-uniform pores as well as non-uniform pore distribution. This variation in pore size, pore arrangement, pore throat and pore geometry lead to the distortion of mechanical movement of ultrasound wave in carbonate reservoirs. This affects the extent of ultrasound wave propagation and transmission of mechanical vibrations experienced in carbonate reservoir rocks and therefore slighter lowers the efficiency of the ultrasound wave. However, in the case of sandstone reservoir rocks the pores throats, pore size geometry, pore distribution and are more uniform. This therefore, enable less ultrasound wave distortion and provides a more uniform front for transmission of ultrasound wave across the core sample. Hence, the oil recovery during application of ultrasound is higher in all the sandstone cores samples compared with all the ultrasound enhanced oil recovery obtained in carbonate reservoirs.

Another pertinent issue is the difference in material composition between carbonate and sandstone rocks. Because carbonate reservoir rocks are calcium carbonates, with Magnesium in the case of dolostones, their transmission acoustic transmission potential is lower than sandstones. Carbonates possess covalent bonds and have lower acoustic transmission potential. Sandstones are mainly composed of silicon and aluminosilicates. Silicon and aluminosilicates have strong ionic bonds that facilitate ultrasound transmission.

4.5.1.5.1 Mechanisms of ultrasound enhanced oil recovery

There are several mechanisms linked to ultrasound in enhancing oil recovery. The main contributors to the recovery in the core samples in which ultrasound was applied are transmission of mechanical vibrations leading to the viscoelastic oscillation of oil. The viscosity of the oil is reduced, and its flow behaviour significantly improved. The ability of the displacing fluid to push additional oil through the complex tortuous micropores of the

core samples is improved as the oil viscosity decreases (Wang et al., 2015). Temperature rises in core sample of a few 2 to 3 degrees Celsius are observed.

The vibrational oscillation of the ultrasound wave changes the interface shape between the oil and water for favourable oil displacement. In carbonate rocks, the wetting is more favourable to oil-wet conditions. A change in the interface of the rock surface and oil contact surface enable release of oil and this action would significantly improve oil recovery. The interfacial tension reduction between oil and water, two immiscible fluids, is reduced as the wave oscillate through the two-fluid sending vibrational force across the boundary layer between oil and water.

Pore deformation and pore wall alteration due to ultrasound wave application opens-up pore throats and pore channels leading to increase in fluid flow (Khosrow Naderi & Babadagli, 2010). The capillary pressure is reduced as pore channels becomes more favourable to flow and micropores open-up to flow. This enhances overall oil displacement drive mechanism and oil recovery. Regardless of the rock type, carbonate or sandstones, ultrasound waves provide the needed mechanical oscillate-vibrations to cause pore deformations. Therefore, pore deformations and pore wall alterations as well as pore channel capillary pressure reduction influenced the oil recovery in this experimental investigation.

It is on record that ultrasound wave oscillation coalesces oil in the micropore and microcracks of the reservoir to larger sizes that can readily be recovered by a displacing fluid (Khosrow Naderi & Babadagli, 2010). The oil coalescence phenomenon is one of the mechanisms in ultrasound enhanced oil recovery in both the sandstone and carbonate core samples.

The application of ultrasound waves also reduces water- oil mobility ratio. This is because as the vibrations intensify, the oil viscosity is lowered. The displacing fluid efficiency is improved, and more oil is recovered.

The creation of microbubble in the rock due to the exposure of the fluids in rock to ultrasound waves leading to bubble growth and eventual collapse improves oil flow (Neeson & Lucas, 2011). The continuous creation of microbubbles and their growth in the reservoir leading to implosions releases a large amount of energy that increases oil recovery (Hamida & Babadagli, 2008a). These cavitation bubbles are central to the changes the reservoir fluids undergo during ultrasound enhanced oil recovery. The oil recovery from the application of ultrasound on the carbonate and sandstone cores in this research would have

been improved by the microbubble growth and collapse. The growth of the micro bubbles, stability of bubbles and implosion of bubbles at the pore scale are dependent on the frequency and intensity of the ultrasound wave and the nature of the reservoir fluid (Hamida & Babadagli, 2005). Initial gas content of the core fluids serves as nucleus for the generation and growth of gas bubbles in the core rock as ultrasound is propagated. Since the gas content plays an important factor in bubble creation and cavitation formation, it implies that oil with high gas content is more responsive to ultrasound enhanced oil recovery. The efficiency of the recovery is dependent on the gas content.

4.5.1.6 Polymer and ultrasound enhanced oil recovery

The highest oil recovery was obtained in both the sandstone and carbonates rock when polymer and ultrasound were applied simultaneously. However, the recovery from the carbonate cores was much lower when compared to recovery from the sandstone cores. In the earlier discussions, the main factors favouring more oil recovery from the sandstone reservoirs than carbonates were identified. Here, the discussion is centred on the displacement of oil with ultrasound and polymer flooding simultaneously.

4.5.1.6.1 Propagation of ultrasound in core sample and injected polymer solution

The propagation of ultrasound waves in the core sample transmits mechanical vibrations across the micropores of both sandstone and carbonate rocks. It causes interfacial tension reduction, oil in micropore coalescence thereby increasing flow potential, oil viscosity reduction, pore and pore throat deformation, cavitation and microbubble implosions. The polymer sweep efficiency is enhanced and previously inaccessible oil is transported to regions accessible to the polymer flood to displace and facilitate recovery. The reduction in oil viscosity also improves the mobility ratio in favour of polymer oil displacement, further increasing overall oil recovery.

4.5.1.6.2 Residual oil saturation

In each of the core flooding assembly operations, it was observed that the residual oil saturation was lower when ultrasound was applied. This is attributed to the mechanical vibrations of the wave leading to all the advantages outlined in section 4.5.1.6.1 (above).

4.5.1.6.3 Acoustic coupling and enhanced wave propagation

Hydrolysed polyacrylamide (HPAM) shows a strong propensity to transmit ultrasound waves for enhanced wave propagation. Previous medical research had indicated the potential for the utilisation of hydrolysed polyacrylamide as gel for acoustic coupling on

human body ultrasound (Prokop et al., 2003). The application of ultrasound in the coreflooding experiments conducted with polymer showed that the polymer exhibits characteristics of an acoustic coupler for enhanced oil recovery. The high volumes (percentage) of oil recovered from the experiments for both the carbonate and sandstone reservoirs support the acoustic coupling properties of ultrasound. The implications are the increased potentials for the extension of the distance of wave propagation as well as increase in the areal extent of oscillating waves transmission. Therefore, mechanisms for enhanced oil recovery are improved upon by introducing HPAM polymer solution as oil displacing agent. In addition, the attenuation time and distance travel are increased by the acoustic coupling properties of the injected HPAM polymer solution. The oscilloscope wave transmission readings during ultrasound propagation with polymer injection showed greater values at CH2 and least attenuation as well as low acoustic impedance. In this investigative experimental research output, it is evident that the application of hydrolysed polyacrylamide HPAM polymer solution for acoustic coupling in enhanced oil recovery is feasible and has potential to improve oil recovery significantly.

Hydrolysed polyacrylamide (HPAM) solution in confined space such as the core sample or oil reservoir where the coiled molecular chain elongation stretch is subject to available pore spacing is exempted from solid polymer which are readily deformed or damaged when subjected to high intensity sound wave. Solid polymers under high intensity ultrasound are candidates for degradation (Price, White, & Clifton, 1995). Price et al did not consider polymers in solutions, but polymer melts. The current proven application of polymer gels (acrylamide) in the medical line in acoustic couple (Prokop et al., 2003) certainly supports the use of HPAM for acoustic couple.

It is the informed view of the researcher that the hysteresis behaviour and viscoelasticity as well as the sweep efficiency of the displacing fluid, HPAM polymer solution, are also enhanced as the wave oscillates and propagates in the core. The oscillating wave enhances the coil stretch of the polymer chain during wave propagation as the wave undergoes rarefaction and compression. Therefore, the high oil recovery observed during the polymer and ultrasound stage of the enhanced oil recovery were also due to the enhanced viscoelasticity of polymer molecular chain stretch and polymer oil drag. Oscillating waves drag the polymer molecular chain increasing the stretch of the coiled molecular chain of the polymer. The potential of dilatancy of the polymer solution is enhanced by the oscillating waves as the polymer transports through the porous media. Thus, limiting the tendency of

the stripping and lowering tendency of viscosity reduction of the HPAM and reducing pseudoplasticity of the injected polymer.

4.5.1.7 Polymer degradation in effluent stream

Degradation of injected HPAM polymer solution in the reservoir is a phenomenon that occurs as the polymer molecular chains are pulled and stretched whilst penetrating the length and breadth of the reservoir (Jouenne, Chakibi, & Levitt, 2018; Seright, 2017; Southwick & Manke, 1988; Yuan & Wood, 2018). Similarly, in laboratory core flooding involving HPAM polymer solutions polymer degradation occurs. A close observation of the effluents during the polymer flooding without ultrasound and polymer with ultrasound indicated similar and uniform degradation. Though, the viscosity of the injected polymer solution exiting the core holder had reduced considerably (by up to 70%), there was virtually no difference in viscosity and other physical properties of the effluents of polymer flooding with and without ultrasound. This, therefore, supports the concept that no additional polymer degradation was caused by the application of ultrasound during polymer floods in the reservoir.

4.5.1.8 Formation Damage during polymer flooding

Some of the challenges encountered during the core flooding operations are illustrated and discussed in this section. In Figure 4.117 and Figure 4.118 two images of damaged Edward brown limestone core are shown, one in a core sleeve and the other in a blocked distribution plug. The formation damage occurred during polymer flooding with pore pressure at 2000psi and overburden pressure at 3,000psi. Even though the Unconfined compressive strength (UCS) of Edward brown is over 4000psi that did not prevent it from collapsing during polymer flooding.

1 Oil deposit **2** Core sample sludge **3** Sleeve pressed inwards

Figure 4.117: Damaged Edward brown core sample in sleeve

1 Sludge on distribution plug **2** Distribution plug **3** Transducer

Figure 4.118: Sludge core sample on core holder distribution plug

In Figure 4.99, the overburden oil formed a sludge with the Edward brown core sample. The carbonate fumes shown in Figure 4.100 near the back-pressure regulator occurred during the collapse. The whitish smoke like fume emanated from the effluent delivery tubing.

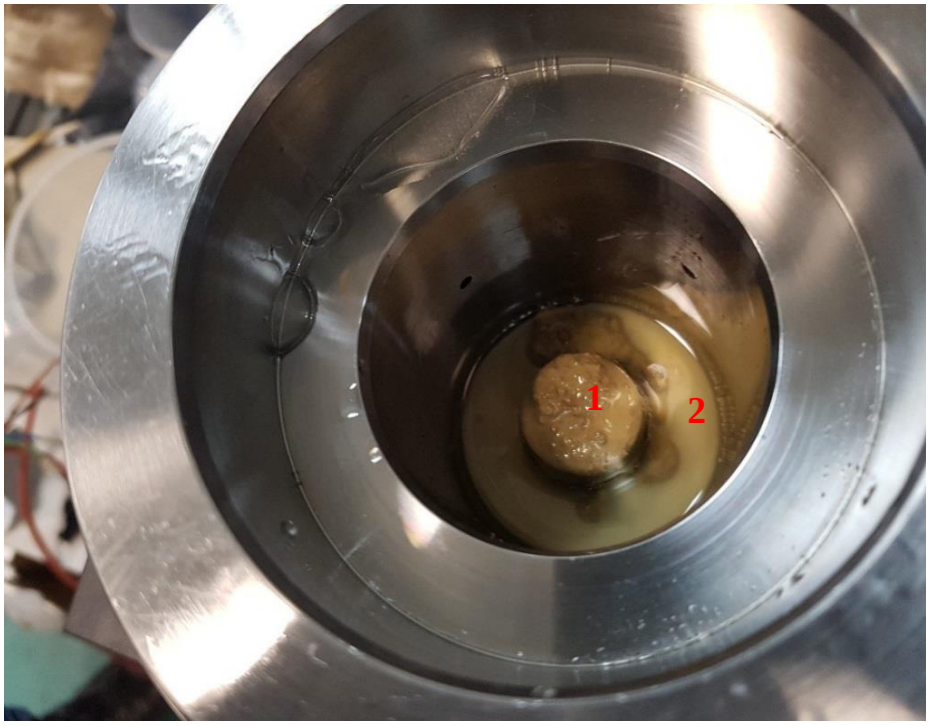

1 Sludge on distribution plug **2** Overburden oil

Figure 4.119: Core holder with damaged core sample and oil

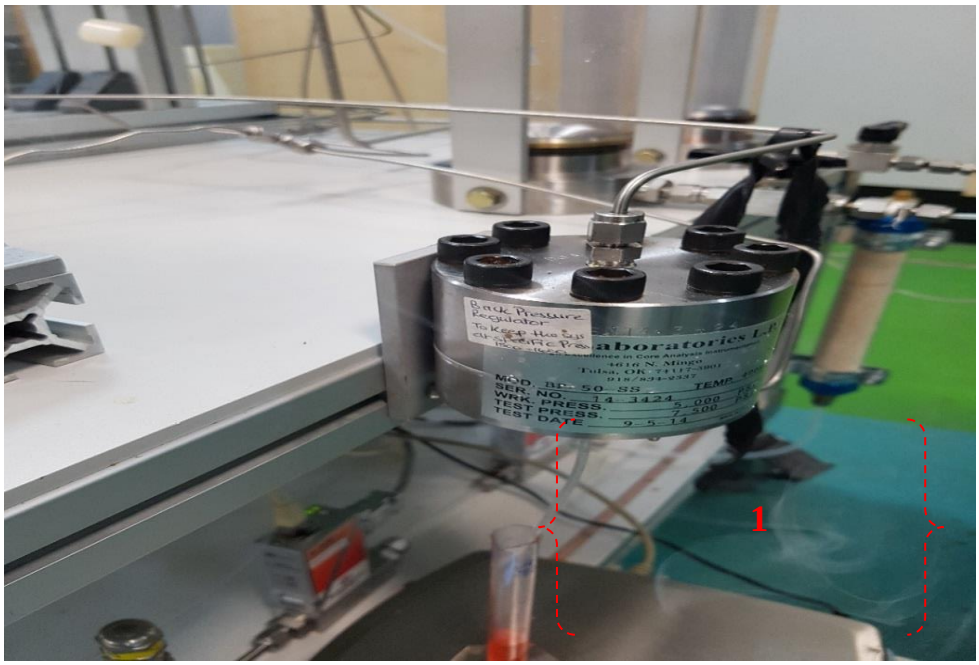

1 Dust (whitish fume) from collapsed core sample)

Figure 4.120: Core dust spreading from effluent tube of the back-pressure regulator

4.6 Chapter Summary

In Chapter Four, the results obtained were presented in tables, reconstructed images and graphs as standard practice. The results were also discussed and instances where similar results had been obtained in previous research experiments, mention was made of those similar findings.

CHAPTER FIVE
CONCLUSIONS AND RECOMMENDATIONS

5.1 Introduction

This chapter details the conclusions drawn from the observations, results and findings obtained in this experimental and investigative research in enhanced oil recovery through the integration of ultrasound and polymer flooding. It also provides recommendations for future research.

5.2 Conclusions

The knowledge gaps identified in oil recovery from sandstone and carbonate reservoirs stemming from the non-availability of concrete data on enhanced oil recovery through integration of ultrasound in conjunction with polymer flooding for the three main reservoir formations, at reservoir conditions, has been substantially addressed. The conclusions that can be drawn from the findings and the results obtained from the experimental investigation are enumerated:

i) The interfacial tension (IFT) behaviour exhibited between oil and reservoir brine is pressure dependent. The higher the reservoir pressure, the higher the interfacial tension. Low pressure reservoir pressure indicates lower interfacial tension behaviour. The significant increase in the oil recovery with the application of ultrasound was contributed by alteration of the interfacial tensions due to the ultrasound vibrations. The ability of ultrasound to lower the pressure drop across the reservoir consequently lowered the interfacial tension, and thus increased oil displacement and enhanced oil recovery

ii) Hydrolysed polyacrylamide (HPAM) exhibits pseudoplasticity and in some instances dilatancy depending on the shearing regime. The values of fluid flow behaviour indices, n, obtained were less than 1. The low values of n showed deviation from Newtonian flow behaviour. Hence, with continuous shearing the viscosity of the hydrolysed polyacrylamide polymer solution decreased. In certain instances, dilatancy is exhibited by the HPAM polymer solution and an apparent thickening occurs.

iii) The viscosity and viscoelasticity of HPAM polymer solution is concentration dependent. In addition, the higher the HPAM concentration the larger the hysteresis envelope. The hysteresis behaviour of a polydispersed HPAM polymer solution increases with polymer solution concentration. Although higher concentrations and higher polydispersity index polymer solutions are desirable for injection, a balance is required to ensure injectivity during polymer flooding.

iv) The oil displacement potential in the integration of ultrasound and polymer flooding is influenced by rock mineralogy and rock surface chemistry of a petroleum reservoir. Sandstones generally exhibit an overall negative charge. This promotes water-wet conditions. Whereas, carbonates exhibit electro-positivity due to the presence of calcium and magnesium ions in the rock surface active sites. Carbonates are therefore generally oil or mixed wet. The application of anionic hydrolysed polyacrylamide polymer during the core flood indicated increased pressure differential across all carbonate rocks compared to sandstone rocks. Therefore, anionic polymer solution should be used for sandstone reservoirs. For the carbonate reservoir rocks, the carbonyl group should be altered for the creation of cationic polymer for increased oil displacement and lowered pressure differentials. Thus, increasing oil recovery.

v) Acoustic propagation in reservoir rocks is influenced by the heterogeneity of a reservoir rock. The sandstone rocks exhibited greater homogeneity and also greater transmission of ultrasound wave propagation than carbonate rocks. Therefore, confirming the role of pore structure and rock type in ultrasound wave transmission and propagation. The computed tomography scans provided details of the pore sizes and pore distribution of the core samples. The pore sizes and pore distributions of sandstone were more uniform and evenly distributed. Whereas all the carbonate core samples showed less uniformity of pore sizes and distribution. This confirms that in terms of pore sizes and pore distribution, sandstones are more homogenous and carbonate more heterogenous. Therefore, in the integration of ultrasound and polymer flooding sandstones are more responsive to acoustic propagation and therefore provide greater potential for oil recovery than carbonates.

vi) Pressure drop profile across the reservoir cores of the carbonates and sandstones during polymer flooding with ultrasound application was significantly lowered. As ultrasound was applied, the pressure drop across the cores decreased. The lowered pressure drops indicated the impact of ultrasound on improving the flow characteristics. The lowered pressure profile was attributed to many factors such as increased permeability, viscoelastic wave propagation, viscosity reduction, coil stretch of the polymer chain molecule and cavitation. Others are acoustic coupling leading to enhance vibro-mechanical wave transmission across the reservoir cores

vii) This research has shown that irrespective of the arrangement of the core samples, either vertical or horizontal, more oil was recovered from sandstone cores than carbonates. Therefore, sandstone reservoirs are more responsive to ultrasound and polymer flooding as well as the integration of both in enhanced oil recovery. The maximum oil recovery in sandstones was 80% while the maximum oil recovery for the carbonates was 68%.

viii) The residual oil saturation (ROS) is significantly lowered by the integration of ultrasound and polymer flooding. The ROS values for sandstones were lower than that of carbonates due to the greater responsiveness of sandstones over carbonates to ultrasound and polymer flooding. The lowest ROS for sandstones was 0.20 while the lowest ROS for carbonates was 0.32

ix) In addition, the observed acoustic coupling of hydrolysed polyacrylamide polymer to increase transmission and propagation of ultrasound waves connected to the core samples, provided increased displacement. Acoustic coupling of hydrolysed polyacrylamide enabled higher oil recovery and enhanced the mechanism of ultrasound transmission with injected hydrolysed polyacrylamide polymer solution.

5.3 Recommendations for future research

The following recommendations are proposed for future research:

i) The power available to excite the acoustic velocity transducers was limited to 360Watts. Future research could apply greater power to determine the potentials of increased power supply.

ii) In addition, the mechanical properties of the core samples such as dynamic moduli and Young's moduli, Poison's ratio as well as bulk and shear modulus could be determined when additional software and hardware facilities for data acquisition are sourced.

iii) The oil utilised in this research had a viscosity of 9.7cp. In the future, the research could be conducted with heavy oil of greater viscosity.

REFERENCES

Abdallah, W., & Stukan, M. (2012). *Interfacial Tension (IFT) and Surface Alteration Interplay*. https://www.onepetro.org:443/download/conference-paper/SPE-161279-MS?id=conference-paper%2FSPE-161279-MS

Abdulfatah, H. K. (2018). *Application of Ultrasonic Waves in Enhancing Oil Recovery in Secondary Recovery Phase*. Paper presented at the SPE Annual Technical Conference and Exhibition, Dallas, Texas, USA. https://doi.org/10.2118/194031-STUhttps://www.onepetro.org:443/download/conference-paper/SPE-194031-STU?id=conference-paper%2FSPE-194031-STU

Agi, A., Junin, R., & Chong, A. S. (2018). Intermittent ultrasonic wave to improve oil recovery. *Journal of Petroleum Science and Engineering, 166*, 577-591. doi:https://doi.org/10.1016/j.petrol.2018.03.097

Al-Amri, M. A., Mahmoud, M. N., Al-Yousef, H. Y., & Al-Ghamdi, T. M. (2015). *Integrated Petrophysical and Reservoir Characterization Workflow to Enhance Permeability and Water Saturation Prediction*. https://www.onepetro.org:443/download/conference-paper/SPE-178028-MS?id=conference-paper%2FSPE-178028-MS

Al-Amrie, O., Peltier, S., Pearce, A., Abu-Dhabi, T., Al-Yafei, A., Morel, D., . . . Nguyen, M. (2015). *The First Successful Chemical EOR Pilot in the UAE: One Spot Pilot in High Temperature, High Salinity Carbonate Reservoir*. https://www.onepetro.org:443/download/conference-paper/SPE-177514-MS?id=conference-paper%2FSPE-177514-MS

Al-Hashmi, A. R., Divers, T., Al-Maamari, R. S., Favero, C., & Thomas, A. (2016). *Improving Polymer Flooding Efficiency in Oman Oil Fields*. https://www.onepetro.org:443/download/conference-paper/SPE-179834-MS?id=conference-paper%2FSPE-179834-MS

Alhomadhi, E., Amro, M., & Almobarky, M. (2013). Experimental application of ultrasound waves to improved oil recovery during waterflooding. *Journal of King Saud University - Engineering Sciences, 26*(1), 103-110. doi:http://dx.doi.org/10.1016/j.jksues.2013.04.002

Alvarado, V., Moradi Bidhendi, M., Garcia-Olvera, G., Morin, B., & Oakey, J. S. (2014). *Interfacial Visco-Elasticity of Crude Oil - Brine: An Alternative EOR Mechanism in Smart Waterflooding*. https://www.onepetro.org:443/download/conference-paper/SPE-169127-MS?id=conference-paper%2FSPE-169127-MS

Amro, M., Al Mobarky, M. A., & Al-Homadhi, E. S. (2007). *Improved Oil Recovery by Application of Sound Waves to Water Flooding*. https://www.onepetro.org:443/download/conference-paper/SPE-105370-MS?id=conference-paper%2FSPE-105370-MS

Auriault, J. L., Borne, L., & Chambon, R. (1985). Dynamics of porous saturated media, checking of the generalized law of Darcy. *The Journal of the Acoustical Society of America, 77*(5), 1641-1650. doi:doi:http://dx.doi.org/10.1121/1.391962

Baldygin, A., Nobes, D. S., & Mitra, S. K. (2014). New Laboratory Core Flooding Experimental System. *Industrial & Engineering Chemistry Research, 53*(34), 13497-13505. doi:10.1021/ie501866e

Bhangu, S. K., & Ashokkumar, M. (2017). Theory of sonochemistry. In *Sonochemistry* (pp. 1-28): Springer.

Biot M. A. (1955). Theory of Propagation of Elastic Waves in a Fluid-Saturated Porous Solid. *The journal of the acoustical of America*.

Biot M. A. (1956). Theory of Propagation of Elastic Waves in a Fluid-Saturated Porous Solid. II Hgh-Frequency Range. *The journal of the acoustical of America*.

Bourbie, T., Coussy, O., & Zinszner, B. (1987). *Acoustics of porous media*. Paris: Paris : Editions Technip

Chen, G., Han, P., Shao, Z., Zhang, X., Ma, M., Lu, K., & Wei, C. (2011). *History Matching Method for High Concentration Viscoelasticity Polymer Flood Pilot in Daqing Oilfield*. https://www.onepetro.org:443/download/conference-paper/SPE-144538-MS?id=conference-paper%2FSPE-144538-MS

Clarke, A., Howe, A. M., Mitchell, J., Staniland, J., & Hawkes, L. A. (2016). How Viscoelastic-Polymer Flooding Enhances Displacement Efficiency. doi:10.2118/174654-PA

Coles, M. E., Hazlett, R. D., Spanne, P., Muegge, E. L., & Furr, M. J. (1995). Characterization of Reservoir Core using Computed Microtomography. doi:10.2118/30542-PA

Craft B.C., & Hawkins M. (1991). *Applied Petroleum Reservoir Engineering* (2nd ed. / revised by Ronald E. Terry. ed.). Upper Saddle River, NJ London: Upper Saddle River, NJ London : Prentice Hall

Craze, R. C. (1950). Performance of Limestone Reservoirs. doi:10.2118/950287-G

Denney, D. (2009). Effect of Elasticity on Displacement Efficiency: High-Concentration-Polymer Flooding. doi:10.2118/0109-0050-JPT

Diallo, M. S., & Appel, E. (2000). Acoustic wave propagation in saturated porous media: reformulation of the Biot/Squirt flow theory. *Journal of Applied Geophysics, 44*(4), 313-325. doi:http://dx.doi.org/10.1016/S0926-9851(00)00009-4

Duhon, R. D., & Campbell, J. M. (1965). The Effect Of Ultrasonic Energy On The Flow Of Fluids In Porous Media. doi:10.2118/1316-MS

Ghamartale, A., Escrochi, M., Riazi, M., & Faghih, A. (2019). Experimental investigation of ultrasonic treatment effectiveness on pore structure. *Ultrasonics Sonochemistry, 51*, 305-314. doi:https://doi.org/10.1016/j.ultsonch.2018.10.002

Gil Cidoncha, J. I. (2007). *Application of Acoustic Waves for Reservoir Stimulation*. Paper presented at the International Oil Conference and

Exhibition, Veracruz, Mexico. https://www.onepetro.org:443/download/conference-paper/SPE-108643-MS?id=conference-paper%2FSPE-108643-MS

Hamida, T., & Babadagli, T. (2005). *Effects of Ultrasonic Waves on Immiscible and Miscible Displacement in Porous Media*. https://www.onepetro.org:443/download/conference-paper/SPE-95327-MS?id=conference-paper%2FSPE-95327-MS

Hamida, T., & Babadagli, T. (2007). Analysis of capillary interaction and oil recovery under ultrasonic waves. *Transport in Porous Media, 70*(2), 231-255. doi:10.1007/s11242-006-9097-9

Hamida, T., & Babadagli, T. (2008a). Displacement of oil by different interfacial tension fluids under ultrasonic waves. *Colloids and Surfaces A: Physicochemical and Engineering Aspects, 316*(1–3), 176-189. doi:http://dx.doi.org/10.1016/j.colsurfa.2007.09.012

Hamida, T., & Babadagli, T. (2008b). Effects of ultrasonic waves on the interfacial forces between oil and water. *Ultrasonics Sonochemistry, 15*(4), 274-278. doi:10.1016/j.ultsonch.2007.09.012

Hamidi, H., Mohammadian, E., Asadullah, M., Azdarpour, A., & Rafati, R. (2015). Effect of ultrasound radiation duration on emulsification and demulsification of paraffin oil and surfactant solution/brine using Hele-shaw models. *Ultrasonics Sonochemistry, 26*, 428-436. doi:http://dx.doi.org/10.1016/j.ultsonch.2015.01.009

Hamidi, H., Mohammadian, E., Rafati, R., Azdarpour, A., & Ing, J. (2015). The effect of ultrasonic waves on the phase behavior of a surfactant–brine–oil system. *Colloids and Surfaces A: Physicochemical and Engineering Aspects, 482*, 27-33. doi:http://dx.doi.org/10.1016/j.colsurfa.2015.04.009

Hermana, M., Ghosh, D. P., & Sum, C. W. (2016). *Optimizing the Lithology and Pore Fluid Separation Using Attenuation Attributes*. https://www.onepetro.org:443/download/conference-paper/OTC-26437-MS?id=conference-paper%2FOTC-26437-MS

Hu, Y. T., Chung, H., & Maxey, J. E. (2015). *What is More Important for Proppant Transport, Viscosity or Elasticity?* https://www.onepetro.org:443/download/conference-paper/SPE-173339-MS?id=conference-paper%2FSPE-173339-MS

Huang, Q., & Sun, Y. (2015). *An Integrated Approach to Quantify the Geological Control of Carbonate Pore Types on Permeability*.

I. Malinouskaya, Li Xiang-Yu, V.V. Mourzenko, J.-F. Thovertb, P.M. Adler. (2011). Acoustic properties of saturated porous media.

Inês, N., Bizarro, P., & Ribeiro, T. (2015). *Integrated Carbonate Reservoir Characterization and Modelling with Depositional and Diagenetic Trends*. https://www.onepetro.org:443/download/conference-paper/SPE-175673-MS?id=conference-paper%2FSPE-175673-MS

Jack Dvorkin, Richard, Nolen-Hoeksema, & Nur, a. A. (1994). The squirt-flow mechanism: Macroscopic description. *GEOPHYSICS, ;, VOL. 59*(NO. 3), P. 428-438.

James J. S., Bernd L, & Nasser A. (2015). Status of Polymer Flooding Technology. *Spe Journal*.

Jeong, C., Kallivokas, L. F., Huh, C., & Lake, L. W. (2014). *Estimation of Oil Production Rates in Reservoirs Exposed to Focused Vibrational Energy*. https://www.onepetro.org:443/download/conference-paper/SPE-169079-MS?id=conference-paper%2FSPE-169079-MS

Johnson, D. L., & Plona, T. J. (1982). Acoustic slow waves and the consolidation transition. *The Journal of the Acoustical Society of America, 72*(2), 556-565. doi:doi:http://dx.doi.org/10.1121/1.388036

Jouenne, S., Chakibi, H., & Levitt, D. (2018). Polymer Stability After Successive Mechanical-Degradation Events. *Spe Journal, 23*(01), 18-33. doi:10.2118/186103-PA

Junin, R., Manan, M., Hamidi, H., Mohammadian, E., Rafati, R., Junid, M., & Azdarpour, A. (2014). A technique for evaluating the oil/heavy-oil viscosity changes under ultrasound in a simulated porous medium. *Ultrasonics, 54*(2), 655-662. doi:10.1016/j.ultras.2013.09.006

Katsevich, A., Frenkel, M., Feser, M., Huang, Z., Andrew, M., Case, T., . . . Thompson, W. (2015). *New Fast and Accurate 3D Micro Computed Tomography Technology for Digital Core Analysis*. https://www.onepetro.org:443/download/conference-paper/SPE-174945-MS?id=conference-paper%2FSPE-174945-MS

Koh, H., Lee, V. B., & Pope, G. A. (2016). *Experimental Investigation of the Effect of Polymers on Residual Oil Saturation*. https://www.onepetro.org:443/download/conference-paper/SPE-179683-MS?id=conference-paper%2FSPE-179683-MS

Leong, T., Ashokkumar, M., & Kentish, S. (2011). The fundamentals of power ultrasound-A review. *Acoustics Australia, 39*, 54-63.

Levitt, D., & Pope, G. A. (2008). *Selection and Screening of Polymers for Enhanced-Oil Recovery*. https://www.onepetro.org:443/download/conference-paper/SPE-113845-MS?id=conference-paper%2FSPE-113845-MS

Li, Z., Delshad, M., Lotfollahi, M., Koh, H., Luo, H., Chang, H. L., . . . Brennan, B. (2014). *Polymer Flooding of a Heavy Oil Reservoir with an Active Aquifer*. https://www.onepetro.org:443/download/conference-paper/SPE-169149-MS?id=conference-paper%2FSPE-169149-MS

Lu, X., Jiang, H., Li, J., Zhao, L., Pei, Y., Zhao, Y., . . . Fang, W. (2015). Polymer Thermal Degradation in High-Temperature Reservoirs. *Petroleum Science & Technology, 33*(17/18), 1571-1579. doi:10.1080/10916466.2015.1072561

Lucia, F. J., Kerans, C., & Jennings, J. W., Jr. (2003). Carbonate Reservoir Characterization. doi:10.2118/82071-JPT

Meribout, M. (2018). *On Using Ultrasonic-assisted Enhanced Oil Recovery (EOR): Recent Practical Achievements and Future Prospects* (Vol. PP).

Mishra, S., Bera, A., & Mandal, A. (2014). Effect of Polymer Adsorption on Permeability Reduction in Enhanced Oil Recovery. *Journal of Petroleum Engineering, 2014*, 1-9. doi:10.1155/2014/395857

Mohammadian, E., Junin, R., Rahmani, O., & Idris, A. K. (2013). Effects of sonication radiation on oil recovery by ultrasonic waves stimulated water-flooding. *Ultrasonics, 53*(2), 607-614. doi:http://dx.doi.org/10.1016/j.ultras.2012.10.006

Mohammadian, E., Shirazi, M. A., & Idris, A. K. (2011). *Enhancing Oil Recovery through Application of Ultrasonic Assisted Waterflooding*. https://www.onepetro.org:443/download/conference-paper/SPE-145014-MS?id=conference-paper%2FSPE-145014-MS

Mullakaev, M. S., Abramov, V. O., & Abramova, A. V. (2015). Development of ultrasonic equipment and technology for well stimulation and enhanced oil recovery. *Journal of Petroleum Science and Engineering, 125*, 201-208. doi:http://dx.doi.org/10.1016/j.petrol.2014.10.024

Naderi, K., & Babadagli, T. (2008). Clarifications on Oil/Heavy Oil Recovery Under Ultrasonic Radiation Through Core and 2D Visualization Experiments. doi:10.2118/08-11-56

Naderi, K., & Babadagli, T. (2010). Influence of intensity and frequency of ultrasonic waves on capillary interaction and oil recovery from different rock types. *Ultrasonics Sonochemistry, 17*(3), 500-508. doi:http://dx.doi.org/10.1016/j.ultsonch.2009.10.022

Neeson, E., & Lucas, M. (2011). *Ultrasonics in enhanced recovery of oil from porous rock.* Paper presented at the IEEE International Ultrasonics Symposium, IUS.

Price, G. J., White, A. J., & Clifton, A. A. (1995). The effect of high-intensity ultrasound on solid polymers. *Polymer, 36*(26), 4919-4925. doi:http://dx.doi.org/10.1016/0032-3861(96)81616-8

Prokop, A. F., Vaezy, S., Noble, M. L., Kaczkowski, P. J., Martin, R. W., & Crum, L. A. (2003). Polyacrylamide gel as an acoustic coupling medium for focused ultrasound therapy. *Ultrasound in Medicine & Biology, 29*(9), 1351-1358. doi:http://dx.doi.org/10.1016/S0301-5629(03)00979-7

Qi, P., Ehrenfried, D. H., Koh, H., & Balhoff, M. T. (2016). Reduction of Residual Oil Saturation in Sandstone Cores by Use of Viscoelastic Polymers. doi:10.2118/179689-PA

Rambeau, O., Alves, M.-H., Andreu, N., Loriau, M., & Passade-Boupat, N. *Management of Viscosity of the Back Produced Viscosified Water*. https://www.onepetro.org:443/download/conference-paper/SPE-179776-MS?id=conference-paper%2FSPE-179776-MS

Rambeau, O., Alves, M.-H., Andreu, N., Loriau, M., & Passade-Boupat, N. (2016). *Management of Viscosity of the Back Produced Viscosified Water*. https://www.onepetro.org:443/download/conference-paper/SPE-179776-MS?id=conference-paper%2FSPE-179776-MS

Ritesh Kumar Sharma, Chopra, S., & Ray, A. K. (2014). Characterization of the dolomite reservoirs.

Rodriguez Manrique, F., Rousseau, D., Bekri, S., Djabourov, M., & Bejarano, C. A. (2014). *Polymer Flooding for Extra-Heavy Oil: New Insights on the Key Polymer Transport Properties in Porous Media*. https://www.onepetro.org:443/download/conference-paper/SPE-172850-MS?id=conference-paper%2FSPE-172850-MS

S., S. A. (2015). Experimental Investigation of Alkaline Surfactant Polymer (ASP) Flooding in Lo Permeabilty Heterogeneous Carbonate Reservoirs. *Spe Journal*.

Saha, R., Uppaluri, R. V. S., & Tiwari, P. (2018). Effects of interfacial tension, oil layer break time, emulsification and wettability alteration on oil recovery for carbonate reservoirs. *Colloids and Surfaces A: Physicochemical and Engineering Aspects, 559*, 92-103. doi:https://doi.org/10.1016/j.colsurfa.2018.09.045

Satter, A., & Iqbal, G. M. (2016). 11 - Primary recovery mechanisms and recovery efficiencies. In *Reservoir Engineering* (pp. 185-193). Boston: Gulf Professional Publishing.

Sayers, C. M., & Woodward, M. J. (2001). *Enhanced Seismic Pore-Pressure Prediction*. https://www.onepetro.org:443/download/conference-paper/OTC-13044-MS?id=conference-paper%2FOTC-13044-MS

Seright, R. S. (2017). How Much Polymer Should Be Injected During a Polymer Flood? Review of Previous and Current Practices. doi:10.2118/179543-PA

Seright, R. S., Campbell, A., Mozley, P., & Han, P. (2010). Stability of Partially Hydrolyzed Polyacrylamides at Elevated Temperatures in the Absence of Divalent Cations. doi:10.2118/121460-PA

Silva, I. P. G., Aguiar, A. A., Rezende, V. P., Monsores, A. L. M., & Lucas, E. F. (2018). A polymer flooding mechanism for mature oil fields: Laboratory measurements and field results interpretation. *Journal of Petroleum Science and Engineering, 161*, 468-475. doi:https://doi.org/10.1016/j.petrol.2017.12.008

Singhai, A., Grande, J. C., & Zhou, Y. (2013). Micro/Nano-CT for visualisation of Internal Structures. *Microscopy Today*.

Skinner, J. T., Tovar, F. D., & Schechter, D. S. (2015). *Computed Tomography for Petrophysical Characterization of Highly Heterogeneous Reservoir Rock*. https://www.onepetro.org:443/download/conference-paper/SPE-177257-MS?id=conference-paper%2FSPE-177257-MS

Song, H., Shi, H., Ji, Z., Wu, X., Li, G., Zhao, H., . . . Hou, X. (2019). The percussive process and energy transfer efficiency of percussive drilling with consideration of rock damage. *International Journal of Rock Mechanics and Mining Sciences, 119*, 1-12. doi:https://doi.org/10.1016/j.ijrmms.2019.04.012

Southwick, J. G., & Manke, C. W. (1988). Molecular Degradation, Injectivity, and Elastic Properties of Polymer Solutions. doi:10.2118/15652-PA

Urbissinova, T. S., Trivedi, J., & Kuru, E. (2010). Effect of Elasticity During Viscoelastic Polymer Flooding: A Possible Mechanism of Increasing the Sweep Efficiency. doi:10.2118/133471-PA

Veerabhadrappa, S. K., Doda, A., Trivedi, J. J., & Kuru, E. (2013). On the Effect of Polymer Elasticity on Secondary and Tertiary Oil Recovery. *Industrial & Engineering Chemistry Research, 52*(51), 18421-18428. doi:10.1021/ie4026456

Veerabhadrappa, S. K., Urbissinova, T., Trivedi, J. J., & Kuru, E. (2010). *Polymer Screening Criteria for EOR Application - A Rheological Characterization Approach*. https://www.onepetro.org:443/download/conference-paper/SPE-144570-MS?id=conference-paper%2FSPE-144570-MS

Wang, Z., Xu, Y., & Suman, B. (2015). Research status and development trend of ultrasonic oil production technique in China. *Ultrasonics Sonochemistry, 26*, 1-8. doi:10.1016/j.ultsonch.2015.01.014

Weimer, R. J., & Tillman, R. W. (1982). *Sandstone Reservoirs*. https://www.onepetro.org:443/download/conference-paper/SPE-10009-MS?id=conference-paper%2FSPE-10009-MS

Wilton, R. R., & Torabi, F. (2013). *Rheological Assessment of the Elasticity of Polymers for Enhanced Heavy Oil Recovery*. https://www.onepetro.org:443/download/conference-paper/SPE-165488-MS?id=conference-paper%2FSPE-165488-MS

Winkler, K., & Murphy III, W. F. (1995). Acoustic Velocity and Attenuation in Porous Rocks.

Withjack, E. M., Devier, C., & Michael, G. (2003). *The Role of X-Ray Computed Tomography in Core Analysis*. https://www.onepetro.org:443/download/conference-paper/SPE-83467-MS?id=conference-paper%2FSPE-83467-MS

Wu, X., Xiong, C., Xu, H., Zhang, J., Lu, C., Lu, X., . . . Yang, Z. (2015). *A Novel Particle-Type Polymer and IOR/EOR Property Evaluation*. https://www.onepetro.org:443/download/conference-paper/SPE-177421-MS?id=conference-paper%2FSPE-177421-MS

Yao, Q., & Han, D.-h. (2009). *Effect of Compaction History On Pore Pressure Prediction*.

Yuan, B., & Wood, D. A. (2018). A comprehensive review of formation damage during enhanced oil recovery. *Journal of Petroleum Science and Engineering, 167*, 287-299. doi:https://doi.org/10.1016/j.petrol.2018.04.018

APPENDICES

APPENDIX A

Table 5:1 Research in ultrasound enhanced oil recovery (1964 to 2020)

No	Year	Author	Paper title	Technique adopted (Experimental-E or Theoretical-T)	Outcome	Limitations (and how these limitations are addressed)
1	1964	Rex D. Duhon (U. of Oklahoma) | John M. Campbell (U. of Oklahoma)	The effect of ultrasonic energy on the flow of fluids in porous media	**(E)** The first documented experimental application of ultrasound for enhanced oil recovery. The researcher applied ultrasound on Torpedo sandstone for core flooding saturated with diesel oil and with saline water for flooding. The pressures applied on the core were low less than 500psi and at room temperature. The magnitude of the sonic frequency was varied, and the oil recovery was measured.	The researcher discovered a higher displacement efficiency with the application of ultrasound.	Did not properly account for the flow behaviour in sandstone as a result of ultrasound on the formation. No investigation was carried out on the pressure changes that could result due to ultrasound and only one type of formation was considered. In the proceeding experimental investigation reservoir conditions were applied with polymer flooding. All these limitations are now properly addressed

No	Year	Author	Paper title	Technique adopted (Experimental-E or Theoretical-T)	Outcome	Limitations (and how these limitations are addressed)
2	1999	Lie Hui Zhang, Peter Ho, Yun Li, Shengning He	Low frequency vibration recovery enhancement process simulation	**(E)** Low frequency vibrations (mechanical waves) were sent into the formation and compared with mathematical models.	Artificial vibrations led to enhance oil recovery	Although there was evidence of increase in recovery, the mechanisms were not investigated. The work showed that vibration increases recovery but did not include polymer flooding
3	2000	Mamadou Sanou Diallo, Erwin Appel	Acoustic wave propagation in saturated porous media: reformulation of the Biot /Squirt flow theory	**(T)** In this paper the researchers highlighted the two waves determined Biot (fast and slow waves) and contended that it did not adequately cater for long wavelength disturbances when compared to the size of the pore and grain which are microscopic and failed to comprehensively account for behaviour in porous medium. Therefore, introduced the squirt flow mechanism which is as a result of flow through the cracks in the surface of a porous medium. A fluid/ rock displacement factor was introduced in this method.	Therefore, introduced the squirt flow mechanism which is as a result of flow through the cracks in the surface of a porous medium. A fluid/ rock displacement factor was introduced in this method.	Though, the researchers attempted to combine the deficiency of the Biot theory and squirt flow theory (which accounts for losses as a result of cracks in the surface of pores through mathematical/numerical modelling, they made several assumptions such as isotropic condition and average pore pressure being independent of the squirt flow length behaviour of the fluid-reformulated BISQ theory. This was to minimise difference between experimental acoustic wave behaviour in a porous medium taking a better behaviour as a result of high permeability formations considered radially flow parameters in the model. Here, clay effect was not accounted for

No	Year	Author	Paper title	Technique adopted (Experimental-E or Theoretical-T)	Outcome	Limitations (and how these limitations are addressed)
						as well as difference viscosity fluids as water was the main consideration. Numerical Analysis with too many assumptions. Hence experimental analysis was used.
4	2004	N. Bjorndalen, M. R. Islam	The effect of microwave and ultrasonic irradiation on crude oil during production with a horizontal well	**(E)** The ultrasonic component involved radiation of crude oil, liquid paraffin and 2.5% asphaltene for 30, 60 and 120s. Liquid were samples passed through a pippete	Ultrasound irradiation suspends particles, Viscosity decreased for the first 60 seconds of radiation, but afterwards increased with time. This was attributed to reorientation of the molecular structure after initial temperature alteration as a result of ultrasound for stability	The delay period between measurement of the viscosity with radiation could have given inadequate readings of viscosity. Instead of microwave, sound wave was used in this research. In addition, the pressure profile was monitored.

No	Year	Author	Paper title	Technique adopted (Experimental-E or Theoretical-T)	Outcome	Limitations (and how these limitations are addressed)
5	2005	T. Hamida and T. Babadagli	Effect of ultrasonic waves on immiscible and miscible displacement in porous media	**(E)** The researchers used (1.5 in diameter and 2.5 in long) Berea sandstone and Indiana Limestone with air, water and surfactants as the wetting phase, while mineral oil and kerosene as oleic phase. The Hele-Shaw cells were used for the imbibition recovery. De-aerated water was utilised to serve as bath.	Pendent drop indicated reduction in interfacial tension, capillary imbibition experiment indicated interface changes. Hele- shaw experiment showed that molecular diffusion was increased with ultrasound.	Although effort was made to explain some of the mechanisms involved in the recovery, there is limitation in terms of applications at room temperature and pressure and use of non-oleic fuels. Therefore, the condition cannot reflect reservoir conditions. The use of capillary imbibition, Hele-shaw and pendent drop neglected the complexity associated with porous media. To address these limitations, reservoir conditions are applied with coreflooding in this experiment.
6	2007	Tarek Hamida, Tayfun Babadagli	Effects of ultrasonic waves on the interfacial forces between oil and water	**(E)** This is a continuation of the earlier experiment conducted on imbibition. The pendant drop method was used to investigate the behaviour of oil (oleic phase) and water interfacial tension in narrower capillaries when subjected to ultrasound. Observations recorded with a video camera	Dripping rate attained maximum at a certain intensity, but declined, as the viscosity increased a higher frequency was needed for a peak rise in dripping rate was observed	Limited observations can be obtained from the visual analysis done. In addition, the same size narrow capillary apertures used for all the varying viscosity oil. Coreflooding at reservoir condition to determine impact on recovery is conducted to address this limitation.

No	Year	Author	Paper title	Technique adopted (Experimental-E or Theoretical-T)	Outcome	Limitations (and how these limitations are addressed)
7	2007	Tarek Hamida	Displacement of oil by different interfacial tension fluids under ultrasonic wave	**(E)** With the use of Hele- Shaw model, the influence of high frequency, high intensity ultrasound on miscible and immiscible displacement of oil. Visual data was obtained through a GUI computer	The researcher concluded that molecular diffusion was one of the mechanisms for recovery enhancement	The experiment could not account for reservoir conditions to ascertain whether at high reservoir pressures molecular diffusion would still hold as a governing mechanism. These limitations were addressed by conducting experiments at reservoir conditions in this research.
8	2007	Jose Gil Cidoncha,	Application of acoustic waves for reservoir stimulation	**(T)** This paper highlighted some of the effects of ultrasonic /acoustic waves in reservoirs. It compared some laboratory investigation with field experiments	Results indicated alteration of wettability, surface tension, permeability, viscosity and mobility ratio. Recovery increased from 32 to 60%	The investigations conducted in the lab did not provide for the spatial distance in which the wave front travelled in the formation (degree of attenuation). The author highlighted insufficient information regarding the properties of the formations in which ultrasound was applied. Coreflooding at reservoir conditions addressed limitation of earlier experiments.

No	Year	Author	Paper title	Technique adopted (Experimental-E or Theoretical-T)	Outcome	Limitations (and how these limitations are addressed)
9	2007	Brian F. Towler, Ashok Kumar Chejara, Saeid Mokhatab	Experimental investigation of ultrasonic wave effects on wax deposition during crude – oil production	**(E)** This paper details the utilisation of 120KHz frequency ultrasound on Wax deposit during production and the temperature monitored using a thermocouple at different crude oil rate.	At 120KHz there was no substantial removal of wax.	The high ultrasound frequency may lead to reservoir damage; this frequency could be used for wax deposit cleaning but might be unsuitable for certain reservoirs. Another limitation is the transducer equally generates heat and the heat effects associated with the transducer alone cannot be distinguished. Optimisation of ultrasound frequency utilised and temperature monitoring are carried out to address these limitations.
10	2007	M.M Amro, M.A. Al-Mobarky, E.S. Al_Homadhi	Improved oil recovery by application of ultrasound waves to waterflooding	**(E)** In this research, the methodology adopted was the flooding of core samples both vertically and horizontally to determine the effectiveness of ultrasound to mobilise crude from the reservoir. Oil/Water relative permeability was calculated to evaluated with ultrasound and in absence of ultrasound.	Increase in oil recovery and wave simulation in vertical flow is more effective where the permeability decreases with depth. In appropriate for unconsolidated reservoirs.	The flooding was limited to only sandstone cores; however, the author did acknowledge, for further research, the possibility of using this same methodology for other types of reservoir formations. To address these limitation, various sandstone core samples are used.

No	Year	Author	Paper title	Technique adopted (Experimental-E or Theoretical-T)	Outcome	Limitations (and how these limitations are addressed)
11	2007	Tarek Hamida Tayfun Babadagli	Analysis of capillary interaction and oil recovery under ultrasonic waves	**(E)** Imbibition cells were used with ultrasound on sandstone and limestone core	Higher recovery was obtained with ultrasound, polymer added yielded 12% increment at 0.03% concentration but less at .009% opined due to degradation. Surfactant increased by 12% little effect on capillary	One of the major limitations of imbibition cell is its inability to portray reservoir phenomenon and integrate other mechanisms of ultrasonic recovery for in depth study. Recovery efficiency is very low and can lead to misleading conclusions. Coreflooding alone could provide adequate reservoir recovery behaviour. Coreflooding is currently considered to address this limitation.
12	2007	Brain F Towler, Ashok Kumar Chejara,and Saeid Mokhatab	Experimental investigations of ultrasonic waves effects on wax deposition during crude-oil production	**(E)** Here, an ultrasonic device was placed near the production tubing to remove wax deposition	Minimal effect was observed.	The minimal effect was attributed to the extra heat generated from the transducer assembly; therefore, it could not ascertain whether the wax deposit removal was as a result of ultrasound or as a result of heat generated by the transducer. Major difference is coreflooding and polymer flooding application.

No	Year	Author	Paper title	Technique adopted (Experimental-E or Theoretical-T)	Outcome	Limitations (and how these limitations are addressed)
13	2007	Hossein Hamidi, Erfan Mohammadian Radzuan Junin, Roozbeh Rafati, Mohammad Manan, Amin	A technique for evaluating the oil/heavy oil viscosity changes under ultrasound in a simulated porous medium.	**(E)** The researchers determined the viscosity and differential pressure changes of fluids in a capillary tube which was subjected to ultrasound in a water bath. The frequencies were varied from 25 to 68kHz. Temperature controlled and uncontrolled condition were applied. The Poiseulle equation of flow was used to obtain the viscosity of oil with and without ultrasound conditions.	Increased recovery, lowered viscosity and temperature increase was witnessed.	Although the application of capillary tube enabled the determination of the viscosity, the accuracy would be in doubt as the capillary tubes give less accurate results since the pressure drops in the tubes, which is generally smooth, is far from the matrix and surface structure of reservoir pore surface. The surfaces are generally none uniform. Only reservoir cores can mimic pore flow behaviour. This limitation is addressed with coreflooding.
14	2008	K. Naderi, T. Babadagli	Clarifications on heavy oil recovery under ultrasonic radiation through core and 2D visualization	**(E)** Capillary imbibition experiments on cylindrical Berea sandstone with ultrasonic radiation with 2D glass beads. Movement of oil was monitored by visualisation. Heavy oil and light oil.	Recovery increased by up to 17%, Oil wet give higher recovery than water wet.	Inadequate spatial experimental analysis for adequate conclusion due to the nature formations used. Sandstone and carbonate reservoir rocks are used in the current research to address these limitations.

No	Year	Author	Paper title	Technique adopted (Experimental-E or Theoretical-T)	Outcome	Limitations (and how these limitations are addressed)
15	2009	Khosrow Naderi, Tayfun Babadagli	Influence of intensity and frequency of ultrasonic waves on capillary interaction and oil recovery from different rock types	**(E)** In this research the Berea sandstone cores were subjected to imbibition cells and experiments conducted with and without ultrasound. The saturation and wettability and oil viscosity were varied. In ensuring an oil wet core dichlorooctamethyltetrasiloxane. (Surfasil). was used to achieve a highly wet coming.	Oil recovery was enhanced, but more in oil wet then water wet, higher viscosities produced less, the higher the frequency, the higher the recovery.	Limited to surface conditions, reservoir conditions were not considered. Limitation is addressed by conducting experiments are reservoir conditions.
16	2011	Eimear Neeson, Margaret Lucas	Ultrasonics in enhanced recovery of oil from porous rock	**(E)** Core samples were saturated with water, kerosene and rapeseed oil and subjected to 20kHz of ultrasound. Abaqus Finite Element Analysis (FAE) was used to determine the cavitation levels from a chart (coloured chart of asxisymmetrical acoustic pressure). Losses were recorded as recovery.	Observed bubble cavitation on rock surfaces leading to the conclusion that cavitation is one of the mechanisms. Fragmentation was adjudged as one of the leading mechanisms.	The only parameters observed in the experiment were degrees of cavitation and mass loss as a result of exposure to ultrasound (at normal atmospheric temperature and pressure), measured as recovery was carried out. This cannot adequately cater for downhole conditions. The mechanism was insufficiently explained. Core flooding with ultrasound is comprehensively investigated to cater for these limitations.

No	Year	Author	Paper title	Technique adopted (Experimental-E or Theoretical-T)	Outcome	Limitations (and how these limitations are addressed)
17	2011	Erfan Mohammadian, Mohammad Amin Shirazi, Ahmad Kamal Idris	Enhancing oil recovery through application of ultrasonic assisted waterflooding	**(E)** In this methodology the researchers flooded artificial cores made of quartz grain (unconsolidated) sand packs at an ultrasonic frequency of 40KHz and 250watts. The relative mobility of water to oil was determined	Similar to other experiments conducted, there was increase in recovery, the emulsions disappeared after 3hrs. Slight temperature rise, viscosity reduction and emulsification and negligible IFT change was observed	The major setback in this experimental approach was the inability to account for other formations. In addition, all measurements were taken at room temperature at pressure far from reservoir pressures. Temperature rise as a result of ultrasound was inadequately monitored to get any favourable measurements to show the effect on IFT. Carbonate and Sandstone core samples are utilised and ultrasound frequency of 20KHz frequency and 360 watts of power in this experimental research to address this limitation.

No	Year	Author	Paper title	Technique adopted (Experimental-E or Theoretical-T)	Outcome	Limitations (and how these limitations are addressed)
18	2012	Erfan Moahmmadian, Radzuan Junin, Omeid Rahmani, Ahmad Kamal Idris	Effects of sonication radiation on oil recovery by ultrasonic waves stimulated water flooding	**(E)** Batch and continuous application of ultrasound on synthetic sand cores through flooding was carried out. Brine conc. was altered for normal to deaerated 3% NaCl for water flooding. Applied frequency of 40 kHz on quartz sand grains as the porous media. Similar oil as Rex Duhan (1964) method were used. However, temperature and viscosity changes were determined.	Recovery increased from 3% to 16% with application of ultrasound. It was also lower for deaerated brine than normal brine. Severe temperature rises occurred. Unstable emulsion produced.	Artificial sandstones have been observed to produce less accurate results than natural formation reservoir rocks. It failed to address impact to different reservoir formations and the flooding was conducted at normal atmospheric pressure. 40KHz frequency ultrasound was used. 20 to 100KHz applied to determine optimum frequency. There was inadequate study of pressure changes due to ultrasound which were attributed to cavitation. This is because formation characteristic was not involved in the analysis. Pressure differential changes are monitored during coreflooding.

No	Year	Author	Paper title	Technique adopted (Experimental-E or Theoretical-T)	Outcome	Limitations (and how these limitations are addressed)
19	2013	Hossein Hamidi, Erfan Mohammadian, Roozbeh Rafati, Amin Azdarpour	A role of ultrasonic waves on oil viscosity changes in porous media	**(E)** The researcher applied various ultrasonic wave of ranges of 25Hz to 68KHz and 100KW to 600KW. Hydrocarbon used were kerosene, synthetic oil and paraffin. The main media was capillary tube. Temperature changes were monitored	The decrease in viscosity was inversely proportional to the frequency and power. Cavitation, temp rise, viscosity reduction are the main mechanisms of ultrasound waves.	The use of capillary tubes in immersion and not reservoir rocks in atmospheric conditions does not give the realistic behaviour in the reservoir. To address these limitations, the behaviours of reservoir fluids were studied at reservoir conditions.
20	2013	Emad Alhomadhi, Mohammad Amro, Mohammed Almobarky	Experimental application of ultrasound waves to improved oil recovery during waterflooding	**(E)** Berea sandstone cores (high and low consolidation) with Saudi crude oil was used at confining pressure of 1500 psi to flood the samples with 5% brine with application of ultrasound. (brine 83% wt NaCl and 17% wt $CaCl_2$. The flooding was also used for poor consolidated sandstone reservoirs. The effect of stimulation on water/oil relative permeability was determined using the Johnson, Bossler, Nauman (JBN) method.	Recovery increased from 2.5 to 5% of residual oil in place. This showed that recovery in best achieved at high water cut. Vertical/horizontal flooding indicated gravitational separation.	Although the researchers were able to determine the saturation levels of the core, the use of only Berea sandstone alone limits generalisation. The 1500 psi pressure in which the flooding was carried out is low compared to actual reservoir condition. The author having limited the research to a Saudi crude of 31.2° API recommended further test to be conducted on other API crude to ascertain the effects on recovery. Carbonate rocks are used and synthetic oil at reservoir conditions to address these limitations.

No	Year	Author	Paper title	Technique adopted (Experimental-E or Theoretical-T)	Outcome	Limitations (and how these limitations are addressed)
21	2013	Hossein Hamidi, Erfan Mohammadian, Radzuan Junin, Roozbeh Rafati, Mohammad Manan	A technique for evaluating the oil/heavy oil viscosity changes under ultrasound in a simulated porous medium	**(E)** Viscous oils were subjected to ultrasound in a water bath. Frequencies of 25, 40 and 68KHz were applied to the oil.	Viscosity decreased in all cases where ultrasound was applied	The experiments were conducted at atmospheric pressures and the results cannot be compared to reservoir pressure. Reservoir conditions of pressure are applied to address the limitations.
22	2013	Anna Abramova, Vladimir Abramov, Vadim Bayaazitov, Artyom Gerasin	Ultrasonic technology for enhanced oil recovery	**(E)** Applied previously defined criteria for well selection candidate for utilisation of ultrasonic waves, the researchers developed a down hole transducer assembly.	After ultrasound had been applied on the field, for almost 2years recovery was high with impact of ultrasound application increasing economic viability (The paper also outlined some of the criteria for field applications)	The mechanism was not adequately discussed. Adequate discussion on recovery mechanism was carried out and experiments conducted in control environment to address these limitations.

No	Year	Author	Paper title	Technique adopted (Experimental-E or Theoretical-T)	Outcome	Limitations (and how these limitations are addressed)
23	2014	Anna Abramova, Vladimir Abramov, Vadim Bayazitov, Artyom Gerasin, Dmitriy Pashin	Ultrasonic technology for enhanced oil recovery	**(E)** The major equipment required for field application of ultrasound was developed. These were identified as generator (10kW), downhole sonotrode, vibrometer, manometer	Based on monitoring of over 100 wells to which ultrasound has been applied 40% to100% increase in oil recovery was observed	Although the authors highlighted some benefits associated with ultrasonic enhanced oil recovery, key mechanisms involved in the recovery for ultrasound were not discussed. Design and fabrication of the ultrasound did not include polymer flooding. However, this limitation has been addressed in this research.
24	2014	Vladimir Alvarado, Mehmoosh, Moradi Bidhendi, Griselda Garcia-Olvera, Bredon Morin, John S. Oakey	Interfacial visco- elasticity of crude oil-brine: An alternative EOR mechanism in smart waterflooding	**(E)** This paper conducted experiments to show the impact of fluid- fluid interaction in low salinity flooding. The salinity of the flooded brine was altered.	It concluded that the low salinity brine and crude oil indicated an interfacial film that was more elastic than that of high salinity.	Though the researcher made some good findings on the role of low salinity flooding on the overall enhanced oil recovery on sandstone reservoirs, the researcher did no work on its impact on carbonate reservoirs. Ultrasound was not applied, and polymer flooding was absent. These limitation are adequately addressed in this research.

No	Year	Author	Paper title	Technique adopted (Experimental-E or Theoretical-T)	Outcome	Limitations (and how these limitations are addressed)
25	2014	Mohammed Mohsin, Mahmoud Meribout	An extended model for ultrasonic-based enhanced oil recovery with experimental validation	**(E)** A proposed ultrasonic EOR was developed on possible field application based on experimental set. An ultrasonic horn was made for insertion downhole.	Potential application of ultrasound as an EOR was highlighted. Simulation was used to justify adoption.	The findings were based on extrapolation. However, the conditions cannot be extrapolated to reservoir conditions of high pressure and temperatures. These limitations are addressed by applying reservoir conditions.
26	2015	Hossein Hamidi, Erfan Mohammadian, Mohammad Asadullah, Amin Azdarpour, Roozbeh Rafati	Effect of ultrasound radiation duration on emulsification and de-emulsification of paraffin oil and surfactant solution/brine using Hele-shaw models	**(E)** Used an ultrasonic bath with visual microscope to analyse the behaviour of emulsions as acoustic waves of 40Hz were irradiated on paraffin (oleic phase) oil and brine. Used simulated porous media etched on a glass sheet and layered with another glass sheet to form Hele-shaw model. Surfactant solution and paraffin were initially injected, and the interphase monitored with a camera.	Intermittent application of ultrasound yields higher emulsions than continuous. Unstable interface, molecular diffusion causing percolation, and Bjerknes forces were concluded	The restriction to only one API gravity oil of 61.28 and only etched glass did not reflect natural reservoir conditions and therefore insufficient to arrive at an adequate conclusion on the effect of ultrasound on emulsion and demulsifications.

No	Year	Author	Paper title	Technique adopted (Experimental-E or Theoretical-T)	Outcome	Limitations (and how these limitations are addressed)
27	2015	Hossein Hamidi, Erfan Mohammadian, Roozbeh Rafati, Amin Azdarpour, James Ing	The effect of ultrasonic waves on the phase behaviour of a surfactant-brine oil system	**(E)** This experiment involved the use of an ultrasonic water bath through which was place in test tube with varied salinity fluid was subjected to ultrasound	Emulsions generation increased with time of exposure. Surfactant IFT was low for low exposure to ultrasound. Vice versa.	The pressures involved were atmospheric and the degree to which the emulsion might have formed can be disputed.
28	2018	Augustine Agi, Radzuan Junin Ramin Shirazi, Gbadamosi Afeez, Nurudeen Yekeen	Comparative study of ultrasound assisted water and surfactant flooding	**(E)** In this paper, the researchers used sand packed in polyvinylchloride holder with meshed placed to contain the sand on both ends of the cylindrical core. Surfactant and water flooding were performed at 40KHz at varying power	The recovery with surfactants was greater than recovery from water flooding. Increased power of ultrasound showed increase oil recovery	The pressures applied were in adequate to mimic reservoir conditions. The temperature was low, and the displacing fluid pressure profile was not monitored. The current research will be conducted at reservoir conditions using reservoir core samples and the pressure profile will be monitored
29	2018	Augustine Agi, Radzuan Junin, Aik Shye Chong	Intermittent ultrasonic wave to improve oil recovery	**(E)** The experiment involved a micromodel in a bath which was subjected to ultrasound waves. Ultrasound waves were applied intermittently and continuously on paraffin saturated micromodels. The degree of desaturation of the micromodels was monitored.	The recovery from intermittent ultrasonic irradiation was observed to be greater than continuous ultrasound application	Micromodels do not reflect the conditions in a reservoir where pressures are high and core properties differ. These limitations are adequately addressed in this research.

No	Year	Author	Paper title	Technique adopted (Experimental-E or Theoretical-T)	Outcome	Limitations (and how these limitations are addressed)
30	2019	Augustine Agi, Radzuan Junin, Mohd Faddli Syamsul, Aik Shye Chong, Afeez Gbadamosi	Intermittent and short duration ultrasound in a simulated porous medium	**E)** The paper investigates the intermittent and short ultrasound application on a micromodel using an ultrasound bath and a camera to snap residual oil depletion.	The recovery from short duration and intermittent application of ultrasound was higher than continuous and long duration.	The limitations include the conditions in which the experiments were conducted that were not a true representation of reservoir conditions. Hence, the proposed investigations are at reservoir conditions and would give more realistic recovery results.
31	2020	Zhenjun Wanga, Ri Fangb,Hangyuan Guo	Advances in ultrasonic production units for enhanced oil recovery in China	T) This paper highlights new developments in ultrasound in field applications, it describes new advances made in China	Promotes the use of ultrasound for enhanced oil recovery	The technology does not include polymer flooding. The research includes polymer flooding.

APPENDIX B Interfacial Tension

Drop Shape Image Analysis

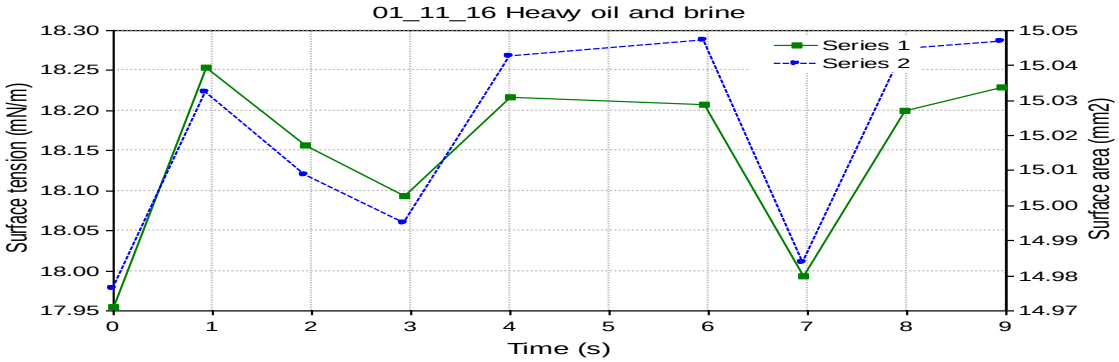

Date : 11/1/2016 Remarks : Comments here
Experiment : 01_11_16 Heavy oil and brine_14 Method : 01_11_16 heavy oil and brine.met
Drop phase : Heavy Oil Density : 0.9322
Extern.phase : Brine (5%) Density : 0.6600
Solid phase : Steel Calculation : Optimized cont.

No.	Time	Gamma	Beta	R0	Area	Volume	Theta	Height	Width	Opt	Messages
1	0.0	17.95	0.164	1.051	14.98	5.78	139.15	2.329	2.170	3	
2	0.9	18.25	0.162	1.054	15.03	5.81	139.40	2.330	2.172	2	
3	1.9	18.16	0.163	1.053	15.01	5.80	139.32	2.328	2.171	3	
4	2.9	18.09	0.163	1.052	14.99	5.79	139.27	2.327	2.170	2	
5	4.0	18.22	0.163	1.054	15.04	5.82	139.35	2.331	2.173	2	
6	4.9	0.00	0.000	0.000	0.00	0.00	0.00	0.000	0.000	0	Sides are too differ
7	6.0	18.21	0.163	1.054	15.05	5.82	139.34	2.330	2.174	2	
8	7.0	17.99	0.164	1.051	14.98	5.78	139.18	2.329	2.170	3	
9	8.0	18.20	0.163	1.054	15.04	5.82	139.33	2.331	2.172	3	
10	8.9	18.23	0.163	1.054	15.05	5.82	139.35	2.330	2.173	2	
Mean:		18.14	0.163	1.053	15.02	5.80	139.30	2.329	2.172		
Stand.dev.:		0.04	0.000	0.000	0.01	0.01	0.03	0.000	0.000		

Drop Shape Image Analysis

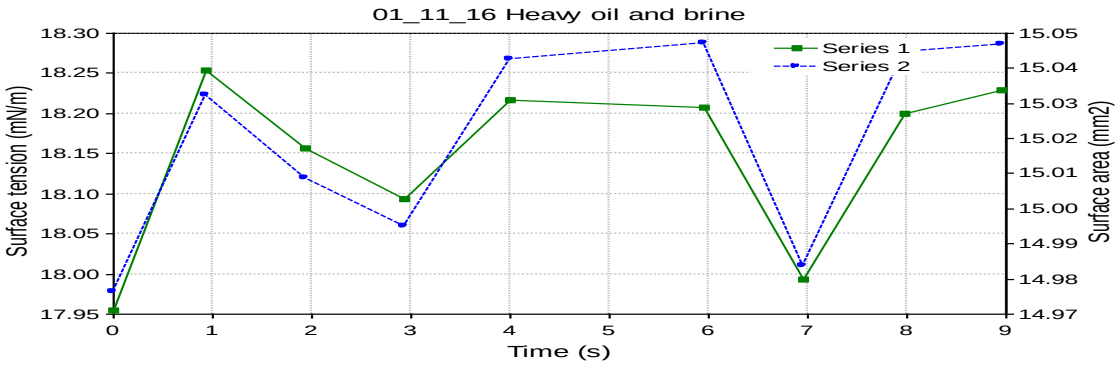

Date : 11/1/2016 Remarks : Comments here
Experiment : 01_11_16 Heavy oil and brine_14 Method : 01_11_16 heavy oil and brine.met
Drop phase : Heavy Oil Density : 0.9322
Extern.phase : Brine (5%) Density : 0.6600
Solid phase : Steel Calculation : Optimized cont.

No.	Time	Gamma	Beta	R0	Area	Volume	Theta	Height	Width	Opt	Messages
1	0.0	17.95	0.164	1.051	14.98	5.78	139.15	2.329	2.170	3	
2	0.9	18.25	0.162	1.054	15.03	5.81	139.40	2.330	2.172	2	
3	1.9	18.16	0.163	1.053	15.01	5.80	139.32	2.328	2.171	3	
4	2.9	18.09	0.163	1.052	14.99	5.79	139.27	2.327	2.170	2	
5	4.0	18.22	0.163	1.054	15.04	5.82	139.35	2.331	2.173	2	
6	4.9	0.00	0.000	0.000	0.00	0.00	0.00	0.000	0.000	0	Sides are too differ
7	6.0	18.21	0.163	1.054	15.05	5.82	139.34	2.330	2.174	2	
8	7.0	17.99	0.164	1.051	14.98	5.78	139.18	2.329	2.170	3	
9	8.0	18.20	0.163	1.054	15.04	5.82	139.33	2.331	2.172	3	
10	8.9	18.23	0.163	1.054	15.05	5.82	139.35	2.330	2.173	2	
Mean:		18.14	0.163	1.053	15.02	5.80	139.30	2.329	2.172		
Stand.dev.:		0.04	0.000	0.000	0.01	0.01	0.03	0.000	0.000		

Drop Shape Image Analysis

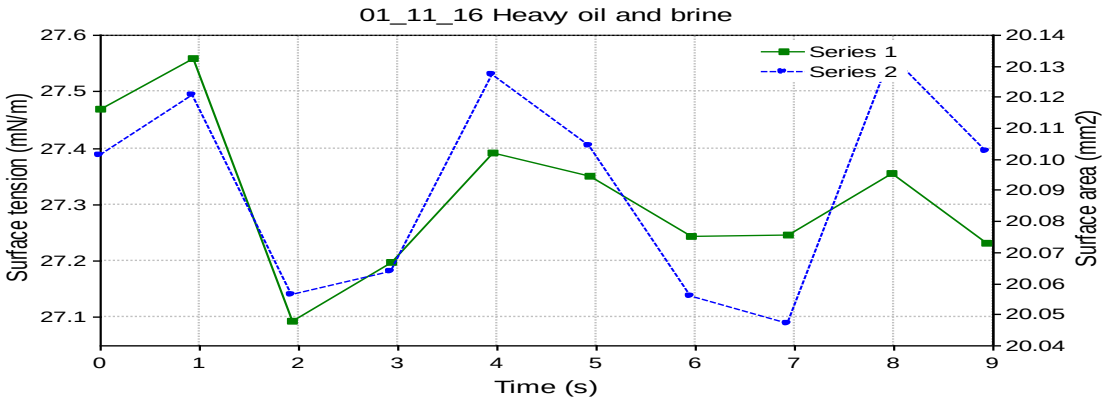

Date : 11/1/2016 Remarks : Comments here
Experiment : 01_11_16 Heavy oil and brine_15 Method : 01_11_16 heavy oil and brine.met
Drop phase : Heavy Oil Density : 0.9322
Extern.phase : Brine (5%) Density : 0.6600
Solid phase : Steel Calculation : Optimized cont.

No.	Time	Gamma	Beta	R0	Area	Volume	Theta	Height	Width	Opt	Messages
1	0.0	27.47	0.145	1.223	20.10	8.91	141.88	2.679	2.515	3	
2	0.9	27.56	0.145	1.224	20.12	8.93	141.93	2.680	2.516	3	
3	1.9	27.09	0.147	1.221	20.06	8.88	141.68	2.678	2.511	2	
4	2.9	27.20	0.146	1.221	20.06	8.88	141.74	2.679	2.513	3	
5	4.0	27.39	0.146	1.223	20.13	8.93	141.81	2.682	2.517	3	
6	4.9	27.35	0.146	1.223	20.10	8.91	141.81	2.681	2.515	2	
7	6.0	27.24	0.146	1.221	20.06	8.88	141.79	2.679	2.512	3	
8	6.9	27.25	0.146	1.222	20.05	8.88	141.75	2.676	2.512	3	
9	8.0	27.36	0.146	1.223	20.13	8.93	141.78	2.684	2.516	3	
10	8.9	27.23	0.147	1.222	20.10	8.92	141.72	2.681	2.515	2	
Mean:		27.31	0.146	1.222	20.09	8.91	141.79	2.680	2.514		
Stand.dev.:		0.04	0.000	0.000	0.01	0.01	0.02	0.001	0.001		

Drop Shape Image Analysis

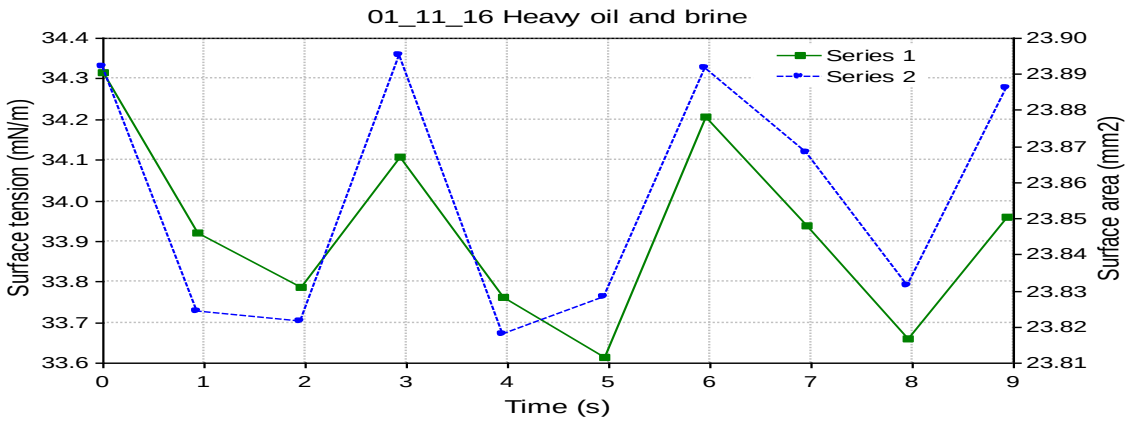

Date : 11/1/2016 Remarks : Comments here
Experiment : 01_11_16 Heavy oil and brine_16 heavy oil and brine.met Method : 01_11_16
Drop phase : Heavy Oil Density : 0.9322
Extern.phase : Brine (5%) Density : 0.6600
Solid phase : Steel Calculation : Optimized cont.

No.	Time	Gamma	Beta	R0	Area	Volume	Theta	Height	Width	Opt	Messages
1	0.0	34.32	0.138	1.334	23.89	11.48	142.94	2.924	2.738	2	
2	0.9	33.92	0.140	1.332	23.82	11.43	142.77	2.923	2.735	3	
3	2.0	33.79	0.140	1.331	23.82	11.43	142.69	2.923	2.735	3	
4	2.9	34.11	0.139	1.334	23.90	11.48	142.82	2.925	2.738	3	
5	4.0	33.76	0.140	1.331	23.82	11.43	142.69	2.921	2.733	2	
6	4.9	33.61	0.141	1.331	23.83	11.42	142.60	2.926	2.733	2	
7	6.0	34.21	0.139	1.333	23.89	11.48	142.89	2.925	2.738	3	
8	6.9	33.94	0.140	1.333	23.87	11.47	142.75	2.923	2.735	2	
9	7.9	33.66	0.140	1.331	23.83	11.43	142.63	2.925	2.733	3	
10	8.9	33.96	0.140	1.333	23.89	11.48	142.74	2.923	2.737	3	
Mean:		33.93	0.140	1.332	23.86	11.45	142.75	2.924	2.736		
Stand.dev.:		0.07	0.000	0.000	0.01	0.01	0.03	0.000	0.001		

Drop Shape Image Analysis

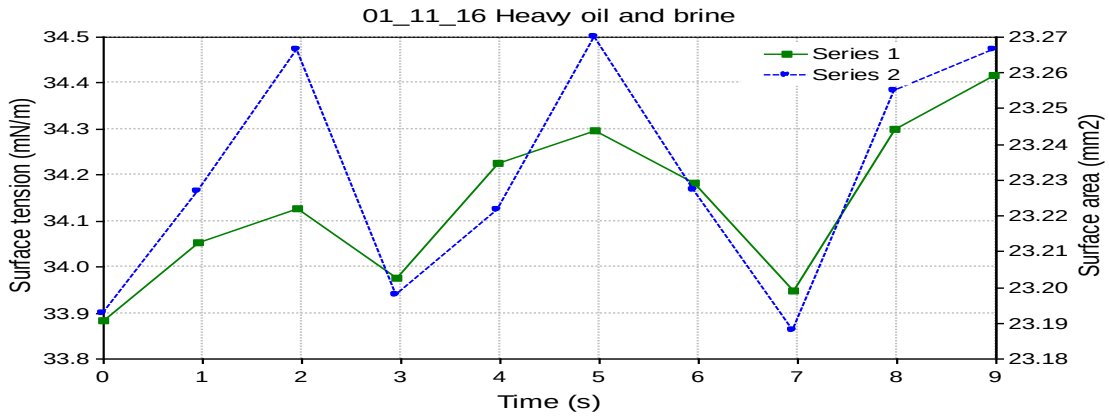

Date : 11/1/2016 Remarks : Comments here
Experiment : 01_11_16 Heavy oil and brine_17 Method : 01_11_16 heavy oil and brine.met
Drop phase : Heavy Oil Density : 0.9322
Extern.phase : Brine (5%) Density : 0.6600
Solid phase : Steel Calculation : Optimized cont.

No.	Time	Gamma	Beta	R0	Area	Volume	Theta	Height	Width	Opt	Messages
1	0.0	33.88	0.137	1.316	23.19	10.99	143.23	2.875	2.701	2	
2	1.0	34.05	0.136	1.318	23.23	11.02	143.26	2.874	2.704	3	
3	2.0	34.13	0.136	1.319	23.27	11.05	143.29	2.879	2.706	3	
4	2.9	33.98	0.136	1.317	23.20	11.00	143.26	2.874	2.702	3	
5	4.0	34.23	0.135	1.317	23.22	11.01	143.39	2.875	2.702	3	
6	5.0	34.30	0.135	1.319	23.27	11.05	143.37	2.877	2.707	3	
7	6.0	34.18	0.136	1.318	23.23	11.02	143.35	2.876	2.704	3	
8	6.9	33.95	0.136	1.316	23.19	10.99	143.26	2.874	2.702	3	
9	8.0	34.30	0.135	1.319	23.26	11.04	143.39	2.876	2.706	3	
10	9.0	34.42	0.135	1.319	23.27	11.05	143.43	2.875	2.707	3	
Mean:		34.14	0.136	1.318	23.23	11.02	143.32	2.875	2.704		
Stand.dev.:		0.05	0.000	0.000	0.01	0.01	0.02	0.000	0.001		

Drop Shape Image Analysis

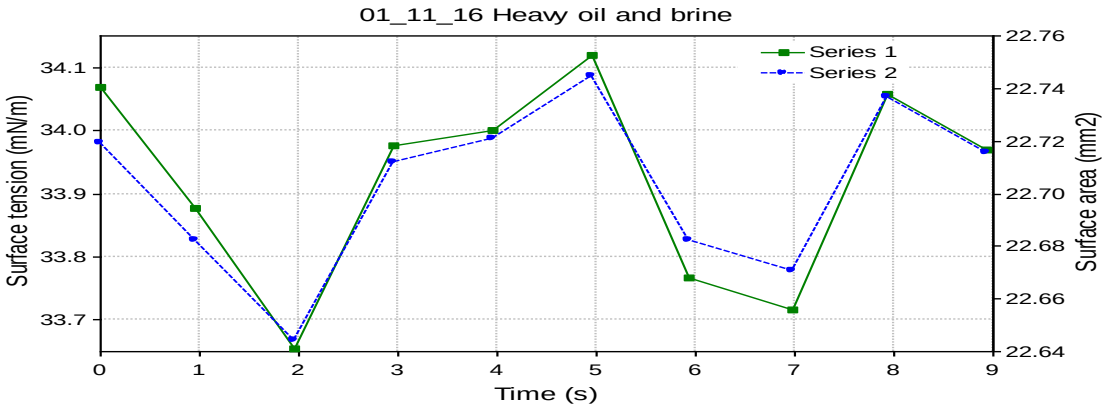

Date : 11/1/2016 Remarks : Comments here
Experiment : 01_11_16 Heavy oil and brine_18 heavy oil and brine.met Method : 01_11_16
Drop phase : Heavy Oil Density : 0.9322
Extern.phase : Brine (5%) Density : 0.6600
Solid phase : Steel Calculation : Optimized cont.

No.	Time	Gamma	Beta	R0	Area	Volume	Theta	Height	Width	Opt	Messages
1	0.0	34.07	0.134	1.306	22.72	10.68	143.59	2.835	2.680	2	
2	1.0	33.88	0.134	1.304	22.68	10.66	143.54	2.835	2.676	3	
3	2.0	33.65	0.135	1.303	22.64	10.62	143.46	2.833	2.674	3	
4	3.0	33.98	0.134	1.305	22.71	10.68	143.55	2.835	2.680	2	
5	3.9	34.00	0.134	1.306	22.72	10.69	143.58	2.836	2.680	3	
6	5.0	34.12	0.133	1.306	22.74	10.70	143.64	2.837	2.681	3	
7	5.9	33.77	0.134	1.304	22.68	10.65	143.49	2.834	2.676	3	
8	7.0	33.72	0.135	1.304	22.67	10.65	143.47	2.834	2.675	3	
9	7.9	34.06	0.134	1.306	22.74	10.70	143.58	2.836	2.681	3	
10	8.9	33.97	0.134	1.305	22.72	10.68	143.57	2.836	2.680	3	
Mean:		33.92	0.134	1.305	22.70	10.67	143.55	2.835	2.678		
Stand.dev.:		0.05	0.000	0.000	0.01	0.01	0.02	0.000	0.001		

Drop Shape Image Analysis

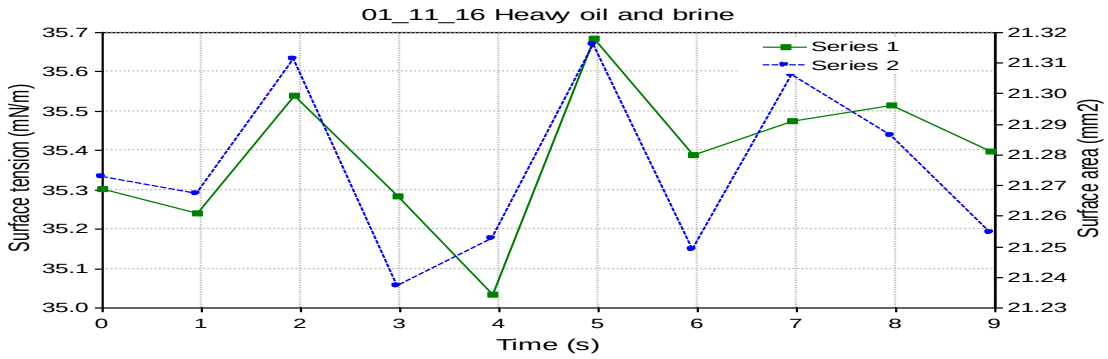

Date : 11/1/2016 Remarks : Comments here
Experiment : 01_11_16 Heavy oil and brine_20 Method : 01_11_16 heavy oil and brine.met
Drop phase : Heavy Oil Density : 0.9322
Extern.phase : Brine (5%) Density : 0.6600
Solid phase : Steel Calculation : Optimized cont.

No.	Time	Gamma	Beta	R0	Area	Volume	Theta	Height	Width	Opt	Messages
1	0.0	35.30	0.123	1.273	21.27	9.76	144.70	2.709	2.607	2	
2	0.9	35.24	0.123	1.273	21.27	9.76	144.67	2.709	2.607	2	
3	1.9	35.54	0.122	1.275	21.31	9.80	144.76	2.710	2.609	2	
4	3.0	35.28	0.122	1.272	21.24	9.74	144.70	2.707	2.605	2	
5	3.9	35.03	0.123	1.272	21.25	9.75	144.61	2.709	2.607	2	
6	5.0	35.68	0.122	1.275	21.32	9.80	144.78	2.709	2.611	2	
7	6.0	35.39	0.122	1.273	21.25	9.75	144.71	2.707	2.607	2	
8	7.0	35.47	0.122	1.274	21.31	9.79	144.83	2.714	2.608	2	
9	7.9	35.51	0.122	1.274	21.29	9.78	144.69	2.708	2.610	2	
10	9.0	35.40	0.122	1.273	21.25	9.75	144.72	2.707	2.607	2	
Mean:		35.39	0.122	1.274	21.28	9.77	144.72	2.709	2.608		
Stand.dev.:		0.06	0.000	0.000	0.01	0.01	0.02	0.001	0.001		

Drop Shape Image Analysis

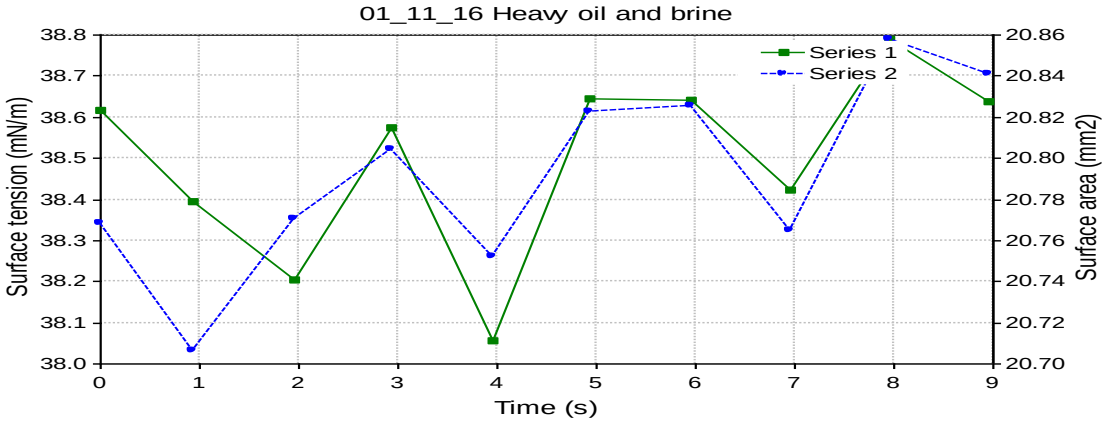

Date : 11/1/2016 Remarks : Comments here
Experiment : 01_11_16 Heavy oil and brine_21 Method : 01_11_16 heavy oil and brine.met
Drop phase : Heavy Oil Density : 0.9322
Extern.phase : Brine (5%) Density : 0.6600
Solid phase : Steel Calculation : Optimized cont.

No.	Time	Gamma	Beta	R0	Area	Volume	Theta	Height	Width	Opt	Messages
1	0.0	38.62	0.111	1.267	20.77	9.47	145.66	2.651	2.588	2	
2	0.9	38.39	0.111	1.264	20.71	9.43	145.64	2.647	2.584	2	
3	2.0	38.21	0.112	1.266	20.77	9.47	145.58	2.654	2.586	2	
4	2.9	38.57	0.111	1.267	20.80	9.49	145.70	2.655	2.590	2	
5	4.0	38.06	0.112	1.265	20.75	9.45	145.59	2.654	2.586	2	
6	4.9	38.64	0.111	1.268	20.82	9.51	145.64	2.655	2.591	2	
7	6.0	38.64	0.111	1.268	20.83	9.50	145.70	2.656	2.591	2	
8	6.9	38.42	0.111	1.266	20.76	9.47	145.61	2.652	2.588	2	
9	8.0	38.79	0.111	1.269	20.86	9.53	145.71	2.656	2.593	2	
10	8.9	38.64	0.111	1.268	20.84	9.51	145.82	2.658	2.590	2	
Mean:		38.50	0.111	1.267	20.79	9.48	145.67	2.654	2.589		
Stand.dev.:		0.07	0.000	0.000	0.01	0.01	0.02	0.001	0.001		

Drop Shape Image Analysis

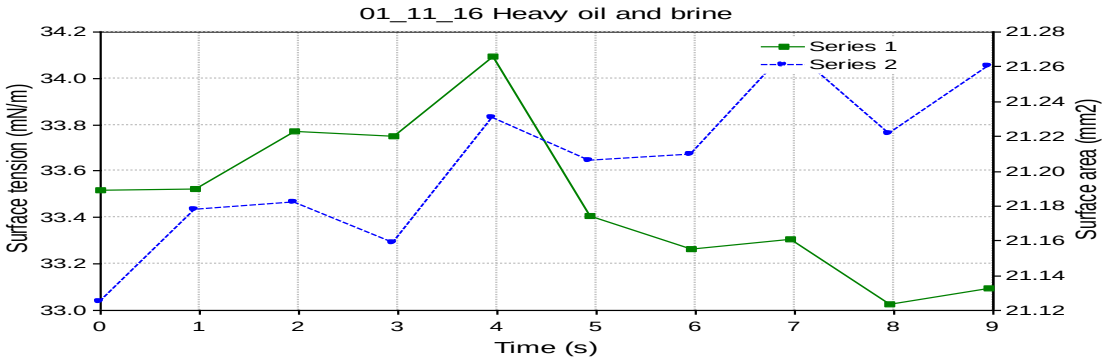

Date	: 11/1/2016	Remarks	: Comments here
Experiment	: 01_11_16 Heavy oil and brine_22	Method	: 01_11_16 heavy oil and brine.met
Drop phase	: Heavy Oil	Density	: 0.9322
Extern.phase	: Brine (5%)	Density	: 0.6600
Solid phase	: Steel	Calculation	: Optimized cont.

No.	Time	Gamma	Beta	R0	Area	Volume	Theta	Height	Width	Opt	Messages
1	0.0	33.52	0.127	1.265	21.12	9.64	144.31	2.715	2.592	2	
2	0.9	33.52	0.128	1.267	21.18	9.68	144.23	2.720	2.597	3	
3	2.0	33.77	0.127	1.267	21.18	9.68	144.32	2.717	2.597	2	
4	3.0	33.75	0.127	1.266	21.16	9.67	144.35	2.715	2.594	3	
5	3.9	34.09	0.126	1.269	21.23	9.72	144.39	2.718	2.602	3	
6	4.9	33.41	0.128	1.267	21.21	9.70	144.17	2.721	2.596	2	
7	6.0	33.26	0.129	1.267	21.21	9.70	144.13	2.723	2.596	2	
8	7.0	33.31	0.129	1.269	21.27	9.74	144.07	2.728	2.602	2	
9	7.9	33.02	0.130	1.267	21.22	9.70	143.98	2.726	2.598	3	
10	9.0	33.10	0.130	1.268	21.26	9.73	144.00	2.729	2.601	3	
Mean:		33.48	0.128	1.267	21.20	9.70	144.20	2.721	2.598		
Stand.dev.:		0.10	0.000	0.000	0.01	0.01	0.05	0.002	0.001		

APPENDIX C Viscometrics

HPAM concentration (ppm)	Viscosity @low shear (cp)	Viscosity @ high shear (cp)	Viscosity @ trendline (cp)	Viscosity @ 40°C (cp)	Viscosity @ 100°C (cp)	Viscosity @170 °C (cp)
2000	85.9	30.0	55	57.2	29.0	19.6
1600	63.3	17.7	29.0	31.6	12.4	7.2
1200	33.0	12.0	18.0	20.3	10.8	7.5
800	22.0	7.0	13.0	13.6	7.2	4.9
400	17.3	1.7	5.0	9.3	3.2	1.7

HPAM concentration (ppm)	Mobility Ratio @ low shear	Mobility ration @ high shear	Mobility ratio @ trendline	Mobility ratio @ 40°C	Mobility ratio @ 100°C (cp)	Mobility ratio @170 °C (cp)
2000	0.1129	0.3233	0.1764	0.1696	0.3345	0.4949
1600	0.1532	0.5480	0.3345	0.3070	0.7823	1.3472
1200	0.2939	0.8083	0.5389	0.4778	0.8981	1.2933
800	0.4409	1.3857	0.7462	0.7132	1.3472	1.9796
400	0.5607	5.7059	1.9400	1.0430	3.0313	5.7059

Time	S. Rate	S. Stress	Viscosity
30	100	6.5	31
60	75	5.8	37.4
90	50	5.2	50.1
120	25	4.5	85.8
150	25	4.5	85.9
180	50	5.2	49.6
210	75	5.8	36.9
240	100	6.4	30.9
270	100	6.4	30.8
300	75	5.7	36.7
330	50	5.1	48.6
360	25	4.4	83.5
390	25	4.4	84.2
420	50	5.1	48.8
450	75	5.7	36.6
480	100	6.5	31
510	100	6.5	31.1
540	75	5.8	37.3
570	50	5.2	49.8
600	25	4.4	84.5
630	25	4.4	84.6
660	50	5.1	49.2
690	75	5.8	37.2
720	100	6.5	31.2

n	K
0.2597	1.82928
0.2735	1.70482
0.275	1.71606
0.2682	1.75905
0.2661	1.77172
0.2626	1.79652
0.2593	1.81856

Time	Shear Rate	Shear Stress	Viscosity	RPM	Temp	Press
30	100	3.1	14.7	59	72.4	2.6
60	75	2.8	17.8	44	72.5	2.6
90	50	2.4	23.3	29	72.6	2.6
120	25	3.1	59.7	15	72.7	2.6
150	25	3.2	60.9	15	72.7	2.5
180	50	2.5	24.4	29	72.8	2.7
210	75	2.8	18.1	44	72.8	2.5
240	100	3.1	14.9	59	72.9	2.4
270	100	3.1	14.7	59	72.9	2.5
300	75	2.8	17.8	44	72.8	2.4
330	50	2.5	23.6	29	72.8	2.4
360	25	3.1	59.2	15	72.8	2.6
390	25	3.3	63.3	15	72.6	2.5
420	50	2.6	25.1	29	72.6	2.4
450	75	2.8	18.2	44	72.5	2.6
480	100	3.1	15	59	72.4	2.5
510	100	3.1	14.8	59	72.3	2.6
540	75	2.8	17.9	44	72.2	2.6
570	50	2.5	23.8	29	72.1	2.3
600	25	2.9	56	15	71.9	2.4
630	25	3.2	61.7	15	71.7	2.4
660	50	2.6	24.9	29	71.6	2.2
690	75	2.7	17.5	44	71.5	2.4
720	100	3	14.4	59	71.3	2.5

Time	Viscosity	Shear Rate	Shear stress	RPM	Temp	Press
30	12.4	100	2.6	59	69	2.7
60	14.6	75	2.3	44	69.3	2.9
90	18.7	50	2	29	69.5	2.9
120	32	25	1.7	15	69.9	2.9
150	31.4	25	1.6	15	70.2	3
180	19	50	2	29	70.5	3
210	14.8	75	2.3	44	70.7	2.9
240	12.2	100	2.6	59	71	2.9
270	12.3	100	2.6	59	71.2	3
300	14.5	75	2.3	44	71.4	2.8
330	19	50	2	29	71.6	2.9
360	29.1	25	1.5	15	71.8	3
390	30.6	25	1.6	15	72	2.8
420	18.2	50	1.9	29	72.2	2.8
450	13.7	75	2.1	44	72.3	2.8
480	11.6	100	2.4	59	72.4	2.8
510	11.7	100	2.4	59	72.5	2.8
540	13.9	75	2.2	44	72.6	2.5
570	18.4	50	1.9	29	72.7	2.8
600	29.6	25	1.5	15	72.7	2.7
630	29.7	25	1.5	15	72.8	2.6
660	18	50	1.9	29	72.7	2.7
690	13.5	75	2.1	44	72.8	2.8
720	11.4	100	2.4	59	72.8	2.7

n	K
0.2807	0.60117
0.3259	0.53273
0.3093	0.54079
0.3395	0.47107
0.3358	0.47544
0.3259	0.48915
0.3009	0.52361

Time	Viscosity	Shear Rate	Shear stress	RPM	Temp	Press
30	100	2	9.5	59	27.5	4.4
60	75	1.7	10.7	44	27.5	4.3
90	50	1.4	13.2	29	27.5	4.2
120	25	1.1	20.4	15	27.5	4.2
150	25	1.1	20.3	15	27.5	4.1
180	50	1.4	13.1	29	28.1	4.1
210	75	1.6	10.4	44	29.3	4.1
240	100	1.8	8.9	59	30.8	4.2
270	100	1.8	8.7	59	32.4	4.1
300	75	1.6	10.1	44	34	4
330	50	1.3	12.8	29	35.7	3.9
360	25	1	19.3	15	37.7	4.2
390	25	1	19.9	15	39.7	4
420	50	1.3	12.6	29	41.1	4
450	75	1.6	10.1	44	42.5	3.9
480	100	1.8	8.4	59	43.8	3.8
510	100	1.8	8.4	59	45	4.1
540	75	1.5	9.8	44	46.1	4.1
570	50	1.3	12.6	29	47.2	3.9
600	25	1	19.7	15	48.6	3.9
630	25	1.1	20.3	15	49.9	4
660	50	1.3	12.4	29	50.8	3.9
690	75	1.5	9.5	44	51.7	3.9
720	100	1.7	8.1	59	52.6	3.9

Time	viscosity	shear rate	Shear stress	RPM	Temp	Pressure
30	1.8	100	0.4	59	68.4	2.4
60	2.3	75	0.4	44	68.7	2.7
90	5.2	50	0.5	29	69.1	2.7
120	11.3	25	0.6	15	69.4	2.6
150	11.2	25	0.6	15	69.8	2.7
180	4.4	50	0.5	29	70	2.5
210	2.5	75	0.4	44	70.3	2.6
240	1.7	100	0.4	59	70.5	2.5
270	1.9	100	0.4	59	70.8	2.7
300	2.3	75	0.4	44	71	2.6
330	3	50	0.3	29	71.2	2.7
360	15.4	25	0.8	15	71.4	2.6
390	14.9	25	0.8	15	71.6	2.7
420	6.7	50	0.7	29	71.8	2.6
450	4.7	75	0.7	44	72	2.7
480	3.2	100	0.7	59	72.1	2.8
510	3	100	0.6	59	72.2	2.7
540	5.6	75	0.9	44	72.3	2.6
570	7.7	50	0.8	29	72.3	2.7
600	17.3	25	0.9	15	72.3	2.6
630	15.6	25	0.8	15	72.6	2.5
660	6.7	50	0.7	29	72.7	2.6
690	3	75	0.5	44	72.8	2.4
720	3	100	0.6	59	72.9	2.7

APPENDIX D Ultrasound- Polymer Injections

1. Horizontal Ultrasound polymer injection

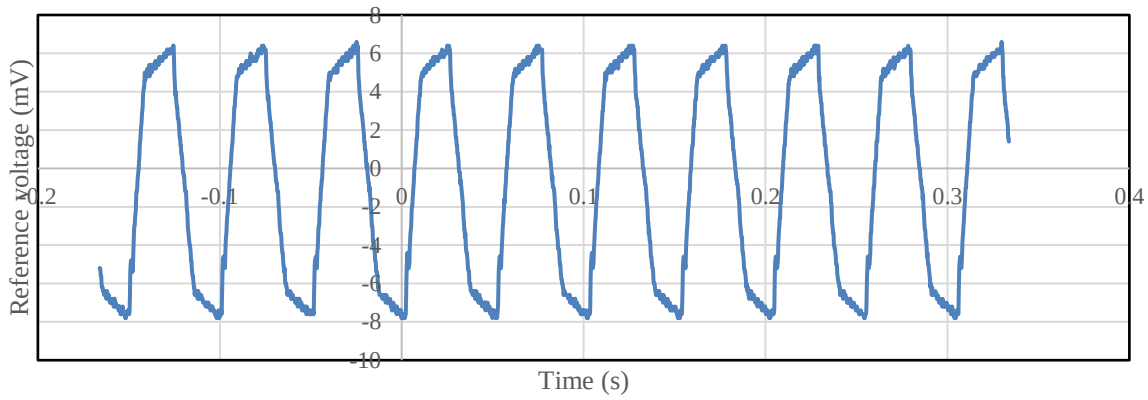

Figure 5.1 Berea Upper sandstone ultrasound and polymer flooding acoustic coupling (Transmitter)

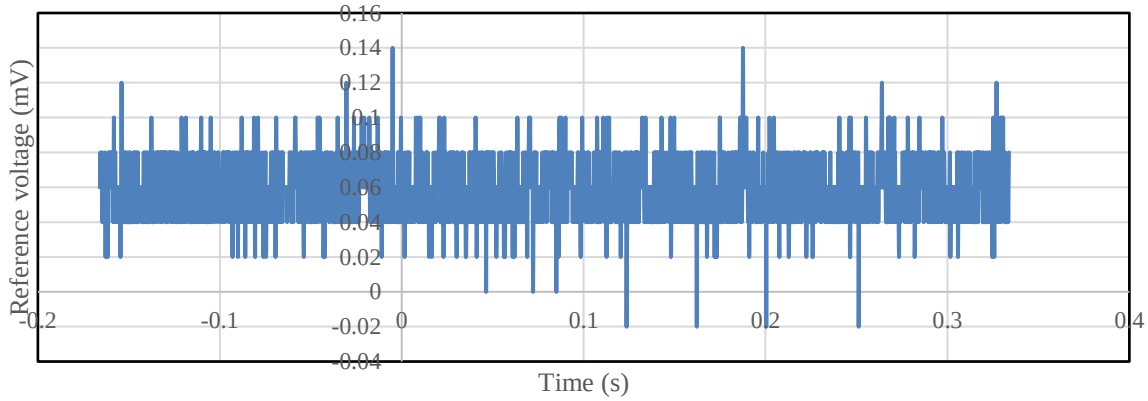

Figure 5.2 Berea Upper sandstone ultrasound and polymer flooding acoustic coupling (Receiver)

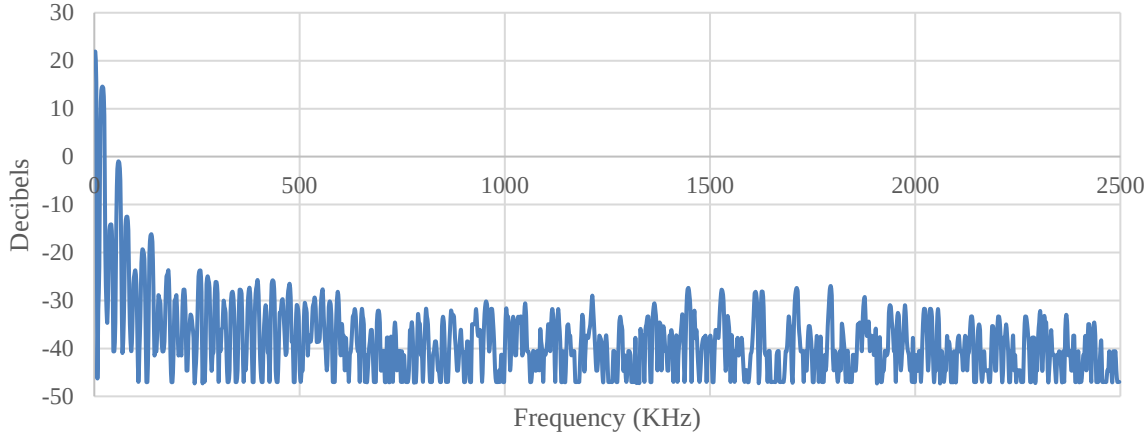

Figure 5.3 Fast Fourier Transform (FFT) showing Spectral view of 20KHz frequency domain for vibration analysis

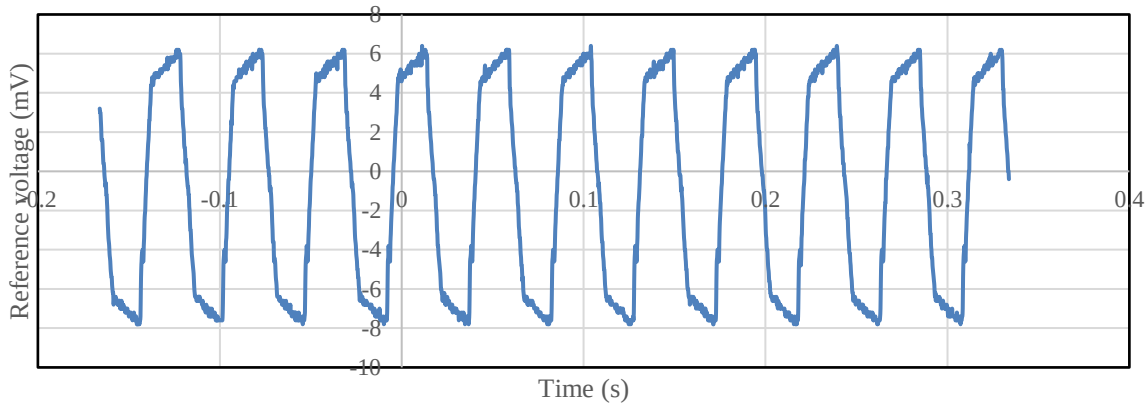

Figure 5.4 Indiana limestone ultrasound and polymer flooding acoustic coupling (Transmitter)

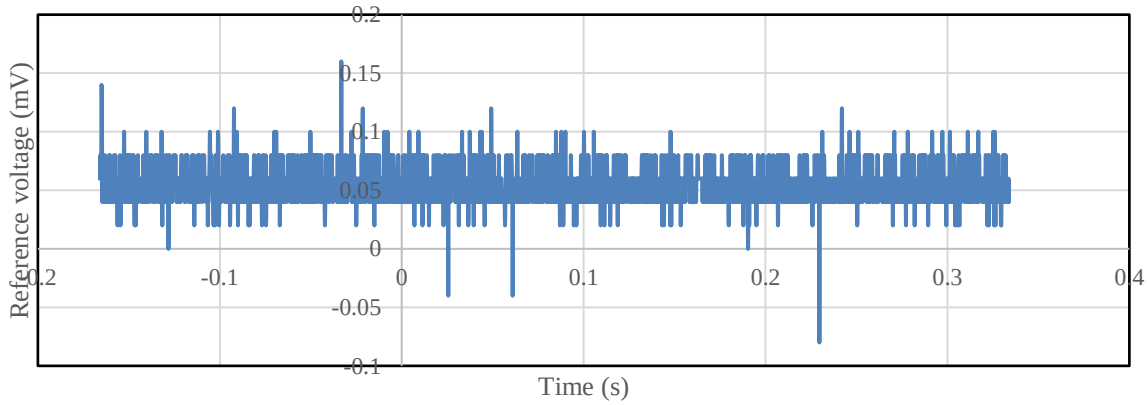

Figure 5.5 Indiana limestone ultrasound and polymer flooding acoustic coupling (Receiver)

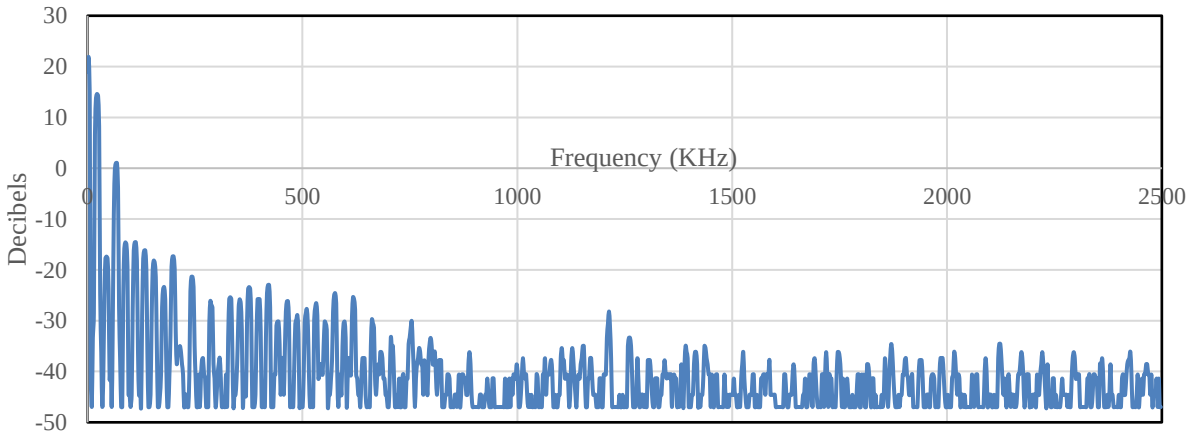

Figure 5.6 Fast Fourier Transform (FFT) showing Spectral view of 20KHz frequency domain for vibration analysis for Indiana limestone

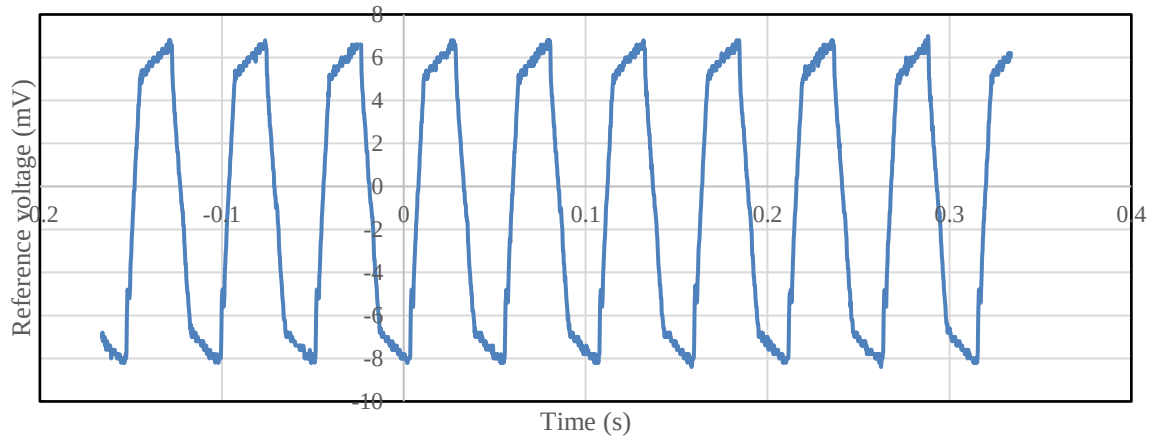

Figure 5.7 Edward brown ultrasound and polymer flooding acoustic coupling (Transmitter)

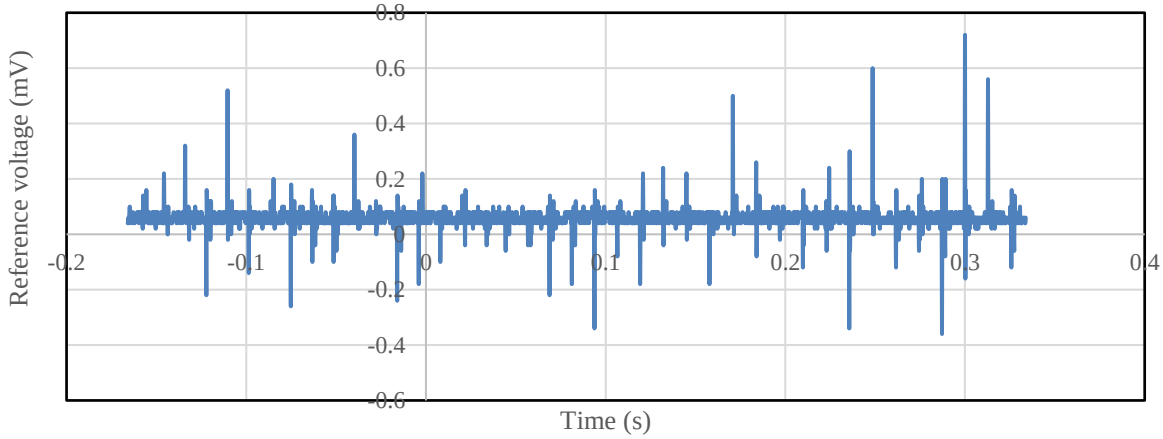

Figure 5.8 Edward brown ultrasound and polymer flooding acoustic coupling (Receiver)

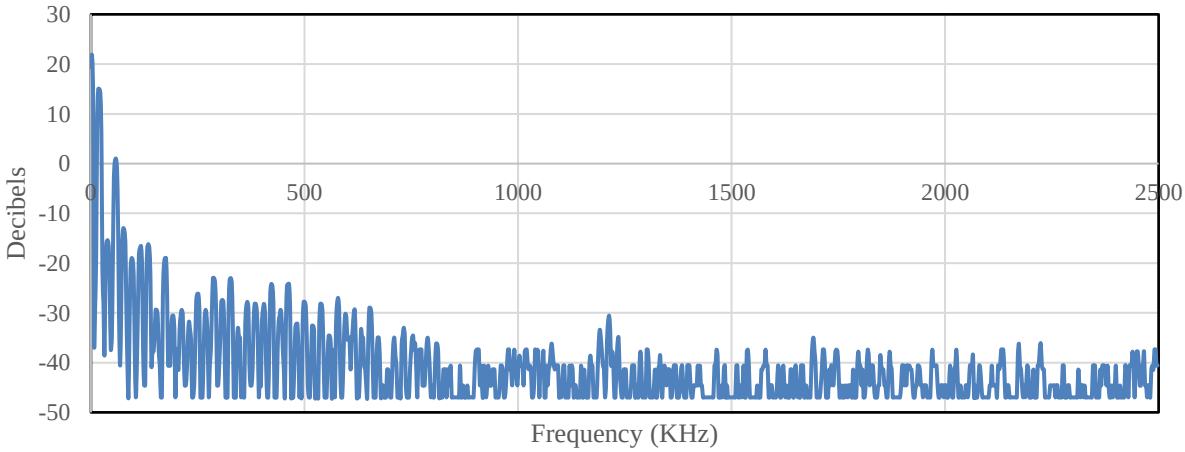

Figure 5.9 Fast Fourier Transform (FFT) showing Spectral view of 20KHz frequency domain for vibration analysis for Edward brown

2. Vertical Ultrasound polymer injection

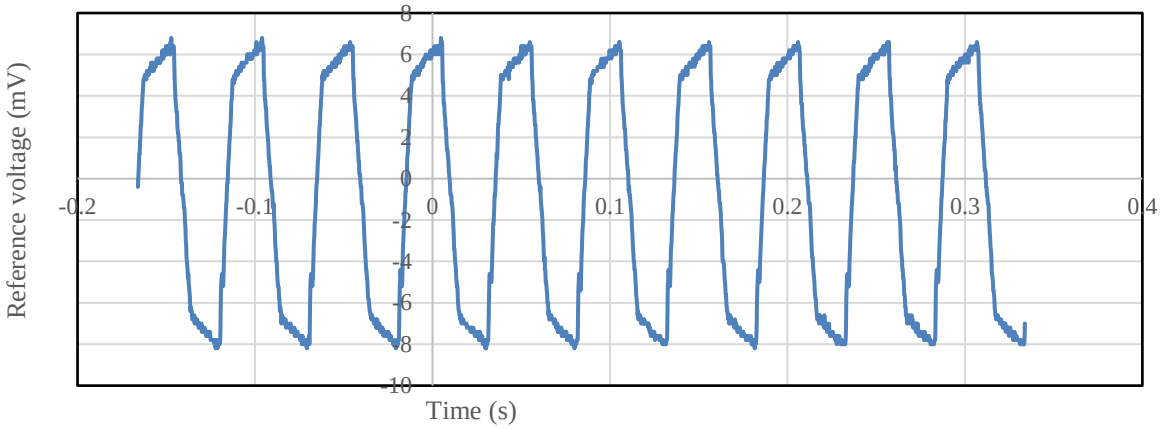

Figure 5.10 Berea Upper sandstone ultrasound and polymer flooding acoustic coupling (Transmitter)

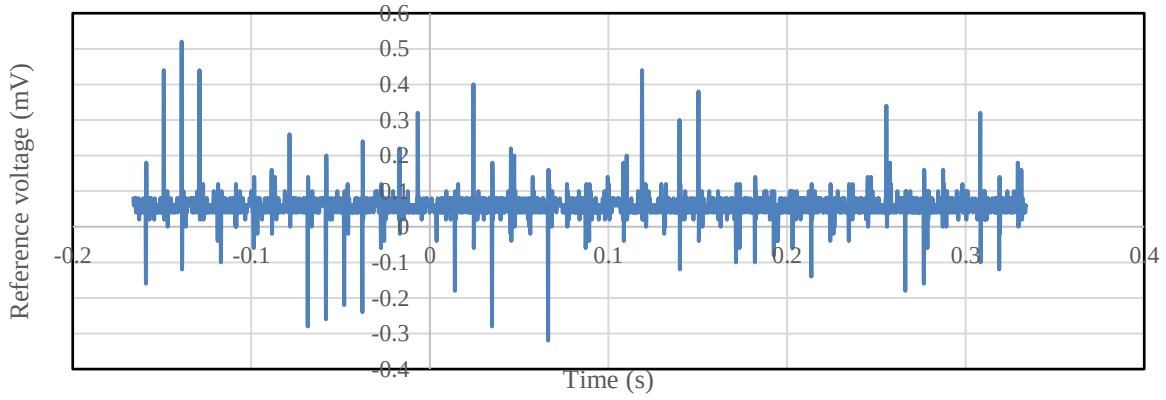

Figure 5.11 Berea upper sandstone ultrasound and polymer flooding acoustic coupling (Receiver)

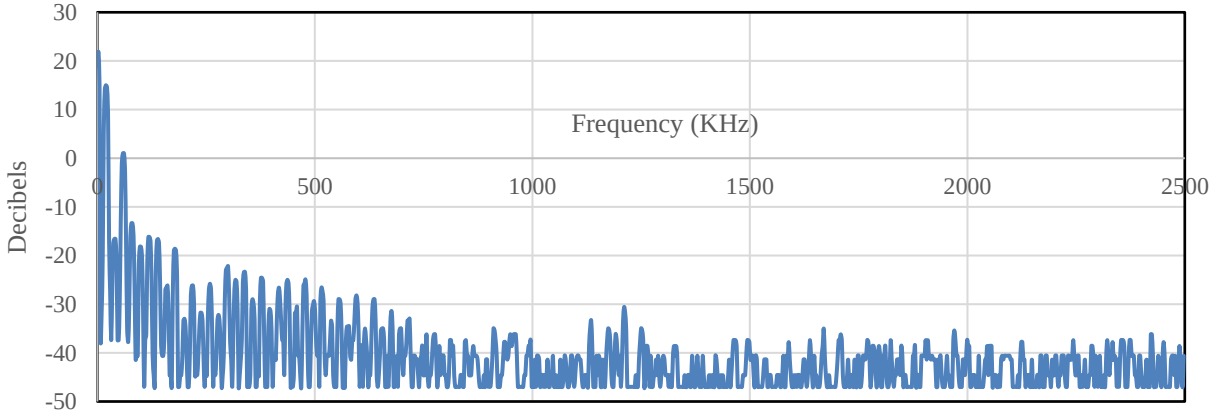

Figure 5.12 Berea upper sandstone Fast Fourier Transform (FFT) showing Spectral view of 20KHz frequency domain for vibration analysis

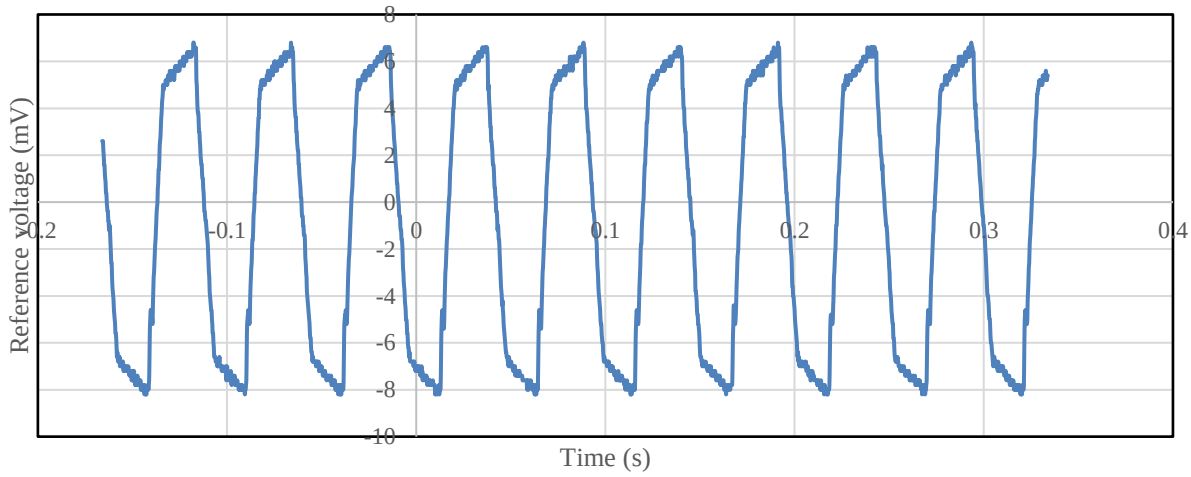

Figure 5.13 Indiana limestone ultrasound and polymer flooding acoustic coupling (Transmitter)

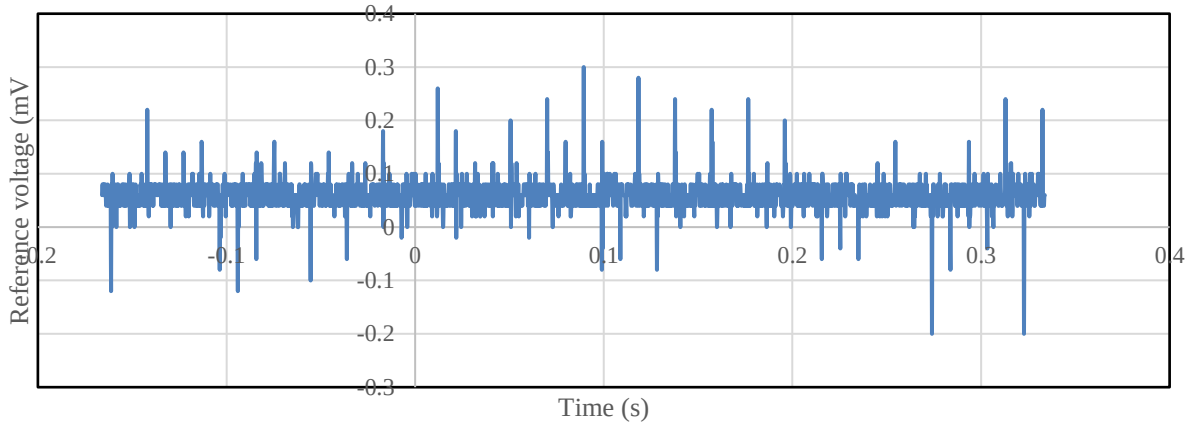

Figure 5.14 Indiana limestone ultrasound and polymer flooding acoustic coupling (Receiver)

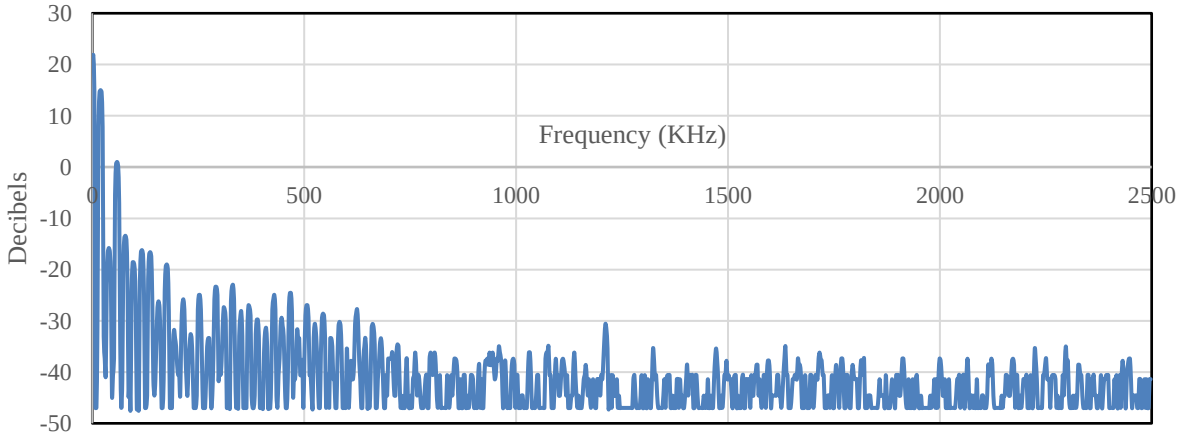

Figure 5.15 Fast Fourier Transform (FFT) showing Spectral view of 20KHz frequency domain for vibration analysis

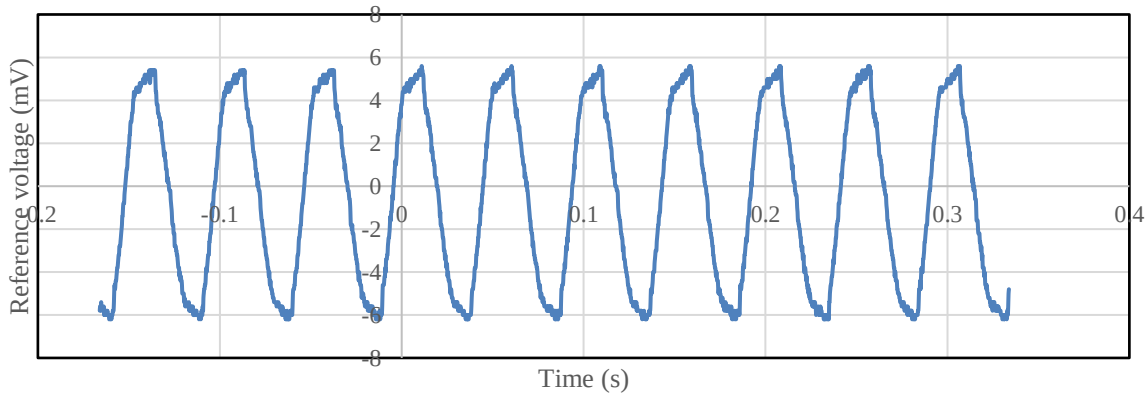

Figure 5.16 Indiana limestone ultrasound and polymer flooding acoustic coupling (Transmitter)

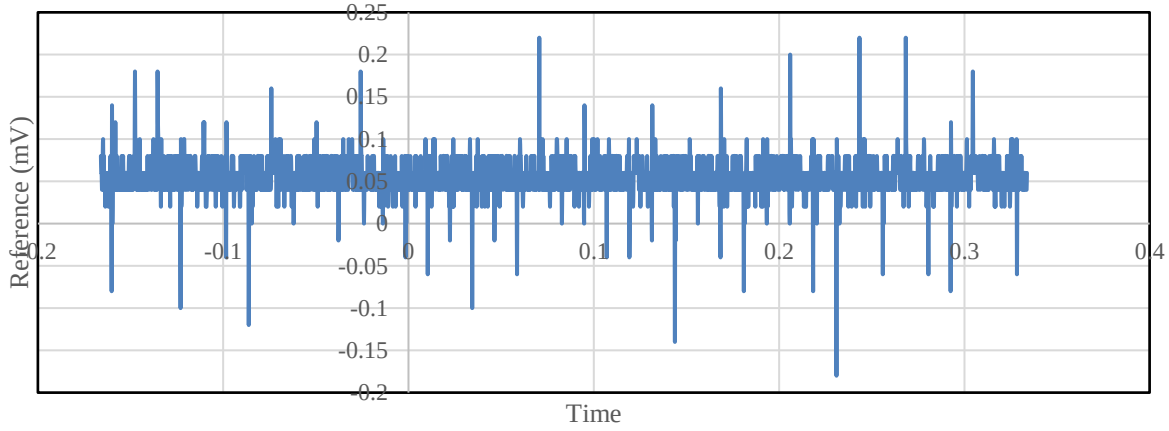

Figure 5.17 Indiana limestone ultrasound and polymer flooding acoustic coupling (Receiver)

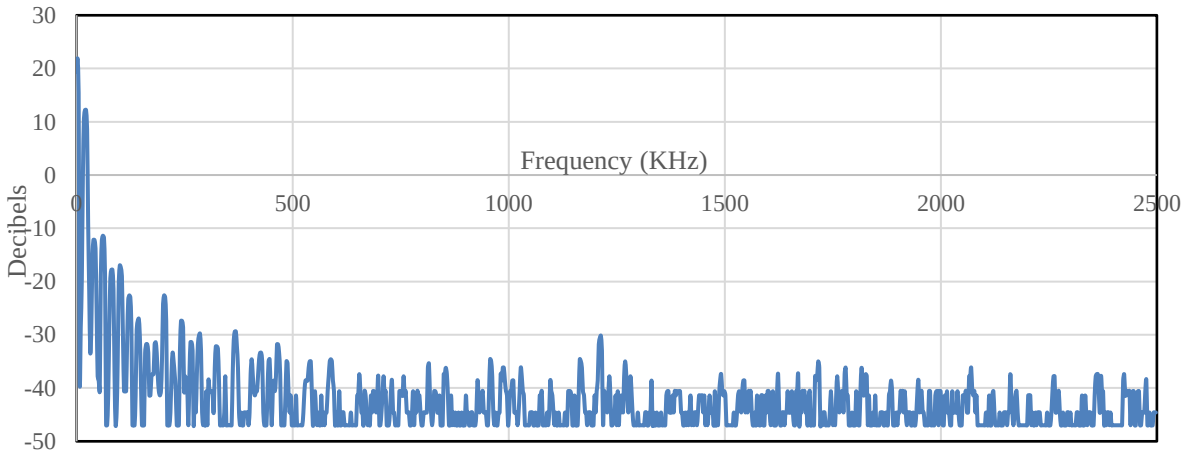

Figure 5.18 Fast Fourier Transform (FFT) showing Spectral view of 20KHz frequency domain for vibration analysis

APPENDIX E Publications in Press (Under review)

Hysteresis and polymer polydispersity for Design and Rheological Characterisation of HPAM Polymer solutions for enhanced oil recovery

K.J. Hassan *, G.C. Enyi and G. G. Nasr

Petroleum and Gas Engineering, University of Salford, Manchester, United Kingdom

Abstract

The study of the flow behaviour of polymer solutions used for enhancing oil recovery is vital in understanding polymer flooding recovery mechanisms and oil recovery potentials when injected into the reservoir. This experimental study investigates the rheology and hysteresis properties of hydrolysed polyacrylamide (HPAM) polymer, in conjunction with polydispersity, for the design and characterisation of field polymer for enhanced oil recovery. Experiments were conducted with the OFITE Model 1100 pressurised viscometer with computer system control which features ORCADA data acquisition software. HPAM solutions of varying concentration and molecular weight distribution were subjected to shear rates in forward (stretch) and reverse (contraction) cycle mode to obtain hysteresis behaviour. The viscometer enabled rheological characterisation of the polymer fluid through generation of viscosity and viscoelasticity data as well as fluid flow behavioural indices. All rheological tests were conducted at reservoir temperatures of 70^{o}C (±2^{o}C). The results obtained from the experiments indicated that polymer hysteresis behaviour is influenced by polymer concentration. The higher the polymer concentration, the larger the hysteresis envelope observed as well as the greater the polymer oil displacement potential. With uniform shear rates of 25 to 100s^{-1} applied on the polymer solutions, the shear stress of hysteresis envelopes increased as polymer concentration increased, ranging from 0.8 to 1.2 lb/100ft^2 (for 400ppm), 1.2lb/100ft^2 to 2.0lb/100ft^2 (for 800ppm) and 1.5lb/100ft^2 to 2.7lb/100ft^2 (for 1200ppm). The size of hysteresis envelope increased with higher concentration at1600ppm and 2000ppm.

Core flooding, at reservoir pressures of 2,000 to 3,000psi and reservoir temperature of 40^{o}C (±2^{o}C) with 400ppm, 800ppm and 1,200ppm HPAM polymer solution produced incremental oil of 30.67%, 37.37% and 41.03% respectively. Though the polymer concentration was varied, the polymer polydispersity was maintained high and constant.

Keywords: Hydrolysed polyacrylamide, hysteresis, viscosity, viscoelasticity, enhanced oil recovery

Green technology: ultrasound enhanced oil recovery in sandstone and carbonate reservoirs

Kabiru J. Hassan, Godpower.C Enyi. and Ghasem. G. Nasr

Petroleum Technology Research Group, University of Salford, Manchester, United Kingdom

Abstract

The decline in oil recovery from existing oil wells and high cost of production and the need for low cost environmentally friendly recovery methods has made ultrasound enhanced oil recovery gain global research attention. In this experimental investigation two major conventional reservoir rocks were considered. Saturated sandstone and carbonate core samples of 1x2inch dimensions were subjected to ultrasound. The frequency applied was 20KHz (±0.5). The ultrasound waves were applied in the secondary recovery stage to determine the efficacy and efficiency of ultrasound wave propagation in a saturated porous media at reservoir conditions - 2,000 to 3,000psi to deplete residual oil saturation. During the initial waterflooding process, the maximum oil recovered from Berea sandstone and Indiana limestone cores were 29.1% and 31.9% of original oil in place (OOIP). However, with the simultaneous application of waterflooding and introduction of ultrasound, the oil recovery after injection of 5PV rose to 69.5% for Berea sandstone and 61.1% for Indiana limestone. Recovery from the sandstones was higher than in carbonate reservoirs. With every injected pore volume an incremental volume of oil was recovered. Though, the total volume of oil recovered increased, the incremental volumes of oil recovered decreased with each additional pore volume injected. The incremental oil volume obtained as additional pore volumes were injected was attributed to the depletion of residual oil saturation (ROS). In a nutshell, this experimental investigation indicated the potentials of ultrasound in depleting residual oil saturation in enhanced oil recovery at reservoir conditions.

Keywords: ultrasound, oil, recovery, frequency, residual oil saturation

Residual oil desaturation potentials of hydrolysed polyacrylamide polymer solutions

Kabiru J. Hassan, Godpower.C Enyi. and Ghasem. G. Nasr

Petroleum Technology Research Group, University of Salford, Manchester, United Kingdom

Abstract

The injection of hydrolysed polyacrylamide (HPAM) polymer solution into the reservoir increases both macroscopic and microscopic sweep efficiency. Thus, favourable mobility ratio between oil and water is enhanced. This experimental study investigated the potentials of hydrolysed polyacrylamide polymer solution to deplete residual oil saturation. The rheological properties of the HPAM polymer solutions at 400ppm, 800ppm and 1200ppm were determined at 70^{o}C (±2) with Model 110 pressurised viscometer with ORCADA data acquisition software. The fluid flow properties and behavioural indices obtained indicated characteristics of a pseudoplastic fluid. Through coreflooding at pump pressures of 1500 to 2000psi, oil was recovered from 1 x 3-inch saturated Berea upper sandstone reservoir core samples with injection of high molecular weight hydrolysed polyacrylamide of 22-24 million Daltons. The mobility ratio at 40 ^{o}C for 400ppm, 800ppm and 1200ppm HPAM polymer concentrations were determined as 0.874, 0.688 and 0.478 respectively. During coreflooding to displace 9.7cp oil, the incremental oil recovery from saturated core of Berea sandstone, after initial primary recovery was highest for 1200ppm followed by 800ppm then 400ppm and least was waterflooding. The residual oil saturations after 5PV injections were 18.99%, .35.56%, 41.85% and 63.34% for 1200ppm, 800ppm, 400ppm and waterflooding respectively. From the results obtained, the higher the concentration of high molecular weight polyacrylamide in injection solution the greater the residual oil desaturation.

Keywords: hydrolysed polyacrylamide**,** residual oil saturation, enhanced oil recovery